Carla Alexandra da Cruz Marchão
Mestre em Engenharia de Estruturas

OPTIMISATION AND DESIGN OF POST-TENSIONING ANCHORAGE CORNER BLISTERS IN CONCRETE BOX GIRDER BRIDGES

Dissertação para obtenção do Grau de Doutor em Engenharia Civil, Especialidade Estruturas

Orientador: Válter José da Guia Lúcio,
Professor Associado, FCT/UNL
Co-orientador: Hans-Rudolf Ganz,
Ganz Consulting

Júri:

Presidente: Prof. Doutor António Manuel Flores Romão de Azevedo Gonçalves Coelho
Arguentes: Prof. Doutor João Carlos de Oliveira Fernandes de Almeida
Prof. Doutor António Lopes Batista

Vogais: Prof. Doutor Francisco Baptista Esteves Virtuoso
Prof. Doutor Válter José da Guia Lúcio
Profª. Doutora Sandra da Conceição Barbosa Nunes
Prof. Doutor António Manuel Pinho Ramos

FACULDADE DE CIÊNCIAS E TECNOLOGIA
UNIVERSIDADE NOVA DE LISBOA

Outubro 2015

To Pedro, Tócas, Leonor and Matilde

Acknowledgments

Throughout these years, there were many people whose contributions, incentive and support have been crucial to conclude this thesis.

First, I would like to thank my supervisor Professor Valter Lúcio for all his valuable insights, fruitful discussions, knowledgeable comments, encouragement and friendship along the years, as well as for accepting my ideas and views.

I also would like to thank my co-supervisor Dr. Hans Rudolf Ganz for his advice and availability to comment and discuss contents and ways forward in a very positive and constructive basis.

I am grateful to Prof. Carlos Chastre for the support on the laboratory tests and Prof. Pinho Ramos for the openness to discuss specific subjects of the research.

For the development of the HPFRC, my appreciation goes to Prof. Sandra Nunes and Prof. Joaquim Figueiras, from FEUP. The HPFRC development was financed by FEDER funds under the Operational Program Factors of Competiveness - COMPETE and by National Funds under FCT - Foundation for Science and Technology through project PTDC/ECM/122446/2010 - Engineered high performance fibre reinforced concrete materials: design, characterization and quality control.

My appreciation goes also to Prof. Ana Brás for the support in the implementation of the concrete production in large scale, tests of concrete in fresh state and rheology, and Dr. Miguel Lourenço for the assistance in the strut-and-tie models.

This research wouldn't have been possible without the sponsorship of industry partners and their representatives namely Dr. José Santiago, Eng. Romeu Reguengo and Eng. Pedro Lopes from Concremat - Prefabricação e Obras Gerais, S.A. for all the support for the construction of the multiple concrete models; Eng. Carlos Moniz from VSL for the financial support, for providing the post-tensioning material and components and for prestressing the specimens in the laboratory tests; Mr. Roland Schepers from KrampeHarex, Eng. Catarina Saraiva from MC-Bauchemie, Eng. Nídia Dias from Sika, Eng. Paulo Pinto from Omnya, Eng. Ângela Nunes from Secil, Eng. Nuno Campos from Teixeira Duarte for all the material and components required for producing the specimens.

This research was financed by FCT/MCTES - Portuguese Foundation for Science and Technology under Research Grant SFRH/BD/46257/2008.

I am also indebted to Eng. Nuno Mamede, Prof. Hugo Biscaia, Dr. Jan Cervenka and

Dr. Vladimir Cervenka for the support with the ATENA software.

My appreciation goes also to Prof. Jorge Pereira da Silva for translating papers from German to Portuguese.

The laboratory tests wouldn't have been possible without the support of the laboratory technicians José Gaspar and Jorge Silvério. I would also like to thank the valuable help of Eng. André Almeida, Eng. Hugo Fernandes and Eng. Micael Inácio.

I would like to thank Mrs. Maria da Luz Sousa and Mrs. Carla Teixeira by the always friendly and helpful support they gave me.

I also would like to acknowledge my colleague and friend Prof. Rui Marreiros for his support on the photographs of the specimens and the tests, and availability to discuss specific parts of the research.

For managing and organising all the logistics from VSL side, for his constant presence during the multiple laboratory tests and for his constant friendship and support I would like to express my sincere gratitude to my brother Vitor Marchão.

I would also like to express my sincere gratitude to Prof. Ana Rita Gião and to all other my friends for their patience, constant help and encouragement.

I would also like to thank my parents-in-law for their friendship and availability.

To my parents, for the unconditional love, care and support throughout my life, my heartfelt gratitude.

Last but not least, I thank my husband and my three children for being my light and my comfort, and for their endless love and presence on my side during all these years.

Abstract

The design of anchorage blisters of internal continuity post-tensioning tendons of bridges built by the cantilever method, presents some peculiarities, not only because they are intermediate anchorages but also because these anchorages are located in blisters, so the prestressing force has to be transferred from the blister the bottom slab and web of the girder.

The high density of steel reinforcement in anchorage blisters is the most common reason for problems with concrete cast *in situ*, resulting in zones with low concrete compacity, leading to concrete crushing failures under the anchor plates. A solution may involve improving the concrete compression and tensile strength.

To meet these requirements a high-performance fibre reinforced self-compacting mixture (HPFRC) was used in anchorage corner blisters of post-tensioning tendons, reducing the concrete cross-section and decreasing the reinforcement needed.

To assess the ultimate capacity and the adequate serviceability of the local anchorage zone after reducing the minimum concrete cross-section and the confining reinforcement, specified by the anchorage device supplier for the particular tendon, load transfer tests were performed.

To investigate the behaviour of anchorage blisters regarding the transmission of stresses to the web and the bottom slab of the girder, and the feasibility of using high performance concrete only in the blister, two half scale models of the inferior corner of a box girder existing bridge were studied: a reference specimen of ordinary reinforced concrete and a HPFRC blister specimen. The design of the reinforcement was based in the tensile forces obtained on strut-and-tie models.

An experimental program was carried out to assess the models used in design and to study the feasibility of using high performance concrete only in the blister, either with casting *in situ*, or with precast solutions.

A non-linear finite element analysis of the tested specimens was also performed and the results compared.

Keywords

post-tensioning, anchorage zones, high-performance concrete, self-compacting concrete, box girder bridge, steel fibres

Resumo

O dimensionamento dos blocos de ancoragem dos cabos de pré-esforço interiores de continuidade, de pontes construídas por avanços sucessivos, apresenta algumas particularidades por se tratar de ancoragens intermédias epor estas ancoragens se localizarem em blocos especialmente dimensionados para este efeito, sendo necessário assegurar a transmissão da força de pré-esforço para a alma e laje de fundo da secção.

A elevada densidade de armadura existente nos blocos de ancoragem constitui a causa mais frequente da ocorrência de roturas devido ao esmagamento do betão atrás da placa da ancoragem. Uma das soluções envolve o aumento da resistência do betão à compressão e à tracção.

Com o objectivo de reduzir as dimensões do bloco de ancoragem e diminuir a armadura de tracção e de confinamento necessárias, utilizou-se um betão auto-compactável de elevado desempenho com fibras metálicas (HPFRC).

Para avaliar a capacidade resistente e adequado comportamento em serviço das zonas de ancoragem após redução da secção transversal mínima de betão e da armadura de reforço, especificadas pelo sistema de pré-esforço, realizaram-se ensaios de transferência de carga.

Para analisar o comportamento dos blocos de ancoragem no que se refere à transmissão da força de pré-esforço para a alma e para a laje de fundo da secção em caixão, e à exequibilidade de utilização de HPFRC apenas no bloco de ancoragem, foram estudados dois modelos reduzidos à escala 1:2 do canto inferior da secção em caixão de uma ponte existente: um modelo de referência em betão armado e um bloco de ancoragem em HPFRC. O dimensionamento das armaduras foi efectuado através de modelos de escoras e tirantes.

Realizou-se um programa experimental com o objectivo de estudar a transmissão da força de pré-esforço para a laje e alma da secção, aferir os modelos utilizados no dimensionamento e estudar a viabilidade da utilização de um betão de elevado desempenho apenas no bloco de ancoragem, quer no caso de betonagem *in situ*, quer com soluções pré-fabricadas.

Efectuou-se uma análise não linear de elementos finitos dos modelos ensaiados, tendo-se comparado os resultados obtidos.

Palavras-chave

pré-esforço, zonas de ancoragem, betão de elevado desempenho, betão auto-compactável, pontes construídas por avanços sucessivos, fibras metálicas

Contents

List of Figures

List of Tables

Nomenclature

Capital Roman Letters

A gross area of the specimen

A' loaded area

A_b effective net area of the bearing plate calculated as the area A' minus the area of openings in the bearing plate

A_{core} confined concrete area surrounded by the spiral

A_c area of concrete

A_{duct} area of the post-tensioning duct

$A_{s,lat}$ area of lateral steel reinforcement

A_s steel reinforcement bar area

A_z area subjected to the assumed uniform compressive state of stress $f_{c,max}$ at distance z

C_1 coefficient that depends on the geometry of loading and on the percentage of steel used

D diameter of the spiral or side dimension of the ties used as lateral reinforcement

F load

F_b maximum load obtained in the three point bending tests

$F_{p0,1k}$ specified characteristic value of 0,1% proof force

F_{pk} characteristic ultimate resisting force of prestressing steel of tendon ($F_{pk} = A_p \times f_{pk}$)

G_f fracture energy of concrete

H extent of anchorage zone along the longitudinal direction

K factor that depends on the size of the spiral or the core area

K_t constant that depends on the concrete tensile strength and the angle of friction

$K_{nn,min}$ interface minimum normal stiffness

K_{nn} interface normal stiffness

$K_{tt,min}$ interface minimum tangential stiffness

K_{tt} interface tangential stiffness

L length of the spiral used as lateral reinforcement

L_{sp} length of the line of contact of the specimen in a tensile splitting test

P_n compressive external normal force

P_{sp} splitting failure load

P_u ultimate bearing force

R_m mean roughness

R_q root mean square roughness

R_t mean peak height

R_{vm} mean valley depth

R_z mean peak-to-valley height

S_F crack shear stiffness factor

SF diameter obtained on the slump flow test

T air temperature

W width of anchorage zone

Small Roman Letters

$\overline{y}$ mean profile height

a block width; side width of cross section of load transfer test specimen, measured in x direction

a' plate width

b side width of cross section of load transfer test specimen, measured in y direction

b' plate depth

c interface cohesion; unit strength of a plain concrete column

c_d coefficient of cohesion

c_r coefficient for aggregate interlock effects at rough interfaces

c_{clear} clear distance between ribs of the reinforcement bars

d displacement

d_f fibre diameter

d_r depth of the confining reinforcement

d_{sp} designated cross-sectional dimension of the specimen in a tensile splitting test

e failure surface eccentricity

f_b maximum bearing pressure; tensile bond strength of the interface

$f_{c,cube}$ concrete cube compressive strength

$f_{ck,cube}$ characteristic compressive strength of concrete for 150 mm cubic specimens

f_{ck} characteristic compressive strength of concrete

$f_{cm,100}$ mean compressive strength of concrete for 100 mm cubic specimens

$f_{cm,cube}$ mean compressive strength of concrete for 150 mm cubic specimens

f_{cm} mean compressive strength of concrete

$f_{ct,b}$ flexural tensile strength of concrete

$f_{ct,sp}$ splitting cylinder tensile strength

f_{ctm} mean value of axial tensile strength of concrete

f_{ct} concrete tensile strength

f_c concrete compressive strength

f_{fc} first cracking strength of the PDCC

f_{lat} lateral confining pressure provided by the reinforcing steel

f_{pk} characteristic tensile strength of prestressing steel

f_r sandstone cube compressive strength

$f_{t,int}$ interface tensile strength

$f_{t,max}$ maximum tensile stress at distance y

f_y yield strength of the reinforcing bar

h total member depth

h_{sp} distance between the tip of the notch and the top of the specimen

k_1 coefficient that addresses the fact that the tensile force in the reinforcement may be limited due to simultaneous bending and/or reduced anchorage of the bars

k_2 coefficient that considers the interaction of bending and axial stress in the connector and also the fact that interface shear failure may already occur at low slip values

l_f fibre length

l_m evaluation length

m $f_c/f_{t,max}$ ratio

m_q factor function of the bearing reinforcing index, q_b

m_r $f_c/(f_t + f_{lat})$ ratio

n number of discrete measurements

n_{plain} bearing strength of plain concrete

n_{reinf} bearing strength of spirally reinforced concrete

p ratio of the longitudinal reinforcement to the concrete core

p' ratio of the hooping to the concrete core

p_j maximum peak height in each sampling length

p_l volumetric percentage of lateral steel referred to the specimen volume

q_b bearing reinforcing index

$r_{c,lim}$ minimum value of the reduction of compressive strength due to cracks

s pitch of the spiral or spacing of the ties used as lateral reinforcement; relative displacement of steel and concrete cross-section (slip)

s_L sampling length

t_v time taken for the fresh concrete to flow out of a V shaped funnel

t_{500} time needed to the concrete to reach the 500 mm diameter on the slump flow test

v_j maximum valley depth in each sampling length

w crack width

w_d critical compressive displacement

w_{sand} measured moisture content of the sand

x minimum specified anchorage centre spacing of the particular tendon in the x direction

y minimum specified anchorage centre spacing of the particular tendon in the y direction

$y(x)$ profile height, at position x

y_i amplitude of each measurement

z position of the maximum tensile stress

Capital Greek Letters

Δ ratio between the mean resistance obtained with basis in the tensile splitting test and the mean resistance referred to the three point bending test

Δ_{water} amount of water added to the mixture in percentage

Small Greek Letters

α constant equal to 0,80 for mortar and 0,90 for concrete

β constant equal to 0,55 for mortar and 0,60 for concrete; multiplier for the plastic flow direction

δ coefficient of variation

η calibration factor that usually ranges from 0,85 to 0,95

μ interface friction coefficient

μ_d coefficient of friction

ν Poisson's ratio

ρ degree of reinforcement crossing the interface

σ_n compressive stress due to external normal force

τ bond stress

τ_{max} maximum value of bond stress

τ_u ultimate shear friction capacity

ε strain

ε_{cp} plastic strain at compressive strength

φ concrete angle of internal friction

Abbreviations

ATENA Advanced Tool for Engineering Nonlinear Analysis

CRC Compact Reinforced Concrete

DSP Densified Small Particle Cement

ECC Engineered Cementitious Composite

FRC Fibre Reinforced Concrete

HFC High-Performance Hybrid-Fibre Concrete

HPC High Performance Concrete

HPFRC High-Performance Fibre Reinforced Concrete

HPFRCC High Performance Fibre Reinforced Cement Based Composite

HPMFRCC High Performance Multi-Modal Fibre Reinforced Cement Based Composite

MDF Macro Defect Free Cement

OC Ordinary Concrete

PDCC Pseudo-Ductile Cementitious Composite

RPC Reactive Powder Concrete

SCC Self-Compacting Concrete

SCFRC Self-Compacting Fibre Reinforced Concrete

SIFCON Slurry Infiltrated Fiber Concrete

UHPC Ultra High Performance Concrete

Chapter 1

Introduction

1.1 Outline

This thesis describes the research work carried out with the aim of optimising post-tensioning anchorage corner blister in concrete box girder bridges with regard to the size and amount of reinforcement adopted in the blisters and to the production process.

This first chapter begins with a brief historical background on post-tensioning and on the analysis methods of anchorage zones. Then, the research motivation is presented and the main objectives are listed. At last, the dissertation plan is described.

1.2 Background and motivation

1.2.1 First advances in prestressed concrete structures

Post-tensioning is a widely used technique whose principle is to create a permanent state of stress in structures with the aim of improving their serviceability behaviour and bearing capacity.

The idea of compressing structural elements with a high strength material such as steel dates back to ancient times, when timber barrels and wheels were stressed with steel hoops. In ancient Egypt this technique was also used in shipbuilding (VSL, 1992).

In the history of modern engineering, the first patent that describes a prestressing system is Thomas Pope's reinforced masonry beam patent of 1811, shown in Figure 1.1.

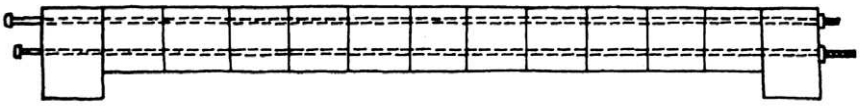

Figure 1.1: Thomas Pope patent on "reinforced" masonry beam (Dooley, 2004)

However, the adoption and success of the prestressing technology in the construction industry was primarily due to the pioneering efforts of Eugène Freyssinet, from France, and Franz Dischinger, from Germany (Dooley, 2004).

In 1928, Eugène Freyssinet registered a patent in France, England (Freyssinet, 1928, Freyssinet, 1929) and in numerous other countries, where the inventor describes a prestress system with the employment of anchoring devices, i.e., devices to "prevent the reinforcing members setting relatively to the concrete when the tension-applying devices are released" (Freyssinet, 1929), as shown in Figure 1.2.

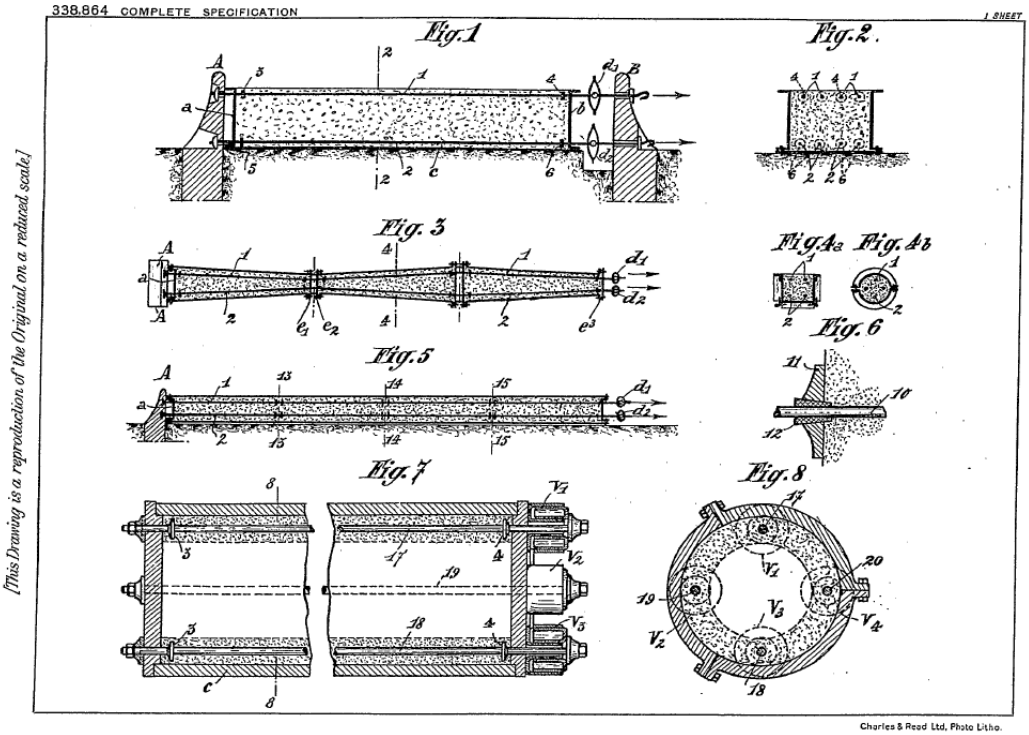

Figure 1.2: Freyssinet patent on "Process for the manufacture of articles of reinforced concrete" (Freyssinet, 1929)

In his patent, Freyssinet also recognised the need of using "reinforcing members metals of very high resistance".

Franz Dischinger was also a pioneer of prestressed concrete, patenting the technique

of external prestressing in 1934, in Germany (Dischinger, 1934), as shown in Figure 1.3.

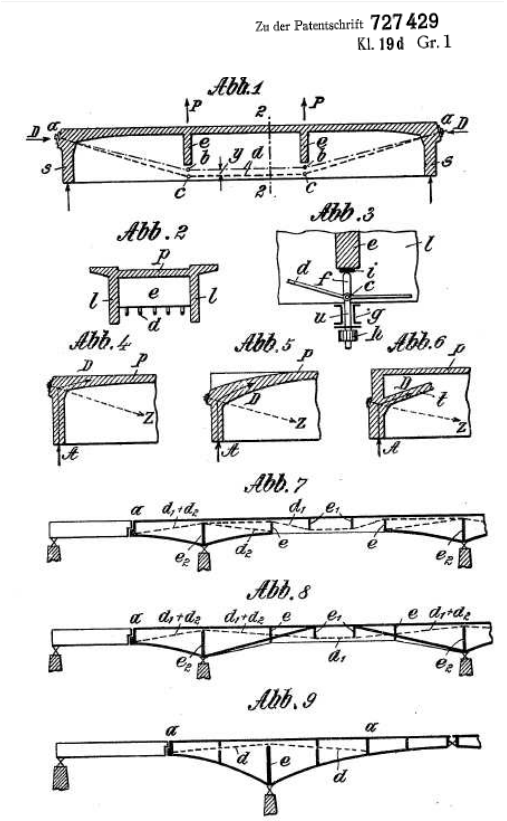

Figure 1.3: Franz Dischinger patent (Dischinger, 1934)

His patent describes the innovative idea of post-tensioning reinforced concrete girders with external tendons.

For determining the value of the prestressing force, Dischinger proposed that "the compression stress produced in the reinforced concrete girder by the tensioning compensates wholly or partly for the tensile stresses produced by the bending moments due to the dead weight and to the load of traffic" (Dischinger, 1935). This design method became known as the "load-balancing" method (VSL, 1992).

In 1936, Dischinger designed the first prestressed concrete beam bridge in the world, the Bridge over valley basin and railway at Aue in Saxony, Germany, as shown in Figure 1.4.

The Aue Bridge is also the first bridge with external prestressing. According to Dooley (2004), Dischinger designed the bridge using the load-balancing method. The tendons were not bonded to the concrete, i.e., they were free to slip when stressed. This solution allowed further tensioning to preserve the initial prestressing profile if significant losses occurred due to shrinkage and creep. This bridge, with a main span of 69 m, is still in service today.

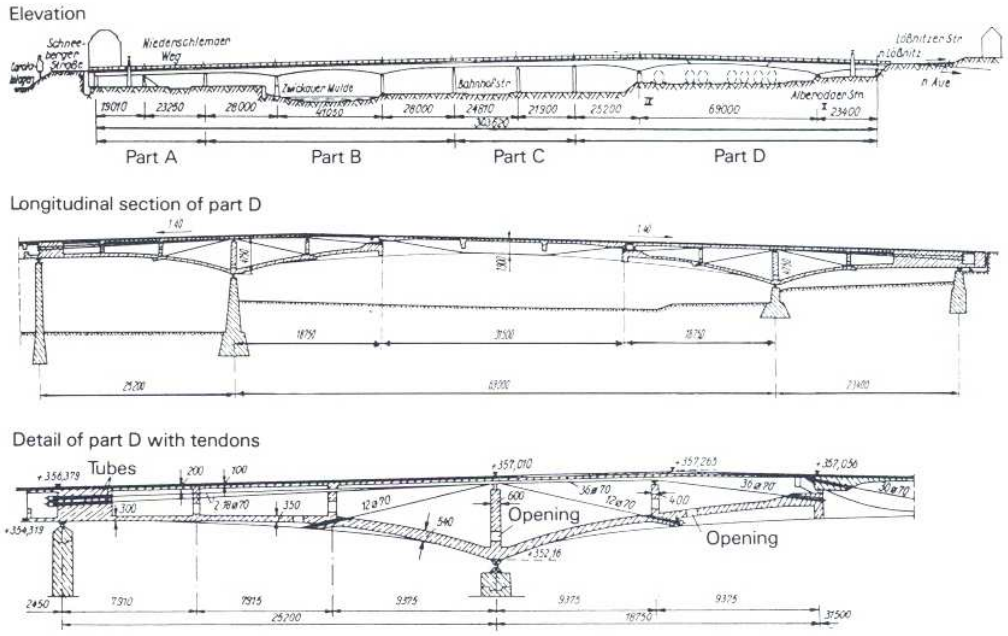

Figure 1.4: Design of the Aue Bridge by Dischinger (VSL, 1992)

While Dischinger was developing an externally post-tensioned prestressing system, Freyssinet was concentrating on a post-tensioned system in which the tendons were bonded with the concrete. The cooperation between Freysinnet and the german company Wayss & Freytag resulted in the design and construction, in 1938, of a farm track bridge near Oelde, with a span of 33 m, on the motorway between Dortmund and Hannover where, for the first time, high tensile prestressing steel arranged inside a concrete section was used (VSL, 1992). This was the first bridge of conventional prestressed concrete.

1.2.2 Anchorage zone design in prestressed concrete structures

The bearing strength in construction materials was first investigated by Bauschinger (1876) with his experiments on sandstone cubic specimens. In 1924, Mörsch presented a strut-and-tie model to study the load paths on concentrically loaded elements (Mörsch, 1924).

With the development of prestressed concrete during the 40's and 50's, the elastic design methods were the most commonly used. The elastic solution presented by Guyon (1953) to determine the bursting stress distribution ahead of a concentric end anchor for different ratios of plate width to member width is still used today (Wollmann, 1992).

In the 60's, numerous studies on anchorage zones were carried out using analysis based on the theory of elasticity as, for example, Gergely et al. (1963), Gergely and Sozen (1967)

and Yettram and Robbins (1969). These studies helped to understand the state of stress in cases of anchorage areas with simple geometry. In the case of more complex anchorage zones, the adaptation from the basic results was more difficult (Yun, 2005). However, in the 70's, with the development of computers and subsequent vulgarisation of finite element analysis, it became possible to analyse more complex zones, with the analysis becoming overly detailed (Rogowsky and Marti, 1996 and Yun, 2005).

In the 80's and 90's strut-and-tie models went back to current design practice. At that time, design recommendations were proposed as a result of the research studies of Sanders (1990), Burdet (1990) and Wollmann (1992).

In the last decade, research that has been carried out focused not only in the safety design of anchorage zones, but also in the use of high performance fibre reinforced concrete in these zones, in order to decrease the amount of steel reinforcement needed and improve its behavior (Haroon et al., 2006, Johnson, 2006).

1.2.3 Motivation

The design of corner anchorage blisters for internal continuity post-tensioning tendons in bridges built with the cantilever method, presents some peculiarities, not only because they are intermediate eccentric anchorages (i.e. the tendons do not extend over the full length of the bridge, so they have to be anchored at intermediate locations along the girder) but also because these anchorages are located in blisters (outside the webs), so the prestressing force has to be transferred from the blister to the bottom slab and the web of the girder.

The consequence of the singularity of these zones, which not unusually require complex geometries, is that the simplified formulas for the design of the reinforcement required to resist transverse tensile forces, due to the application of point loads, proposed by the current standards are not sufficient, as they do not cover all the effects that require reinforcement.

Apart from issues related to the design and safety assessment, the high density of steel reinforcement in anchorage blisters is the most common reason for problems with concrete cast *in situ*. The results are zones with low concrete compacity, which may lead to concrete crushing failures under the anchor plates. Additionally, the optimisation of the element dimensions decreases the space for placing the anchor head and the steel reinforcement. Moreover, it is common practice that detail design drawings do not show anchorage zone details thus, it is the responsibility of the post-tensioning sub-contractor to design and detail these areas. In most cases, these drawings show anchorage details and anchorage zone reinforcement, but not the remaining ordinary reinforcement in the region. This

may lead to physical conflicts between the ordinary reinforcement and the anchorage zone reinforcement, and/or with the post-tensioning duct and anchorage, which results in an excessive density of steel reinforcement in anchorage zones.

1.3 Objectives

The main purpose of this work is to implement a solution to reduce the size and reinforcement of post-tensioning anchorage blisters and to provide alternatives to facilitate the execution of the anchorage blister on site in order to reduce the execution time.

To fulfill this purpose, the following sequential objectives have been established:

- study of a high performance fibre reinforced concrete (HPFRC) specifically developed to use in post-tensioning anchorage zones;
- assess the possibility of reducing the concrete cross-section and the amount of confining reinforcement specified by the anchorage device supplier for a particular tendon by using a HPFRC;
- understand the behaviour of the local anchorage zone and the influence of the confining reinforcement in the bearing strength by performing non-linear finite element analysis;
- investigate the behaviour of anchorage blisters regarding the transmission of stresses to the web and the bottom slab of the girder;
- evaluate the feasibility of using high performance concrete only in blisters, either with casting in situ, or with precast solutions;
- assess the blister models test results and simulate the behaviour to failure of the specimens by performing non-linear finite element analysis.

1.4 Dissertation outline

This thesis is divided into six chapters, including the present one and is organised according to the objectives listed above.

In this first chapter, a brief historical background on post-tensioning and on the analysis methods of anchorage zones and the research motivation are presented. Then, the main objectives are listed followed by the dissertation plan.

The second chapter deals with the high performance concrete specifically developed to use in post-tensioning anchorage zones. A short literature review of the first developments of fiber reinforced concrete and the description of different high performance and ultra high performance concretes are presented. The composition of the HPFRC mixture is provided and the constituent materials are characterised. The results of fresh concrete tests are

presented and justified, and the HPFRC workability is also analysed. The results of mechanical tests are presented and analysed, followed by shrinkage measurements.

Since the use of HPFRC is intended to allow the reduction of the concrete cross-section and the amount of confining reinforcement specified by the anchorage device supplier for a particular tendon, an experimental program to assess both the ultimate capacity and the adequate serviceability of the local anchorage zone was carried out. This program, presented in the third chapter, was based on load transfer tests specified in the Guideline ETAG 013 (European Organisation for Technical Approvals, 2002). Chapter 3 starts with a literature review on the research carried out on the bearing strength of concrete (plain, reinforced and reinforced high performance), and on load transfer tests regarding the test specimen, test procedure and acceptance criteria, according to three different guiding documents (FIP Recomendation, 1993, AASHTO, 2002 and European Organisation for Technical Approvals, 2002). After, the experimental program is described regarding test specimens, test procedure and experimental results. A comparison of the experimental results with models in the literature is then presented and discussed. At last, the non-linear analysis of the tested specimens is presented and the results are compared.

Chapter 4 presents the design of half-scale anchorage blister models used to investigate the behaviour of anchorage blisters regarding the transmission of stresses to the web and the bottom slab of the girder and the feasibility of using high performance concrete in the blister only. Since it was intended to design the steel reinforcement of the test specimens using strut-and-tie models, the chapter begins with a short literature review on developments on these type of models. Then, the specimens are described regarding the choice of geometry and layout of the prestressing tendons. The results of the elastic analysis are shown and the developed strut-and-tie models are presented and justified. Based on the strut-and-tie models the calculation of reinforcement is explained and detailed.

To study the transmission of prestressing force to the slab and web of the section, assess the models used in design and to study the feasibility of using high performance concrete only in the blister, either with casting in situ, either with precast solutions, three half scale models of the lower corner of a box girder bridge were tested: a reference specimen of ordinary reinforced concrete and two high performance fibre reinforced concrete (HPFRC) blister specimens. The three specimens had the same geometry, except for the anchorage blisters whose dimensions were reduced in the HPFRC blister specimens, and included a corner blister for two anchors, with a portion of the slab and the web contiguous. Chapter 5 begins by showing the execution of the anchorage blister specimens. The monitoring equipment and the test procedure are also described, and the results of the tests are presented and discussed. The non-linear finite element analysis of the anchorage blister models is presented and the results are compared with the ones obtained in the experimental tests. Then, the resistance of the interface between the HPFRC precast

blister and the slab and web of the model is determined using the the formulation proposed by the Model Code 2010 (2012), based in Randl (2013). At last, design and detailing recommendations are provided and the conclusions are presented.

Chapter 6 starts with a summary overview of the thesis followed by the description of the main conclusions and recommendations of this study. The future developments are presented at the end of the chapter.

Chapter 2

High Performance Fibre Reinforced Concrete

2.1 Introduction

Despite research works that have been published about anchorage zones in post-tensioned structures, problems during construction and throughout the life of these structures, such as cracking or local failures, still occur. These problems are mainly due to a high density of steel reinforcement, resulting in sections with low concrete compacity which may lead to concrete crushing failures under the anchor plates. The solution of this problem may involve the reduction of the reinforcement density by improving the concrete compressive and tensile strengths.

In order to meet this requirement a high-performance fibre reinforced self-compacting mixture (HPFRC) was developed to use in anchorage zones of post-tensioning tendons.

High performance fibre reinforced concrete (HPFRC) is a cementitious material that can be seen as an improvement of ordinary fibre reinforced concretes and high performance concretes, allowing the combination of strength and ductility, but also higher durability (Walraven, 2009). HPFRC has also the advantage of belonging to the family of self compacting concretes, ensuring a complete filling of the moulds and the embedding of the reinforcement and prestressing tendons, without the need for vibration, even in structures with zones of high density of reinforcement and without compromising the full penetrating and embedding function of the matrix (Marchão et al., 2012, Naaman, 2008).

Because of its high compressive strength, the volume of HPFRC is about 1/3 to 1/2 of that of conventional concrete for comparable structural elements (Ganz, 2008). Thus, the higher cost of HPFRC can be compensated by using it in particular areas of the structure,

where it is possible to leverage on the benefits of its characteristics.

This chapter starts with a short literature review of the first developments of fiber reinforced concrete, and different high performance and ultra high performance concretes are then described.

Then, the composition of the HPFRC mixture is provided, as well as the constituent materials characterisation.

The results of concrete fresh state tests, namely the slump flow and v-funnel tests, are then presented and justified. In order to analyse the HPFRC workability, the results of mini-slump tests, stability tests and rheological measurements are provided and discussed.

Finally, the results of mechanical tests, namely uniaxial compression tests, tensile splitting tests, three point bending tests and static modulus of elasticity tests are presented and analysed, followed by shrinkage measurements which closes the chapter.

2.2 Literature review - Historical developments

2.2.1 First advances on fiber reinforced concrete (FRC)

The idea of using fibers to reinforce brittle materials comes from ancient times: Egyptians used mud mixed with straw to bind dried bricks, in Scandinavia asbestos fibers were used to strengthen pottery and Romans included pieces of horsehair in the construction to prevent their concrete from cracking. With the invention of portland cement in 1824, by Joseph Aspdin (Aspdin, 1824), and its evolution as a building material, there were several attempts to improve its behaviour by including fibers.

From the middle of the nineteenth century numerous patents have been granted for various methods of incorporating wire or metallic elements into the concrete. Joseph-Louis Lambot's original French patent on wire-reinforced boats was issued in 1847. In his patent, Lambot describes the use of continuous fibres in the form of wires or wire meshes to create a new building material, known as ferrocement (Naaman, 1985).

The first US patent on steel fiber reinforced concrete "Improvement in Artificial Stone" was filed by Bérard (1874), in California, who suggested the use of granular waste iron in a concrete mix to create a "very hard and compact stone".

Bérard was followed by Eddy (1894) with the patent "Composition for Artificial Stone" where the use of wrought iron or steel turnings in long fibers in a concrete mix is recommended, as well as the use of pressure or ramming to compact the composition during the process of filling.

Whitacre (1908) developed a patent on "Concrete Reinforcement" for using diverging flexible metallic wires wrapped around a longitudinal metallic bar, as shown in Figure 2.1a.

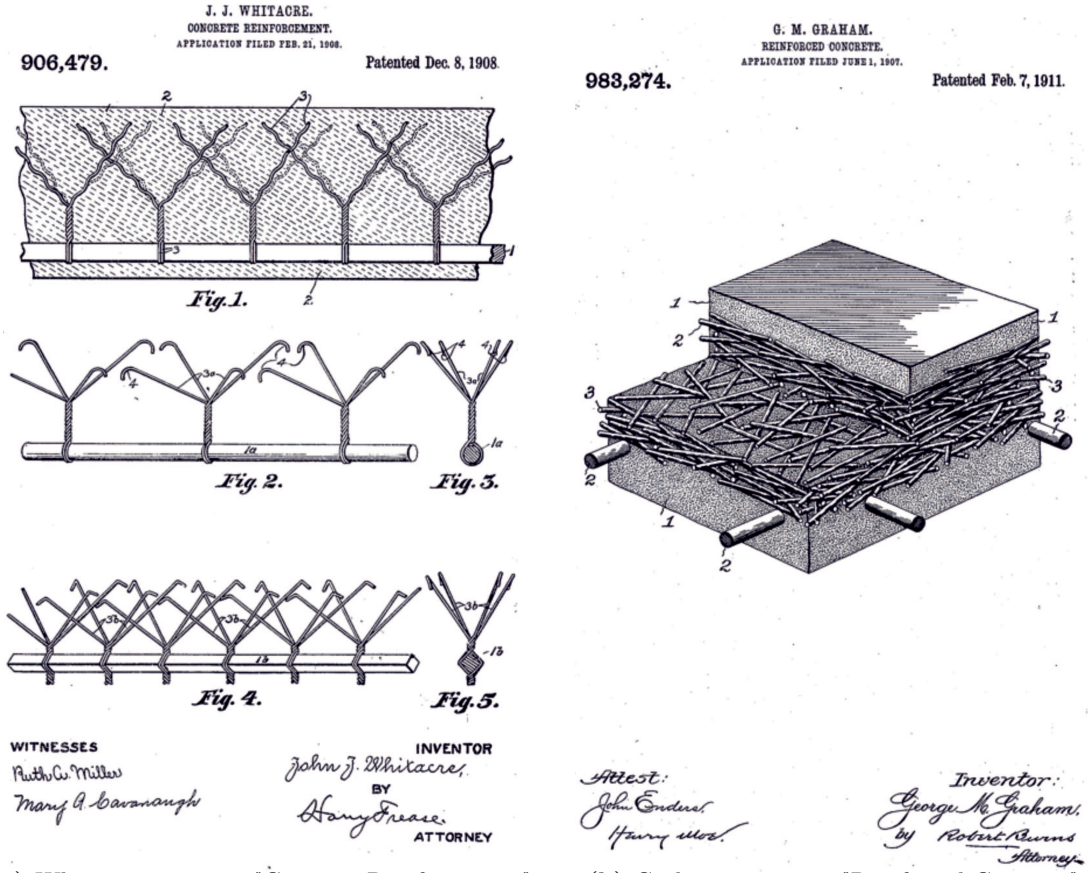

(a) Whitacre patent on "Concrete Reinforcement" **(b)** Graham patent on "Reinforced Concrete"

Figure 2.1: US patents on reinforced concrete by Whitacre (1908) and Graham (1911)

Porter (1910) mentioned the investigation made in order to increase the crushing and tensile strength of concrete by adding steel cut nails, or spikes, to a concrete mix. In the author's opinion, the solution of introducing small pieces of steel in the concrete mixtures would come into use in a not very distant future, making concrete a more homogeneous structural material.

Graham (1911) registered a patent, shown in Figure 2.1b, consisting of short sections of wire placed on the top surface of the concrete mass, forming a layer that allowed the wires to sink by gravity until they reach the reinforcing bars. These bars would prevent the short sections of wire to go further down. The inventor claimed to be a solution that allowed a floor with great strength and stability, requiring minimum thicknesses when compared to traditional solutions of the time. This solution seems to be one of the earliest versions of SIFCON (slurry infiltrated fiber concrete), as it is known today.

One year later, Weakley (1912) registered a patent consisting of connected wire loops

of desired or preferred form arranged at angles to each other or alternately in vertical and horizontal disposition, to ensure a durable bond with concrete, as shown in Figure 2.2a.

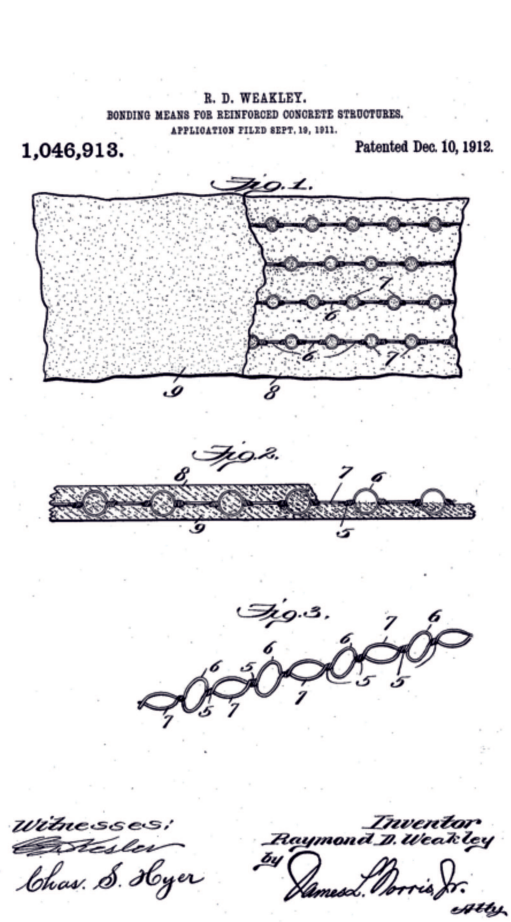

(a) Weakley US patent on "Bonding Means for Reinforced Concrete Structures"

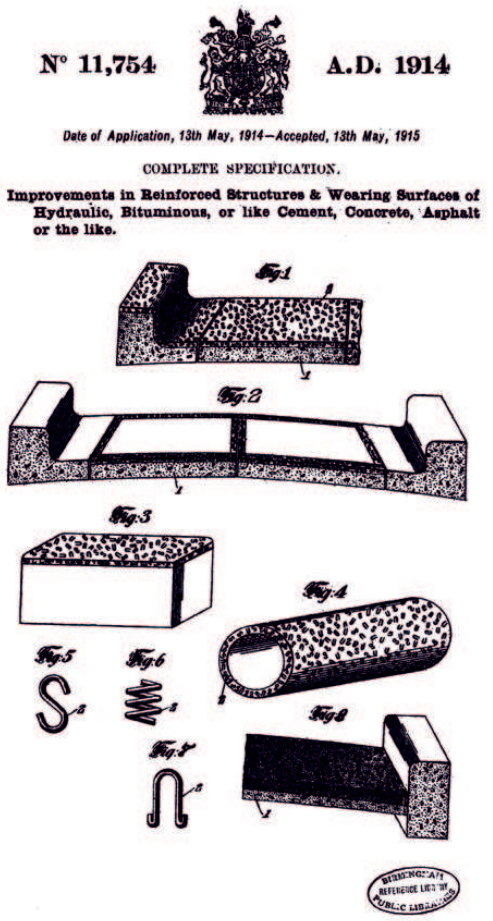

(b) Ficklen GB patent on "Improvements in Reinforced Structures(...)"

Figure 2.2: Patents on fibre-reinforced concrete by Weakley (1912) and Ficklen (1914)

The first British patent was taken out by Ficklen (1914). With the aim of improving the strength and toughness of concrete elements and wear resistance of surfaces, Ficklen proposed the reinforcement of concrete structures by metal pieces of tortuous shapes (S-shaped, coiled or U-shaped) and uniform maximum size of 50 mm in the direction of their greatest dimension, as shown in Figure 2.2b. The tortuous shape of the reinforcement was intended to ensure the anchorage of the elements in the concrete. According to the author, the metallic elements provided the tensile and compressive strength necessary to resist expansion and contraction, so that creep, cracking and folding of concrete surfacing layers could be practically eliminated. In addition, the added strength of the material, due to the metal, allowed the reduction of the thickness of the surfacing layers or other elements of concrete.

Alfsen (1918) in his patent filed in France, sought to solve the problem of low tensile

strength of concrete with a solution consisting of mixing small longitudinal bodies of steel or wood in a concrete mass. The inventor also suggests that the surface of the longitudinal elements must be rough and, if possible, with bent extremities, in order to provide a better adherence to the concrete.

Meischke-Smith (1920) proposed the use of a homogeneous mixture of cement and short pieces of twisted flat steel wire, as shown in Figure 2.3a. The recommended dimensions for the wire are 25 mm in length, 0,25 mm in thickness and a width of 1,20 mm. The aim of the inventor was to increase the resistance of the concrete in order to cease the use of steel rods, saving a great amount of time and skilled labour.

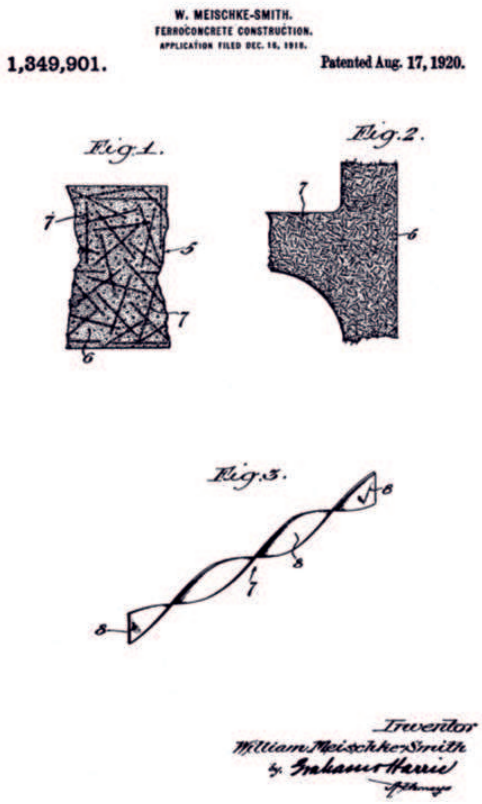

(a) Meischke-Smith US patent on "Ferroconcrete Construction"

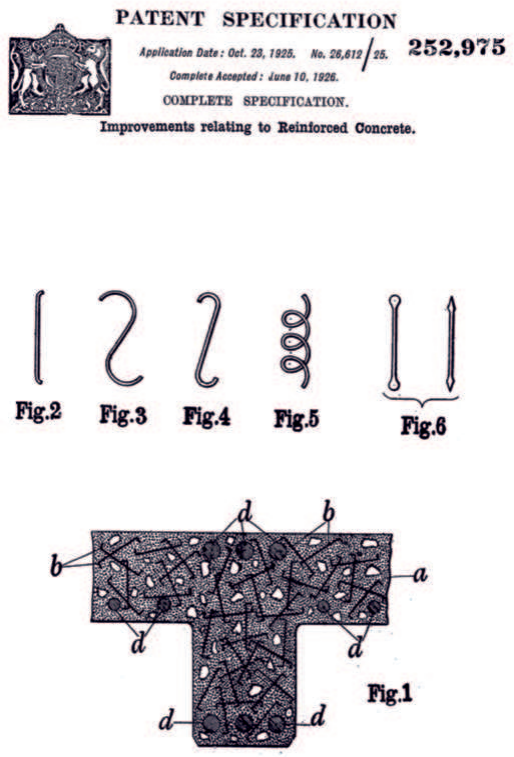

(b) Rotinoff GB patent on "Improvements Relating to Reinforced Concrete"

Figure 2.3: Patents on fibre-reinforced concrete by Meischke-Smith (1920) and Rotinoff (1926)

Kleinlogel (1921) registered the patent "Method of Producing a Workable Artificial Iron Mass", for mixing a large volume of iron particles with cement and water, in order to produce a concrete mass capable of being chilled, turned, sawed and filled, just like an iron mass. The iron particles should have a maximum dimension of 2 mm and a minimum dimension of 0,33 mm.

Rotinoff (1926) was the first to use the term *reinforced steel fiber concrete* in his British patent "Improvements Relating to Reinforced Concrete". The invention of Rotinoff con-

sisted of incorporating steel fibers, from about 13 mm in length, in concrete, by adding it or mixing it with the aggregate, cement, sand and water. The steel fiber reinforcement should be used in combination with ordinary reinforced concrete. The author presents various possible forms of the steel-fibers including fibers with bent ends and spiral configurations, as shown in Figure 2.3b.

One year later, Martin (1927) described in his patent, illustrated in Figure 2.4a, the use of small pieces of plain or crimped steel or iron wire, mixed with concrete, to act as reinforcement of the concrete, and to be used in pipes. The author recommends the use of No. 12 wire gauge (2 mm in diameter) with lengths ranging from 25 mm to 102 mm.

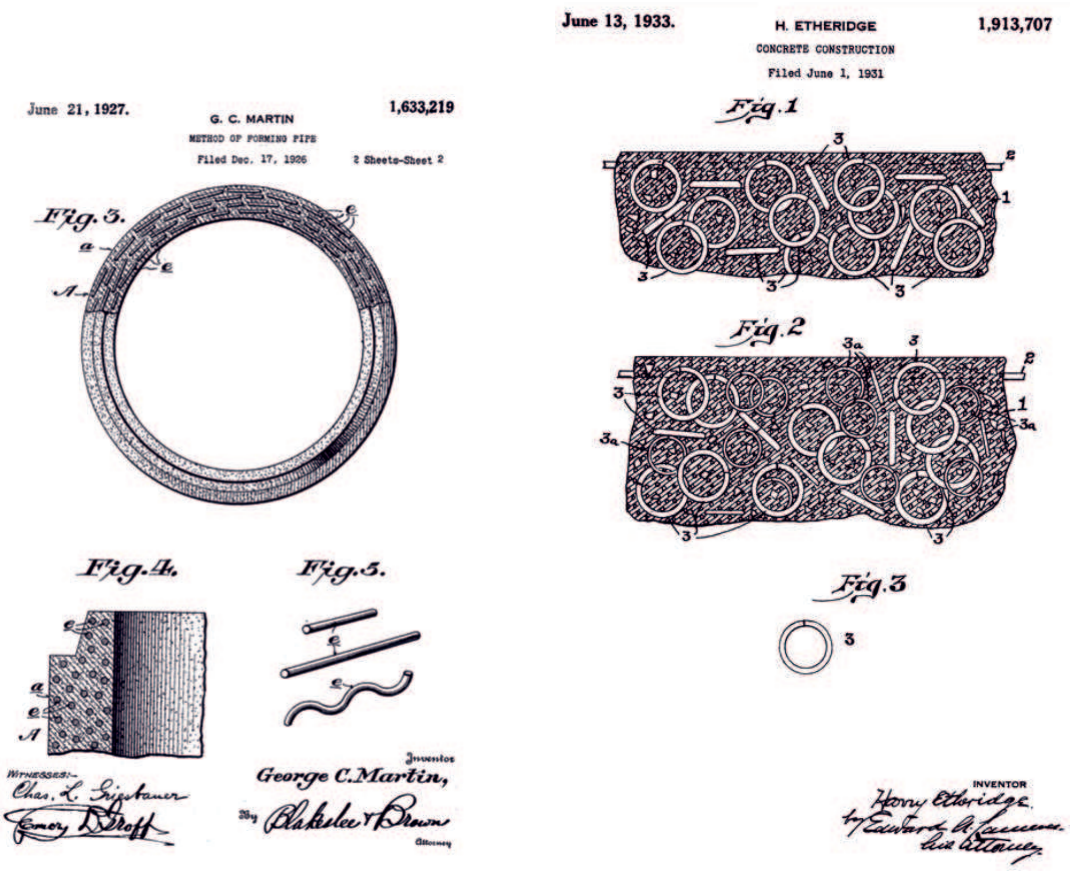

(a) Martin patent on "Method of Forming Pipe" **(b)** Etheridge patent on "Concrete Construction"

Figure 2.4: US Patents on fibre-reinforced concrete by Martin (1927) and Etheridge (1933)

Etheridge (1933) improved the shape of the fibers to add to concrete mixtures, by proposing the use of metallic "annuli" fibers of different sizes and diameters, overlapping to each other and disposed at different angles, as shown in Figure 2.4b. According to Etheridge patent, the proposed solution is intended to complement the existing steel reinforcement, mitigating the occurrence of local cracking. The inventor suggested the use of annuli with diameters from 25 mm to 89 mm and a gauge of material from 1,6 mm to 6,4 mm.

In his British patent, Zitkevič (1917) proposed the addition of thin, flexible, soft iron wire to the mass of concrete, in order to obtain a greater tensile and shearing strength. The thin wire should be uniformly distributed in the concrete and should have a length (l_f) of around 100-150 mm and a diameter (d_f) of 1 mm. The recommended aspect ratio (l_f/d_f) is very similar to the one currently used in steel fiber concrete. The iron wires should be flexible enough in order to become deformed during mixing with the concrete and conform themselves to the shape of the stone aggregates in the concrete, and thin to provide the greatest possible contacting and adhesion surfaces between the predeterminate quantity of iron and concrete. Zitkevič recommends the use of approximately 50 kg of wire per cubic metre of concrete.

In his patent (1943 in England and 1954 in the United States), Constantinesco described the use of short coils of helical elements made of corrugated wire, arranged in a three-dimensional and uniformly distributed mattress inside of a mould later filled with a suitable cement mass. Constantinesco recommended the use of No. 20 to No. 33 wire gauge, i.e. wire with diameters ranging from 0,18 mm to 0,8 mm, and aspect ratios of 100. The material thus obtained, after setting and hardening was described as having a three-dimensional and uniformly increased resistance to compression, tension, shearing and bending in every direction. Figure 2.5a shows the moulding equipment, as well as the various types of helical elements used.

The research done by Romualdi and Batson (1963) and Romualdi and Mandel (1964) on closely spaced wires and randomly distributed fibres in the early 60's demonstrated the effectiveness of short steel fibers in increasing strength and crack controlling of concrete. This research was the basis for a patent (Romualdi, 1969) on fibre spacing and concrete covering situations of short wire fibres randomly and uniformly distributed, straight continuous wire strands or long continuous wires in the form of a mesh, as illustrated in Figure 2.5b.

The development of FRC has continued and a large number of other fibre materials were studied, such as glass (Biryukovich et al., 1965, Vekey and Majumdar, 1970, Ali et al., 1975), carbon, synthetics and natural fibres. In the early 70 were also published some works on the reinforcement of brittle materials with fibres (Kelly, 1972, Aveston and Kelly, 1973).

According to Mielenz (1984), from the decade of 60, the development in the field of additions and high range water-reducing admixtures (superplasticizers) constituted a major step forward, allowing an evolution in terms of the composition of concrete mixtures.

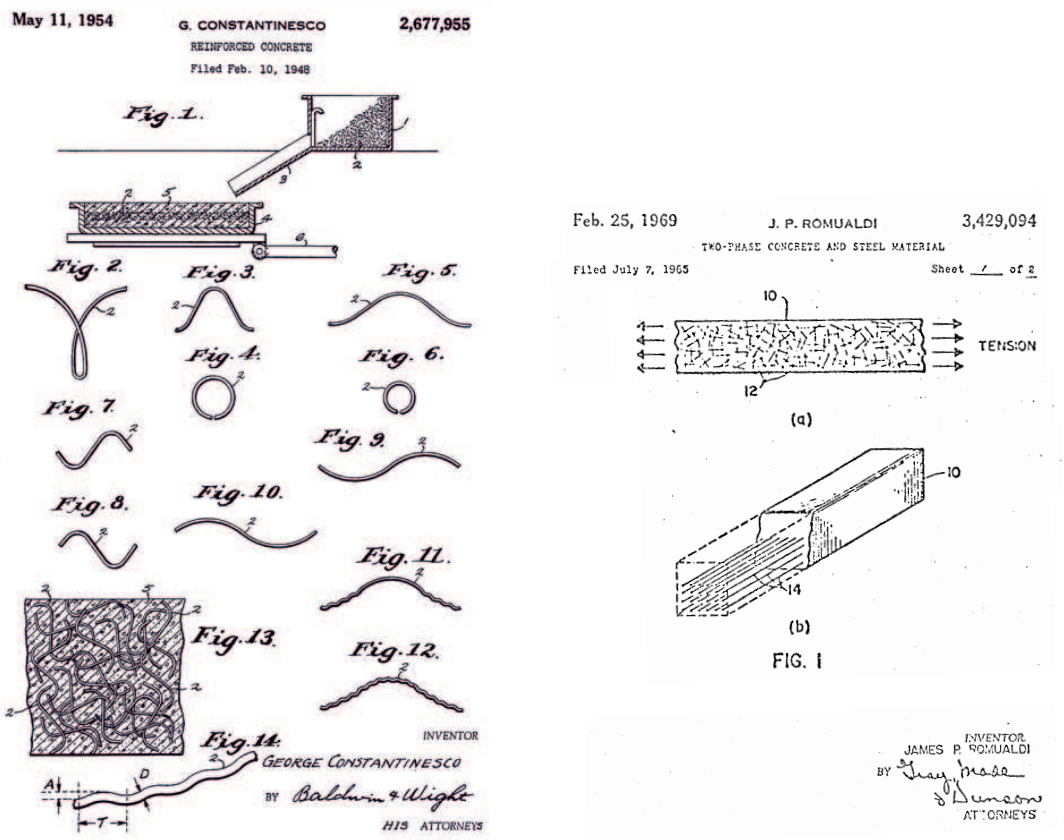

(a) Constantinesco patent on "Reinforced Concrete" **(b)** Romualdi patent on "Two-Phase Concrete and Steel Material"

Figure 2.5: US patents on reinforced concrete by Constantinesco (1954) and Romualdi (1969)

2.2.2 Modern progresses

2.2.2.1 High performance concretes (HPC)

Slurry infiltrated fibre concrete (SIFCON)

In his 1982 patent, Lankard developed Slurry Infiltrated Fibre Concrete in order to solve the difficulties experienced in mixing and placing conventional steel fibre reinforced concretes with concentrations of fibres above 2,0% of the composite volume (Lankard, 1984). The preparation of SIFCON consisted in the placement of steel fibres in a mold and subsequent infiltration of a fine grained cement based slurry, aided by external vibration. This production process allowed the use of a relatively high fibre contents (up to 18%) for commonly used fibres at the time.

In the late 1980's, Naaman and co-workers published several works (Naaman, 1987, Homrich and Naaman, 1988) presenting the results of their extensive evaluation of the tensile and compressive properties of SIFCON composites.

High performance multi-modal fibre reinforced cement composites (HPMFRCC)

The need for two different lengths of steel fibers in concrete was first justified by Rossi et al. (1987): short length fibres would be more effective for microcracking and long fibers for macrocracking.

Rossi (1997) presented the results of his investigation at the LCPC (Laboratoire Central des Ponts et Chaussets), in France, on different high performance fibre reinforced cement composites containing different steel fiber lengths. The author concluded that the mixture of shorter and longer fibres lead to the improvement of the mechanical behaviour of the composite, concerning the increase of toughness and ductility.

The high performance fiber reinforced cement composites (HPFRCC) developed was called high performance multi-modal fiber reinforced cement composites (HPMFRCC).

Self-compacting concrete (SCC)

In the early 80's, the problem of the durability of concrete structures was a major topic of interest in Japan and was even viewed as a major problem facing Japanese society due to the gradual reduction in the number of skilled workers in Japan's construction industry and consequent insufficient compaction of structural concrete (Okamura, 1997; Okamura et al., 2000). One solution for achieving durable concrete structures, independently of the quality of construction work, was the employment of self-compacting concrete (SCC), first proposed by Okamura in 1986 at the occasion of Japan Cement Association Meeting (Okamura et al., 2005).

The first prototype was developed in August 1988 by Ozawa, Maekawa and Okamura, at the University of Tokyo, and was called *High Performance Concrete*. This terminology was changed to SCC when HPC started to be mainly used for high strength concrete.

According to Ozawa et al. (1992), the requirements for the performance of High Performance Concrete were:

1. In the fresh state, having high deformability and high resistance to segregation for various boundary conditions, for achieving high performances even without compaction, ie, this concrete should homogenously spread due to its own weight, without requiring to be vibrated;
2. In early age, having sufficient cracking resistance to the tensile stress deriving from drying shrinkage and temperature rise due to generation of heat of hydration, preventing cracks from spoiling appearance of concrete structures and inhibiting the corrosion of reinforcing bars in concrete;

3. In the hardened state, presenting small permeability for protection against external factors, and appropriate strength.

Okamura and Ouchi (2003) established a rational mix-design method and an appropriate acceptance testing method to be used on-site over self-compacting concrete.

Self-compacting fibre reinforced concrete (SCFRC)

Self-compacting fibre reinforced concrete (SCFRC) was developed to combine the advantages and to extend the possibilities of both SCC and FRC (Grünewald, 2004).

Groth and Nemegeer (1999) published a study concerning the addition of fibres to SCC mixtures. The authors focused on the questions of mix design, workability and mechanical properties of the SCC mixtures with fibres.

Groth and Nemegeer observed that the lack of external vibration affected the fibre orientation. The vibration often has a positive effect, with the fibres tending to be aligned with the structural geometry. When there is no external vibration, the fibres orientation seem to depend on the flow direction.

The authors concluded that the utilisation of steel fibre reinforcement in self-compacting concrete was possible without unfavourable effects on the workability. Regarding resistance, the authors concluded that SCFRC strength was at least the same when compared to usual vibrated concrete.

Khayat and Roussel (1999) performed a set of experimental tests with the aim of investigate the feasibility of producing self-compacting fibre reinforced concrete to be cast in place with a minimum or no vibration. Sixteen mixtures without or with steel fibres 38 mm long, at 0,5% and 1% of the mixture volume, were analysed. The mixtures were prepared with various types of binary and ternary cementitious materials[1] and water/cement ratios ranging from 0,37 to 0,45.

To study the free deformability of the SCC, the authors have chosen the slump-flow test, while the restricted deformability was evaluated using V-funnel flow and filling capacity tests. The rheological parameters and compressive strength were also determined.

The sixteen mixtures were adjusted to obtain slump-flow values of 530 mm ± 15 mm (SCC-530 mixtures) and 650 mm ± 15 mm (SCC-650 mixtures). The characteristics of these mixtures were compared to those of a conventional fibre reinforced concrete with a targeted slump consistency of 200 mm.

[1]Binary cementitious materials contains portland cement and one supplementary cementitious material. Ternary cementitious materials contains portland cement and two supplementary cementitious materials.

The authors reached the following conclusions:

1. With the 38 mm long fibres, high deformability was obtained when the volume of fibres was limited to 0,5% of the mixture volume. At 1%, the filling capacity was low but still considerably greater than that of the conventional mixture. By decreasing the fibre length to ensure compatibility with the smallest distance between the reinforcement bars and molds, the filling capacity of the SCFRC with 1% volume of fibres would increase;
2. Both the SCC-650 mixtures made with a water to cement ratio of 0,37 and no viscosity-enhancing agent (VEA), and the mixtures with a water to cement ratio of 0,42 and VEA, developed similar fresh properties and toughness characteristics considerably greater than conventional concrete subjected to internal vibration. The former mixtures type exhibited higher strength because of their lower water to cement ratio and more favourable binder type;
3. The increase of fibre volume from 0,5% to 1% of the mixture volume resulted in a significant increase in ductility, as in the case of conventional mixture with 200 mm slump.

Miao et al. (2003) investigated mix design and mechanical properties of self-compacting steel fibre reinforced concrete. Three mixtures with different fibre contents of 0,5, 1,0 and 1,5%, and one mixture of plain concrete with high fluidity were developed. The studied parameters included compressive and flexural strength, flexural toughness, shrinkage and creep.

The fibres used were hooked-end steel fibres 30 mm long with a 0,5 mm diameter (aspect ratio of 60) and the water/binder ratio of the mixture was fixed at 0,32 to assure a concrete with high strength.

The authors obtained mixtures with high fluidity and balling free fibrous concrete without bleeding or segregation at a maximum fibre content of 1,0%. For 1,5% fibre volume it was difficult to obtain a good workability, and the air content increased sharply.

Regarding the properties of SCFRC, Miao, Chern and Yang concluded that:

1. The addition of steel fibres improved the compressive strength of SCFRC at early ages (3 and 7 days). However, as concrete age increased, the fibrous to plain concrete strength ratio decreased;
2. The flexural strength of SCC improved significantly with the addition of steel fibres;
3. Both autogenous and drying shrinkage of SCFRC depend on the fibre content, decreasing linearly at a rate of 170×10^{-6} for each percent of steel fibres added;
4. The addition of steel fibres had a negligible effect on the compressive creep of the studied concrete mixtures.

In the Delft University of Technology, a research project was performed by Grünewald

(2004) with the objective of optimising SCFRC in the fresh and the hardened state and to model its behaviour in order to provide reliable design tools. Experimental and numerical studies were performed to evaluate the effect of the steel fibres on the packing density of the granular skeleton. The effect of the type and the content of steel fibres on the characteristics of SCC in the fresh state was also assessed. The optimised mixtures from the studies on SCFRC in the fresh state were tested to bending. In order to study the influence of the production process on fibre orientation, three full-scale tests on piles, tunnel segments and large beams were carried out.

Grünewald concluded that, with regard to the fresh state, the addition of steel fibers to SCC decreased the packing density, requiring a higher content of finer grains to compensate it, and affected the key characteristics of SCC. In the hardened state, the bending behaviour of SCFRC has a better performance and a lower variation compared to SFRC. It was observed that the production process affected significantly the orientation of the fibres which were rarely randomly oriented. According to the author, the preferred orientation of the fibres could be considered as an advantage or, the opposite, as an intrinsic weakness of SCFRC.

Engineered cementitious composites (ECC)

Engineered cementitious composite (ECC) is a class of ultra ductile fibre reinforced cementitious composites, and was originally developed at the University of Michigan by Li and co-workers in the early 1990's (Li, 2003).

ECC has a typical average tensile strength of 4 to 6 MPa (Li, 2008) and shows a tensile strain-hardening behaviour with strain capacity up to 6% (Li, 1998), although the constituent materials used are similar to those of fibre reinforced concrete (FRC): water, cement, sand (coarse aggregates are not used as they tend to adversely affect the unique ductile behaviour of the composite), fibre, and some common chemical additives (Li and Kanda, 1998), as shown in Table 2.1.

Table 2.1: Mix design proportions by weight of ECC-M45 (adapted from Li, 2008)

Constituent materials	Parts by weight
Cement	100
Fly ash	120
Sand	80
Water	56
High-range water reducer	1,2
Fibre (vol. %)	2

A typical composition employs a water/cement ratio and sand/cement ratio of 0,5 or lower (Li and Kanda, 1998) and a volume of 2% or less of discontinuous fibres (Li, 2002), making the mixing process of ECC similar to that employed in mixing normal concrete (Li and Kanda, 1998).

The ultra-high ductility, that can be seen in the graph in Figure 2.6, is achieved by optimising the microstructure of the composite employing micromechanical models (Li, 1998) that account for the mechanical interactions between the fibre, the matrix and the interface. ECC may be regarded as an optimised HPFRC (Li, 2002).

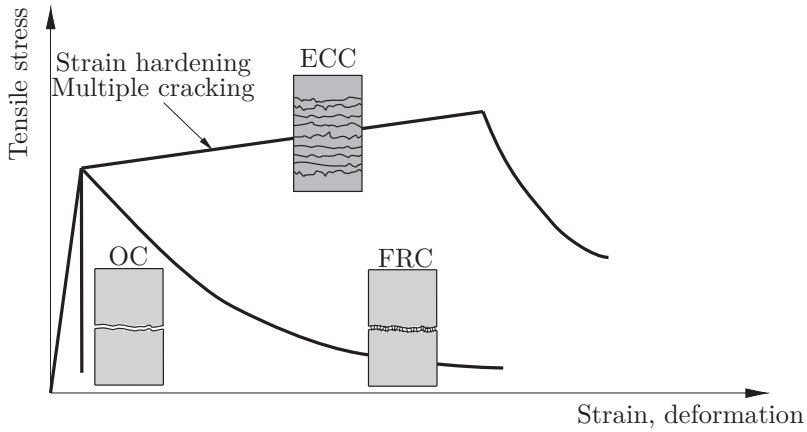

Figure 2.6: Tensile stress-strain behaviour of cementitious matrices (Li and Fischer, 2002)

ECC can be cast (including self-compacting casting (Kong et al., 2003)), extruded (Stang and Li, 1999) or sprayed (Kim et al. 2003, Li et al. 2009).

Hybrid-fibre concrete (HFC)

After the research works of Rossi (1997) and Sato et al. (2000) on HPMFRCC, Marković (2006) developed a high-performance hybrid-fibre concrete.

According to the author, the basic purpose of combining short and long fibres was to improve the tensile strength by the action of short fibres and the ductility by the action of long fibres. Besides, to ensure that the orientation of fibres was always similar for the same way of casting and that no segregation or clustering of fibres occurred, HFC was also a self-compacting concrete. The self-compactability was also a guarantee for the overall quality of structural elements made of HPC.

2.2.2.2 Ultra-high performance concretes (UHPC)

Much research work was done with the aim of increasing mechanical strength of concrete until Eugène Freyssinet (Freyssinet and Seailles, 1932) first demonstrated that applying

pressure during concrete setting could increase its strength. In the early 70's, strength values of 655 MPa in compression and 64 MPa in tension were achieved on heat-cured samples under elevated pressures (Roy and Gouda, 1973).

Macro defect free cement (MDF)

According to Bennett (2002) macro defect free cement (MDF) arose in the late 1970's, in Runcorn in England, when chemists at ICI Special Projects team, lead by Derek Birchall were looking for a inorganic material that could replace polymers and certain metals, like aluminium, without its high energy production costs.

Birchall et al. (1981a) demonstrated that the flexural weakness of cement was due to the presence of large voids which were largely undetected by conventional methods of pore analysis. The removal of such macro-defects resulted in flexural strengths up to 70 MPa, despite the large volume of gel pores remaining in the material.

Researchers found that the introduction of small proportions of water-soluble polymers into the cement and water mix reduced significantly inter-particle friction and surface tension, which allowed particles to pack more closely, resulting in a major increase of the tensile strength. In addition, by using a water/cement ratio of less than 0,2 and by working the fresh material with gentle compression, it was possible to reduce the voids to less than 0,1% of the volume. The paste was then molded into desired shapes by extrusion, pressing or other conventional process used in the production of plastics. MDF presented a flexural strength exceeding 150 MPa (Bennett, 2002).

Figure 2.7 presents an example of application of macro defect free cement.

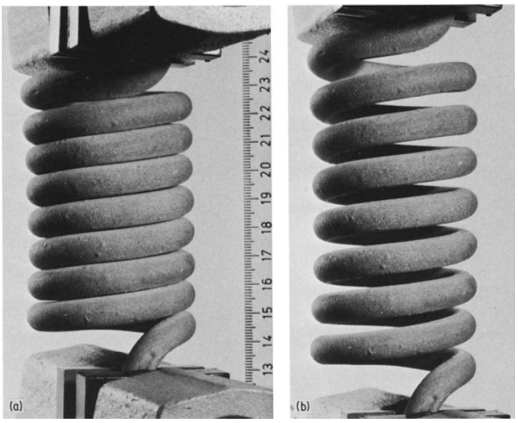

(a) Spring made from MDF cement

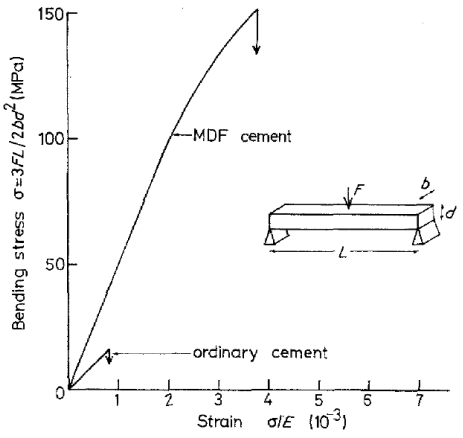

(b) Stress-strain curves from three-point bending test of ordinary and MDF cement

Figure 2.7: Application and behaviour of MDF cement (Birchall et al., 1982a)

Table 2.2 shows an example of composition of MDF cement.

Table 2.2: Mix design of MDF cement (Birchall et al., 1982a, Birchall et al., 1982b)

Constituent materials	Parts by weight
Portland cement	100
Water-soluble or water-dispersive organic polymer or copolymer	1-15
Water	22

MDF cement was patented in Europe (Birchall et al., 1981b) and in the United States (Birchall et al., 1983). In 1985, Alford and Birchall published the results of their study on the mechanical properties of MDF cement - fibre laminates. The composite consisted of one or more mats of fibrous material pressed between sheets of 1 and 2 mm in thickness of moldable MDF cement. The mix design of the moldable MDF cement matrix is shown in Table 2.3.

Table 2.3: Mix design of the MDF cement matrix (adapted from Alford and Birchall, 1985)

Constituent materials	Parts by weight
Cement (Secar 71 by Lafarge)	100
Polyvinyl alcohol-acetate (Gohsenol Nippon Gohsei)	7
Glycerol	0,7
Water	9,8

The stress-stain curve of unreinforced MDF and ordinary cement is compared with fibre reinforced MDF in Figure 2.8.

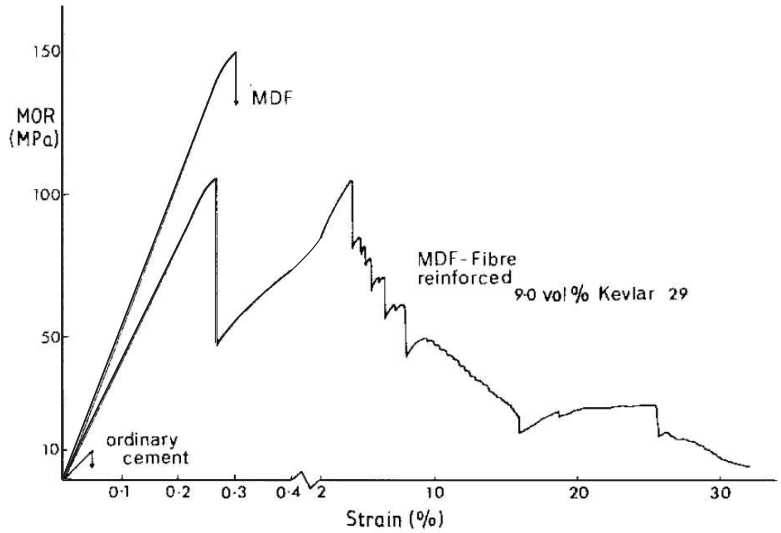

Figure 2.8: Bending stress-strain curve of ordinary cement, MDF cement and fibre reinforced MDF cement (Alford and Birchall, 1985)

As shown, in spite of the flexural strength have decreased when compared with the flexural strength of MDF cement, the ductility increased substantially.

Fiber reinforced MDF was patented in Canada (Alford, 1987).

Densified small particle cement (DSP)

Densified small particle cement (DSP) was presented by Bache (1991) and was the basis for patents in Europe (Bache, 1979) and in the United States (Bache, 1986). This material presented a high compressive strength (120-270 MPa), achieved by controlling the particle size distribution of the cement to minimise the void space between cement grains, and by using a extremely low water content (0,13 - 0,18 by weight of cement plus ultra-fine particles). The dense packing was attained by using a large quantity of superplasticizer. Table 2.4 shows an example of mix composition of DSP.

Table 2.4: Mix design of DSP (adapted from Bache, 1986)

Constituent materials	Parts by weight
Cement	100
Silica	20
Superplasticizer (Mighty)	6,4
Sand	134
Stone 4/18 mm	74
Stone 8/18 mm	146
Water	19

Bache added silica dust to Portland cement in order to fill the voids left by the cement particles. The silica had the additional advantage of reacting chemically with the cement paste to become an integral part of the cementitious matrix. The use of a superplasticizer conferred the necessary workability so that DSP could be poured into forms and moulds (Bennett, 2002). Densified small particle cement was later commercialised under the name Densit®.

Compact reinforced concrete (CRC)

According to Buitelaar (2004), in the period between 1982 and 1986 intensive research was developed to find solutions for the high autogenous shrinkage and the brittleness of the DSP materials.

In 1987, Bache (1987) patented compact reinforced concrete, which was developed at the Cement & Concrete Laboratory of Aalborg Portland. CRC consisted of a DSP

matrix with a high concentration of reinforcement and an increased strain capacity by the addition of a special fibre reinforcement. The CRC compressive and tensile strength can reach 250-350 MPa and 15 MPa, respectively. An example of a mix composition of CRC is presented in Table 2.5.

Table 2.5: Mix design of CRC (adapted from Bache, 1987)

Constituent materials	Parts by weight
White portland cement	100
Microsilica	24
Powder dispersing agent (Flube)	3
Quartz sand	158
Water	22
Fibers	60

Figure 2.9 presents an example of a CRC element and its behaviour.

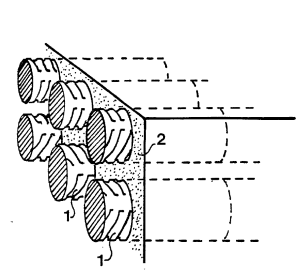

1 - heavy main reinforcement

2 - fibre reinforced matrix

(a) Typical CRC structure

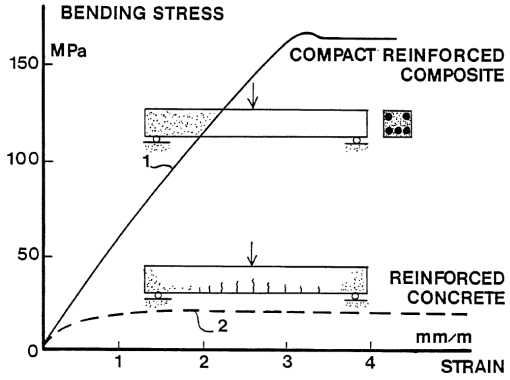

(b) Behaviour in bending of a CRC beam and a steel reinforced concrete beam

Figure 2.9: Application and behaviour of CRC (Bache, 1987)

Reactive powder concrete (RPC)

Reactive powder concretes were developed by Richard and Cheyrezy (1995) at Bouygues and are characterised by a high quantity of silica fume and very low water to cement ratio (Cheyrezy et al., 1995). Their compressive strength is between 200 and 800 MPa (RPC200 and RPC800, respectively) and their flexural strength can reach 140 MPa (Dugat et al., 1996).

The high compressive strengths were achieved through the elimination of coarse aggregates and its replacement by fine sand in order to increase the homogeneity of the material, optimisation of the granular mixture by the use of packing models (Larrard and Sedran,

1994) to increase compactness, improvement of the microstructure by heat treatment after curing and under pressure and incorporation of small-sized steel fibres to improve ductility (Cheyrezy et al., 1995, Dugat et al., 1996). The use of superplasticizers and silica fume allowed the reduction of the water to cement ratio to less than 0,15.

The constituent materials and mix design of RCP are shown in Table 2.6.

Table 2.6: RPC mix design proportions by weight (adapted from Richard and Cheyrezy, 1995)

	RPC200				RPC800	
	Non fibred		Fibred		Silica aggregates	Steel aggregates
Portland cement	100	100	100	100	100	100
Silica fume	25	23	25	23	23	23
Sand (150-600 μm)	110	110	110	110	50	-
Crushed quartz ($d_{50} = 10\mu m$)	-	39	-	39	39	39
Superplasticizer (Polyacrylate)	1,6	1,9	1,6	1,9	1,9	1,9
Steel fibre (L=12 mm)	-	-	17,5	17,5	-	-
Steel fiber (L=3 mm)	-	-	-	-	63	63
Steel aggregates (<800 μm)	-	-	-	-	-	149
Water	15	17	17	19	19	19
Compacting pressure	-	-	-	-	50 MPa	50 MPa
Heat treatment temperature	20°C	90°C	20°C	90°C	250-400°C	250-400°C

Based on the RPC initial research, the Ductal® technology was developed by the combined efforts of three companies, Lafarge, Bouygues and Rhodia (Acker and Behloul, 2004).

2.3 High performance fibre reinforced concrete (HPFRC) mixture

The matrix for a high performance fiber reinforced concrete can be a cement paste, a mortar (paste with sand) or a concrete (mortar with coarse aggregates or gravel). Its key components are cement, supplementary cementitious materials (such as silica fume or fly ash), superplasticizer, fine aggregates and water (Naaman, 2008, Shi et al., 2008).

According to Naaman (2008), the use of supplementary cementitious materials has the advantage of help providing a denser composite, reducing the porosity, improving fresh properties, improving strength, corrosion resistance and durability, controlling the hydration reaction, etc.

Usually, the mixture proportions of a HPC are characterised by the use of a relatively low water content (150-175 kg/m^3) and high binder content. The typical silica fume to cement weight ratio is 5% to 10%. The use of silica fume usually requires the use of a high range water reducer (Shi et al., 2008).

Regarding the properties of self-compactability, the fundamental idea is to lubricate the aggregate grains with a thin layer of cement paste so that the shear stresses between them in the fresh mixture can be decreased, and mixture can become flowable. Thus, self-compacting concretes have an increased quantity of binder components compared to conventional concretes (Marković, 2006).

In close cooperation with LABEST/FEUP a high-performance self-compacting fibre reinforced mortar mixture (HPFRC) was specifically developed for the present research. According to Li (2008), and as most HPFRC studies available in the technical literature (Marković, 2006, Graybeal and Hartmann, 2003), this mixture does not contain coarse aggregates and should therefore be classified as a fiber-reinforced cement paste or mortar.

2.3.1 Materials characterisation

The mortar used in this study was prepared with ternary mixtures of cement (CEM I 42.5 R, provided by Secil-Outão), limestone filler (BETOCARB®-HP-OU, provided by Omnya Comital) and silica fume in suspension with 50% solids content (Centrilit Fume SX, provided by MC-Bauchemie) with a specific gravity of 3,10, 2,68 and 1,38, respectively. The average particle size of cement and limestone filler was 14,6 and 5,36 μm, respectively. The particles of silica fume have a size 50 to 100 times lower than that of cement particles. The superplasticizer used (Viscocrete® 20HE, supplied by Sika®) consists of modified carboxylates and has a specific gravity of 1,08 and 40% solid content. The sand used was provided by CONCREMAT, having a specific gravity of 2630 kg/m^3 (dry material) and 0,3% absorption. The size distribution is given in Figure 2.10 (Marchão et al., 2012).

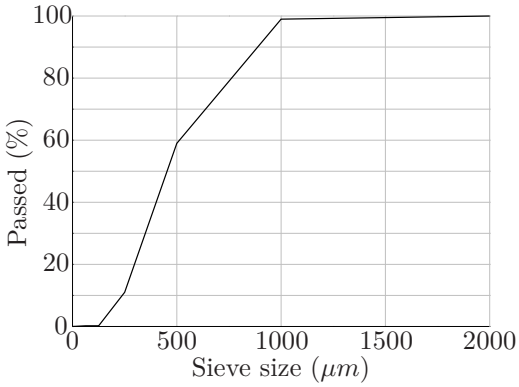

Figure 2.10: Grading of sand

With regard to fibres, and taking into account the fact that the HPFRC was intended to be used in areas with high density of reinforcement and prestressing tendons, were chosen three different types of metallic microfibres with circular cross section and different lengths, supplied by KrampeHarex® from Germany (see Figure 2.11).

(a) DM 6/0.175 **(b)** DM 9/0.175 **(c)** DM 12/0.175

Figure 2.11: Different types of fibres used in this study

The properties of the fibres are summarised in Table 2.7.

Table 2.7: Properties of steel fibres used in this study

Reference	Form	Tensile strength (MPa)	l_f (mm)	d_f (mm)	l_f/d_f
DM 6/0.175	straight	2100	6	0,175	34
DM 9/0.175	straight	2100	9	0,175	51
DM 12/0.175	straight	2100	12	0,175	69

2.3.2 Mixture composition

Initially, the mixture of a reference mortar was adjusted to achieve the lowest possible water to cement ratio (w/c) while maintaining a spread value that ensured the properties of self-compactability. The composition of this reference mortar (HPC), that was also studied and utilised, is presented in Table 2.8.

The water to cement ratio is 25% and the silica fume to cement weight ratio is 5%. The sand content of the reference mixture is 40%. Note that the quantity of water is corrected taking into account the water present in the suspension of silica and in the superplasticizer, and the water needed to saturate an initially dry sand.

In a second phase, the steel fibres were integrated in the reference mix by replacing an equivalent volume of sand. The behaviour of several mixtures of HPFRC with different amounts and types of steel fibers was evaluated in the fresh and hardened states. The

mixture including 3% metal fibers with 9 mm in length was chosen (Marchão et al., 2012). The mixture composition is shown in Table 2.8.

Table 2.8: Mix proportions of HPC and HPFRC

Constituent materials	Quantities (kg/m^3)	
	HPC	HPFRC
cement	810,60	810,60
silica fume	81,06	81,06
limestone filler	317,58	317,58
sand	1040,00	961,10
water	156,80	156,80
superplasticizer	11,16	11,16
steel fibres	-	235,50

2.3.3 Mixing procedure

The optimal mixing procedure consists of:

1. Mix sand, powder materials and silica fume with 80% of the mixing water for 2,5 minutes;
2. Stop the mixer to scrape material adhering to the mixing bowl and mix for another 2,5 minutes;
3. Add the remaining 20% of water with 75% of the superplasticizer and mix for 2,5 minutes;
4. Stop the mixer again to scrape material adhering to the bowl, add the remaining superplasticizer and mix for another 1,5 minutes;
5. Add the fibres and finally mix mortar for another 2 minutes.

The mixer should always be set at low speed.

Note that the mixing times are increased, relative to what is usually used with conventional self-compacting mortars, in order to achieve a good dispersion of the silica fume particles (Marchão et al., 2012).

2.4 Experimental programme - HPFRC production and test results

Since the test specimens would be produced at the precast company CONCREMAT - Préfabricação e Obras Gerais, S.A., it became necessary to calibrate the HPFRC mixture

for large scale production, because the properties of concrete for the envisaged composition could differ from the ones obtained in the laboratory.

The production of HPFRC on site is shown in Figure 2.12.

Figure 2.12: Production of HPFRC on site

The mixer that was used was a planetary mixer Galletti P750, with a volumetric capacity of 750 litres, a planetary and spider speed of 20 and 45 rpm, respectively, and a pan motor power of 30 kW.

The mixtures were prepared in 330 l batches. So, to calibrate the mixtures composition, and for economical reasons, HPC was produced before HPFRC.

2.4.1 Adopted mixing procedure

The mixing procedure was optimised for large scale production. The mixing sequence consisted of:

1. Pre-mixing of sand and powder materials for 30 s;
2. Addition of silica fume, 80% of the mixing water, 75% of the superplasticizer and mixing for 5 minutes;
3. Addition of the rest of the water and superplasticizer and mixing for 4 minutes;
4. Addition of the fibres and finally mixing mortar for another 2 minutes.

2.4.2 Assessment of the water content

Regarding water content, in large scale production it is neither possible to dry the sand nor to accurately measure its moisture content, which makes it difficult to correct the amount of water to add to the mixture. The moisture content of the sand at its surface and the one below the surface differs.

Concerning air temperature, the mixture was extremely sensitive to high temperatures. It was not possible to achieve adequate workability without requiring the addition of significant amounts of water.

The water content was assessed with basis on the results of the fresh state tests, mainly the slump flow test.

Table 2.9 shows, for each HPC and HPFRC mixture, the amount of water added to each mixture (Δ_{water}) taking into account the air temperature (T) and the measured moisture content of the sand (w_{sand}). It also indicates the final water to cement ratio taking into account the water included in the suspension of silica fume and superplasticizer, as well as the water included in the sand. The values of the diameter obtained on the slump flow test (SF) are also presented.

Table 2.9: Climacteric conditions, measured moisture content of the sand and added water amount in the various mixtures of HPC and HPFRC

Mixture		Month	T (°C)	w_{sand}	Δ_{water}	w/c	SF (mm)
HPC	A	March	12	1,7%	-9%	0,25	930
	B'	March	14	3,8%	-13%	0,27	600
	B	March	14	3,8%	-9%	0,28	670
HPFRC	A	April	19	3,6%	-3%	0,29	720
	-	July	35	0,2%	-1%	0,25	500
	-	July	35	0,2%	3%	0,26	[a]
	B'	Sept	30	2,0%	4%	0,28	[a]
	B	Sept	30	2,0%	10%	0,29	880
	C'	July	22	0,5%	-1%	0,25	[a]
	C	July	21	0,5%	12%	0,28	[b]
	D	Sept	26	0,1%	30%	0,32	900

[a] The mixture did not reach enough workability to allow the performance of the slump flow test

[b] The workability loss of the mixture was very fast and did not allow the execution of the slump flow test

It should be noted that from all the mixtures produced, only mixtures HPC A and B, and HPFRC A, B, C and D were used and studied with regard to determination of its mechanical properties.

2.4.3 Characterisation of the fresh state

Because it is a self-compacting concrete and, as stated before, with the aim of calibrating mixture composition, characterising the fresh state of the mortar and assess the key properties of fresh SCC, slump flow test and V-funnel test were performed.

Slump flow test

The slump flow test, that should normally be specified for all SCCs, is used to evaluate the flowing ability of a fresh mix in non-confined conditions. Test results are the slump-flow diameter (SF) and the time needed to reach the 500 mm diameter (t_{500}), which give, respectively, an indication of flowability and filling ability, and relative viscosity of SCC (BIBM et al., 2005). Besides assessing viscosity, and according to BIBM et al. (2005), during mix development, it can be helpful to measure and record the t_{500} time while doing the slump-flow test as a way of confirming uniformity of the SCC from batch to batch. The procedure for determining SF and t_{500} for self-compacting concrete is described in EN 12350-8 (2010). Figure 2.13a shows the slump flow test for a HPFRC mixture.

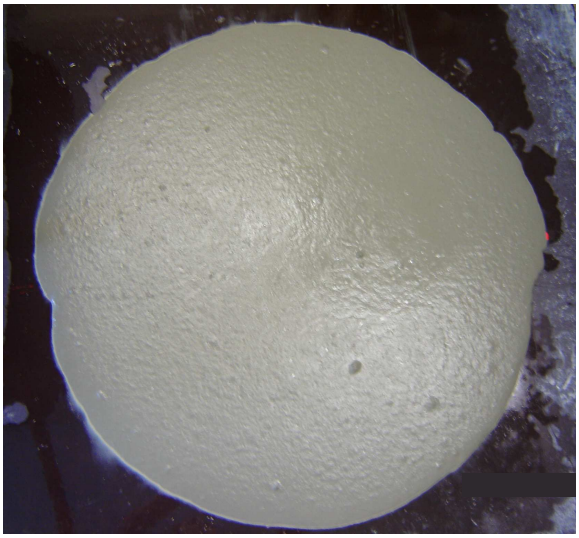

(a) Slump flow test

(b) V-funnel test

Figure 2.13: Characterisation of the fresh state tests for HPFRC

V-funnel test

The V-funnel test is used to evaluate the viscosity and filling ability of self-compacting concrete. The test result is the time taken for the fresh concrete to flow out of a V-shaped funnel (t_v). The procedure for determining t_v for self-compacting concrete is described

in EN 12350-9 (2010). Figure 2.13b shows the V-funnel used in the test of a HPFRC mixture.

Table 2.10 shows the results of the tests in the fresh state for the studied mixtures.

Table 2.10: Slump flow and V-funnel test results of HPC and HPFRC mixtures

Mixture		Slump flow test		V-funnel test
		SF (mm)	t_{500} (s)	t_v (s)
HPC	A	930	3,1	19,4
	B	670	8,5	16,3
HPFRC	A	720	4,5	16,5
	B	880	-	10,3
	D	900	5,8	-

As previously mentioned, the HPC mixtures were produced before the HPFRC mixtures to assess the factory production of larger quantities. For this reason, and coupled with the fact that the mixture has proved to be very sensitive to water content and to air temperature, the variation of values obtained in the tests for the fresh state was very wide (for example, for the slump flow diameter, values of 930 and 670 mm were obtained for HPC mixtures and the values obtained for HPFRC mixtures range between 720 and 900 mm).

According to BIBM et al. (2005) and despite all the foregoing:

- The slump flow diameter obtained for mixtures HPFRC A and HPC B (between 660 mm and 750 mm) are suitable for normal applications;
- The slump flow diameter obtained for mixtures HPFRC B, HPFRC D and HPC A (values higher than 850 mm) indicate that great care should be taken regarding segregation, but are consistent with a mortar mixture, without coarse aggregates;
- The t_{500} (values higher than 2 s) and the t_v values obtained (between 9 and 25 s) indicates that with increasing flow time it is more likely to exhibit thixotropic effects, which may be helpful in limiting formwork pressure and improving segregation resistance. Negative effects may be experienced regarding surface finish (blow holes) and sensitivity to stoppages or delays between successive lifts.

2.4.4 Rheological properties

In addition to the tests in the fresh state and with the aim of analysing the HPFRC workability, several tests were carried out, namely, mini-slump, stability tests and rheological measurements using a rotational rheometer in a plate (Marchão et al., 2012).

For these tests, the high performance concrete (with and without fibres) was also produced in laboratory, as shown in Figure 2.14.

Figure 2.14: Production of HPFRC in laboratory conditions

The mixer used in laboratory was a Beba B 80-T pan mixer, with a volumetric capacity of 80 litres, a rotation speed of 44 rpm and a motor power of 1,1 kW.

Stability tests

According to Van Rickstal (2000), the instability of a grout (or mortar, in this case) can be assessed measuring the evolution of the density of the mixture with time in the fresh state because, as the more unstable is the grout, the more the density will decrease. In an unstable grout, the heavy particles of the dispersion sink to the bottom of the recipient by gravity, resulting in a loss of heavy particles in the top region. This leads to the reduction of the density of the grout in the upper sections. Small density variations denote a more stable concrete, a negligible bleeding effect and a smaller flocculation rate (Marchão et al., 2012).

In order to measure over time the changes in the density of freshly mixed mortar, 500 ml of mortar (without fibres) was poured into a 500 ml glass graduated cylinder placed under a balance. A cylindrical object suspended from the balance was placed inside the cup with concrete, as shown in Figure 2.15, and the measured mass variation was recorded during

45 minutes.

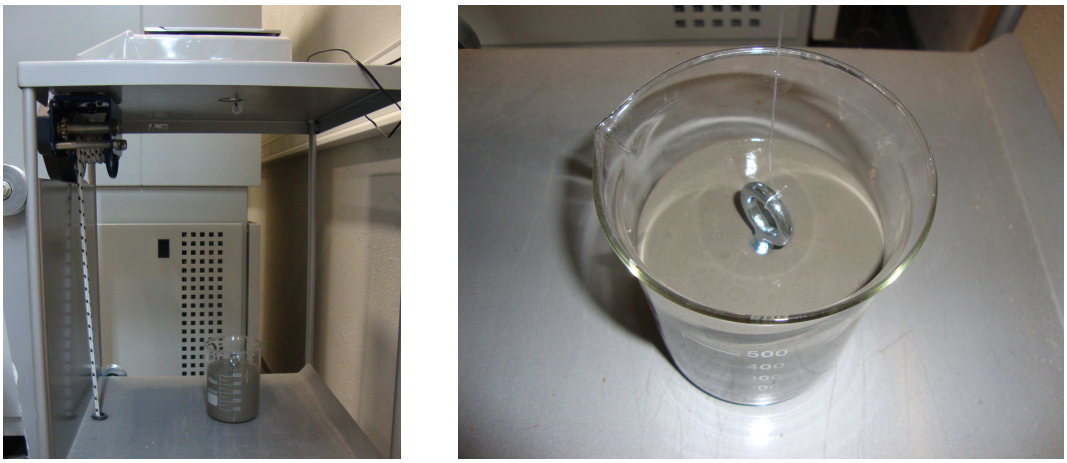

(a) Stability test device adopted **(b)** Detail of the device

Figure 2.15: Stability tests for fresh HPC

From the analysis of the results, and since the HPC was tested during its resting time, it was concluded that the thixotropic effect and flocculation, in particular, were of great importance, especially in the first 30 minutes after what the HPC workability loss became relevant, probably due to significant hydration effects (Marchão et al., 2012).

Mini-slump test

The mini-slump test is used to determine the "workability" of fresh HPFRC and was performed for the HPFRC produced in laboratory and on site (precast factory). For this purpose, a hollow cylinder with 50 mm height and 34 mm internal diameter was adopted as shown in Figure 2.16.

Figure 2.16: Performance of mini-slump test

The spread diameter was measured for the optimum HPFRC composition, for different resting times, up to 30 minutes. The results of the test can be observed in Figures 2.17 and 2.18, for mixtures produced respectively in laboratory and on site.

(a) Test after production **(b)** Test after 15 min. **(c)** Test after 30 min.

Figure 2.17: Mini-slump test for laboratory conditions

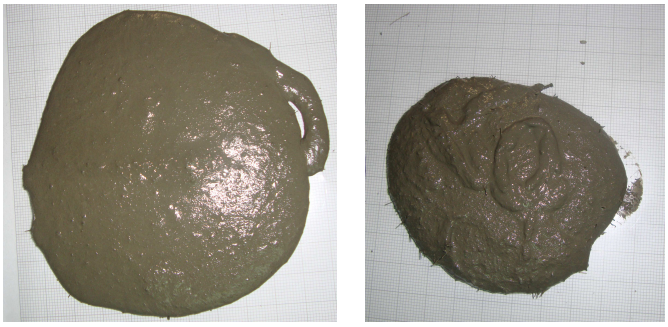

(a) Test after production **(b)** Test after 15 min.

Figure 2.18: Mini-slump test for on site conditions

Figure 2.19 shows the values obtained for the performed mini-slump tests.

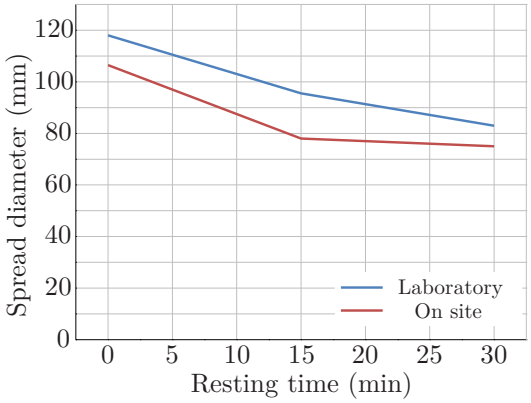

Figure 2.19: HPFRC spread diameter evolution

As it can be observed the HPFRC workability is higher for laboratory environment than for on site production. On the first 15 min the workability loss is higher for both situations. On site measurements show that, between 15 and 30 min, the HPFRC workability tends to become constant but smaller than in laboratory environment.

Rheological measurements

Since the rotational rheometer device can not be used for mixtures with fibers, only the fresh HPC mixture without fibres was tested at different temperatures (from 20°C to 30°C). The yield stress was calculated for each temperature.

Figure 2.20 presents the values of yield stress for different mortar temperatures, confirming that for this mixture, temperatures higher than 25°C can lead to workability loss.

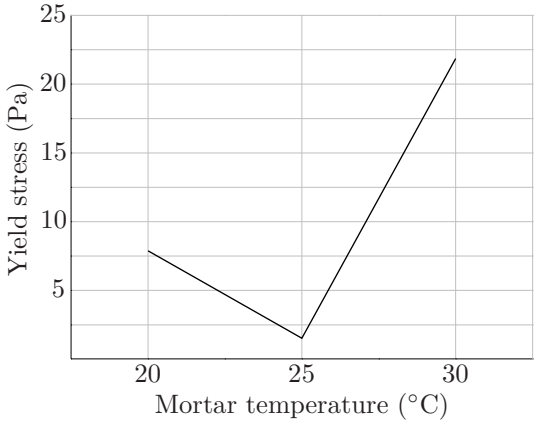

Figure 2.20: Yield stress values of HPC

2.4.5 Mechanical properties

In order to determine the mechanical properties of the HPC and HPFRC developed, uniaxial compression tests, tensile splitting tests, three point bending tests and static modulus of elasticity tests were performed.

The equipment used for the uniaxial compression tests, the tensile splitting test and also to determine the static modulus of elasticity was a *FORM+TEST Seidner* 3000D servo-controlled compression testing machine (upgraded by *walter+bay*) with a load capacity up to 3000 kN and displacement capacity up to 50 mm.

For all the tests, the data acquisition equipment used was a *HBM Spider8*, with eight channels per basic device. The data acquisition software used was the *HBM catman 6.0*.

2.4.5.1 Compressive strength

The compressive strength was evaluated through uniaxial compression tests. These tests were performed in accordance with EN 12390-3 (2001), except that the application of loading was performed under displacement control condition with a displacement speed of 0,02 mm/s until failure. The vertical displacements were measured with TML displacement

transducers. Figure 2.21 presents a typical setup for the testing of a cubic specimen.

Figure 2.21: Test setup for uniaxial compression tests

Cubic specimens with 150 mm and 100 mm, and cylindrical specimens with 150 mm diameter and 300 mm height were used. The geometry of the specimens is in accordance with the recommendations of EN 12390-1 (2000). The cylindrical specimens were cast using iron moulds, while for the cubic specimens plastic moulds were used.

HPC mixtures

The failure modes of the HPC cubic specimens are shown in Figure 2.22.

Figure 2.22: Failure mode of a HPC cubic specimen

As the mixtures of HPC were the first to be produced and studied, and since the compressive strength at 28 days of age of the concrete was unknown, it was decided to use cubes of 150 mm for the tests at 7 and 14 days and cubes of 100 mm for the tests at 28 days, to avoid attaining the maximum capacity of the compression machine without failure of the 150 mm cubic specimens.

For the studied HPC mixtures, the values of the mean compressive strength for 100 mm cubic specimens are presented in Table 2.11.

Table 2.11: Compression test results of HPC cubic specimens of 100 mm at the age of 28 days

HPC mixture	Number of specimens	$f_{cm,100}$ (MPa)	δ
A	6	118,5	4,5%
B	3	117,8	3,6%

In Table 2.11, the coefficient of variation (δ) shows the extent of variability in relation to the mean value and is defined as the ratio of the standard deviation to the mean value, as shown in equation (2.1):

$$\delta = \sqrt{\frac{1}{n-1}\sum_{i=1}^{n}\left(\frac{f_{ci}-f_{cm}}{f_{cm}}\right)^2} \tag{2.1}$$

The stress-strain relation obtained from these tests are shown in Figure 2.23.

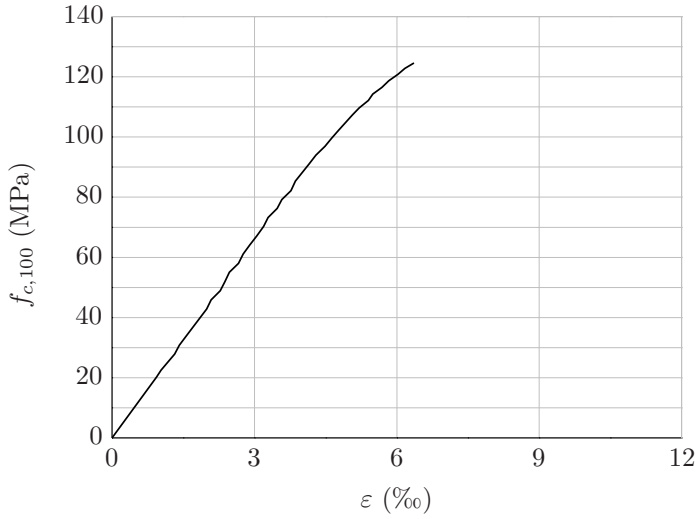

Figure 2.23: Stress-strain diagram of a HPC 100 mm cube

It should be noted that the strain values indicated in Figure 2.23 result from the compression test of a cubic specimen and, therefore, are not representative of a uniaxial state of compression.

HPFRC mixtures

The failure modes of the HPFRC cubic and cylinder specimens are shown in Figures 2.24 and 2.25, respectively.

Figure 2.24: Failure mode of a HPFRC cubic specimen

Figure 2.25: Failure mode of a HPFRC cylinder specimen

Although only 3 or 6 specimens were tested in each case, the characteristic compressive strength of concrete (f_{ck}) was obtained from the values of the mean compressive strength achieved in the tests assuming the normal distribution equation (2.2) for the compressive strength, as presented below.

$$f_{ck} = (1 - 1,64 \cdot \delta) \cdot f_{cm} \tag{2.2}$$

where δ is the coefficient of variation and f_{cm} is the mean compressive strength of concrete.

The values of the mean compressive strength and characteristic compressive strength for 150 mm cubic specimens and cylinder specimens are presented in Tables 2.12 and 2.13.

Table 2.12: Compressive strength of HPFRC cubic specimens of 150 mm at the age of 28 days

HPFRC mixture	Number of specimens	$f_{cm,cube}$ (MPa)	δ	$f_{ck,cube}$ (MPa)
A	3	112,2	6,5%	100,1
B	3	109,0	1,3%	106,6
C	3	106,7	5,6%	97,0
D	3	101,6	4,9%	93,4

Table 2.13: Compressive strength of HPFRC cylindrical specimens at the age of 28 days

HPFRC mixture	Number of specimens	f_{cm} (MPa)	δ	f_{ck} (MPa)
C	3	116,7	0,6%	115,5
D	3	97,8	4,1%	91,2

Table 2.14 shows the comparison between the compression test results for HPFRC mixtures, obtained from the testing of cylinders and 150 mm cubes, and the ratio between the compression strengths of the two types of test specimens, at the age of 28 days.

Table 2.14: Relation between the compression test results of cylinders and cubes of 150 mm, at the age of 28 days

HPFRC mixture	f_{cm} (MPa)		$f_{cm}/f_{cm,cube}$
	cylinder	cube	
C	116,7	106,7	1,09
D	97,8	101,6	0,96

The results presented in Table 2.14 lead to a mean ratio between the resistance obtained by cylindrical specimens and cubic specimens of 1,03, differing to what is commonly presented in the literature (Neville, 1975, Malaikah, 2005) and recommended in codes (EN 1992-1-1, 2004). This value can be explained by the fact that, as mentioned above, the cylindrical specimens were cast using iron moulds and the cubic specimens using plastic moulds.

According to the results of the compression tests performed by Imam et al. (1995) on different specimens types, cast from iron or plastic moulds, the author concluded that plastic moulds produced concrete with a strength lower than that of the concrete cast from iron moulds. Carrasquillo and Carrasquillo (1988) had already found that the mould material influenced the results of the resistance of the specimens. Moreover, Imam et al. (1995) achieved higher resistance in cylindrical specimens cast in iron moulds than in 150 mm cubic specimens cast into plastic moulds.

Yi et al. (2006) also achieved a slightly higher strength for cylinder specimens than that of the corresponding cubes, for concrete strengths higher than 65 MPa. The author performed several tests in cubes and cylinders to study the effect of specimen sizes, specimen shapes and placement directions on the compressive strength of concrete.

Regarding the cubic specimens of 100 mm, the compression test results at the age of 28 days are shown in Table 2.15.

Table 2.15: Compression test results of HPFRC cubic specimens of 100 mm at the age of 28 days

HPFRC mixture	Number of specimens	$f_{cm,100}$ (MPa)	δ
A	3	119,7	2,0%
B	3	118,5	8,5%
C	6	112,7	4,9%
D	3	103,2	8,6%

Table 2.16 shows the comparison between the compression test results for the HPFRC mixtures, obtained from the testing of 150 mm and 100 mm cubes, and the ratio between the compression strengths of the two types of test specimens, at the age of 28 days.

Table 2.16: Relation between the compression test results of cubic specimens of 150 mm and of 100 mm, at the age of 28 days

HPFRC	f_{cm} (MPa)		$f_{cm}/f_{cm,100}$
mixture	150 mm	100 mm	
A	112,2	119,7	0,94
B	109,0	118,5	0,92
C	106,7	112,7	0,95
D	101,6	103,2	0,98

From the results of the performed tests, it has been observed an average difference of 5% between the compression strengths achieved with the 150 mm cubes and the 100 mm

cubes, which is in agreement with Imam et al. (1995) who concluded that there is a 5% drop in the compressive strength for each 50 mm increase in cube width size.

Figure 2.26 shows the evolution with time of the mean compressive strength for three mixtures of HPFRC, referred to 150 mm cubes.

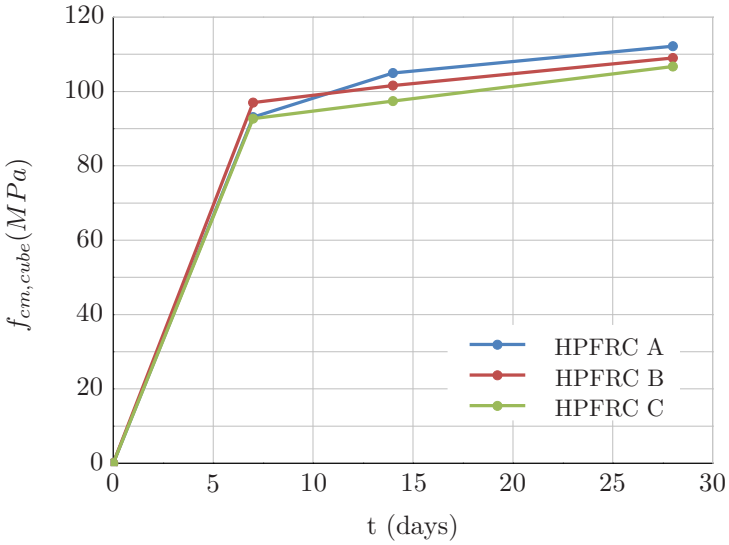

Figure 2.26: Evolution of the HPFRC strength over time

The values are presented in Table 2.17.

Table 2.17: Compression test results of cubic specimens of 150 mm for various ages of concrete

		7 days		14 days		28 days	
HPFRC mixture	Number of specimens	$f_{cm,cube}$ (MPa)	δ	$f_{cm,cube}$ (MPa)	δ	$f_{cm,cube}$ (MPa)	δ
A	3	93,1	0,8%	105,0	3,6%	112,2	6,5%
B	3	97,0	3,2%	101,6	7,8%	109,0	1,3%
C	3	92,7	3,0%	97,4	3,8%	106,7	5,6%

Through the analysis of the values presented above, it can be concluded that all mixtures presented a 7-day strength between 83% and 89% of the 28-day strength. With 14 days, the strength range between 91% and 94% of the strength at 28 days.

Figure 2.27 shows the stress-strain diagrams obtained from compression tests of 150 mm cubic specimens for various ages of one mixture of HPFRC. It should be noted that the strain values indicated in Figure 2.27 result from the compression tests of cubic specimens and, therefore, are not representative of uniaxial states of compression.

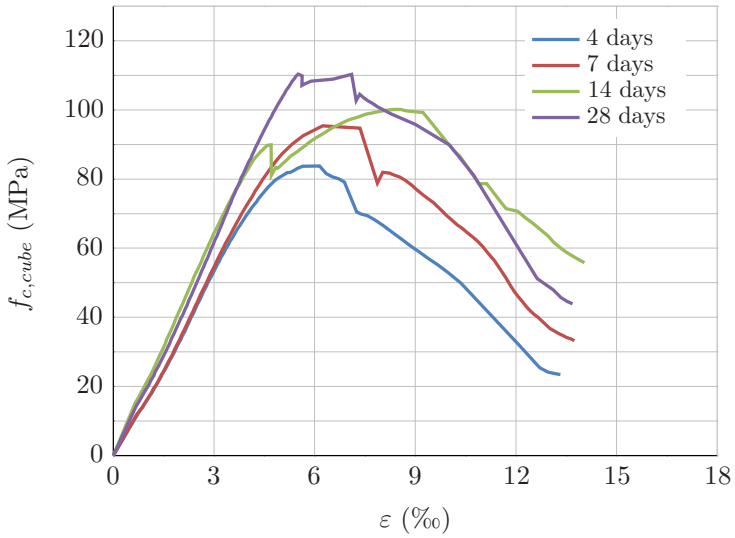

Figure 2.27: Stress-strain diagrams of HPFRC 150 mm cubes for various ages of concrete

2.4.5.2 Tensile strength

The concrete tensile strength was assessed by tensile splitting tests and three point bending tests, due to the difficulty in applying direct tension to concrete.

Tensile splitting tests

Tensile splitting tests were performed in accordance with EN 12390-6 (2000), except that the application of loading was done under displacement control condition with a displacement speed of 0,02 mm/s until failure. Figure 2.28 presents a typical setup for the tests.

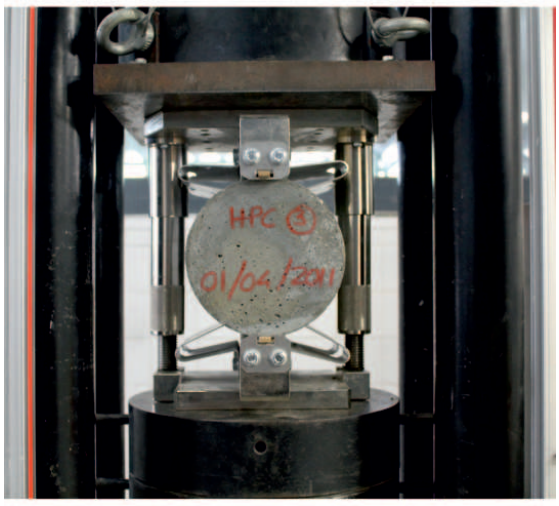

Figure 2.28: Test setup for tensile splitting tests

According to Denneman et al. (2011), the tensile splitting test has the advantage of being performed on cylindrical specimens using a standard compression testing machine. However, it only provides a measure of HPFRC tensile strength and does not provide suitable data on the post crack behaviour of the material.

HPC mixtures

Regarding HPC mixtures, Figure 2.29 shows the failure mode of the cylindrical specimens in the tensile splitting tests.

Figure 2.29: Failure mode of a HPC cylinder in the tensile splitting test

From the values of the splitting maximum loads achieved in the tests, and according to EN 12390-6 (2000), the tensile splitting strength ($f_{ct,sp}$) is given by equation (2.3):

$$f_{ct,sp} = \frac{2P_{sp}}{\pi \cdot L_{sp} \cdot d_{sp}} \tag{2.3}$$

where,

P_{sp} is the splitting maximum load;
L_{sp} is the length of the line of contact of the specimen;
d_{sp} is the designated cross-sectional dimension of the specimen.

According to EN 1992-1-1 (2004), and based on the value of the tensile splitting strength, an approximate value of the mean value of axial tensile strength (f_{ctm}) may be obtained from equation (3.32):

$$f_{ctm} = 0,9 \cdot f_{ct,sp} \tag{2.4}$$

Table 2.18 presents the values of the tensile splitting strength and mean axial tensile strength for the HPC studied mixtures.

Table 2.18: Tensile splitting strength and related mean tensile strength of HPC cylindrical specimens at the age of 28 days

HPC mixture	Number of specimens	$f_{ct,sp}$ (MPa)	δ	f_{ctm} (MPa)
A	5	3,3	12,8%	3,0
B	6	3,7	14,2%	3,3

HPFRC mixtures

Figure 2.30 shows the failure mode of HPFRC cylinders in the tensile splitting tests.

Figure 2.30: Failure mode of a HPFRC cylinder in the tensile splitting test

The Table 2.19, given below, presents the values of the tensile splitting strength and mean axial tensile strength for the HPFRC studied mixtures.

Table 2.19: Tensile splitting strength and related mean tensile strength of HPFRC cylindrical specimens at the age of 28 days

HPFRC mixture	Number of specimens	$f_{ct,sp}$ (MPa)	δ	f_{ctm} (MPa)
A	3	12,3	10,5%	11,1
B	3	9,6	13,1%	8,6
C	6	11,1	16,9%	10,0
D	6	8,8	16,4%	8,0

Three point bending tests

The tensile behaviour of HPC and HPFRC under bending was evaluated through three-point bending tests on notched beams of 150 mm × 150 mm × 600 mm with 450 mm span, according to EN 12390-5 (2000) and EN 14651 (2007). The notches were 25 mm depth. The load was applied through an actuator with a maximum capacity of 200 kN, using a load cell of 200 kN. The tests were performed under displacement control condition. The middle span deflection was measured with TML displacement transducers. Figure 2.31 presents a typical setup for the test of a beam.

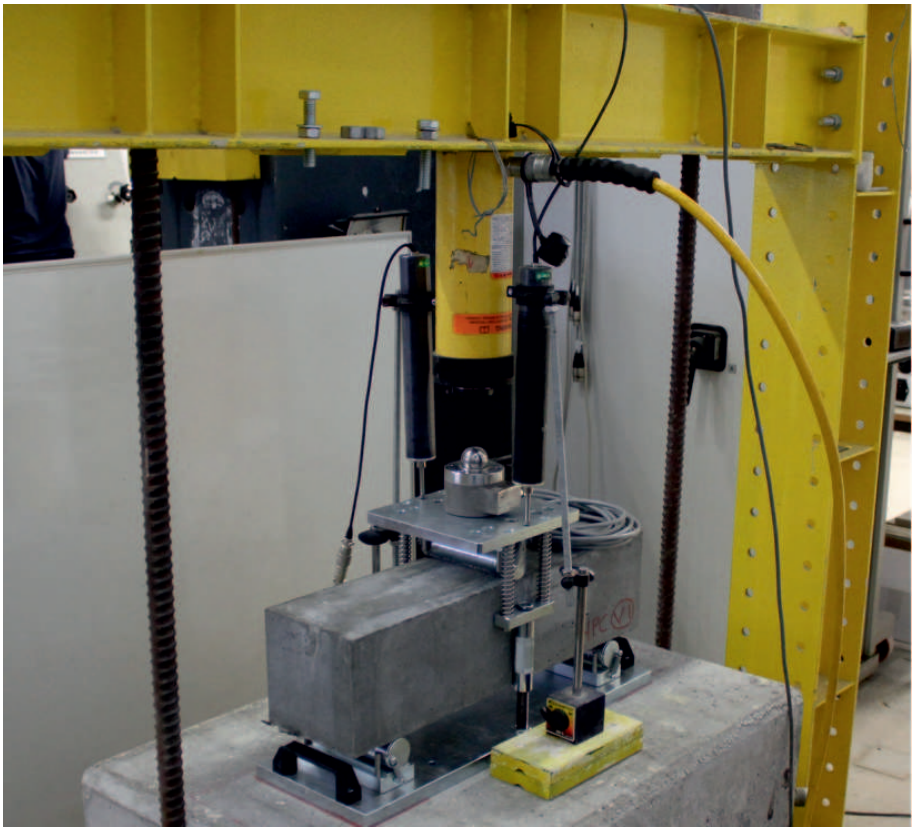

Figure 2.31: Test setup for three point bending tests

HPC mixtures

The failure mode of the HPC beams is shown in Figure 2.32.

Figure 2.33 presents the evolution of the vertical middle span displacement (d) with the applied load (F) obtained in the tests of the beams, for one of the HPC mixtures.

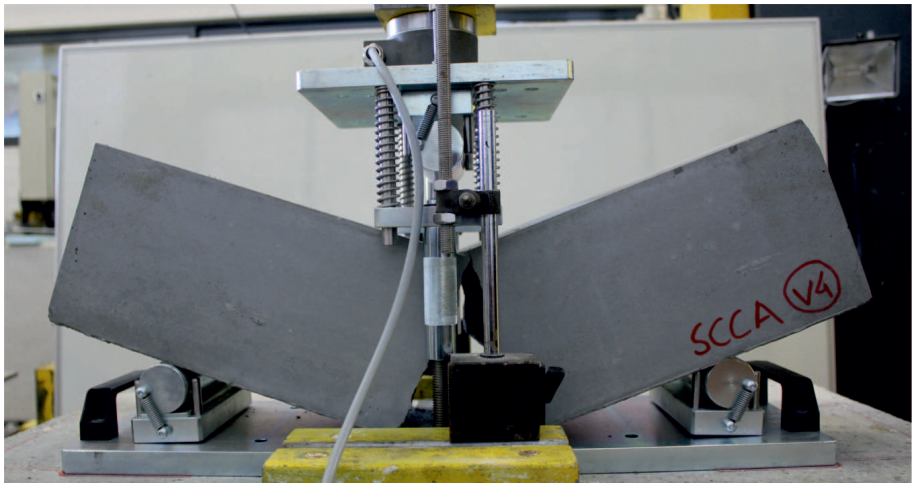

Figure 2.32: Failure mode of a HPC beam

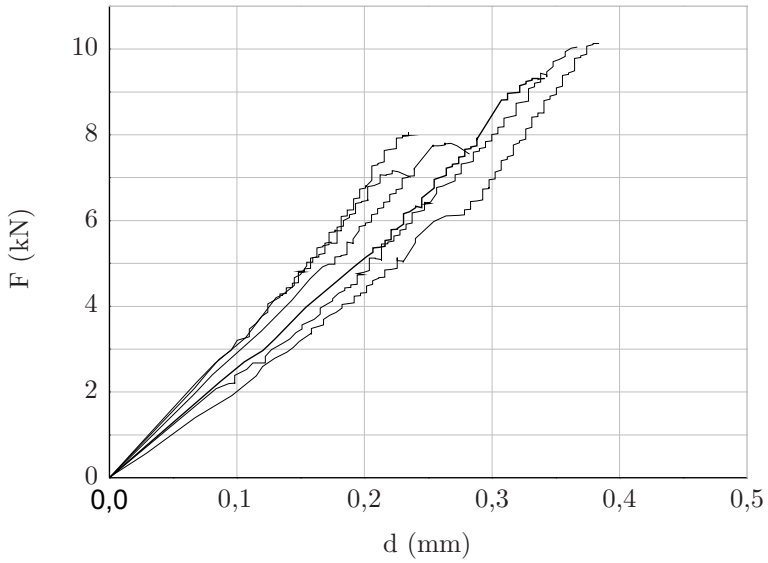

Figure 2.33: Load-displacement diagrams of HPC beams

The flexural tensile strength ($f_{ct,b}$) was calculated according to EN 14651 (2007), by equation (2.5):

$$f_{ct,b} = \frac{3 \cdot F_b \cdot l}{2 \cdot b \cdot h_{sp}^2} \tag{2.5}$$

where,

F_b is the maximum load obtained in the three point bending tests;
b is the width of the specimen in millimetres;
l is the span length in millimetres;
h_{sp} is the distance between the tip of the notch and the top of the specimen, in millimetres.

The mean tensile strength was determined by equation (2.6) (EN 1992-1-1, 2004):

$$f_{ctm} = \frac{f_{ct,b}}{1,6 - h/1000} \tag{2.6}$$

where h is the total depth of the beam in millimetres.

The values of the tensile strength calculated through the three point bending test results are presented in Table 2.20.

Table 2.20: Bending tests results and related mean tensile strength at the age of 28 days for HPC mixtures

HPC mixture	Number of specimens	$f_{ct,b}$ (MPa)	δ	f_{ctm}
A	6	3,0	15,3%	2,1
B	6	2,6	16,3%	1,8

HPFRC mixtures

Regarding HPFRC mixtures, Figure 2.34 shows the failure mode of the tested beams.

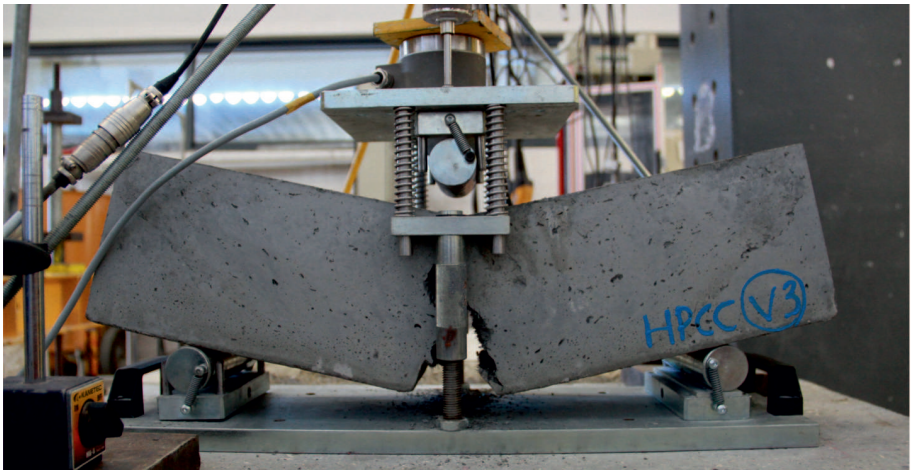

Figure 2.34: Failure mode of a HPFRC beam

Figure 2.35 shows the load-vertical displacement relations obtained in the tests of the beams for one of the HPFRC mixtures.

For the HPFRC mixtures, the values of the tensile strength computed using the three point bending test results are presented in Table 2.21.

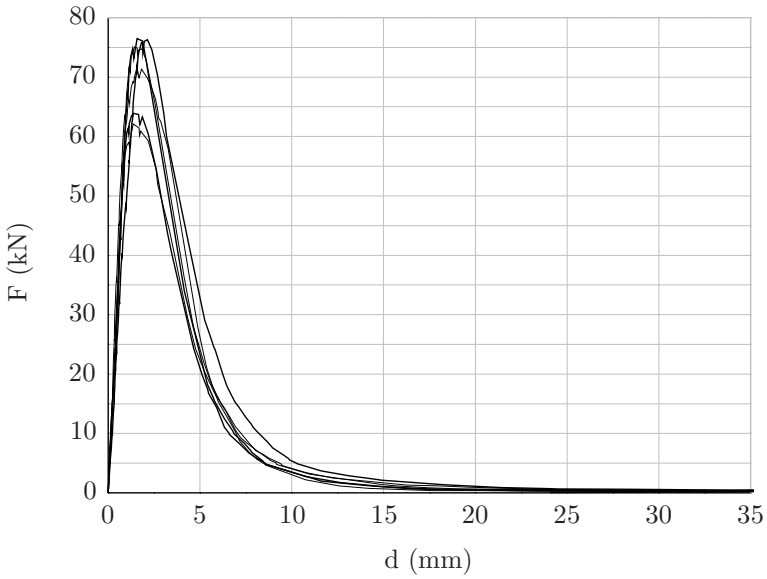

Figure 2.35: Load-displacement diagrams of HPFRC beams

Table 2.21: Bending tests results and related mean tensile strength at the age of 28 days for HPFRC mixtures

HPFRC mixture	Number of specimens	$f_{ct,b}$ (MPa)	δ	f_{ctm} (MPa)
A	5	16,0	15,2%	10,8
B	5	17,7	16,4%	12,0
C	6	21,3	10,0%	14,4
D	6	15,1	16,4%	10,3

Comparison between the tensile resistance values obtained

The comparison between the values of the mean tensile resistance obtained by the two different tests (tensile splitting tests and three point bending tests) for HPC and HPFRC mixtures is presented in Tables 2.22 and 2.23.

Table 2.22: Mean tensile resistance for HPC mixtures

HPC	f_{ctm} (MPa)		Δ
mixture	Tensile splitting tests	Three point bending tests	
A	3,0	2,1	1,43
B	3,3	1,8	1,83

Table 2.23: Mean tensile resistance for HPFRC mixtures

HPFRC	f_{ctm} (MPa)		Δ
mixture	Tensile splitting tests	Three point bending tests	
A	11,1	10,8	1,03
B	8,6	12,0	0,72
C	10,0	14,4	0,69
D	8,0	10,3	0,78

In Tables 2.22 and 2.23, Δ is the ratio between the mean resistance obtained with basis in the tensile splitting test and the mean resistance referred to the three point bending test.

From the analysis of the results, it can be concluded that the ratio between the resistances calculated from the splitting and bending test are different from those documented in the literature (Zhou et al., 1995, Bhanja and Sengupta, 2005). It can be observed, however, different trends for concrete with and without fibers. Regarding the two studied mixtures of HPC, the values of the ratios obtained are 1,43 and 1,83 (average of 1,63). For HPFRC mixtures the average ratio is 0,81.

It should be noted that the results of both tests have a large dispersion, with coefficients of variation between 10,0% and 16,9%. However, the results of the tensile splitting test present lower variability. This fact is confirmed by Arıoglu et al. (2006), who states that the tensile splitting test of a cylindrical specimen is the simplest and most reliable method from the three most common tests (direct tension, flexure and splitting tension) to determine the tensile strength of concrete.

2.4.5.3 Secant modulus of elasticity tests

The tests for determining the secant modulus of elasticity of concrete were performed according to LNEC E 397 (1993). The specimens used were cylinders with a diameter of 150 mm and 300 mm height. The test consisted in a cyclical loading between 1,0 MPa (17,7 kN) and, approximately, one third of the compressive strength at a constant rate of 0,5 MPa/s, corresponding to 8,8 kN/s. The test specimens were subjected to two load cycles, with a waiting period of 30 seconds in each level corresponding to the minimum and maximum compression applied.

The axial displacement reading was carried out by displacement transducers on opposite sides of the specimen and symmetrically placed around the middle of the specimen. The displacement transducers were fixed using metal rings, as shown in Figure 2.36.

Figure 2.36: Test setup for determination of the static modulus of elasticity of a HPFRC mixture

The values of the secant modulus of elasticity obtained by the test results are presented in Table 2.24.

Table 2.24: Static modulus of elasticity at the age of 28 days for HPFRC mixtures

HPFRC mixture	Number of specimens	E_c (GPa)	δ
A	6	43,5	2,8%
B	3	44,6	1,5%
C	3	41,7	2,9%

From the experimental results, equation (2.7) given below was adjusted for determining the modulus of elasticity of the HPFRC.

$$E_{cm} = 7650 \cdot f_{ck,cube}^{3/8} \tag{2.7}$$

where $f_{ck,cube}$ is in MPa.

2.4.6 Shrinkage

Shrinkage tests were made according to LNEC E 398 (1993). The specimens were cast in prismatic moulds with 40 $\times$ 40 $\times$ 160 mm^3 and demoulded the next day. After, the specimens were kept at a constant temperature of 20°C with a constant relative humidity of 50%.

The strain was measured using Demec locating discs for mechanical extensometer measurement of concrete surface strains.

The shrinkage test results are presented in Figures 2.37 and 2.38 for HPC and HPFRC mixtures, respectively.

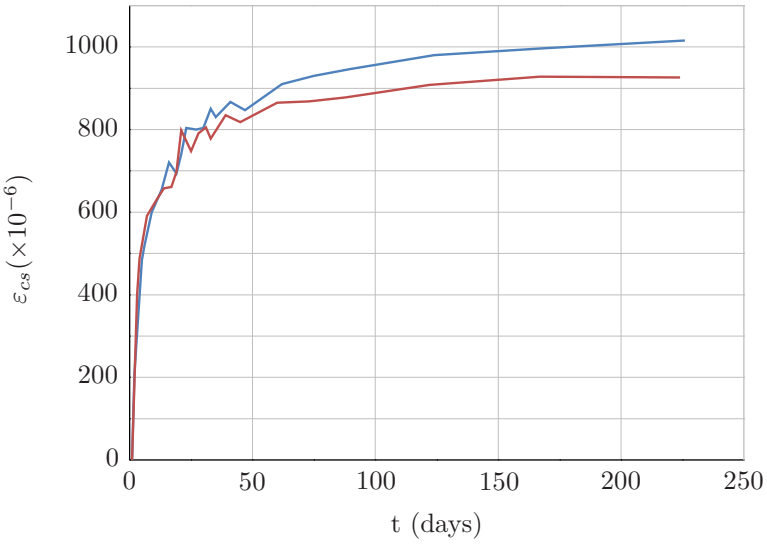

Figure 2.37: Shrinkage test results of HPC mixtures

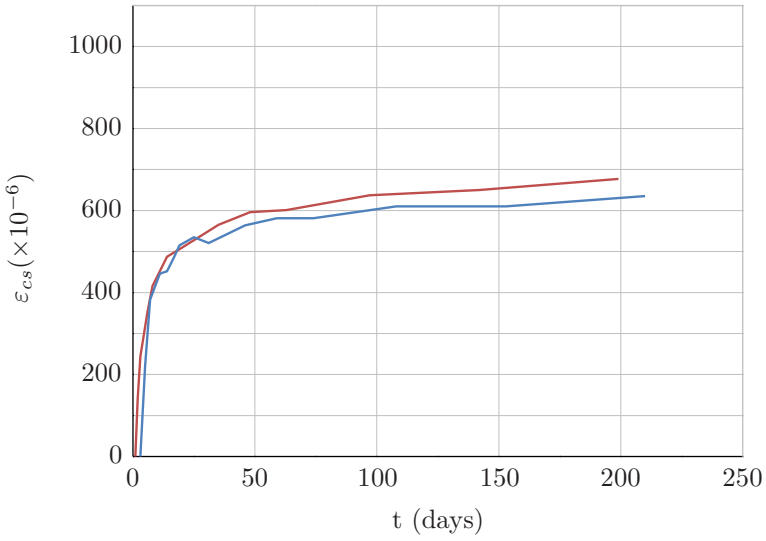

Figure 2.38: Shrinkage test results of HPFRC mixtures

Observing the graphs above it can be concluded that the shrinkage strain of the HPC and HPFRC mixtures is higher than that of conventional concrete. It can also be concluded that the presence of fibers decreases the shrinkage strain.

Chapter 3

Local Anchorage Zone

3.1 Introduction

In post-tensioned structures, the prestressing force is transferred to the concrete either in the form of friction and deviation forces, distributed along the tendon's curved length, or in the form of concentrated forces in the end of the tendons, at the anchorages. These forces can generally be used to counter-balance other loads and thus control deflections and reduce cracking.

In anchorage zones, the concentrated prestressing force is transferred from the anchorage device to the concrete and then spreads out, until a linear stress distribution over the cross-section of the element is reached. The extension of the anchorage zone can be estimated according to Saint Venant's Principle[1]. According to this principle, the anchorage zone can be considered the region ahead of the anchor which extends along the tendon axis for a distance equal to the overall depth of the section (Rogowsky and Marti, 1996).

Within a NCHRP[2] research project, at the University of Texas in Austin, Breen et al. (1987) introduced the concept of dividing the anchorage zone in two separate zones: the local and the general zone. As shown in Figure 3.1, the local zone is the prism of concrete surrounding and immediately ahead of the anchorage device and including the confining reinforcement, through which the concentrated force applied to the anchorage device is transferred to the general zone. The general zone is the remaining volume of the anchorage zone.

[1]This principle states that the strains that can be produced in a body by the application, to a small part of its surface, of a system of forces statically equivalent to zero force and zero couple, are of negligible magnitude at distances which are large compared with the linear dimensions of the part (Love, 1906).

[2]The National Cooperative Highway Research Program (NCHRP) conducts research in problematic areas that affect highway planning, design, construction, operation, and maintenance in the USA. The NCHRP is managed by the Cooperative Research Programs of the Transportation Research Board.

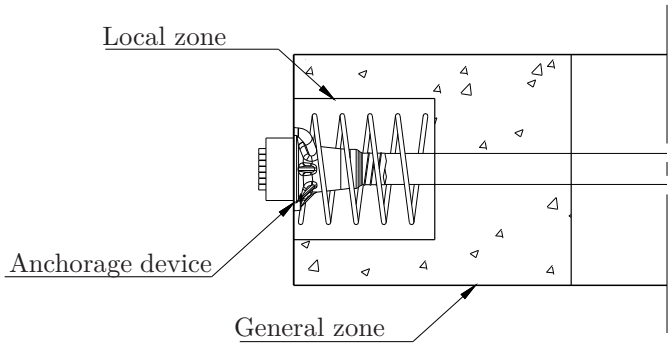

Figure 3.1: Anchorage zone - Local zone and general zone

Because the local zone is very close to the anchorage device, its behaviour is strongly influenced by the characteristics of the specific anchorage device. The geometry and the state of stress of the local zone are very complex, not only because of the anchorage device geometry, but also because of the duct hole, the confining reinforcement and the large tendon force (Burdet, 1990).

With the aim of reducing the concrete cross-section and decreasing the amount of reinforcement steel needed in anchorage zones, a high-performance fibre reinforced self-compacting mixture was developed. Previous studies (Haroon et al., 2006, Leung et al., 2009, Gomes and Nunes, 2010) have shown the efficiency of high performance concretes with regard to the reduction of confining steel reinforcement in those areas.

In order to reduce the minimum concrete cross-section and the confining reinforcement, specified by the anchorage device supplier for the particular anchorage, an experimental program to assess both the ultimate capacity and the adequate serviceability of the local anchorage zone was carried out. The load transfer test specified in the Guideline ETAG 013 (European Organisation for Technical Approvals, 2002) was performed.

In this chapter, a literature review on the research carried out on the bearing strength of plain or reinforced concrete, and reinforced high performance concrete is presented. Then, the load transfer tests are briefly described, with regard to the test specimen, test procedure and acceptance criteria, according to three different guiding documents: FIP Recomendation (1993), AASHTO (2002) and European Organisation for Technical Approvals (2002).

After the literature review, the experimental program is described regarding test specimens, test procedure and experimental results. A comparison of the experimental results with models found in the literature is then presented and discussed.

Finally, the non-linear analysis of the tested specimens is presented and the results are compared.

3.2 Literature review

3.2.1 Unreinforced concrete bearing strength

The bearing strength in construction materials was first investigated by Bauschinger (1876). Bauschinger, referred by Ichiki (1950) and Shelson (1957), performed a set of experimental tests on sandstone cubic specimens (with dimensions 100 mm × 100 mm × 100 mm) under concentric loading, varying the size of the loaded area by steel plates. The results of Bauschinger's test are shown in Figure 3.2.

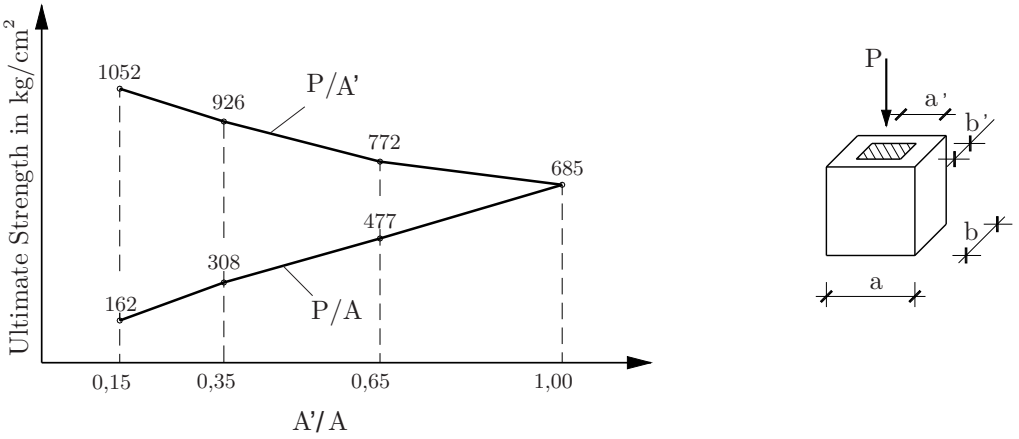

Figure 3.2: Test results by Bauschinger on sandstone specimens (adapted from Ichiki, 1950)

In the Figure 3.2 above, the areas A and A' are the gross area of the specimen (a × b) and the loaded area (a' × b'), respectively.

As a result of his experiments, Bauschinger proposed the allowed bearing strength equation (3.1) given below:

$$f_b = f_r \cdot \sqrt[3]{\frac{A}{A'}} \tag{3.1}$$

where,

f_b is the maximum bearing pressure;
f_r is the sandstone cube compressive strength.

However, this equation led to incorrect results for concrete so Billig (1948), referred by Bergmeister et al. (1993), performed a set of tests on concrete cylinders loaded through rigid bearing plates and developed the equation (3.2) for permissible bearing stresses:

$$f_b = 0,6 f_c \cdot \sqrt[3]{\frac{A}{A'}} \leq f_c \tag{3.2}$$

where f_c is the concrete cylinder compressive strength.

With the aim of testing and evaluating the allowable bearing stress formula recommended in the "Standard Specification for Reinforced Concrete" of the Civil Engineering Society of Japan (equation (3.3)), Ichiki (1950) tested 22 specimens with dimensions 300 mm × 300 mm × 360 mm. All specimens were concentrically loaded with square and circular bearing steel plates with different dimensions.

$$f_b = \frac{f_{c,28}}{3,5} \cdot \sqrt[3]{\frac{A}{A'}} \leq 120\ kg/cm^2 \tag{3.3}$$

where $f_{c,28}$ is the concrete compressive strength at the age of 28 days.

The test results are shown in Figure 3.3.

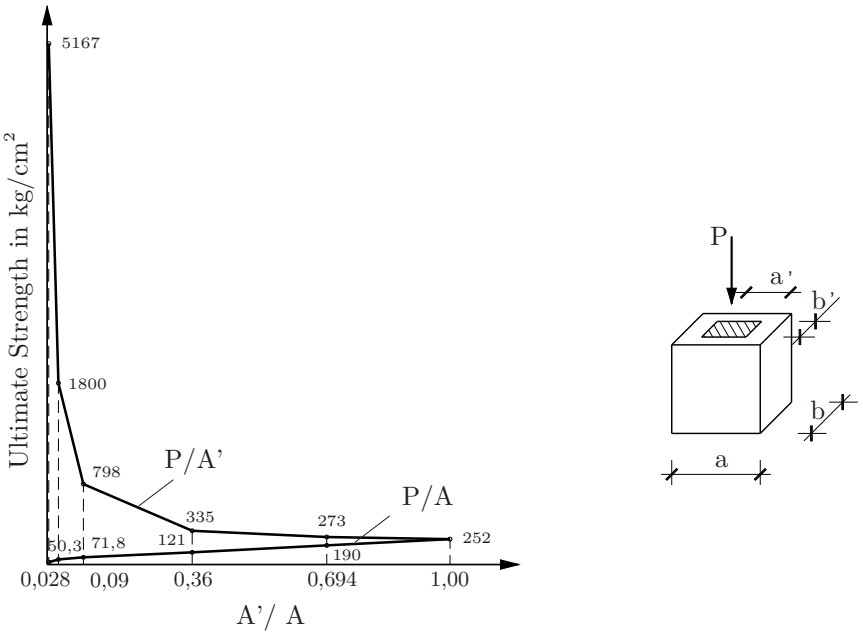

Figure 3.3: Test results by Ichiki on concrete specimens (adapted from Ichiki, 1950)

Regarding test results, Ichiki proposed the adoption of the square root formula shown in equation (3.4).

$$f_b = 1,1\frac{f_{c,28}}{3,5} \cdot \sqrt{\frac{A}{A'}} \leq 1140\ kg/cm^2 \tag{3.4}$$

Komendant (1952) published the square root formula shown in equation (3.5), for determining the allowable compressive stress under an anchorage plate.

$$f_b = f_c \cdot \sqrt{\frac{A}{A'}} \tag{3.5}$$

According to Middendorf (1963), Komendant developed his formula from tests, and also discovered that as the surrounding concrete area increased the actual bearing stress under the plate could exceed the 28 day compressive stress many times.

Meyerhof (1953), based on the tests carried out by previous researchers on concrete and rock, concluded that the material failed by splitting or shearing along one or several rupture surfaces. Based on Mohr-Coulomb's theory of rupture[3], Meyerhof proposed a relation to determine the bearing capacity of a strip footing, using the cohesion and the angle of internal friction of the concrete.

In order to obtain more information, in particular for large blocks, Meyerhof performed 28 tests on concrete footings with several height/width ratios (1:1, 1:2, 1:3 and 1:4) and circular base plate, whose results are shown in Figure 3.4. The author concluded that the bearing capacity increases in direct proportion to the ratio h/2a.

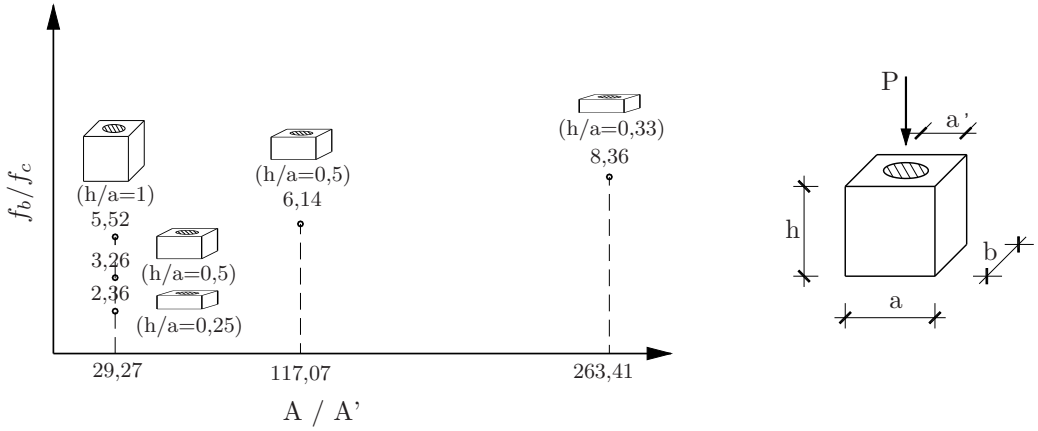

Figure 3.4: Test results by Meyerhof (1953) on concrete footings

Shelson (1957) carried out a test program to determine the maximum bearing pressure of concrete footings through steel base plates. The effect of rigid versus flexible base plates was also studied. The test program consisted of loading 8 in. concrete cubes to failure through square mild steel base plates, 1/4 in. thick, with different side dimensions (1, 1,41, 2, 2,83 and 3 in. were used). In order to study the effect of rigid and flexible base plates, in some cases the load was applied to the plate in a 1 in. square area of the base plate, and in the remaining tests, the load was applied over the entire surface area of the base plate.

Figure 3.5 shows the test results obtained by Shelson for the last mentioned case (load applied over the entire surface of the base plate).

[3]The Mohr-Coulomb failure criterion, or internal-friction theory, considers two basic types of failures: sliding failure and splitting failure. In sliding failure a fracture surface develops inclined to the direction of the maximum compressive stress and the movement of the resulting failure planes is parallel with respect to each other. This is the most likely to happen in a typical bearing test, when a cone or pyramid is developed under the bearing plate at failure. In splitting failure the fracture plane is generated normal to the axis of the tensile stress and the planes tend to separate in opposite directions (Bonetti, 2005).

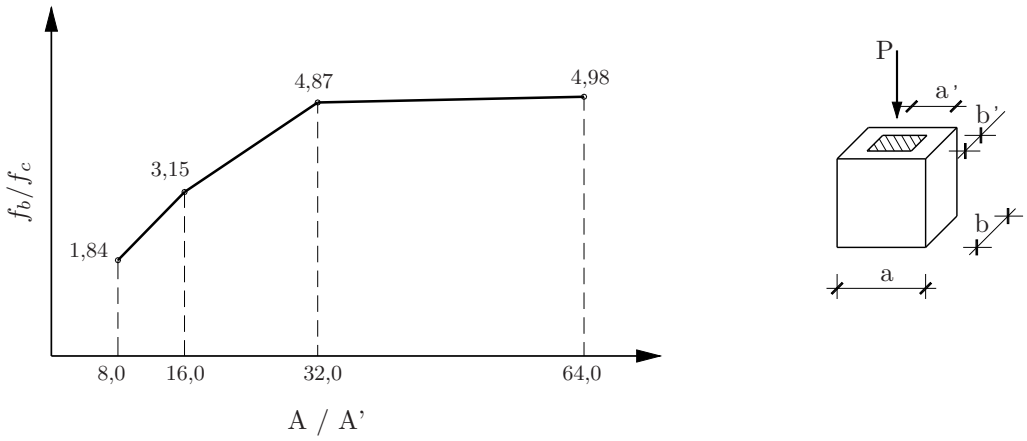

Figure 3.5: Test results by Shelson (1957) on concrete cubes

Based on the tests results, the author proposed the relation shown in equation (3.6) for the permissible bearing pressure on concrete.

$$f_b = 0,25 f_c \left(\frac{A}{A'}\right)^{0,3} \tag{3.6}$$

During the period between 1952 and 1956, Middendorf (1963) performed several tests on concrete cylinders loaded through circular steel plates to assess the validity of Komendant and Billig's formulas (square root and cube root of related geometrical areas, respectively). The test program consisted of loading 8 in. diameter by 16 in. long cylinders to failure through centred circular plates, with ratios A/A' ranging between 1 and 7. He found a good correlation between Komendant's square root formula and his bearing tests.

During 1959 and 1960 the author proposed a new series of tests to explore the consistency of the A/A' ratio for concrete of various ages (1 to 28 days) and various strengths (f_c ranging from 27,5 to 40 MPa), varying sizes and shapes of bearing plates (both rectangular and circular) and using plates tilted from the 90° normal position in relation to the tendon axis. The specimens utilized consisted of 6 in. diameter by 12 in. long cylinders and blocks with dimensions 7 in. × 7 in. × 12 in., loaded through both circular and rectangular plates. Middendorf recommended the replacement of the cube root formula with the square root formula, as well as the increase of the limitation of bearing stress under the plate from f_c to probably $3f_c$. The author concluded that his recommendations were applicable to concrete with f_c ranging from 27,5 to 40 MPa.

It is noteworthy that the equations given above to determine the bearing capacity, already include safety factors and are therefore equations for design.

Au and Baird (1960) published the results of their investigation on the bearing capacity of square concrete blocks whose area was 2 to 16 times the contact area. The effects of the maximum aggregate size and the depth of the blocks had also been considered. The specimens used in the tests consisted of 8 in. concrete cubes and blocks with dimensions

8 in. × 8 in. × 4 in., loaded through square steel base plates. The specimens were cast from two mixes of concrete: one with small aggregates and the other with large aggregates, with compressive strengths of 58,6 MPa and 31,0 MPa, respectively. The results of the test are show in Figure 3.6.

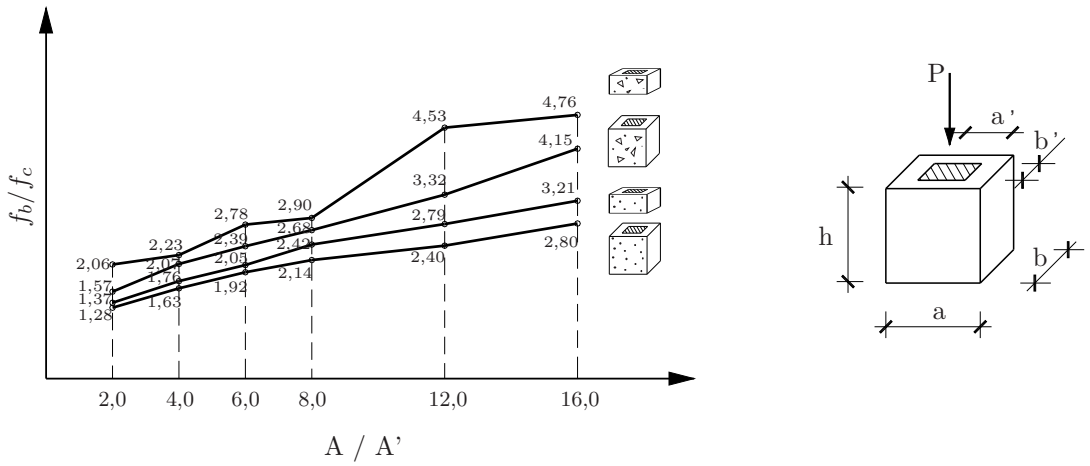

Figure 3.6: Test results by Au and Baird (1960) on concrete blocks

Au and Baird developed a theory on the formation of an inverted pyramid under the loading plate. They assumed that the pyramid formation could be caused by secondary bending due to the uneven bottom surface of the concrete block. This inverted pyramid would be forced down by the applied bearing pressure and would produce splitting of the concrete as a result of a horizontal splitting pressure acting on the inverted pyramid. The resultant of these pressures was assumed to produce combined tension and bending in the concrete block.

From 1968 to 1970, at the University of Sydney, Hawkins studied the bearing strength of concrete loaded through rigid (Hawkins, 1968b) and flexible plates (Hawkins, 1968a), and under strip loading (Hawkins, 1970), performing several tests on concrete blocks, loaded under different test conditions.

In the paper dealing with rigid plates, the author presented the results of 18 series of tests, performed with the aim of studying the effects, on the bearing strength, of concentric and eccentric loading, geometry of specimen and of loading plate, and type and strength of concrete. The majority of specimens were 6 in. cubes loaded through 3/4 in. thick steel plates.

During the tests, Hawkins observed that the first failure warning was the formation of vertical cracks on the sides of the specimen closest to the loaded area (Figure 3.7(a)). When the maximum load was reached, a conical wedge punched out from beneath the bearing plate (Figure 3.7(b)) and the radial cracks emerged on the loading surface (Figure 3.7(c)).

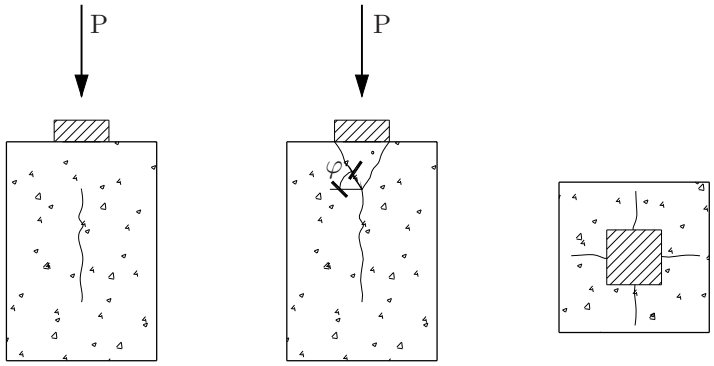

(a) Vertical cracks (b) Failure cone (c) Radial cracks

Figure 3.7: Failure mechanism in bearing tests of plain concrete blocks by Hawkins (1968b)

Hawkins developed the expression for bearing strength shown in equation (3.7), based on failure modes observed in the tests.

$$f_b = f_c + K_t\sqrt{f_c}\left(\sqrt{\frac{A}{A'}} - 1\right) \tag{3.7}$$

where K_t is a constant that depends on the concrete tensile strength and the angle of friction, both determined experimentally, which varied from 50 to 65, and can de determined using equation (3.8). Hawkins suggested a value of K_t=50 for design purposes.

$$K_t = Bcot^2(\varphi) \tag{3.8}$$

where,

$B = f_{ct}/\sqrt{f_c}$;
f_{ct} is the concrete tensile strength;
φ is the concrete angle of internal friction.

Additionally, the author recommended that the effective unloaded area should be concentric with and geometrically similar to the load plate. Hawkins also suggested alternative formulations for strip loading and edge loading of concrete surfaces, and proposed a criterion to verify whether a load plate can be considered rigid.

Hyland and Chen (1970) carried out an experimental program on concrete cylinders. One of the purposes of the investigation was to attempt to provide an experimental verification on the assumption of perfectly plastic behaviour of concrete. In addition, it was also investigated the effect of base friction and specimen height on bearing capacity, as well as the effect of a hole concentrically located under the loaded area to have a close representation of an anchorage zone in post-tensioned concrete members.

The specimens utilised, schematically shown in Figures 3.8(a) and 3.8(b), consisted of 6 in. diameter cylinders with heights of 6 in., 3 in. and 2 in., loaded through circular

plates with diameters of 3/2 in. and 2 in.. Cylinders were tested with and without a 5/8 in. diameter hole.

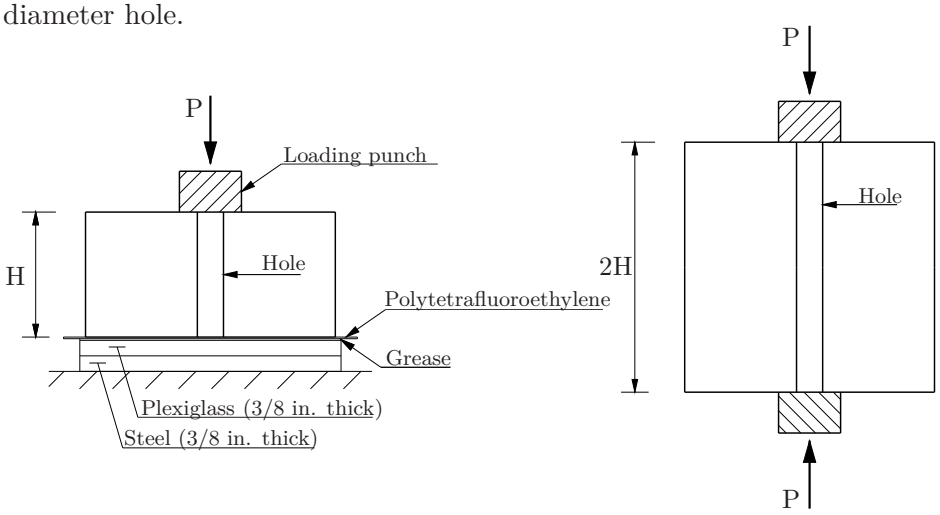

(a) Plastic Base Arrangement (b) Double Punch Arrangement

Figure 3.8: Hyland and Chen (1970) specimens

From the tests results, the authors concluded that:

- Chen and Drucker's solution provided an accurate upper bound for tests results when the ratio between the height and the diameter of the specimen was less than 2,0. For greater values of that ratio the assumption is no longer valid and crack propagation dominates;
- Friction on the base of punch-loaded blocks causes no increase in their load bearing capacity and did not appear to have influence on strain distribution;
- The presence of the centre hole in a specimen did not appear to have a significant effect on the observed bearing strength, reinforcing the idea that failure was controlled by the attainment of ultimate tensile stress and the ability to distribute tensile stress throughout the specimens' volume resulted in increased bearing capacity.

In the late 60's, at the Indian Institute of Technology, Niyogi (1973) performed 1422 tests on plain and reinforced concrete blocks. In Niyogi's opinion, the materials, composition, size of specimens and, sometimes, the ratio of areas of the loaded surface of the specimen and bearing plate adopted by previous works of different researchers varied widely and, as such, a proper comparison and correlation of the test data became difficult. The variables of his study included the geometry - dimensions of loaded surface of specimen relative to those of the bearing plate, relative height of specimen (ratio of the height to the width of specimen) and the disposition of the bearing plate relative to the centre of the loaded surface -, nature of the supporting bed (rigid and elastic), the bearing area at the supported end of specimen or concentrated loading from opposite ends of specimen, mix proportions and strength of concrete, size of specimen (size effect) and amount and geometry of reinforcement.

The specimens used in the tests were in majority 8 in. cubes and 8 in. square prisms of varying heights (4, 6, 12, 16 and 24 in.), loaded through strip, rectangular and square steel bearing plates of various areas and 1/2 in. thick.

Niyogi proposed the following equation (3.9) to determine the ultimate bearing stress under concentric conditions.

$$\frac{f_b}{f_{c,cube}} = 0,42\left(\frac{a}{a'} + \frac{a}{b'} + 1\right) - 0,29\left[\left(\frac{a}{a'} - \frac{a}{b'}\right)^2 + 5,06\right]^{1/2} \tag{3.9}$$

where,

$f_{c,cube}$ is the concrete cube compressive strength;
a is the block width;
a' is the plate width;
b' is the plate depth.

Niyogi also concluded that the relative height of the specimen influences the bearing strength of concrete. In general, the strength decreased with increasing height of specimen, particularly for values of the ratio A/A' equal or inferior to 8 . This effect was emphasised for larger loaded areas. For heights smaller than the block side dimension and ratios A/A' superiors to 8, the bearing strength decreased with decreasing specimen height.

Wheen and Rogers (1978) carried out an experimental study in which a range of prismatic rectangular and square unreinforced blocks was tested to establish their bearing capacity. In this study, the blocks were loaded through small embedded square steel plates with an axial duct, to simulate the configuration of a prestressing anchorage. To examine the validity of Guyon's "symmetrical prism" concept[4], they also tested blocks loaded through pairs of anchorages. The geometry of the single anchor blocks is shown in Figure 3.9.

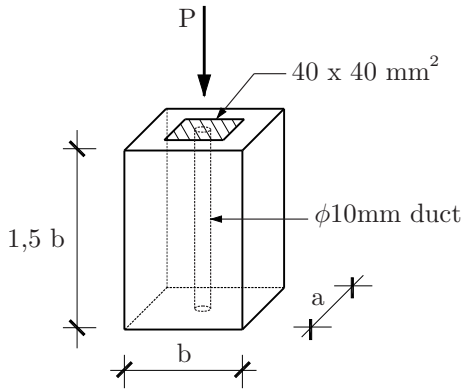

Figure 3.9: Geometry of single anchor blocks (Wheen and Rogers, 1978)

[4]Guyon (1953) proposed that an end block loaded with a number of anchorages could be divided into a number of such symmetrical prisms with length equal to the width of the prism. These symmetrical prisms could then be designed independently as single anchorage end blocks.

For the dimensions a and b, being a the smaller, were adopted the values 50 mm, 75 mm, 100 mm, 125 mm and 150 mm. The geometry of the cross section consisted in all possible combinations of these dimensions.

During the tests, the authors observed that the failure of the prismatic square and nearly square blocks was characterised, at first, by the formation of longitudinal radial planes of cracking from the anchor plate, and subsequent formation of an inverted pyramid of concrete below the anchor plate. The narrow rectangular blocks failed by the formation of a longitudinal plane of splitting, parallel to the short side of the rectangle, and subsequent formation of an inverted pyramid of concrete below the anchor plate.

From the test results, Wheen and Rogers concluded that the strength of the specimens was clearly determined by the minimum side dimension of the specimen, yet the nature of the failure could be very different depending on the cross-section' shape.

In 1995, at the Virginia Polytechnic Institute and State University, Bonetti (2005) performed a set of seven experimental tests series to determine how the shape and size of the bearing plate, the concrete weight (normal or lightweight) and strength, and the duct size affected the ultimate strength of the concrete. The specimens used in the tests consisted of 8 in. × 8 in. × 16 in. concrete square prisms and 6 in. diameter by 12 in. long concrete cylinders.

The first series of tests, conducted over 47 specimens, tested the effects of the shape of the plate in relation to the shape of the block and the effect of the ratio A/A' on the ultimate bearing strength. The specimens (square prisms and cylinders) were loaded through both circular and rectangular plates. At least two specimens were tested for each A/A' ratio considered: 2, 4, 6, 8, 12 and 16.

After the first series of tests, it was determined that the target range of A/A' ratios to be more closely investigated was the range between 1,5 and 6, and that the shape of the plate did not significantly affect the ultimate bearing strength for the same A/A' ratio. Therefore, in the second series of tests 28 specimens were tested (square section prismatic blocks and cylinders) with ratios of A/A' varying between 1,5 and 6. Only square bearing plates were used, except for the ratio A/A' = 1,5, in which a hexagonal plate was utilised.

The third series of tests investigated the influence of the aspect ratio (height/width) of the specimen on the bearing strength. 14 cylinders were tested with 6 in. diameter and 3, 4, 6, 8, 9, 12 and 18 in. heights, corresponding to aspect ratios of 0,5, 0,66, 1, 1,33, 1,5, 2 and 3, respectively. The A/A' ratio was kept constant with a value of 4.

The fourth series of tests studied the effect of the use of a lightweight concrete mix on the bearing strength. The specimens utilised consisted of 18 concrete cylinders with a characteristic concrete strength of 55 MPa. The A/A' ratio varied from 1,5 to 16. The

plate shape varied also in this series: hexagonal for A/A' = 1,5, square plates for A/A' = 2, 2,5, 3, 4, 6 and circular for A/A' = 8, 12, 16.

The effect of high strength concrete on the bearing strength was tested in the fifth and sixth series of tests. In both series concrete cylinders with the A/A' ratio ranging between 1,5 to 16 were used. The fifth and sixth series of tests contained 19 specimens with characteristic concrete strengths of 55 MPa and 15 specimens with characteristic concrete strengths of 76 MPa, respectively.

The seventh series of tests, conducted on 12 cylinders tested the effect of the duct size. Ten of the specimens presented a concentric hole with diameters varying from 0,94 in. to 3,38 in.

Using the Mohr's failure criterion, Bonetti proposed the equation (3.10) to determine the ultimate bearing strength of plain concrete specimens with regular section and concentrically loaded:

$$P_u = \frac{A \cdot f_c}{m\beta + \alpha} \tag{3.10}$$

where,

P_u is the ultimate bearing force;
m is the $f_c/f_{t,max}$ ratio;
$f_{t,max}$ is the maximum concrete tensile stress.

The variables presented in equation (3.10) are illustrated in Figure 3.10, where z is the position of the maximum tensile stress $f_{t,max}$ and A_z is the area subjected to the assumed uniform compressive state of stress $f_{c,max}$ at distance z.

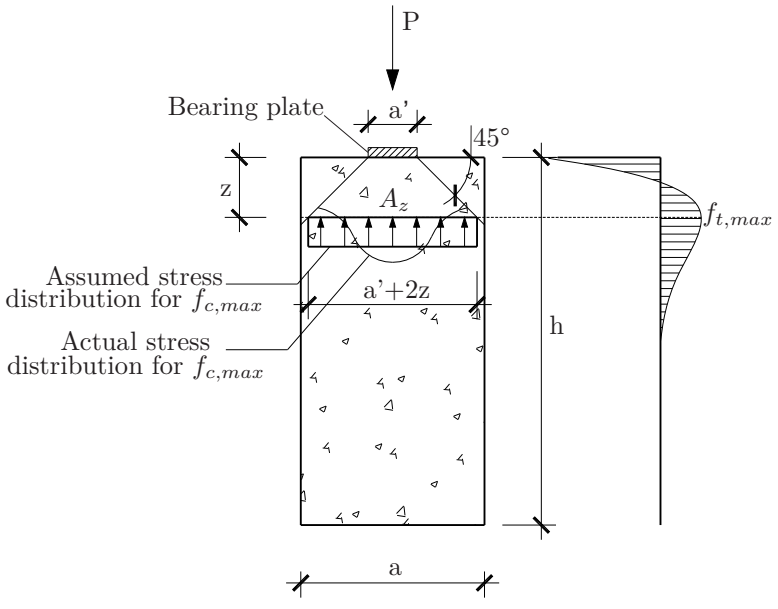

Figure 3.10: Description of variables (Bonetti, 2005)

The parameter β can be determined by the equation (3.11).

$$\beta = \frac{0,114}{(a'/a)^{1,03}} \qquad \text{for} \quad \frac{a'}{a} < 0,5 \tag{3.11a}$$

$$\beta = 0,466 - 0,469\left(\frac{a'}{a}\right) \qquad \text{for} \quad \frac{a'}{a} \geq 0,5 \tag{3.11b}$$

The parameter α depends on the point where the maximum tensile stress occurs and can be determined by the equation (3.12), presented below.

$$\alpha = 1,0 \qquad \text{for} \quad z \geq \frac{a-a'}{2} \tag{3.12a}$$

$$\alpha = \frac{A}{A_z} \qquad \text{for} \quad z < \frac{a-a'}{2} \tag{3.12b}$$

where,

$A_z = (a' + 2z)^2$, for quadrangular prismatic blocks loaded through square plates
$A_z = (\pi/4)(a' + 2z)^2$, for cylindrical blocks loaded through round plates

The position of the maximum tensile stress is a function of the a'/a ratio (see Figure 3.10) and can be determined by the equation (3.13).

$$z = 0,20ln\left(\frac{a'}{a}\right) + 0,56 \qquad \text{for} \quad \frac{a'}{a} < 0,5 \tag{3.13a}$$

$$z = 0,17\left(\frac{a'}{a}\right) + 0,34 \qquad \text{for} \quad \frac{a'}{a} \geq 0,5 \tag{3.13b}$$

From his research, Bonetti observed that the failure mode of plain concrete specimens is characterised by the formation of a failure cone or pyramid under the bearing plate, followed by the splitting of the block. He concluded that the duct size has a negligible influence in the ultimate bearing strength, as well as the plate shape, for ratios A/A' between 2 and 16.

3.2.2 Reinforced concrete bearing strength

Although in the early twentieth century was already known that lateral restraint increased the resistance of materials in compression, Considère, according to Talbot (1907), was the first to use, develop and investigate the properties of "hooped" concrete[5] in construction.

Considère (1903) performed his first experiments in 1898. These were on prisms of concrete of different qualities and surrounded by hoops of various arrangements and sizes. These prisms were submitted to increasing pressures and the shortenings were measured together with the loads. The author also tested prisms of "hooped" sand.

[5] confined concrete with spiral reinforcement

From the first test results, Considère observed that the results of hooping were less advantageous for the coefficient of elasticity and, therefore, for the resistance to flexure as a column, than for the crushing resistance. So, in 1902, Considère tested 38 prisms of octagonal section of 150 mm diameter with spirally wound wire and longitudinal rods, for different concrete compositions. Aiming to study both crushing resistance and elasticity, and ductility of hooped concrete, lengths of 500 mm and 1300 mm, respectively, were adopted for the prisms.

After analysing the results, Considère concluded that the strength of hooped concrete could be considered as being the sum of the compressive resistance of the concrete without reinforcement, the compressive resistance of the longitudinal rods stressed to their elastic limit and a added strength given by the spiral that corresponded to 2,4 times the compressive resistance obtained with the same amount of reinforcement of the hooping, in the shape of longitudinal rods.

Considère (1907a) collected and discussed various experiments on hooped concrete. In this article, the author presented his revised conclusions on the properties and applicability of this form of reinforced concrete. Considère (1907b) suggested that the strength of a short hooped concrete column could be calculated as the addition of the contributions of plain concrete, longitudinal reinforcement and hooping reinforcement and proposed the equation (3.14).

$$f_b = 1,5c + 2400p + 5100p' \tag{3.14}$$

where,

f_b in pounds per square inch;
c is the unit strength of a plain concrete column (in pounds per square inch);
p is the ratio of the longitudinal reinforcement to the concrete core;
p' is the ratio of the hooping to the concrete core.

Hooped concrete was patented in France, Germany, England, United States, etc., and the Minister of Public Works of France issued instructions authorising the use of this form of construction.

In 1905, at the Testing Laboratory of the Royal Technical High School of Stuttgart, Bach (1905), referred by Mörsch (1909), conducted some tests on reinforced concrete with the aim of studying the influence of transverse and longitudinal reinforcement in the strength of a column. The specimens used consisted of concrete prisms with 250 mm by 250 mm in section and 1000 mm long. Part of the specimens were of plain concrete and the others had a reinforcement of 4 rods with 7 mm ties each, as shown in Figure 3.11. For each stress increment the total compression, the elastic deformation and the permanent set were measured.

According to Mörsch (1909), as the owners of the German rights under Considère's

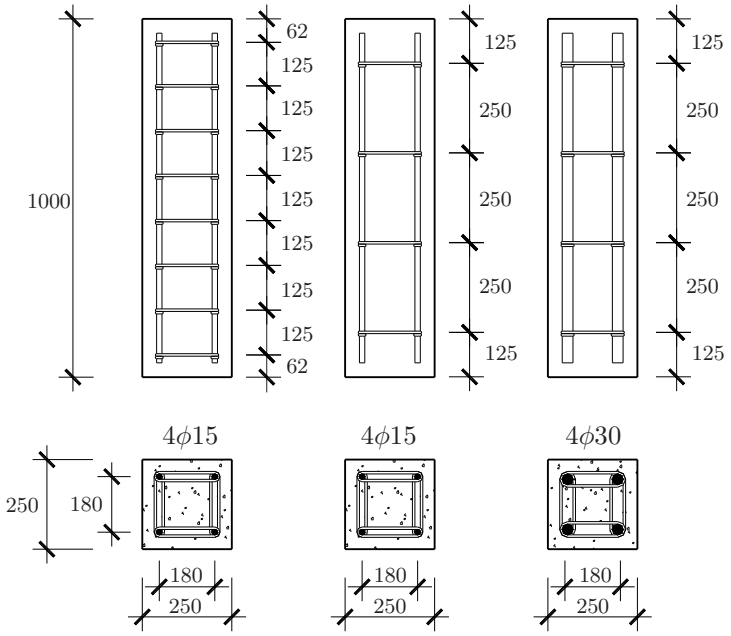

Figure 3.11: Bach's test specimens (adapted from Mörsch, 1909)

patents deemed it advisable to institute experiments with specimens manufactured without special care, the specimens were built at a building site, and tested in the Testing Laboratory of the Royal Technical High School of Stuttgart. These tests were also published by Bach (1905). The specimens, whose geometry is shown in Figure 3.12, had an octagonal section with a short diameter of 275 mm and a height of 1000 mm. Two sets of tests were made in which the pitch of the spiral was highly increased.

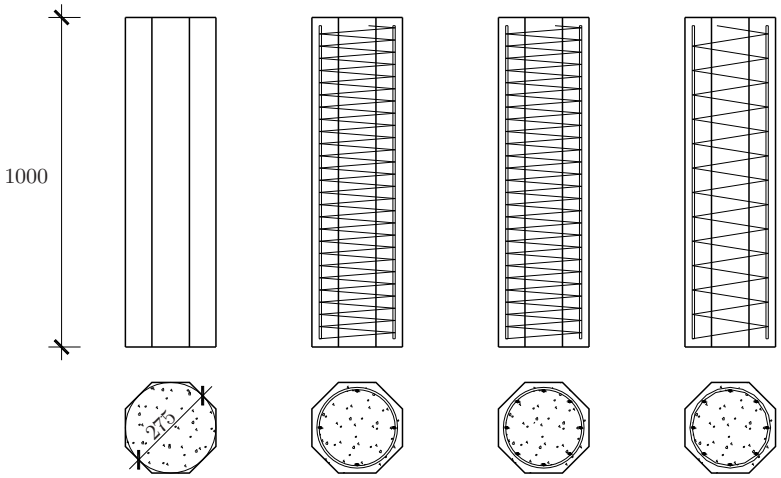

Figure 3.12: Bach's test specimens on hooped concrete (adapted from Mörsch, 1909)

In spite of the defects in the specimens, the strength obtained corresponded approximately with the expected results, and exceeded them for the specimens with the least reinforcement.

In 1925, at the University of Illinois Richart, Brandtzaeg and Brown performed some experimental tests to study the concrete failure under compressive stresses applied in bi-axial and triaxial compression (Richart et al., 1928), using a hydraulic pressure apparatus.

The tests were conducted on 100 mm diameter concrete cylinders, 200 mm and 560 mm long, with fluid pressure applied to the curved sides and an axial load applied by a load test machine. They also performed tests on plain concrete and on spirally reinforced concrete under simple compression (Richart et al., 1929). Different mixtures of concrete and mortar were used, varying the ratio of cement, water and aggregates.

The purpose of these tests was to study the internal action of the material as it breaks down under compressive stress, and the influence of lateral stresses on the axial capacity of concrete.

They found out that many of the numerical results of the tests were in line with the internal friction theory of sliding failure. However, the great increase in lateral deformations observed could not be reconciled with a conception of failure as taking place through a sliding on plane surfaces continuous throughout the material.

They noted that the added strength produced by a given lateral oil pressure was nearly constant, regardless of the concrete mixture. The curves (with the lateral oil pressure as abscissa and the maximum axial load as ordinate) obtained for the three mixtures were similar, with ordinates differing only by the differences in strength of the specimens tested in simple compression. These results showed to be in line with the results of the tests of spirally reinforced concrete, in which the increase in the ultimate strength produced by the lateral pressure developed by the spiral reinforcement was equal to 4,1 times the lateral pressure, as reflected in the proposed equation (3.15).

$$f_b = f_c + 4,1 f_{lat} \tag{3.15}$$

where f_{lat} is the lateral confining pressure.

In 1975, Niyogi published the results of his experimental work on reinforced concrete specimens (Niyogi, 1975). With the aim of studying the effect of the reinforcement ratio and the effect of the diameter and extent of the spiral, Niyogi performed 154 tests in 200 mm concrete cubes, reinforced with spirals or grids of steel. In the specimens reinforced with spirals it was considered two diameters (large and small), and was varied the spiral length (overall or partial length of the specimen) and the number of turns.

From the results of the tests, the author concluded that the lateral reinforcement significantly increased the ultimate bearing strength of the concrete and the cracking load, and that single large diameter spirals gave the highest efficiency for the same percentage of steel. Niyogi also concluded that the bearing strength of spirally reinforced concrete compared to that of plain concrete could be expressed as a function of the volumetric

percentage of lateral steel, and proposed the relationship presented in equation (3.16).

$$\frac{n_{reinf}}{n_{plain}} = 1 + Kp_l \tag{3.16}$$

where,

n_{reinf} is the bearing strength of spirally reinforced concrete;
n_{plain} is the bearing strength of plain concrete;
K is a factor that depends on the size of the spiral or the core area (for large spirals a conservative value of K=0,55 may be adopted);
p_l is volumetric percentage of lateral steel referred to the specimen volume.

Wurm and Daschner (1977) and (1983), referred by Breen et al. (1991) and Bonetti (2005), performed 130 experimental tests mainly on spirally reinforced specimens, with the aim of studying the effects of the A/A' ratio, the influence of the quantity and type of lateral reinforcement, sustained loading, post-tensioning duct effects, eccentricity of the anchorage and concrete age. The specimens used in the tests consisted of 300 mm × 300 mm × 600 mm concrete blocks loaded with a ratio of A/A' equal to 4.

Their major conclusions were that:

- spirals were the most efficient form of reinforcement;
- if confining reinforcement were too short a crushing of the concrete occurred at the base of the confinement;
- the post-tensioning duct reduced the ultimate load;
- the ultimate loads for specimens with sustained loading were 20 percent lower than those loaded short term.

The authors also concluded that an increase of the reinforcing ratio produced an increase of the ultimate bearing strength up to a point of saturation. Beyond this point, the increase of reinforcing steel no longer contributes to increasing the ultimate bearing strength.

Suzuki and Nakatsuka (1982) conducted a set of experimental tests on mortar and concrete cylinders, with the aim of clarifying the failure mechanism of anchorage zones with circular spiral reinforcement and study the influence of the area of the bearing plate, the amount of reinforcement and the covering depth of concrete.

In the first phase, they tested 18 mortar cylinders with 150 mm in diameter and 300 mm in height, and 8 concrete cylinders, 7 with 200 mm diameter and 500 mm in height and the remainder with 250 mm diameter and 630 mm in height.

A second phase of tests was carried out to examine the adequacy of deduced equations on the bearing strength using larger concrete specimens with various pitches of spiral reinforcement and various covering depths.

Figure 3.13 shows the geometry of the specimens.

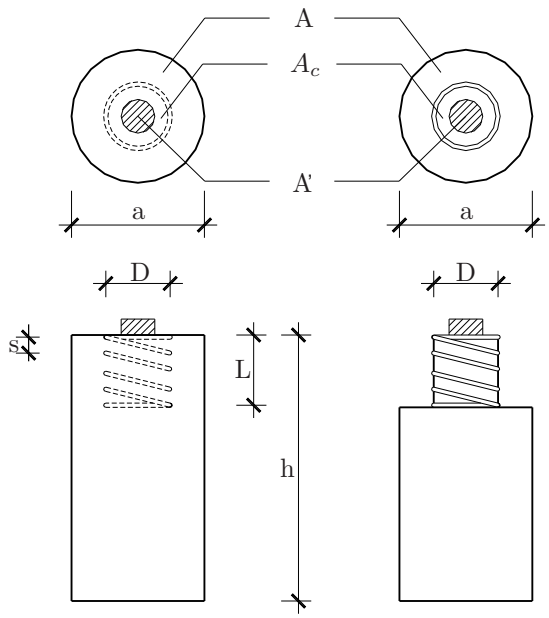

Figure 3.13: Suzuki and Nakatsuka's test specimens (adapted from Suzuki and Nakatsuka, 1982)

The authors observed the failure modes of reinforced specimens shown in Figure 3.14.

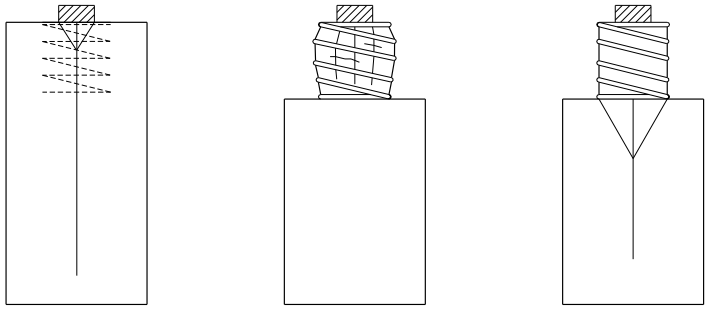

a) Model I(a) b) Model I(b) c) Model II

Figure 3.14: Failure models of specimens (adapted from Suzuki and Nakatsuka, 1982)

Specimens with little or no reinforcement presented a failure mode (Model I(a)) characterised by remarkable longitudinal cracks. In the second failure mode (Model I(b)) the formation of a circular crack around the reinforcement was more perceptible, followed by the separation of the mortar cover from the core surrounded by the spiral reinforcement. In the third failure mode (Model II) splitting failure occurred, not in the core, but in the unreinforced zone below, together with the formation of a slip cone.

According to the results of their tests, the authors proposed three equations (3.17a), (3.17b) and (3.17c) to determine the ultimate bearing strength of the specimens, depending if the model of failure was I(a), I(b) or II, respectively.

$$P_u = \alpha \left(\frac{A}{A'}\right)^{\beta} f_c \cdot A_{core} \tag{3.17a}$$

$$P_u = m_q \cdot \alpha \left(\frac{A}{A'}\right)^{\beta} f_c \cdot A_{core} \tag{3.17b}$$

$$P_u = \alpha \left(\frac{A}{A_{core}}\right)^{\beta} \left(\frac{A_{core}}{A_1}\right) f_c \cdot A_{core} \tag{3.17c}$$

where,

α is a constant equal to 0,80 for mortar and 0,90 for concrete;
β is a constant equal to 0,55 for mortar and 0,60 for concrete;
A_{core} is the confined concrete area surrounded by the spiral.

The factor m_q depends on the bearing reinforcing index q_b and can be determined using the equation (3.18) and the equation (3.19), respectively.

$$m_q = 2,4 q_b^{0,4} + 1,0 \tag{3.18}$$

$$q_b = \frac{2A_s}{sD} \cdot \frac{f_y}{f_c} \tag{3.19}$$

where,

A_s is the steel reinforcement bar area;
s is the pitch of the spiral;
D is the diameter of the spiral;
f_y is the yield strength of the reinforcing bar.

Suzuki and Nakatsuka (1984) published the results of another set of experimental tests, this time in concrete blocks, with square and circular cross sections, loaded through square bearing plate and with circular spiral reinforcement. The variables considered were the influence of the area of the bearing plate, the amount of reinforcement, the covering depth and the concrete strength.

The specimens used in the tests consisted of 150 mm diameter and 300 mm high concrete cylinders and quadrangular prismatic blocks with dimensions 150 mm × 300 mm, 230 mm × 460 mm, 200 mm × 400 mm and 300 mm × 600 mm loaded through square steel base plates. Figure 3.15 shows the geometry of the specimens.

The authors recorded, in this case, two modes of failure similar to model I(b) and model II, observed previously.

Schlaich and Schafer (1989), referred by Bergmeister et al. (1993), proposed the equation (3.20) to determine the confined bearing strength for specimens with spiral confining reinforcement.

$$f_b = 1,1 f_c \cdot \sqrt{\frac{A}{A'}} + 5,2 \cdot \frac{A_s f_y}{sD} \leq 3,3 f_c \tag{3.20}$$

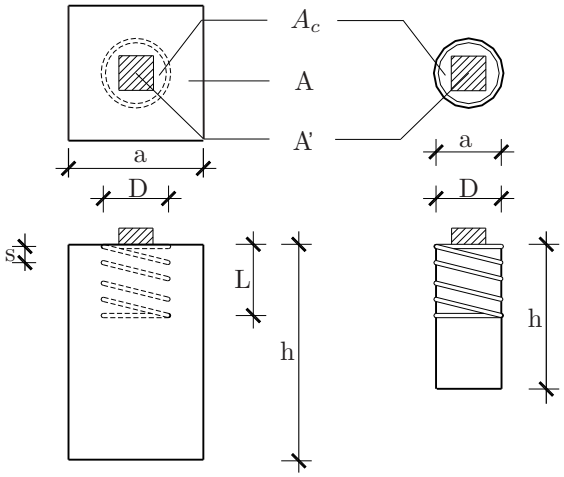

Figure 3.15: Suzuki and Nakatsuka's test specimens (adapted from Suzuki and Nakatsuka, 1984)

For square compression struts and square confinement reinforcement, the lateral pressure could be determined considering half of the equivalent circular compression strength.

At the University of Texas at Austin, under the NCHRP Report 356 (Breen et al., 1991), Roberts conducted a detailed study of behaviour and design of the local anchorage zone. The variables investigated included edge distance, spiral parameters, supplementary reinforcement, type of anchorage device, concrete strength, loading history, and interaction with the general zone. In this study, Roberts performed 31 tests, to evaluate the behaviour, test criteria and design procedures for the local anchorage zone.

After the examination of the extensive work of Niyogi (1973, 1975) and Schlaich and Schafer (1989), Roberts concluded that the most effective expression to compute the ultimate load capacity of an anchorage device would be the one which incorporated both the confinement of surrounding concrete (the A/A' ratio effect) and the confinement provided by the reinforcement (the f_{lat} effect) and proposed equation (3.21).

$$P_u = 0,8 f_c \sqrt{\frac{A}{A'}} A_b + 4,1 f_{lat} \left(1 - \frac{s}{D}\right)^2 A_{core} \tag{3.21}$$

where,

A is the maximum area of the portion of the supporting surface that is similar to the loaded area and concentric with it;

A' is the gross area of sufficiently rigid bearing plates or, for less rigid bearing plates, the area geometrically similar to the wedge plate with dimensions increased by twice the bearing plate thickness;

A_b is the effective net area of the bearing plate calculated as the area A' minus the area of openings in the bearing plate;

f_{lat} is the lateral confining pressure provided by the reinforcing steel (see Figure 3.16);

s is the pitch of the spiral or spacing of the ties used as lateral reinforcement;

D is the diameter of the spiral or side dimension of the ties.

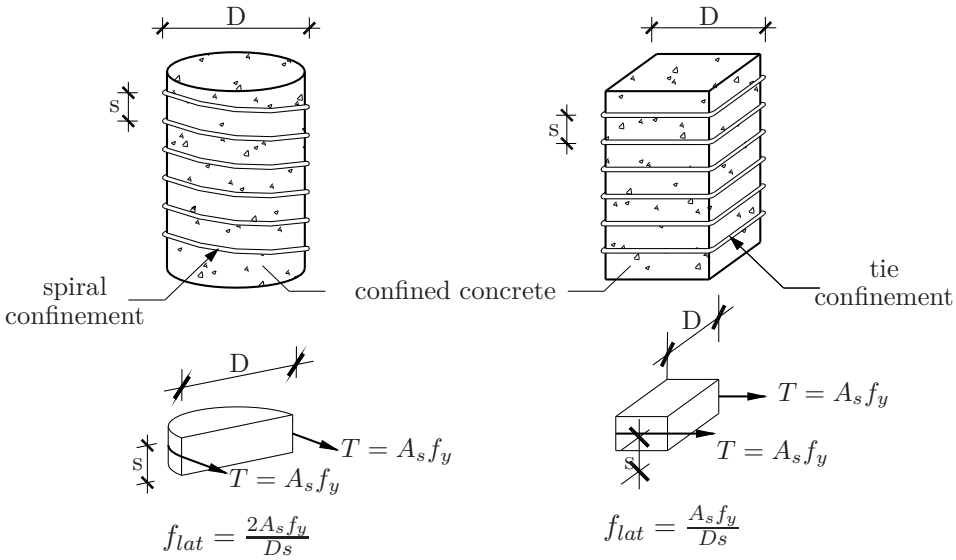

a) Lateral pressure for spirals b) Lateral pressure for ties

Figure 3.16: Lateral pressure for confinement reinforcement (adapted from Breen et al., 1991)

The factor $(1 - s/D)^2$ present in equation (3.21) takes into account the effectiveness of the confining reinforcement based on its pitch and outside diameter. Due to the arching effect between turns in a spiral, shown in Figure 3.17 a), the actual area of well-confined concrete is somewhat smaller than the area of the full cross section within the spiral.

In the f_{lat} expression for ties, presented in Figure 3.16, it is implicit a factor of 0,5 that takes into account the fact that confinement with ties is most effective near the corners of the ties, but less effective elsewhere, as shown in Figure 3.17b).

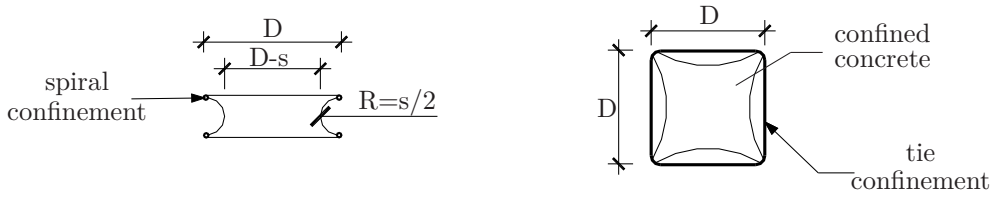

a) Reduced confined area between turns b) Tie confinement reduced area

Figure 3.17: Effective confined area (adapted from Breen et al., 1991)

According to Breen et al. (1991), equation (3.21) is only useful for preliminary evaluation of anchorage device capacity and for sizing confining reinforcement. The formula was not presented for code use because it did not ensure satisfactory condition of the local zone at service loads.

The Post-tensioning Institute (Wollmann and Roberts-Wollmann, 2000) published a equation similar to equation (3.21) for extrapolation of special bearing plate acceptance

test results but with slight modifications as presented in equation (3.22).

$$P_u = \eta\,(P_c + P_s) \leq 3 f_c A_b \tag{3.22a}$$

$$P_c = 0,8 f_c A_b \sqrt{A/A'} \leq 2 f_c A_b \tag{3.22b}$$

$$P_s = 4,1 f_{lat} A_{core} \tag{3.22c}$$

where η is a calibration factor that usually ranges from 0,85 to 0,95. The definition of the terms used is illustrated in Figure 3.18.

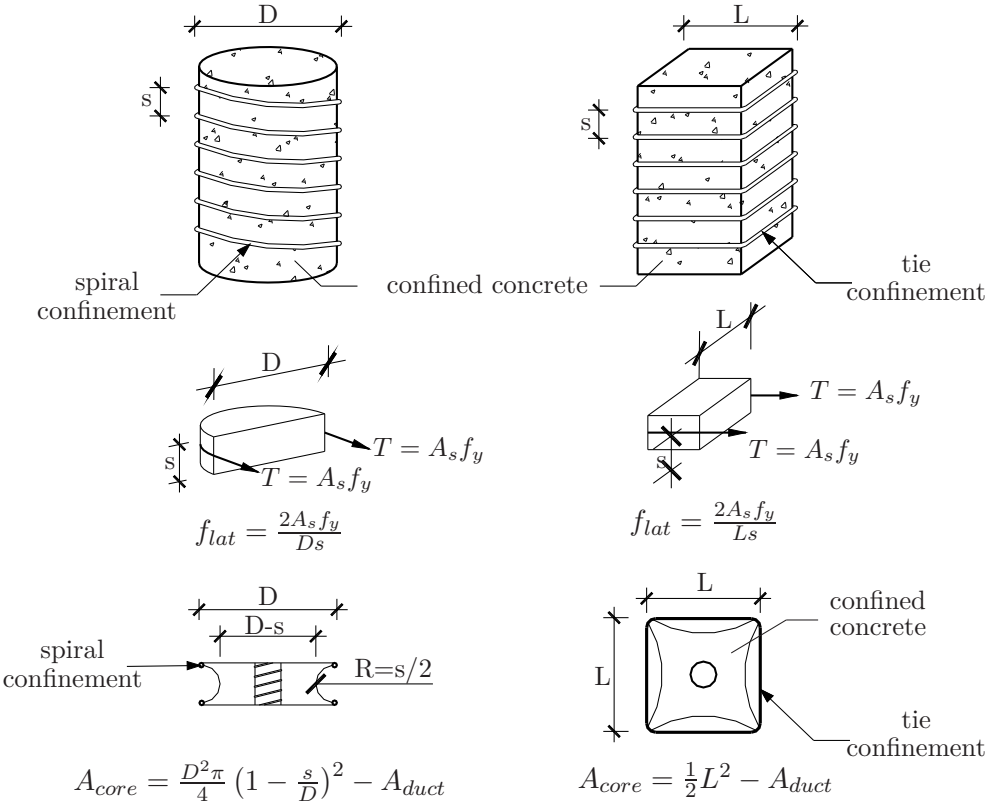

a) Spiral confinement reinforcement b) Tie confinement reinforcement

Figure 3.18: Local anchorage zone confinement reinforcement (adapted from Wollmann and Roberts-Wollmann, 2000)

With the aim of studying the bearing capacity of reinforced and plain concrete blocks, tested under a variety of loading configurations, Ahmed et al. (1998) tested 39 reinforced and plain specimens. The test program was divided in two series, the first one of small blocks (200 mm × 200 mm × 300 mm) and the second one of large blocks (400 mm × 400 mm × 600 mm) of concrete specimens. In the first series, 35 reinforced and plain small concrete specimens were tested to determine the increase in the bearing strength resulting from using different classes of lateral reinforcement, covering the full depth of the block. Five different types of reinforcement were used, three-dimensional and two-dimensional grids, as shown in Figure 3.19.

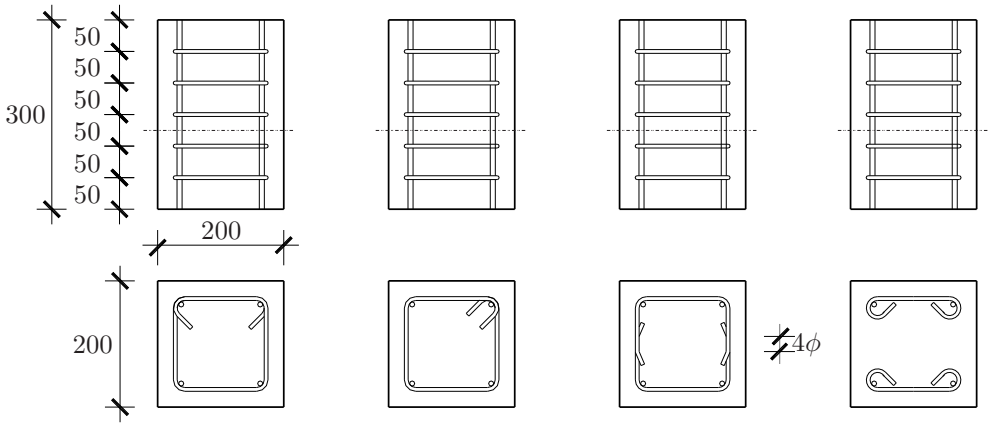

Figure 3.19: Types of reinforcement adopted by Ahmed et al. (1998)

Seven specimens comprising the above classes of reinforcement, as well as plain concrete were cast. The specimens were tested under one of the following geometric variations: square loaded area concentric, eccentric and biaxial on specimen, and rectangular and strip loaded area concentric and eccentric on specimen. During the tests the authors observed that reinforcements Class 1, 2 and 3a increased the resistance of the specimens against initial cracking, while reinforcement Class 3b was less effective.

From the results of the tests, they concluded that the failure of all specimens was of a tensile nature and the variations in bearing strengths were more closely related to the tensile strength of concrete than the cube compressive strength and recommended the use of a nominal amount of lateral reinforcement, even when not required by the calculation. From the limited test on large scale specimens, together with results from Niyogi, the investigation pointed out to a factor of $1/S^{1/4}$, where S is the scale factor.

Ahmed et al. (1998) proposed the equation (3.23) to determine the ultimate bearing capacity of the tested specimens.

$$f_b = f_{c,cube}\left[3\left(\frac{A_{s,lat}}{A_c}\right)\left(\frac{A}{A'}\right) + C_1\right] \tag{3.23}$$

where,

$A_{s,lat}$ is the area of lateral steel reinforcement;
A_c is the area of concrete;
C_1 is a coefficient that depends on the geometry of loading and percentage of steel used.

Also as part of his master's thesis at the Virginia Polytechnic Institute and State University, Bonetti (2005) proposed to study the effect of the lateral reinforcement ratio on the ultimate bearing strength, performing a new test series. The specimens used in the tests consisted of 42 concrete square prisms with dimensions 8 in. × 8 in. × 16 in.. The types of

lateral reinforcement consisted of spirals, ties and a combination of both. The specimens were loaded through steel bearing plates, with ratios A/A' of 3 and 4.

From the results of his tests, Bonetti concluded that the ultimate bearing strength increases with the increase of the mechanical reinforcement ratio. However the test results suggest that for values of $\omega > 0{,}50$, no further benefit is achieved with additional increase of the reinforcement ratio.

Using the Mohr's failure criterion, Bonetti proposed the equation (3.24) to determine the ultimate bearing strength of reinforced concrete specimens concentrically loaded:

$$P_u = \frac{1,25A \cdot f_c}{m_r\beta + \alpha} \tag{3.24}$$

where,

m_r is the $f_c/(f_{ct,sp} + f_{lat})$ ratio;
$f_{ct,sp}$ is the splitting cylinder tensile strength;
α and β are defined in equations (3.12) and (3.11), respectively.

3.2.3 Reinforced high performance concrete

Ay (2004) performed six test series to study the bearing strength of steel fiber cement based composites (SFCBC) under strip loading. The purpose of the tests was to prove to the concrete industry that SFCBC could replace ordinary reinforced concrete (ORC). The author chose the dimensions of specimens shown in Figure 3.20, and previously adopted by Ibell and Burgoyne (1993), in order to compare his tests results with the ones obtained by the latter on reinforced concrete specimens.

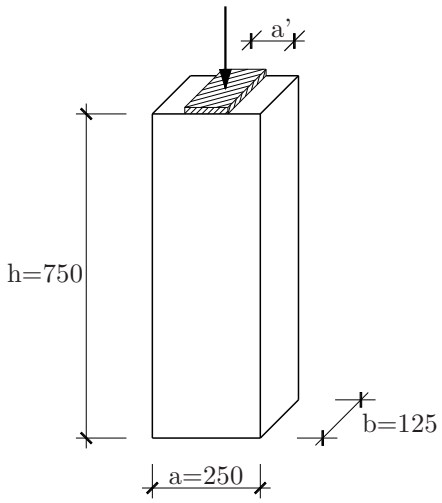

Figure 3.20: Geometry of the test specimens (Ay, 2004)

The application of strip loads in research done by Ibell and Burgoyne (1993) was motivated by the lower complexity presented by two-dimensional analysis when compared with three-dimensional analysis. Moreover, they stated that in most cases the anchorages were located in the webs, which showed planar character for being thin. Additionally, Ibell and Burgoyne wanted to be able to compare their test results with two-dimensional analytical models.

Some of the specimens were covered with a central artificial crack in the longitudinal direction, perpendicular to the face of load application, in order to investigate if any significant energy dissipated along the crack.

Table 3.1 presents a brief description of the test series and the concentration ratios (a'/a) of strip loads adopted.

Table 3.1: Test series of SFCBC (Ay, 2004)

Test Series	Type of concrete	Artificial crack	Concentration ratio
I	Unreinforced concrete	No	0,1; 0,3; 0,5; 0,7; 1,0
II	Unreinforced concrete	Yes	0,3; 0,5
III	SFCBC $V_f = 1,5\%$	No	0,1; 0,3; 0,5; 0,7
IV	SFCBC $V_f = 1,5\%$	Yes	0,3; 0,5; 0,7
V	SFCBC $V_f = 3,0\%$	No	0,1; 0,3; 0,5; 0,7
VI	SFCBC $V_f = 3,0\%$	Yes	0,3; 0,5; 0,7

The mechanical properties of the concrete used in the tests are shown in Table 3.2.

Table 3.2: Properties of the plain concrete and SFCBC (Ay, 2004)

Type of concrete	f_c (MPa)	$f_{c,cube}$ (MPa)	$f_{ct,sp}$ (MPa)	E_c (GPa)
Plain concrete	157,8	160,3	7,3	43,5
SFCBC $V_f = 1,5\%$	161,3	176,9	16,2	46,7
SFCBC $V_f = 3,0\%$	160,2	180,5	25,0	44,7

The ordinary reinforced concrete used by Ibell and Burgoyne presented a compressive strength f_c= 60 MPa and a split cylinder tensile strength $f_{ct,sp} \cong 4$ MPa.

The comparison between ORC (Ibell and Burgoyne, 1993) and SFCBC with 1,5% and 3,0% volume of fibres (Ay, 2004) for ultimate strength under different strip loading is shown in Table 3.3. In the table, d_r is the depth of the confining reinforcement.

Table 3.3: Comparison between ORC (Ibell and Burgoyne, 1993) and SFCBC with $V_f = 1,5\%$ and $V_f = 3,0\%$ (Ay, 2004) for ultimate strength under different strip loading

	ORC			SFCBC ($V_f = 1,5\%$)	SFCBC ($V_f = 3,0\%$)
a' (mm)	Stirrups	$\rho = A_s/(b \cdot d_r)$	P_u (kN)	P_u (kN)	P_u (kN)
25	$13\phi4$	0,0052	412	801	1053
75	$11\phi6,1$	0,0103	991	1727	2012
125	$8\phi6,1$	0,0075	1255	2812	2790
175	$10\phi4$	0,0040	1295	3341	3037

It should be noted that Ibell and Burgoyne (1993) conducted several tests under different strip loadings, while the amount and spacing of the steel reinforcement changed. In the former comparison the highest ultimate strengths accomplished for each concentration ratio were presented.

Ay observed that the ratio between the ultimate strengths of ORC and SFBC increased with the width of the loading plate. According to the author, this could be due to the enhancement of the tensile strength capacity of the composite, provided by the fibers, which was decisive for the ultimate load capacity in lower load concentration ratios.

From the test results, Ay concluded that the inclusion of fibers enhanced both cracking and ultimate load capacities. The inclusion of high amount of fibers ($V_f = 3,0\%$) gave a substantial increase in the cracking loads, but the contribution to the ultimate load capacity was not significant.

With the aim of reducing or eliminating the confining steel from anchorage zones of post-tensioned girders, Haroon et al. (2006) published the results of their study on the effect of steel fiber-reinforced concrete (FRC) in the local anchorage zone. The investigated variables were the concrete strength and variation of spiral and skin reinforcement.

The test program consisted of performing the AASHTO Special Anchorage Device Acceptance Test (AASHTO, 2002) in 318 mm × 318 mm × 635 mm concrete prisms loaded through VSL anchorages type EC 5-7. The type and percentage of fibres used in FRC mixtures, as well as the average compressive strengths and tensile strengths obtained for plain concrete and FRC are defined in Table 3.4.

Table 3.4: Properties of FRC and plain concrete (Haroon et al., 2006)

Steel fiber type	Volume fraction (%)	Compressive strength (MPa)	Tensile strength (MPa)
None	-	43,8	4,3
Hooked-end	0,75	51,0	5,0
Hooked-end	1,0	51,7	6,0
Deformed	1,0	50,6	4,8

From the test results the authors concluded that for specimens with identical type and amount of fibers, and with spiral and skin reinforcement, the failure load of the specimen increased and the crack width decreased with increasing compressive strengths. For 1,0% hooked-end fiber specimens, the best performing configuration satisfying the AASHTO criteria was the one without spiral and skin reinforcement and with a minimum compressive strength of 40,7 MPa. This configuration resulted in a total elimination of the secondary reinforcement. Similar results were achieved for specimens with 0,75% hooked-end and 1,0% deformed fibers, with minimum compressive strengths of 48,6 MPa and 48 MPa, respectively. For specimens without fibers, the AASHTO acceptance criteria could not be achieved with reduction of the secondary steel from the usual spiral and skin reinforcement configuration.

Holschemacher et al. (2004) performed an experimental program in order to investigate the load bearing capacity and the failure behaviour of ultra-high strength concrete under concentrated loading. The tested specimens consisted of plain and reinforced concrete (with spiral reinforcement) with different heights, as shown in Figure 3.21.

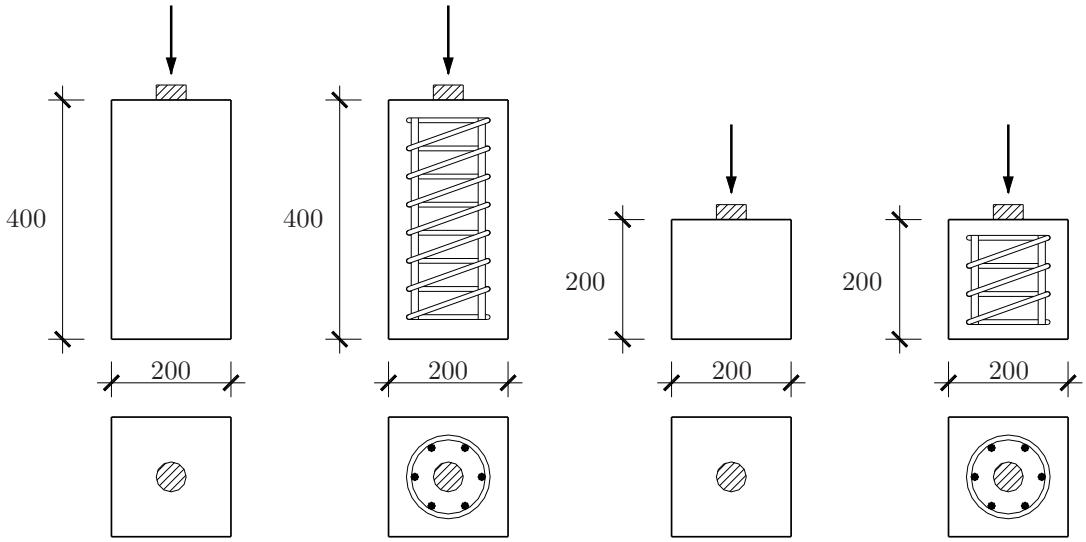

Figure 3.21: Geometry and reinforcement of the test specimens (Holschemacher et al., 2004)

Three types of concrete were tested in order to study the influence of concrete strength and composition on the load bearing capacity and behaviour.

The tested specimens were 12 prisms with dimensions of 200 mm × 200 mm × 400 mm and 24 prisms with dimensions of 200 mm × 200 mm × 200 mm. Half of the prisms were made of plain concrete. The other half had spiral reinforcement with a bar diameter of 8 mm and a pitch of 42 mm and main reinforcing bars were 12 mm. The load was applied by cylindrical loading stamps with diameters of 30 mm and 50 mm.

In order to take into account the concrete composition, three different compositions

were used: a classical reactive powder concrete (UHSC1), a ultra high strength concrete (UHSC2) with crushed aggregates with 5 mm maximum grain size and a high strength concrete (HSC). The concrete properties after 28 days are presented in Table 3.5.

Table 3.5: Hardened concrete properties (Holschemacher et al., 2004)

	f_c (MPa)	$f_{c,cube}$ (MPa)	$f_{ct,sp}$ (MPa)	E_c (MPa)
UHSC1	147	148	12,2	47,1
UHSC2	144	144	10,9	52,9
HSC	62	66	5,1	33,3

Table 3.6 presents a summary of the characteristics of the tested specimens.

Table 3.6: Characteristics of the specimens tested by Holschemacher et al. (2004)

Type of concrete	Diameter of loading stamp (mm)	Height of specimen (mm)	Reinforced/Plain	Number of specimens
UHSC1	30	200	Plain	3
			Reinforced	3
		400	Plain	3
			Reinforced	3
	50	200	Plain	3
			Reinforced	3
		400	Plain	3
			Reinforced	3
UHSC2	50	400	Plain	3
			Reinforced	3
HSC	50	400	Plain	3
			Reinforced	3

During the tests, the authors observed that the specimens made of plain concrete failed by splitting. The specimens loaded with the small loading area split up abruptly at failure. The large loading area caused the formation of a loading core. In both cases a concrete wedge was shaped under the loading stamp. The specimens with spiral reinforcement presented a more ductile behaviour at failure, when compared to the specimens of plain concrete. The confinement provided by the reinforcement led to the formation of several radial cracks with a homogeneous distribution starting from the loading area. Some of this cracks spread to the lateral faces, along the height of the specimens.

From the analysis of the test results, Holschemacher et al. (2004) concluded that even for the plain concrete specimens, the failure load was superior to the corresponding cylinder

concrete strength. The specimens with spiral reinforcement presented higher failure load than the plain concrete specimens, although the reinforcement had no visible influence on the initial crack load and on the stiffness of the specimens before cracking. With regard to the size of the loaded area, the authors found that the reduction of the area led to an increase of the breaking load. The applied HSC presented a higher concentrated load referring to the compressive strength. The dependence of the concentrated load on the tensile strength, which increases under-proportionally with the compressive strength, led to lower values for UHSC.

With the aim of studying the application of pseudo-ductile cementitious composites (PDCC) at the anchorage zone of post-tensioned concrete members, Leung et al. (2009) performed an experimental program using rectangular concrete columns loaded under concentrated compression. The test specimen was a prism with dimensions of 150 mm × 150 mm × 500 mm loaded through steel bearing plates, with A/A' ratios of 1,56, 2,78 and 6,25. The authors performed two test series: in the first series three kinds of specimens were tested - plain concrete specimens, concrete specimens with PDCC applied at the anchorage zone and concrete specimens with steel stirrups placed along the whole length - and it were adopted different dimensions of the steel bearing plate in order to study the effect of the A/A' ratio; in the second series, the specimens were prepared with plain concrete or concrete with PDCC of different compositions at the anchorage zone, to study the effect of PDCC strength and ductility on the load bearing capacity. The characteristics of the specimens adopted in the test series are described in Table 3.7.

Table 3.7: Details of the specimens of the two series (Leung et al., 2009)

Test Series	Test set	Concrete mix	PDCC mix	Ratio A/A'	Stirrups	Number of specimens
1	1.1.1	I	None	2,78	None	3
	1.1.2	I	I	2,78	None	3
	1.1.3	I	None	2,78	$\phi 6//0,40$	3
	1.2.1	II	None	6,25	None	3
	1.2.2	II	I	6,25	None	3
	1.2.3	II	None	6,25	$\phi 10//0,40$	3
	1.3.1	II	None	1,56	None	3
	1.3.2	II	I	1,56	None	3
	1.3.3	II	None	1,56	$\phi 6//0,30$	3
2	2.1.1	III	None	2,78	None	3
	2.1.2	III	I	2,78	None	3
	2.1.3	III	II	2,78	None	3
	2.1.4	III	III	2,78	None	3
	2.2	IV	None	2,78	None	3

The mechanical properties of the concrete and PDCC used in the specimens are presented in Table 3.8 and Table 3.9, respectively.

Table 3.8: Mechanical properties of the concrete used by Leung et al. (2009)

Test Series	Concrete mix	Compressive strength (MPa)
1	I	39,0
	II	57,3
2	III	70,0
	IV	83,8

Table 3.9: Mechanical properties of the PDCC used by Leung et al. (2009)

Test Series	PDCC mix	Compressive strength (MPa)	First cracking strength of PDCC (MPa)
1	I	52,7	2,80
2	I	58,7	3,16
	II	42,6	3,77
	III	83,5	4,25

Leung et al. proposed equation 3.25 for determining the splitting failure load for members with PDCC at the anchorage zone.

$$P_{sp} = 0,9H \times W \times f_{fc} \tag{3.25}$$

where,

P_{sp} is the splitting failure load;

H is the extent of anchorage zone along the longitudinal direction (corresponds to the larger dimension of the cross-section);

W is the width of anchorage zone (smaller dimension of the cross-section);

f_{fc} is the first cracking strength of the PDCC.

The authors major conclusions were that:

- the use of PDCC at the anchorage zone could significantly increase the failure load under concentrated compression, when compared to control plain concrete specimens and even with specimens with steel stirrups in moderate amount;
- specimens heavily reinforced with stirrups reached a higher failure load when compared with specimens with PDCC at the anchorage zone.
- depending on the situation, PDCC can be used to replace all or part of the confining steel reinforcement in the anchorage zone, thus facilitating the construction process, and avoiding difficulties with the compaction of concrete among congested reinforcements.

3.2.4 Load transfer tests

The design of the local anchorage zone is strongly influenced by the characteristics of the anchorage device. The simple design models presented earlier, in this chapter, are suitable for plain steel plates and simple bearing plate anchorages. Recent standards (EN 1992-1-1, 2004, AASHTO, 2002) require that the strength of the local anchorage zone, when using special anchorage devices, should be verified by performing load transfer tests (Cervenka and Ganz, 2014).

3.2.4.1 FIP Recomendation (1993)

According to FIP Recomendation (1993), the load transfer test is performed to verify the transfer of the prestressing force from the mechanical anchorage and its components to the concrete.

Test specimen

The test specimen should be a concrete prism tested in axial compression and containing the anchorage components that will be embedded in the structural concrete. The side lengths of the prism should correspond to the minimum axial spacings of the particular tendon in the structure. The height of the specimen should be at least two times the larger dimension of the cross-section.

The prism must contain the confining reinforcement specified for the particular system and tendon. The use of additional reinforcement is permitted provided that the area of longitudinal reinforcing bars does not exceed 200 mm^2, and the area of secondary reinforcement (stirrups uniformly distributed along the height of the specimen) is less than 50 kg/m^3 concrete.

Test procedure

The test procedure is presented in Figure 3.22.

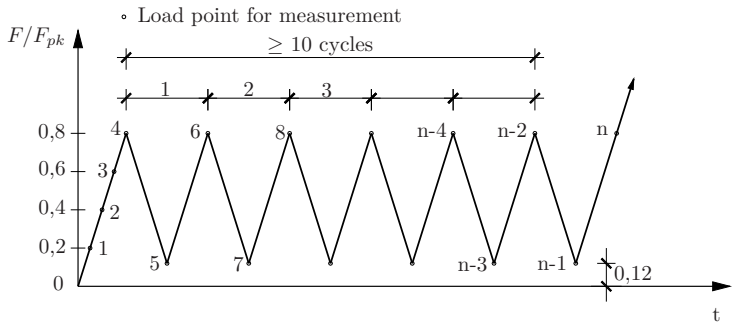

Figure 3.22: FIP Recomendation (1993) load transfer test

As shown in Figure 3.22 above, the load should be applied in increments of 20% up to 80% of the characteristic strength of the prestressing steel, F_{pk}. Then, at least ten slow load cycles should be performed between an upper load of 0,8 F_{pk} and a lower load of 0,12 F_{pk}. Cyclic loading should be continued until strain readings and crack widths stabilise. Following cyclic loading, the specimen should be loaded incrementally to failure. For the test, a calibrated testing machine should be used.

The strains can be assumed to have stabilised if the increase of strain in the last two load cycles is less than 5%. Crack widths are considered stabilised if they do not change by more than 0,02 mm over the last two cycles.

Longitudinal and transverse concrete strains, on side faces of the specimen in the region of maximum bursting effect, and crack widths and patterns, should be recorded under the upper and lower load at different times for increasing numbers of load cycles. The maximum load should also be reported.

Acceptance criteria

The maximum allowed crack width is 0,10 mm upon first attainment of upper force of 0,8 F_{pk}, where F_{pk} is the characteristic ultimate resisting force of prestressing steel of tendon, and upon last attainment of lower force of 0,12 F_{pk}. The maximum allowed crack width at 0,8 F_{pk} after the conclusion of the cyclic loading is 0,25 mm. The measured failure load must exceed 1,1 F_{pk}.

3.2.4.2 AASHTO (2002)

The AASHTO (2002) was based on the work performed at the University of Texas at Austin, under the NCHRP Report 356, by Breen et al. (1991).

AASHTO Specifications (AASHTO, 2002) classify the anchorage plates in two main groups: the basic anchorage and the special anchorage devices. As shown in Figure 3.23(a) the basic anchorage device is usually composed by a regular square or rectangular bearing plate and a anchor head. The bearing plate must have sufficient stiffness, so that a uniform stress distribution under the plate can be considered. The strength of local zone can be determined by simple calculations, so no acceptance test is required. The special anchorage device, as shown in Figure 3.23(b) is composed by a bearing plate with a complex geometry and an anchor head. These plates sometimes include more than one bearing surface and their strength must be determined by load transfer tests.

AASHTO (2002) recommends testing the local zone of special anchorage devices by one of three testing procedures: cyclic loading, sustained loading or monotonic loading. The loads specified for the tests are given in fractions of the characteristic ultimate resisting force of the largest tendon that the anchorage device is designed to accommodate.

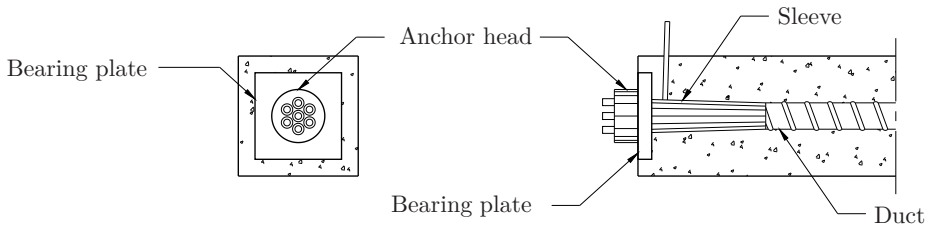

(a) Basic anchorage device

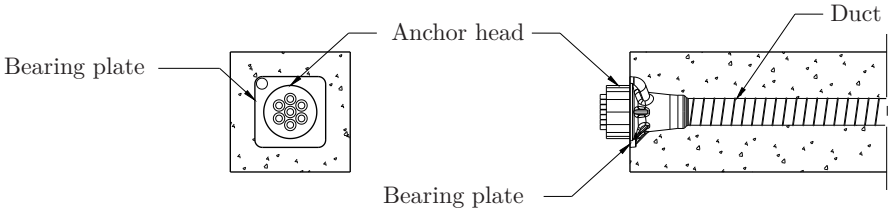

(b) Special anchorage device

Figure 3.23: Types of anchorage devices according to AASHTO (2002)

Test specimen

The test specimen should consist of a square or rectangular concrete prism with cross-section dimensions corresponding to the smaller of twice the minimum edge distance or the minimum spacing between anchorages, specified by the anchorage device supplier. The length of the block should be at least two times the larger of the cross-section dimensions. The specimen should contain the anchorage components that will be embedded in the structural concrete, the confining reinforcing steel specified by the anchorage device supplier, as well as an empty duct of size appropriate for the maximum tendon size which can be accommodated by the anchorage device. In addition to the confining reinforcement, supplementary skin reinforcement may also be adopted, but not exceeding a volumetric ratio of 0,01.

Cyclic loading test

The cyclic loading test is the most usual test. In this test, shown in Figure 3.24(a), the load should be increased to 0,8 F_{pk}. Then, the load should be cycled between 0,1 F_{pk} and 0,8 F_{pk}, for at least 10 cycles, until crack widths stabilise. Crack widths are considered to be stabilised if they do not change by more than 0,025 mm (0,001 in.) over the last three readings. After completing the cyclic loading, the specimen should be loaded until failure or, if limited by the capacity of the loading equipment, to at least 1,1 F_{pk}.

Crack widths and crack patterns should be recorded at the initial load of 0,8 F_{pk}, at least at the last three consecutive peak loadings before termination of the cyclic loading, and at 0,9 F_{pk}. The maximum load should be reported.

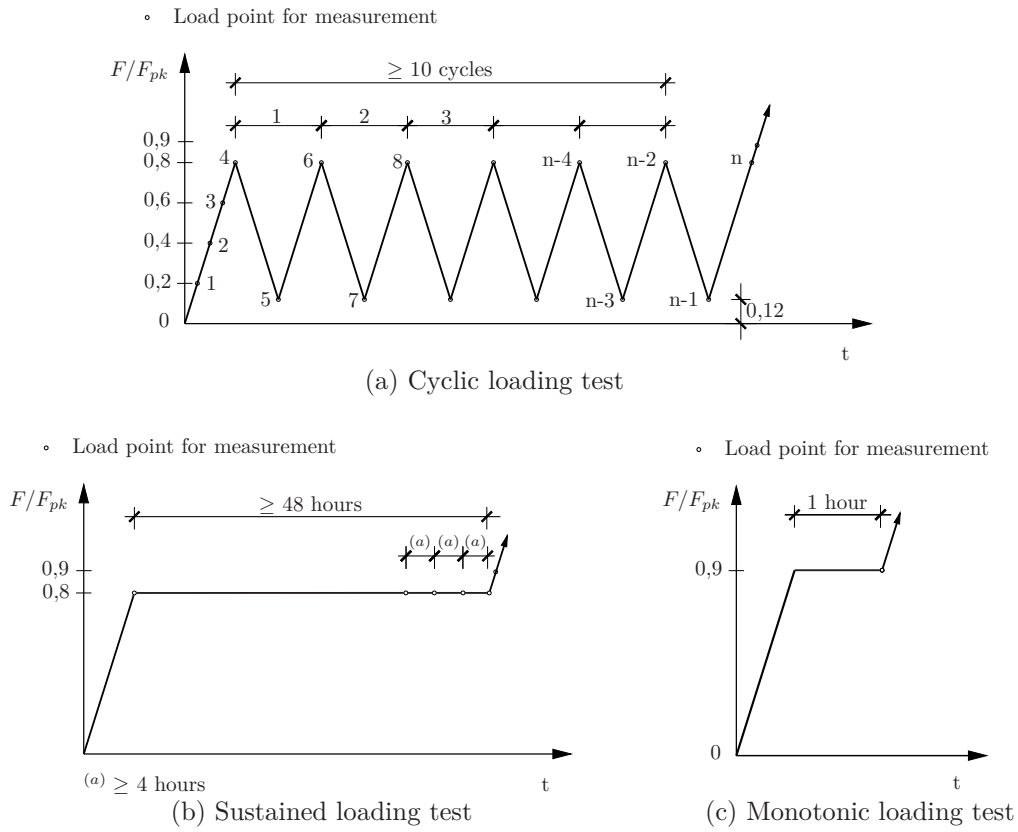

(a) Cyclic loading test

(b) Sustained loading test

(c) Monotonic loading test

Figure 3.24: AASHTO (2002) tests for the local zone of special anchorage devices

Sustained loading test

In sustained loading test, shown in Figure 3.24(b), the load should be increased to 0,8 F_{pk} and held constant for, at least, 48 hours or until crack widths stabilise. Crack widths are considered stabilised if they do not change by more than 0,025 mm (0,001 in.) over the last three readings at intervals of not less than four hours during the last twelve hours. After completing the sustained loading, the specimen should be loaded until failure or, if limited by the capacity of the loading equipment, to at least 1,1 F_{pk}.

Crack widths and crack patterns should be recorded at the initial load of 0,8 F_{pk}, at least three times before termination of the sustained loading, and during loading to failure at 0,9 F_{pk}. The maximum load should also be reported.

Monotonic loading test

In monotonic loading test, shown in Figure 3.24(c), the load should be increased to 0,9 F_{pk} and held constant for 1 hour. The specimen should then be loaded until failure or, if limited by the capacity of the loading equipment, to at least 1,2 F_{pk}.

Crack widths and crack patterns should be recorded at the load of 0,9 F_{pk} after the one hour period, and during loading to failure at 1,2 F_{pk}. The maximum load should also be reported.

Acceptance criteria

The strength of the anchorage zone must exceed 1,1 F_{pk} for the specimens tested under cyclic or sustained loading and 1,2 F_{pk} for the specimens tested under monotonic loading.

In the case of a moderately aggressive environment, the maximum allowed crack width is 0,25 mm at 0,8 F_{pk} after the conclusion of the cyclic or sustained loading, or at 0,9 F_{pk} after 1 hour period for monotonic loading. At 0,9 F_{pk} for cyclic or sustained loading, or at 1,0 F_{pk} for monotonic loading, the maximum crack width allowed is 0,40 mm. For higher aggressively environments, the crack width criteria shall be not more than half.

3.2.4.3 European Organisation for Technical Approvals (2002)

The test specified in ETAG 013 (European Organisation for Technical Approvals, 2002) is very similar to the test specified by FIP Recomendation (1993) and consists of loading a prismatic concrete block containing the anchorage components and confinement reinforcement which will be embedded in the structural concrete. The compression load is applied directly to the bearing plate by means of an anchor head.

Test specimen

The test specimen, shown in Figure 3.25 is a concrete prism with a cross-section ($A_c = a \times b$) corresponding to the minimum cross-section in axial compression specified by the anchorage device supplier for the particular tendon and concrete strength class.

For the reference dimensions a and b, the minimum anchorage centre spacing in the structure x and y, in x and y directions, respectively, and minimum edge distances, can be derived according to the rule presented in equation (3.26).

$$A_c = x \cdot y = a \cdot b \tag{3.26}$$

where,

a, b are the side widths of the test specimen (ETA reference dimensions) in x and y directions, respectively;

x, y are the minimum specified anchorage centre spacing of the particular tendon, and/or twice the specified edge distance of the tendon, whichever is smaller.

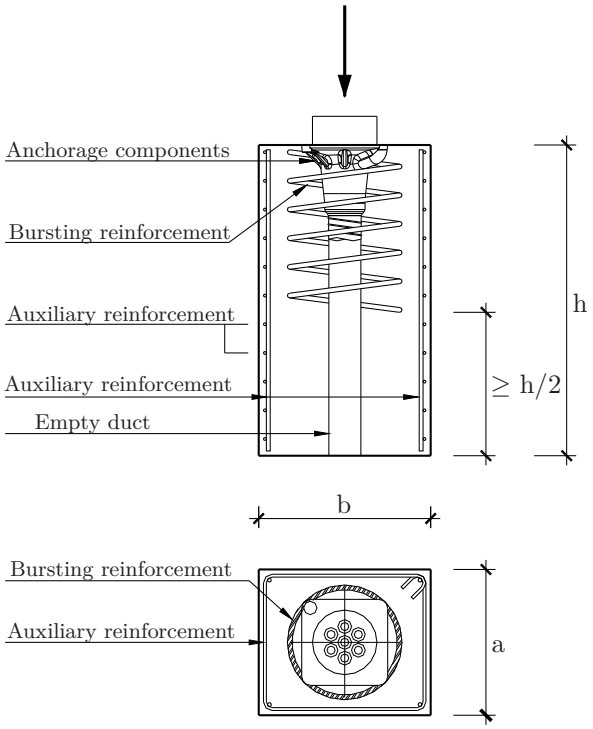

Figure 3.25: European Organisation for Technical Approvals (2002) test specimen for load transfer test

The actual spacing / centre distance and edge distance in the structure shall comply with the relations presented in equation (3.27).

$$x \geq 0,85a \tag{3.27a}$$

$$y \leq 1,15b \tag{3.27b}$$

The height of the prism is required to be at least two times the larger of the cross-section dimensions. The height of the unreinforced or less reinforced part of the prism, away from the tendon anchorage, shall be at least 0,5h long.

The specimen must contain the confining reinforcement specified for the particular system and tendon. The use of additional reinforcement is permitted provided that the area of longitudinal reinforcing bars does not exceed 0,003 A_c, and the area of secondary reinforcement (stirrups uniformly distributed along the height of the specimen) is less than 50 kg/m^3 concrete. The concrete cover to the reinforcement should be 10 mm.

Test procedure

For the test a calibrated testing machine should be used. As shown in Figure 3.26, the load should be increased in steps of 0,2 F_{pk}, up to 0,8 F_{pk}. Then, at least ten slow load cycles should be performed between 0,8 F_{pk} and 0,12 F_{pk}. Cyclic loading should be

continued until stabilisation of strain readings and crack widths. Following cyclic loading, the specimen should be loaded continuously to failure.

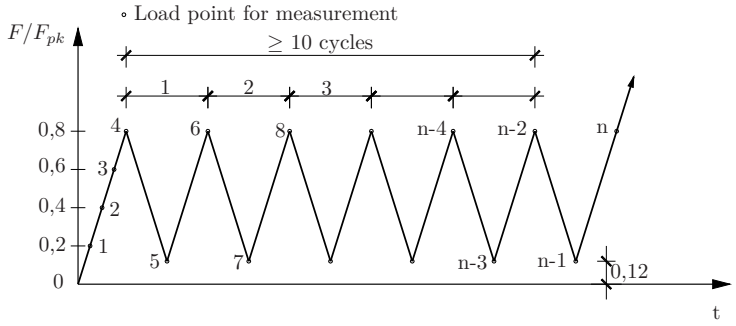

Figure 3.26: European Organisation for Technical Approvals (2002) load transfer test

Crack widths can be assumed to have stabilised if their width under upper load complies with the condition expressed in equation (3.28).

$$w_n - w_{n-4} \leq 1/3(w_{n-4} - w_0) \tag{3.28}$$

where w is the crack width and w_0 is the crack width observed when the upper force of 0,8 F_{pk} is reached for the first time.

Longitudinal and transversal strains can be considered to have stabilised if the increase of strain under the upper load complies with the condition expressed in equation (3.29)

$$\varepsilon_n - \varepsilon_{n-4} \leq 1/3(\varepsilon_{n-4} - \varepsilon_0) \tag{3.29}$$

where ε is the strain. The strain ε_0 is the value observed when the upper force of 0,8 F_{pk} is reached for the first time.

Longitudinal and transverse concrete strains, on at least two side faces of the specimen in the region of maximum bursting effect, and crack widths and patterns on the side faces of the specimen, should be recorded under the upper and lower load. The maximum load should also be reported.

Acceptance criteria

The maximum allowed crack width is 0,15 mm upon first attainment of upper force of 0,8 F_{pk} and upon last attainment of lower force of 0,12 F_{pk}. The maximum allowed crack width at 0,8 F_{pk} after the conclusion of the cyclic loading is 0,25 mm. The measured failure load must exceed 1,1 F_{pk}.

3.3 Experimental program

Since one of the purposes of using high performance concrete in anchorage zones is to reduce not only the minimum concrete cross-section but also the confining reinforcement, both specified by the anchorage device supplier for the particular tendon, an experimental program to assess both ultimate capacity and adequate serviceability of the local anchorage zone was carried out. Thus, the load transfer test specified in the European Organisation for Technical Approvals (2002) was performed.

3.3.1 Specimen geometry

The experimental program included eight ordinary reinforced concrete (ORC) prismatic specimens with 305 mm × 305 mm × 650 mm (four specimens P1 and four specimens P2) as shown in Figure 3.27, and eight high performance concrete prismatic specimens: one HPFRC specimen with 305 mm × 305 mm × 650 mm (specimen P3), one HPC specimen (specimen P4) and six HPFRC prismatic specimens (three specimens P5 and three P6) with 210 mm × 210 mm × 420 mm, shown in Figure 3.28.

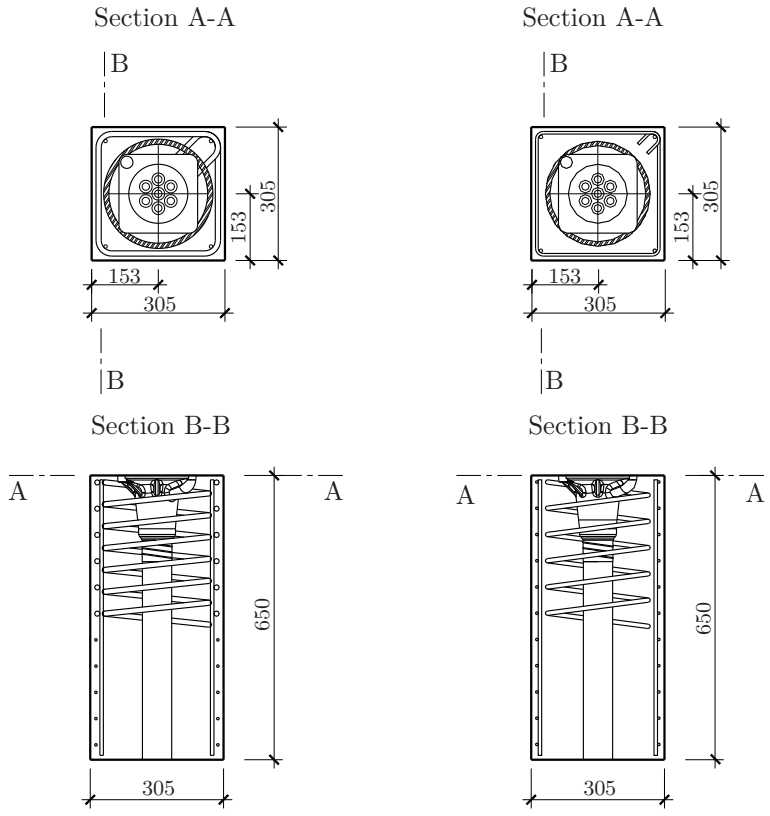

(a) Test specimen P1 (b) Test specimen P2

Figure 3.27: Test specimens of ordinary reinforced concrete

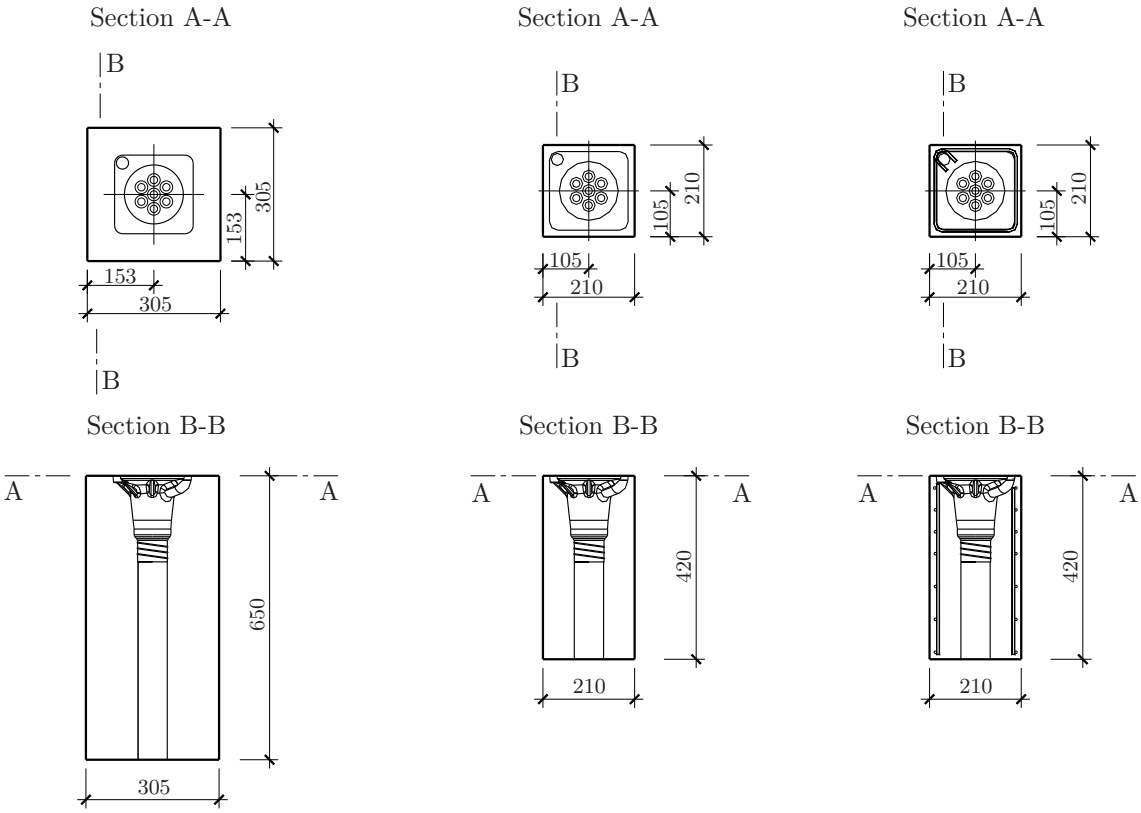

(a) Test specimen P3 (b) Test specimen P4 and P5 (c) Test specimen P6

Figure 3.28: Test specimens of high performance self-compacting concrete

The main differences between the six types of specimens are briefly described below:

- Specimens P1 were ORC reference specimens with dimensions and reinforcement specified by the anchorage device supplier (VSL International, 2008);
- Specimens P2 were made with the same concrete and dimensions of the reference specimens, but the steel confinement used in the reference blister model was adopted;
- Specimen P3 had the same dimensions of the previous, but was made with high performance fibre reinforced self-compacting concrete and without reinforcement;
- Specimens P4 and P5 were made of HPC and HPFRC, respectively, but with smaller dimensions and without confinement reinforcement;
- Specimens P6 were made with HPFRC, with the same dimensions as P4 and P5, but with a small amount of confinement stirrups.

In specimens P4, P5 and P6 the intention was to reduce the cross-section area to the minimum possible so, the width of the specimens was defined considering the width of the anchorage bearing plate to which was added the concrete cover on each side. Regarding the concrete cover, because it was a half scale model, 15 mm were adopted.

It was decided to test a specimen of HPC (without fibers), specimen P4, since the steel fibers are expensive and require an extra step in the mixing procedure of the HPFRC.

The characteristics of the prismatic test specimens and the definition of the confining reinforcement are summarized in Tables 3.10 and 3.11, respectively.

Table 3.10: Characteristics of the test specimens

Specimen	N. specimens	Dimensions (mm^3)	Concrete type	Type of reinf.
P1	4	305×305×650	ORC	Spiral+Stirrups
P2	4	305×305×650	ORC	Spiral
P3	1	305×305×650	HPFRC	-
P4	1	210×210×420	HPC	-
P5	3	210×210×420	HPFRC	-
P6	3	210×210×420	HPFRC	Stirrups

Table 3.11: Test specimens confining reinforcement

	Spiral				Stirrups			
Specimen	ϕ (mm)	D (mm)	s (mm)	n. turns	ϕ (mm)	L (mm)	s (mm)	n. stirrups
P1	12	250	50	6	12	285	60	6
P2	10	230	60	6	-	-	-	-
P6	-	-	-	-	6	190	50	4

-The diameter D or side length L is measured from outside to outside of the steel bars.
-The pitch or spacing s refers to the distance measured from centre to centre of the bars.

In specimens P1 and P2, additional reinforcement of 4ϕ8 longitudinal reinforcing bars, as well as ϕ6 stirrups with 60 mm spacing uniformly distributed along the half height or full height, respectively, were adopted. In specimens P6, the additional reinforcement consisted of 4ϕ6 longitudinal reinforcing bars and ϕ6 stirrups with 75 mm spacing uniformly distributed along the half height of the prism. The reinforcing steel grade was A500NR SD.

The stressing anchorage used in the specimens was a VSL anchorage Type GC for seven strands of 0,6", with a 180 × 180 mm^2 bearing plate. Corrugated steel ducts with internal and external diameters of 60 mm and 67 mm, respectively, were also adopted.

All specimens were cast horizontally, as shown in Figure 3.29.

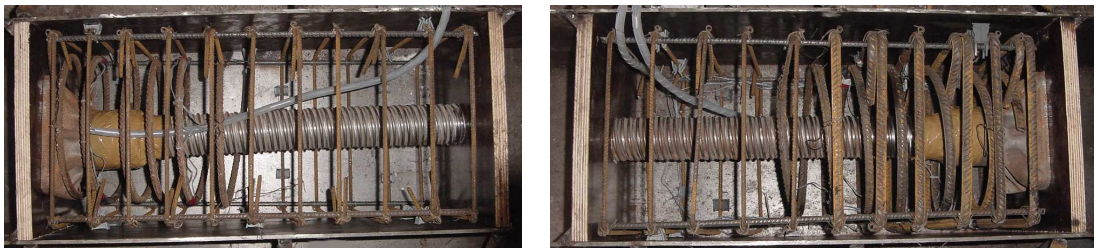

(a) Specimens P1 **(b)** Specimens P2

Figure 3.29: Specimens P1 and P2 reinforcement

3.3.2 Monitoring equipment

Before casting, a total of sixteen strain gauges (model TML type FLA-5-11-5L) in specimens P1 and P6, and eight strain gauges in specimens P2, were affixed to diametrically opposite sides of selected reinforcing bars, whose position is indicated in Figure 3.30. The numbering shown in the figures below refers to pairs of strain gauges.

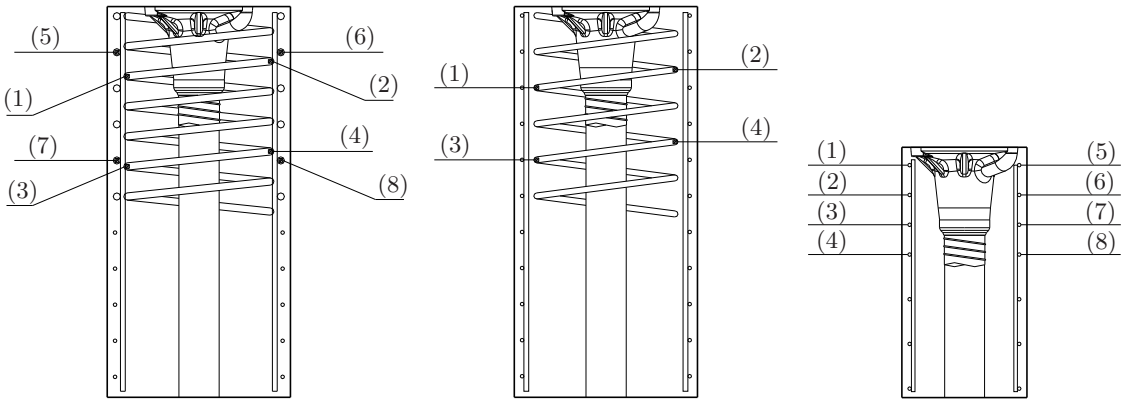

(a) Specimens P1 **(b)** Specimens P2 **(c)** Specimens P6

Figure 3.30: Specimens P1, P2 and P6 strain gauges

Figure 3.31 presents some details and the positioning of the strain gauges used.

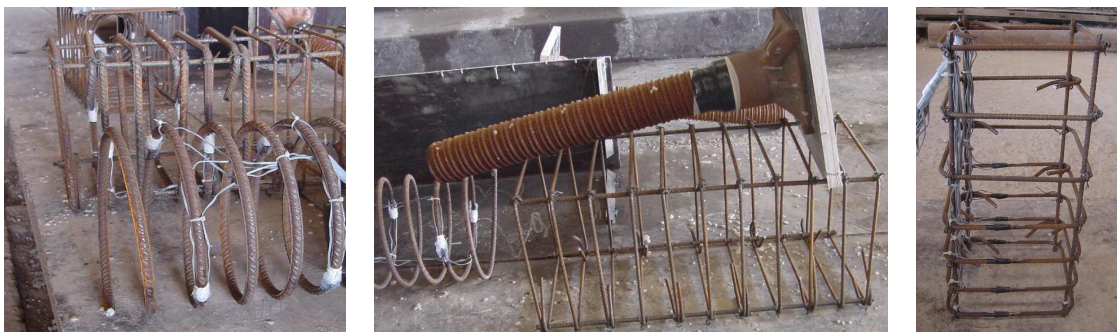

(a) Specimens P1 **(b)** Specimens P2 **(c)** Specimens P6

Figure 3.31: Specimens P1, P2 and P6 strain gauges

In specimens P1, P2 and P3, the vertical surface strains were measured with displacement transducers TML type PI-2-200 on two faces of the block. DEMEC locating discs for mechanical extensometer measurement of concrete horizontal surface strains were placed on two faces of the specimens. The location of the referred measuring equipment is given in Figures 3.32 and 3.33.

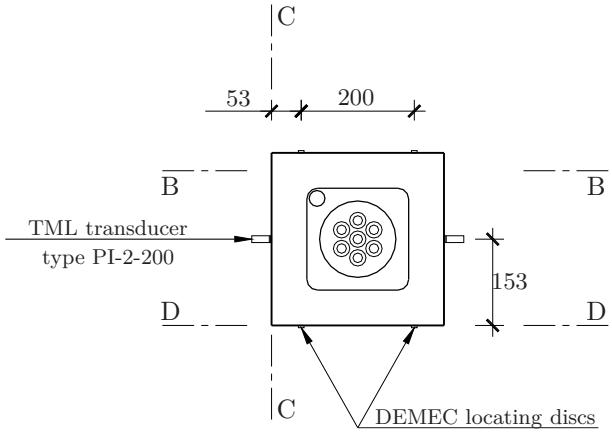

Figure 3.32: Location of the measuring equipment of specimens P1, P2 and P3 - Section A-A

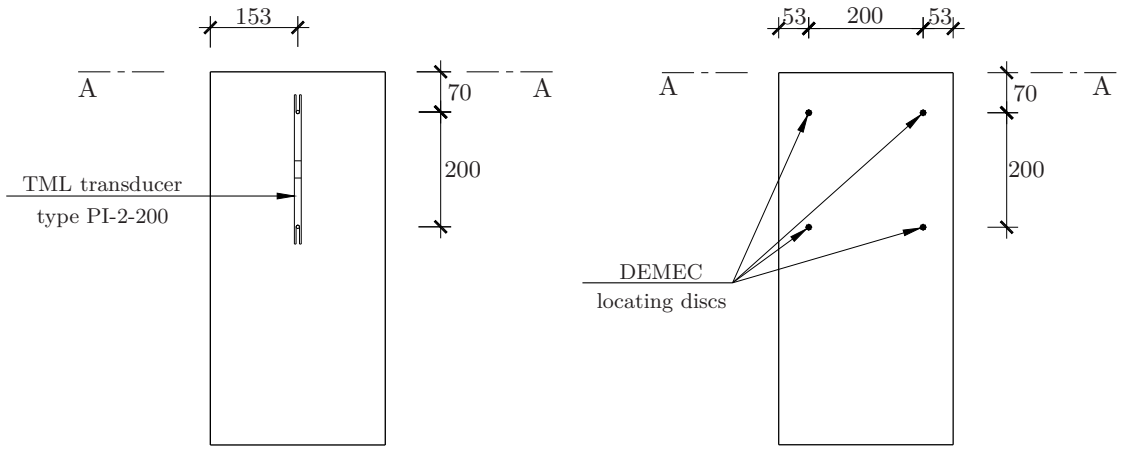

(a) Section C-C **(b)** Section B-B

Figure 3.33: Location of the measuring equipment of specimens P1, P2 and P3

The measuring equipment is shown in Figure 3.34.

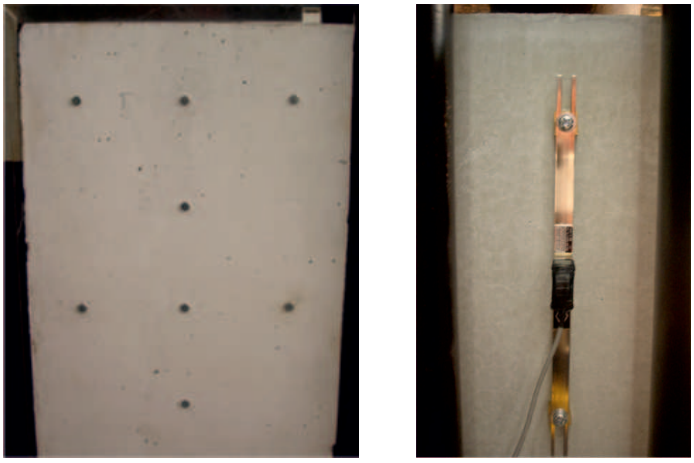

(a) DEMEC locating disks **(b)** Displacement transducer

Figure 3.34: Specimens P1, P2 and P3 measuring equipment

In specimens P4, P5 and P6, the vertical and horizontal surface strains were both measured with displacement transducers TML type PI-2-200 and PI-2-150 on two faces of the block, on the locations shown in Figures 3.35 and 3.36.

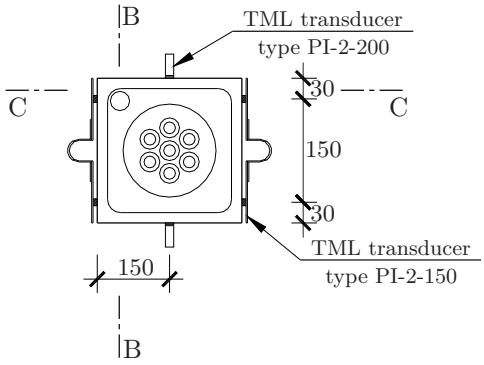

Figure 3.35: Location of the measuring equipment of specimens P4, P5 and P6 - Section A-A

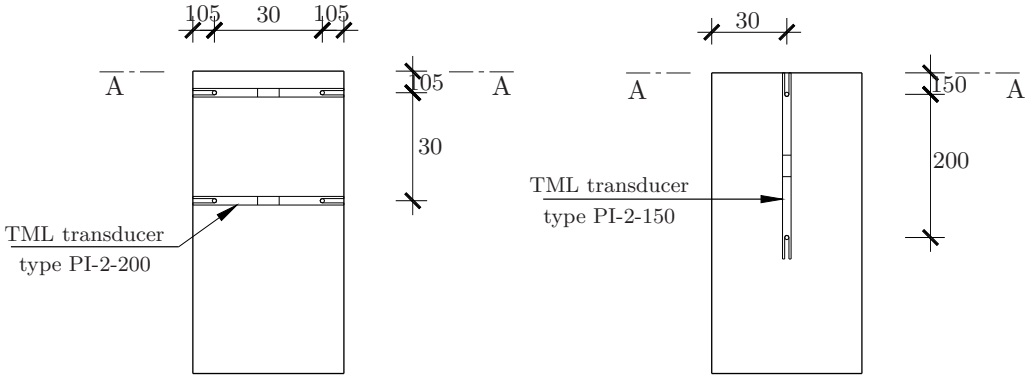

(a) Section B-B **(b)** Section C-C

Figure 3.36: Location of the measuring equipment of specimens P4, P5 and P6

Figure 3.37 illustrates the measuring equipment.

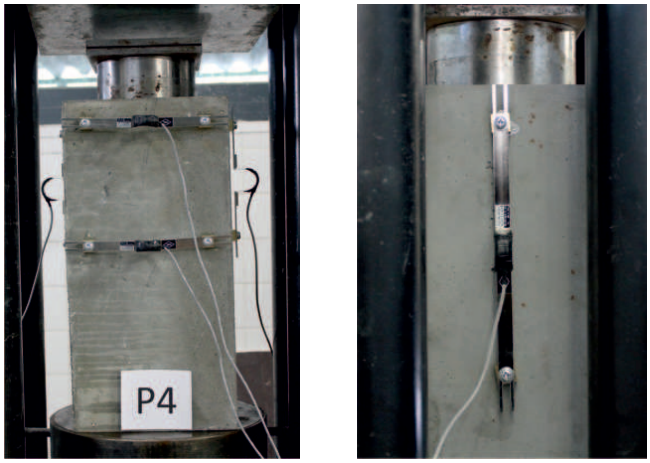

(a) Horizontal transducers **(b)** Vertical transducers

Figure 3.37: Specimens P4, P5 and P6 measuring equipment

The strain gauges and the displacement transducers were connected to a computerised data acquisition system.

3.3.3 Test procedure and measurements

The equipment used for testing was a servo-controlled compression machine with a load capacity up to 3000 kN and displacement capacity up to 50 mm. The data acquisition equipment used was a *HBM Spider8*, with eight measurement channels per basic device. The data acquisition software used was *HBM catman 6.0*. Figure 3.38 presents a typical setup for the testing of a square prism.

Figure 3.38: Test Setup for specimens P4, P5 and P6

The specimens were loaded through a 135 mm diameter and 60 mm high anchor head, placed on top of the stressing anchorage. The anchorage used in the tests is intended for a maximum of seven strands type 0,6", each strand with a maximum nominal area of 150 mm^2, a tensile strength of 1860 MPa and a characteristic ultimate resisting force of 1953,0 kN. Accordingly, during the load transfer test ten load cycles were carried out between 234,4 kN $(0,12F_{pk})$ and 1562,4 kN $(0,8F_{pk})$. Following cyclic loading, the specimens were loaded continuously to failure. The measured breaking load should be superior to 2148,3 kN $(1,1F_{pk})$.

3.3.4 Experimental results

3.3.4.1 Ordinary reinforced concrete specimens

In the ordinary reinforced concrete specimens (P1 and P2), all the cracks developed during the load cycles were located in the upper half of the specimens. The first cracks to appear were vertical in the middle of the specimen and horizontal cracks at a distance of approximately 70 mm from the top of the specimens. As shown in Figures 3.39 and 3.40, at failure, cracks propagated to the bottom half and also developed at the top surface of the specimen.

(a) Top view **(b)** Side view **(c)** Side view

Figure 3.39: Specimen P1A after testing

(a) Top view **(b)** Side view **(c)** Side view

Figure 3.40: Specimen P2 after testing

Results of parameters recorded throughout the test

The relation between the applied vertical load and the total vertical displacement is presented in Figures 3.41a and 3.41b for specimens type P1 and P2, respectively.

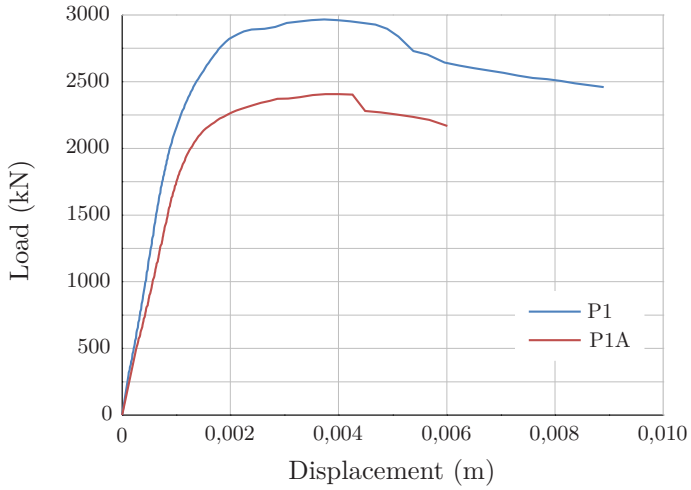

(a) Specimens P1 and P1A

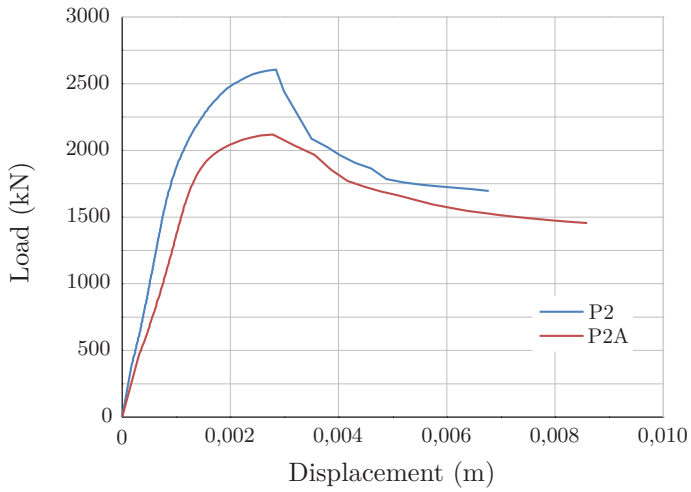

(b) Specimens P2 and P2A

Figure 3.41: Load vs vertical displacement relations

The load-displacement relationships presented in Figure 3.41 above, were obtained neglecting the cyclic loading and considering only the final phase of the experimental test, in which the specimens were loaded continuously to failure.

The load-displacement relationship of specimens P1B, P1C, P2B and P2C is not presented because, unfortunately, due to a data acquisition problem the vertical displacement was not recorded.

Figures 3.43 to 3.49 show the relation between the confining reinforcement strain and the applied load for the ordinary reinforced concrete specimens.

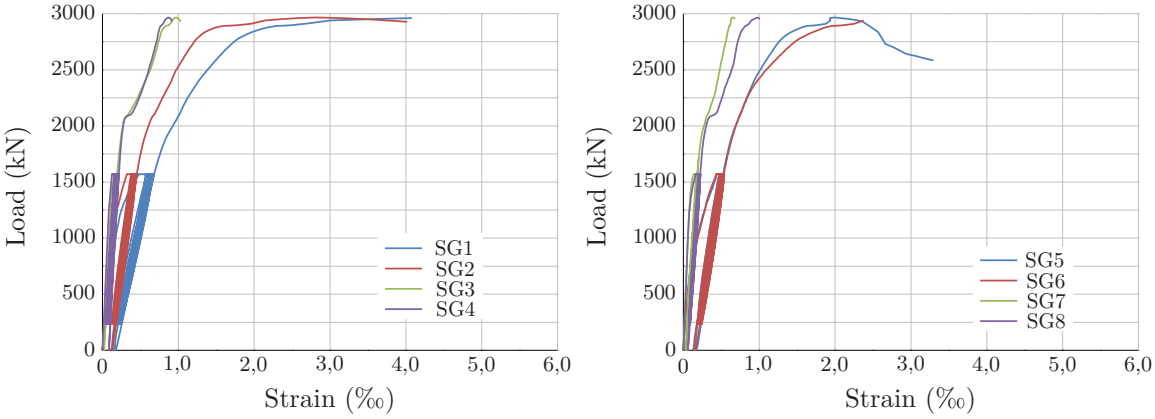

(a) Spiral - Strain Gauges 1 to 4 **(b)** Stirrups - Strain Gauges 5 to 8

Figure 3.42: Specimen P1 - Load vs reinforcement strain relations

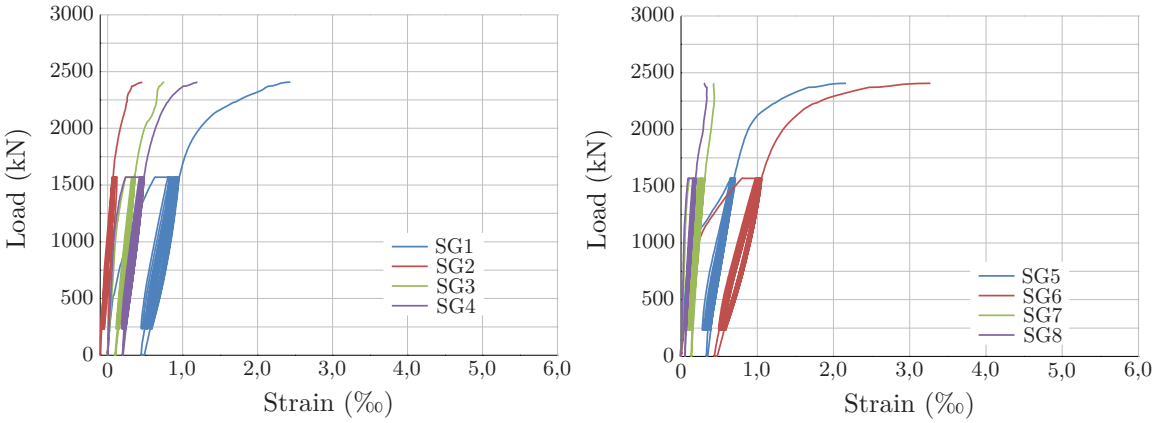

(a) Spiral - Strain Gauges 1 to 4 **(b)** Stirrups - Strain Gauges 5 to 8

Figure 3.43: Specimen P1A - Load vs reinforcement strain relations

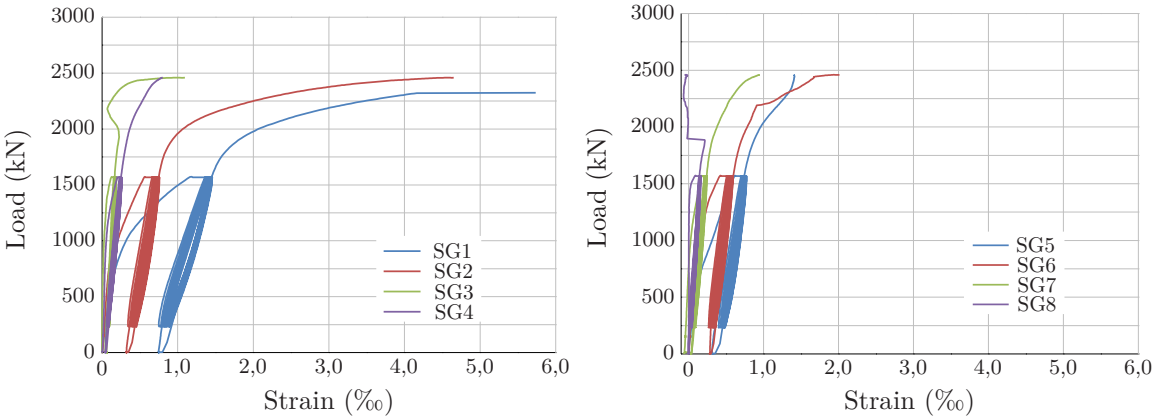

(a) Spiral - Strain Gauges 1 to 4 **(b)** Stirrups - Strain Gauges 5 to 8

Figure 3.44: Specimen P1B - Load vs reinforcement strain relations

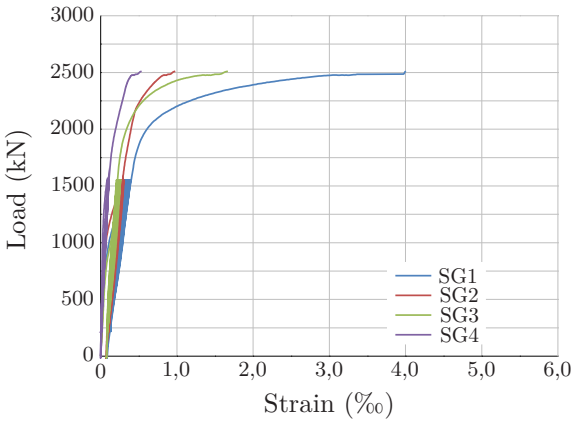

(a) Spiral - Strain Gauges 1 to 4

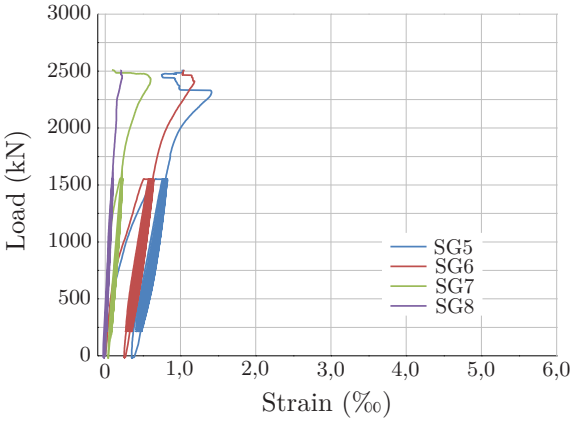

(b) Stirrups - Strain Gauges 5 to 8

Figure 3.45: Specimen P1C - Load vs reinforcement strain relations

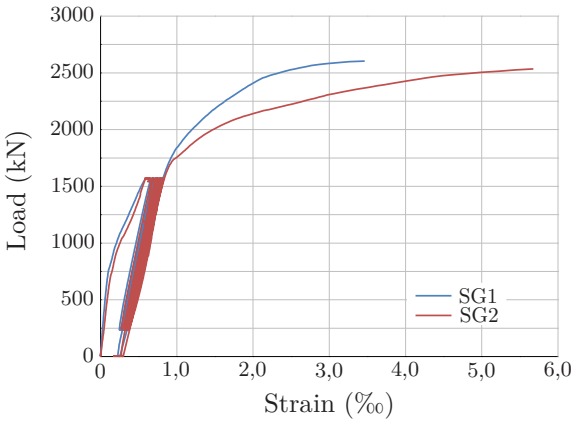

(a) Strain Gauges 1 and 2

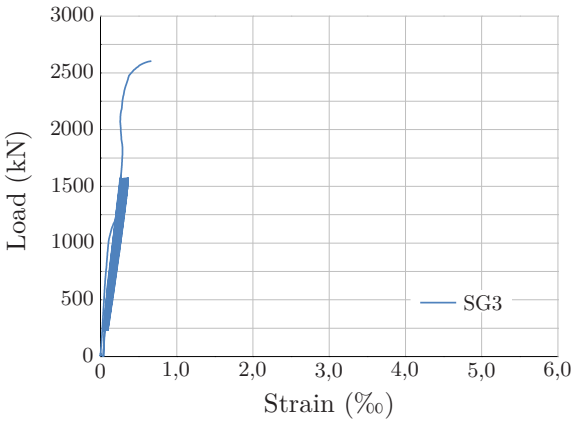

(b) Strain Gauge 4

Figure 3.46: Specimen P2 - Load vs reinforcement strain relations

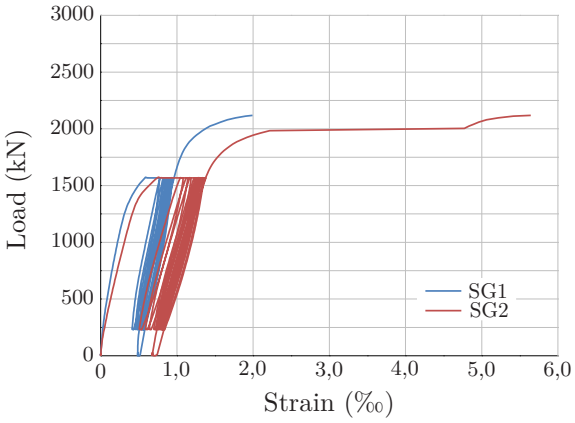

(a) Strain Gauges 1 and 2

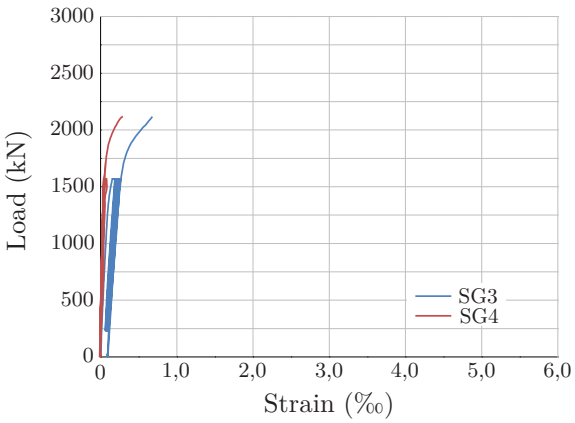

(b) Strain Gauges 3 and 4

Figure 3.47: Specimen P2A - Load vs reinforcement strain relations

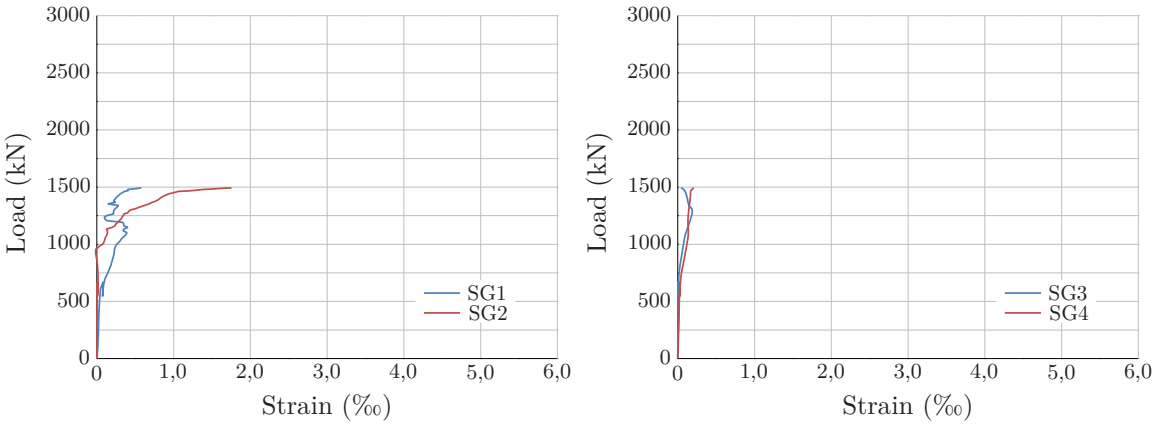

(a) Strain Gauges 1 and 2 **(b)** Strain Gauges 3 and 4

Figure 3.48: Specimen P2B - Load vs reinforcement strain relations

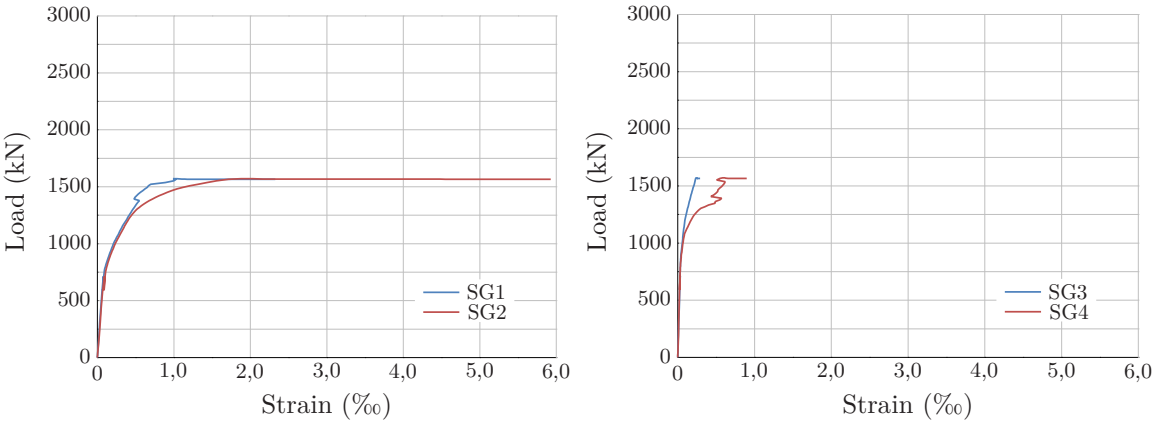

(a) Strain Gauges 1 and 2 **(b)** Strain Gauges 3 and 4

Figure 3.49: Specimen P2C - Load vs reinforcement strain relations

The recorded crack widths and failure loads are presented in Tables 3.12 and 3.13. In each case, based on the acceptance criterion of the load transfer test described above, is also indicated whether the specimen passed or failed the test.

Table 3.12: Crack widths and ultimate load capacity of the specimens P1

Specimen	Crack widths w (mm)			P_u	Acceptance
	P_1	P_2	P_3	(kN)	
P1	0,02	0	0,05	2965,8	Pass
P1A	0,15	0,15	0,20	2406,6	Pass
P1B	0,10	0,10	0,20	2460,0	Pass
P1C	0,10	0,10	0,15	2504,9	Pass

Table 3.13: Crack widths and ultimate load capacity of the specimens P2

Specimen	Crack widths w (mm)			P_u	Acceptance
	P_1	P_2	P_3	(kN)	
P2	0,05	0,05	0,10	2604,3	Pass
P2A	0,20	0,30	0,40	2118,3	Fail
P2B	-	-	-	1495,8	Fail[a]
P2C	0,40	-	-	1563,5	Fail[b]

[a] The specimen failed before reaching the maximum load of the first cycle

[b] The specimen was about to fail when reaching the maximum load of the first cycle

In Tables 3.12 and 3.13 P_1, P_2 and P_3 represents the first attainment of upper force of $0,8F_{pk}$, last attainment of lower force of $0,12F_{pk}$ and last attainment of upper force of $0,8F_{pk}$, respectively.

Materials Characterisation

For each test specimen, the concrete characteristics at the time of the tests are indicated in Table 3.14.

Table 3.14: Concrete characteristics of the specimens

Specimen	f_c (MPa)	$f_{c,cube}$ (MPa)	$f_{ct,sp}$ (MPa)
P1	52,2	65,2	4,6
P1A	29,4	36,7	3,2
P1B and P1C	27,8	34,7	2,8
P2	52,2	65,2	4,6
P2A	29,4	36,7	3,2
P2B and P2C	26,5	33,1	2,6

In Table 3.14, the mean compressive strength of concrete for cubic specimens was determined by uniaxial compression tests. The mean compressive strength for cylinder specimens was obtained using the usual relation proposed by EN 1992-1-1 (2004) and presented in equation (3.30). The tensile splitting strength was obtained by tensile splitting tests, with the exception of specimens P1 and P2. For the latter, the tensile splitting strength was estimated from the compressive strength, using the relations recommended in EN 1992-1-1 (2004), and presented in equations (3.31) and (3.32) below.

$$f_c = 0,8 f_{c,cube} \tag{3.30}$$

$$f_{ct,sp} = \frac{f_{ctm}}{0,9} \tag{3.31}$$

$$f_{ctm} = 0,30 \times f_{ck}^{2/3} \tag{3.32}$$

The mechanical characteristics of the reinforcing steel were obtained by performing direct tensile tests according to EN 10002-1 (2001).

Six test specimens of each diameter were tested using a tensile testing machine INSTRON 1343 with a 250 kN load capacity. The stress-strain diagrams obtained during the tests are presented in Figure 3.50.

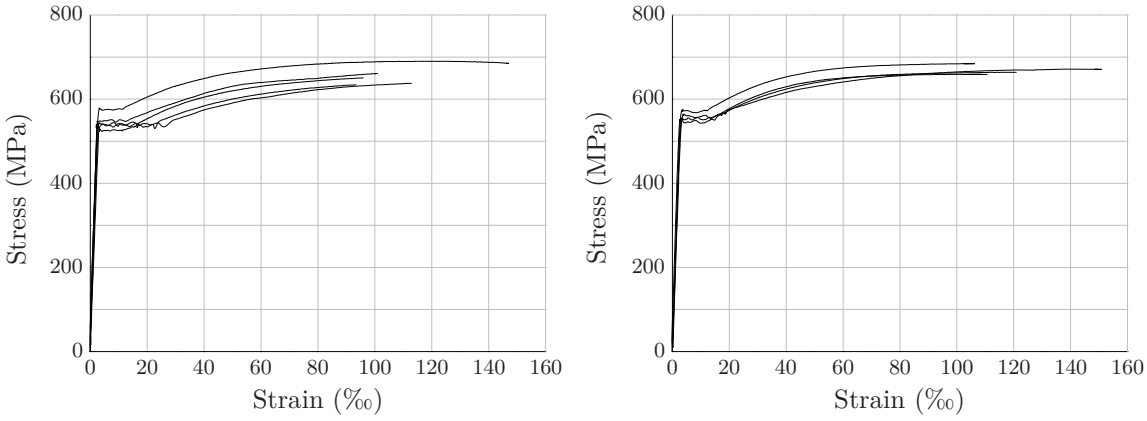

(a) Bars with 10 mm diameter **(b)** Bars with 12 mm diameter

Figure 3.50: Steel reinforcement stress-strain diagrams

Table 3.15 presents the mean values of the yield strength f_y, maximum strength f_u and strain of steel reinforcement at maximum load ε_u.

Table 3.15: Steel reinforcement characteristics

Bar diameter (mm)	f_y (MPa)	f_u (MPa)	ε_u
10	561	673	11,4%
12	542	657	10,9%

The modulus of elasticity of the steel has not been determined experimentally. The typical value of 200 GPa was adopted.

3.3.4.2 High performance concrete specimens

Throughout the test of specimen P3, the maximum capacity of the compression test machine was attained without failure or significant cracking of the specimen, as shown in Figure 3.51.

Figure 3.51: Specimen P3 after testing

The failure of specimen P4 (cast with high performance self-compacting concrete without steel fibres) occurred suddenly with bursting and spalling of concrete. The failure was brittle and explosive, as shown in Figure 3.52.

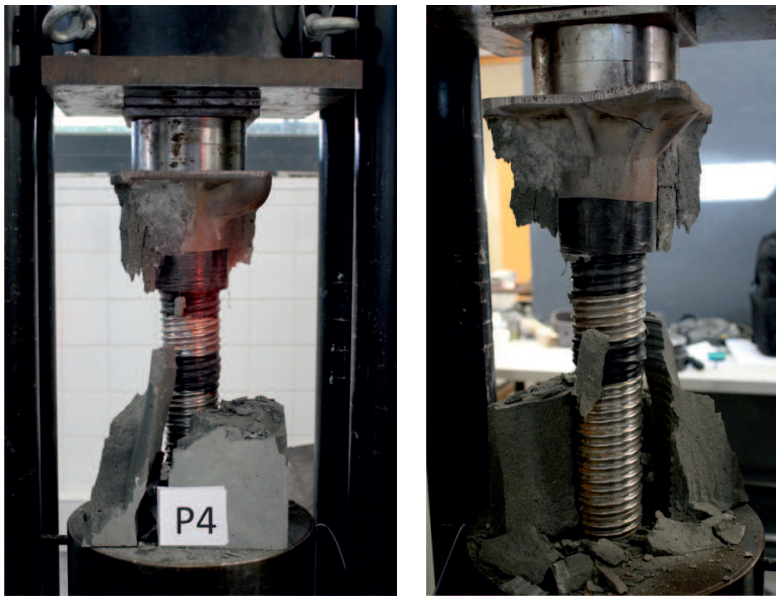

(a) Side view **(b)** Side view

Figure 3.52: Specimen P4 after testing

In specimens P5, during the application of the first load, a vertical crack developed in the middle of the specimen along the full height, on two opposite faces. In this specimen, cast with high performance fibre reinforced self-compacting concrete, no spalling or brittle failure of concrete was observed. As shown in Figure 3.53, the presence of fibres prevented

the increase of the crack width and helped to maintain the integrity of the specimen. However, it was found that the fibres showed a preferential orientation, so that the only cracked faces were the two opposite faces parallel to the direction of concrete pouring.

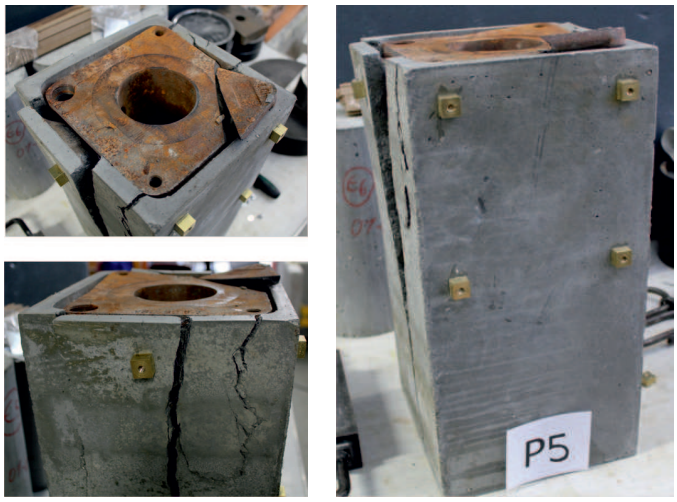

(a) Top views **(b)** Side view

Figure 3.53: Specimen P5 after testing

Specimens P6 behaved far better than P5 throughout the test regarding crack width. As shown in Figure 3.54, at failure, multiple vertical and horizontal cracks are visible.

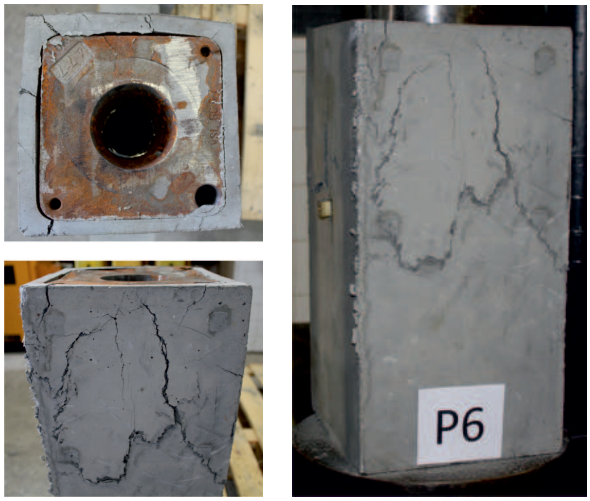

(a) Top views **(b)** Side view

Figure 3.54: Specimen P6 after testing

Results of parameters recorded throughout the test

The relation between the applied vertical load and the total vertical displacement is presented in Figures 3.55a, 3.55b and 3.55c for specimens type P4, P5 and P6, respectively.

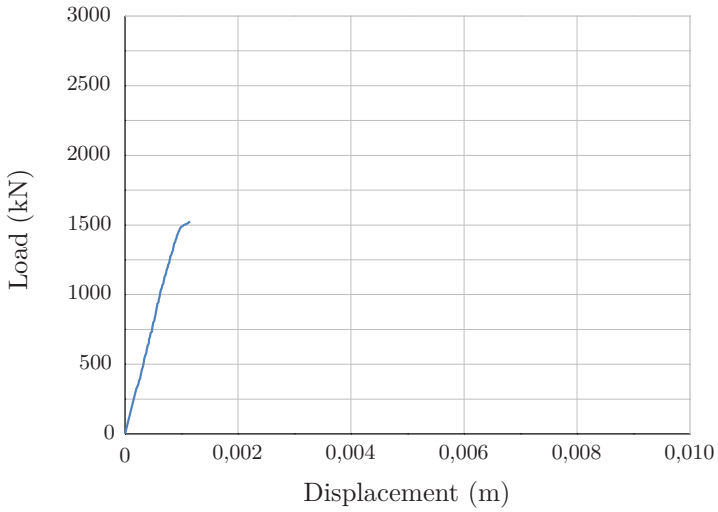

(a) Specimen P4

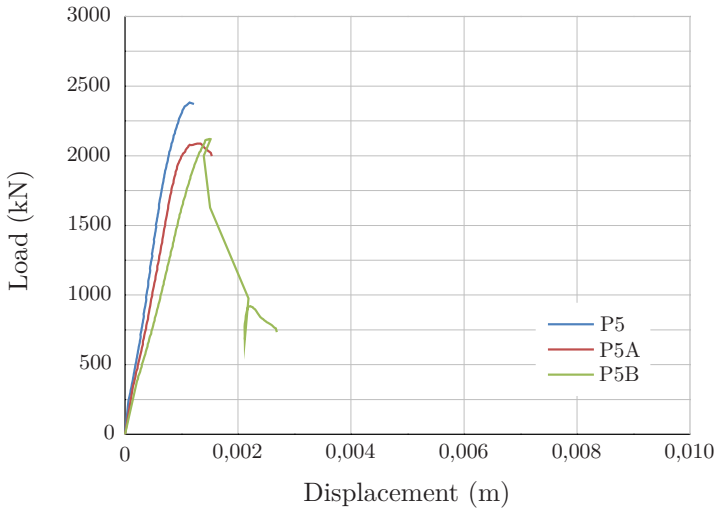

(b) Specimen P5

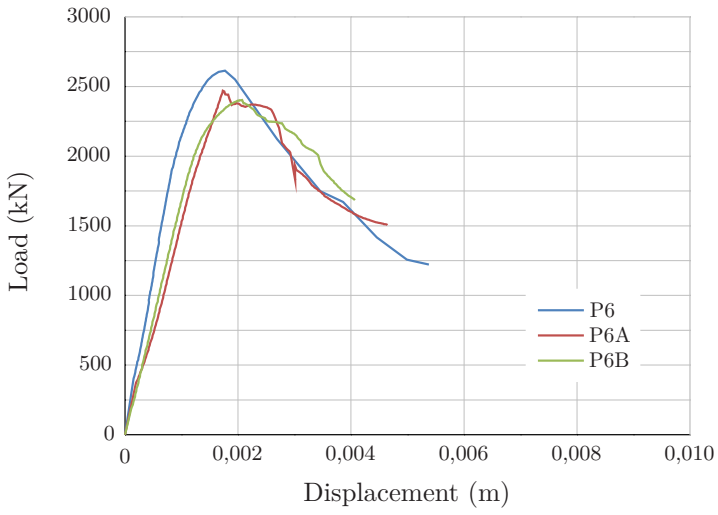

(c) Specimen P6

Figure 3.55: Load vs vertical displacement relations

Figure 3.56 shows the relation between the applied vertical load and the reinforcement strain for specimens P6, P6A and P6B.

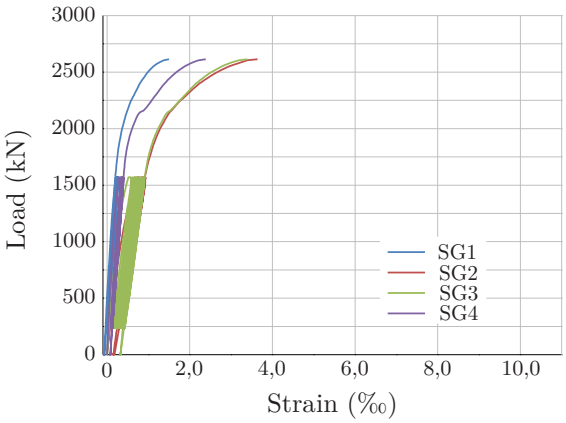

(a) Specimen P6 - Strain Gauges 1 to 4

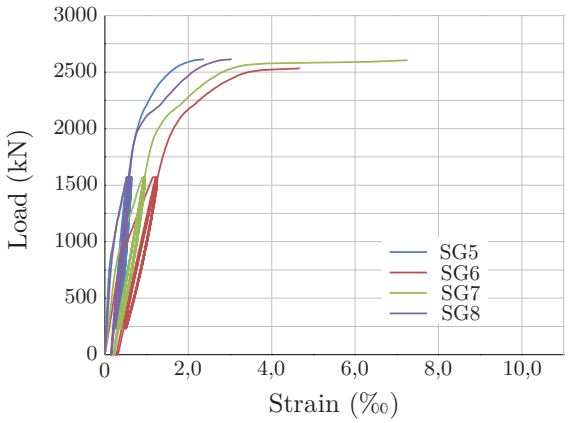

(b) Specimen P6 - Strain Gauges 5 to 8

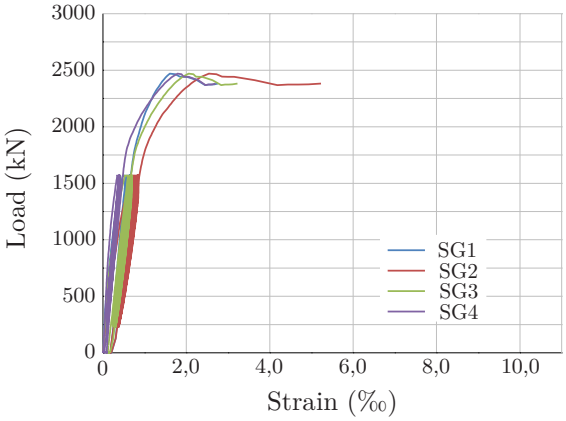

(c) Specimen P6A - Strain Gauges 1 to 4

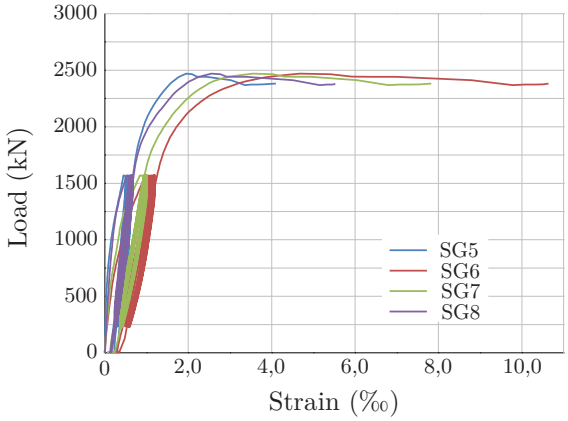

(d) Specimen P6A - Strain Gauges 5 to 8

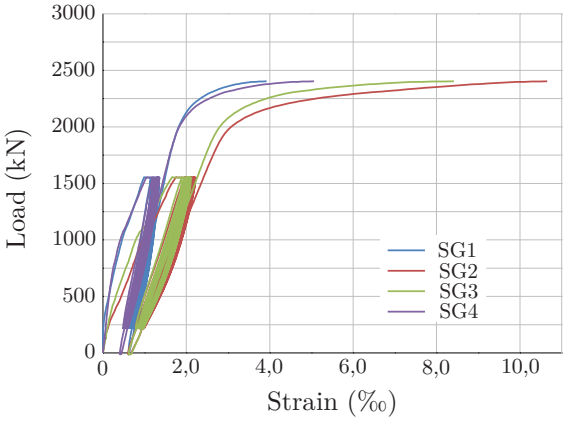

(e) Specimen P6B - Strain Gauges 1 to 4

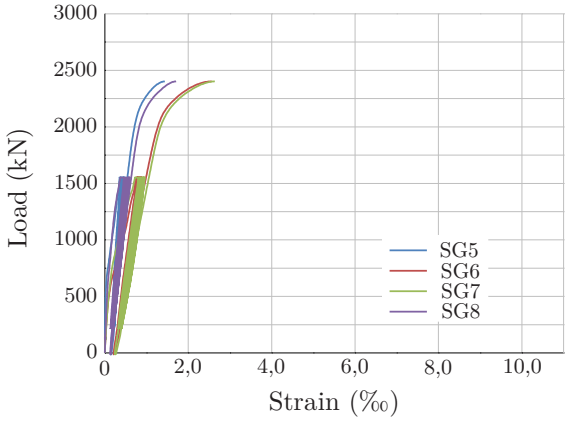

(f) Specimen P6B - Strain Gauges 5 to 8

Figure 3.56: Load vs reinforcement strain relations for specimens P6, P6A and P6B

The recorded crack widths and failure loads are presented in Table 3.16 where, in each case, based on the acceptance criterion of the load transfer test described above, is also indicated whether the test passed or failed.

Table 3.16: Crack widths and ultimate load capacity of test specimens

Specimen	Crack widths w (mm)			P_u	Acceptance
	P_1	P_2	P_3	(kN)	
P3	0	0	0,05	3039,0[a]	Pass
P4	-	-	-	1524,0	Fail
P5	0,35	0,25	0,45	2367,0	Fail
P5A	0,35	0,25	0,40	2087,9	Fail
P5B	0,20	0,15	0,30	2117,4	Fail
P6	0	0,05	0,075	2593,0	Pass
P6A	0,15	0,15	0,25	2371,1	Pass
P6B	0,05	0,05	0,10	2403,8	Pass

[a] The specimen did not fail

In the Table 3.16 above, P_1, P_2 and P_3 represents the first attainment of upper force of $0,8F_{pk}$, last attainment of lower force of $0,12F_{pk}$ and last attainment of upper force of $0,8F_{pk}$, respectively.

Materials Characterisation

Table 3.17 presents the concrete characteristics for each test specimen.

Table 3.17: Concrete characteristics of test specimens

Specimen	HPFRC mixture[a]	t (days)	f_c (MPa)	$f_{c,cube}$ (MPa)	$f_{ct,sp}$ (MPa)
P3	B	29	112,3	109,0	9,6
P4	HPC B	32	94,4	114,1[b]	3,7
P5	A	68	122,0	125,6	13,6
P5A and P5B	C	27	116,7	106,7	11,1
P6	B	29	112,3	109,0	9,6
P6A and P6B	D	27	97,8	101,6	8,8

[a] This designation corresponds to the one introduced and described in Chapter 2

[b] This value refers to the mean concrete compressive strength obtained for 100 mm cubic specimens

As described for the case of ORC specimens, the mechanical characteristics of the reinforcing steel were obtained by performing direct tensile tests according to EN 10002-1

(2001). In this case, three test specimens of 6 mm diameter were tested using a tensile testing machine INSTRON 1343 with a 250 kN load capacity.

The stress-strain diagram obtained during the test is presented in Figure 3.57.

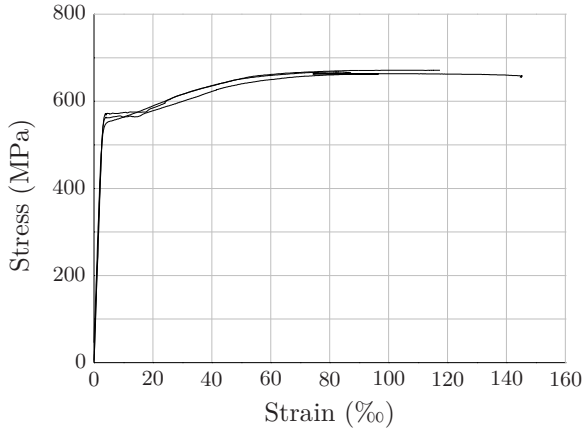

Figure 3.57: Stress-strain diagram for bars with 6 mm diameter

Table 3.18 presents the mean values of the yield strength f_y, maximum strength f_u and strain of steel reinforcement at maximum load ε_u.

Table 3.18: Steel reinforcement characteristics

Bar diameter (mm)	f_y (MPa)	f_u (MPa)	ε_u
6	564	667	11,6%

3.3.4.3 Conclusions of the test results

From the analysis of the results it can be concluded that, with the exception of the specimen P1A, for specimens with identical type and amount of reinforcement, the failure load of the specimen increased and the crack width decreased with increasing compressive and tensile strengths.

The use of HPFRC allows the suppression of the confining reinforcement for the type of anchorage utilised if the same concrete section is used as specified for the ordinary reinforced concrete specimens. The use of HPFRC also allows the reduction of the concrete cross-section and of the confining reinforcement. The suppression of all the confining reinforcement is however not advisable, since the non-randomness of fibre orientation can lead to formation of cracks with unacceptable width.

3.4 Comparison of test results with models of other authors

3.4.1 Unreinforced high performance concrete specimens

Tables 3.19, 3.20, 3.21 and 3.22 present the predicted failure loads of the unreinforced high performance concrete specimens, determined with the expressions proposed by Hawkins (1968b), Niyogi (1973), Roberts (Breen et al., 1991) and Bonetti (2005), respectively, and the comparison with experimental values.

Table 3.19: Ultimate predicted load according to equation (3.7) by Hawkins (1968b)

Specimen	A_b (mm^2)	A (mm^2)	A' (mm^2)	$P_{u,pred}$ (kN)	$P_{u,test}/P_{u,pred}$
P4	27864	44100	32400	2701,7	0,56
P5	27864	44100	32400	3479,0	0,68
P5A	27864	44100	32400	3331,0	0,63
P5B	27864	44100	32400	3331,0	0,64

Table 3.20: Ultimate predicted load according to equation (3.9) by Niyogi (1973)

Specimen	a (mm)	a' (mm)	$P_{u,pred}$ (kN)	$P_{u,test}/P_{u,pred}$
P4	210	180	2458,2	0,62
P5	210	180	3175,7	0,75
P5A	210	180	3038,9	0,69
P5B	210	180	3038,9	0,70

Table 3.21: Ultimate predicted load according to equation (3.21) by Roberts (Breen et al., 1991)

Specimen	A_b (mm^2)	A (mm^2)	A' (mm^2)	$P_{u,pred}$ (kN)	$P_{u,test}/P_{u,pred}$
P4	27864	44100	32400	2455,0	0,62
P5	27864	44100	32400	3171,4	0,75
P5A	27864	44100	32400	3034,9	0,69
P5B	27864	44100	32400	3034,9	0,70

Table 3.22: Ultimate predicted load according to equation (3.10) by Bonetti (2005)

Specimen	a'/a	β	z	α	m	$P_{u,pred}$ (kN)	$P_{u,test}/P_{u,pred}$
P4	0,86	0,064	0,49	1	25,51	1581,2	0,96
P5	0,86	0,064	0,49	1	8,96	3417,9	0,69
P5A	0,86	0,064	0,49	1	10,51	3076,4	0,68
P5B	0,86	0,064	0,49	1	10,51	3076,4	0,69

Table 3.23 shows the average (μ), standard deviation (σ) and coefficient of variation (C_v) of the experimental and predicted failure load ratio for the analysed authors.

Table 3.23: Average, standard deviation and coefficient of variation of the $P_{u,test}/P_{u,pred}$ ratio for the analysed authors

Author	μ	σ	C_v
Hawkins	0,63	0,08	0,08
Niyogi	0,69	0,05	0,08
Roberts	0,69	0,05	0,08
Bonetti	0,76	0,14	0,18

As expected, the predicted failure loads are significantly higher than those obtained in laboratory tests, as per Table 3.23, herein above. The main reason is the use of special anchorage devices instead of simple plates, for which equations (3.7), (3.9), (3.21) and (3.10) were assessed.

Equation (3.10) by Bonetti (2005) is the one that provides the most exact result which was obtained for specimen P4 without fibers in its composition and having consequently a very low tensile strength compared to the compressive strength.

Regarding specimens P5, equation (3.9) by Niyogi (1973) and equation (3.21) by Roberts (Breen et al., 1991) are the ones that are closer to the experimental results providing, however, non-conservative loads. It should be noted that equation (3.9) does not take into account the existence of post-tensioning duct and the value of the concrete tensile strength.

3.4.2 Reinforced concrete specimens

In order to assess the performance of proposed solutions by Niyogi (1975), Roberts (Breen et al., 1991) and Bonetti (2005) to predict the failure loads of reinforced specimens, the values obtained through equations (3.16), (3.21) and (3.24), respectively, will be compared with the experimental results.

Specimens P1

Tables 3.24, 3.25 and 3.26 present the predicted failure loads of specimens P1 and the comparison with experimental values.

Table 3.24: Ultimate predicted load according to equation (3.16) by Niyogi (1975)

Specimen	a (mm)	a' (mm)	n_{plain} (kN)	p_l	K	$P_{u,pred}$ (kN)	$P_{u,test}/P_{u,pred}$
P1	305	180	2163,7	0,040	55	6956,3	0,43
P1A	305	180	1217,9	0,040	55	3915,6	0,61
P1B/P1C	305	180	1152,9	0,040	55	3706,5	0,70/0,71

Table 3.25: Ultimate predicted load according to equation (3.21) by Roberts (Breen et al., 1991)

Specimen	spiral		stirrups		$P_{u,pred}$ (kN)	$P_{u,test}/P_{u,pred}$
	f_{lat} (kN/m^2)	A_{core} (mm^2)	f_{lat} (kN/m^2)	A_{core} (mm^2)		
P1	9799,4	27890	7163,3	37087	4179,9	0,71
P1A	9799,4	27890	7163,3	37087	3318,7	0,73
P1B/P1C	9799,4	27890	7163,3	37087	3259,5	0,75/0,77

Table 3.26: Ultimate predicted load according to equation (3.24) by Bonetti (2005)

Specimen	f_{lat} (kN/m^2)	m_r	a'/a	β	α	$P_{u,pred}$ (kN)	$P_{u,test}/P_{u,pred}$
P1	13381,0	2,90	0,59	0,19	1	3915,9	0,76
P1A	13381,0	1,77	0,59	0,19	1	2556,9	0,95
P1B/P1C	13381,0	1,72	0,59	0,19	1	2439,0	1,01/1,03

Excluding the effect of the stirrups in confinement, the achieved predicted failure loads of specimens P1, determined by the proposed expressions and the comparison with experimental values, are shown in Tables 3.27, 3.28 and 3.29, respectively.

Table 3.27: Ultimate predicted load according to equation (3.16) by Niyogi (1975), excluding the effect of the stirrups in confinement

Specimen	a (mm)	a' (mm)	n_{plain} (kN)	p_l	K	$P_{u,pred}$ (kN)	$P_{u,test}/P_{u,pred}$
P1	305	180	2163,7	0,018	55	4325,4	0,69
P1A	305	180	1217,9	0,018	55	2434,7	0,99
P1B/P1C	305	180	1152,9	0,018	55	2304,7	1,07/1,09

Table 3.28: Ultimate predicted load according to equation (3.21) by Roberts (Breen et al., 1991), excluding the effect of the stirrups in confinement

Specimen	f_{lat} (kN/m^2)	A_{core} (mm^2)	$P_{u,pred}$ (kN)	$P_{u,test}/P_{u,pred}$
P1	9799,4	27890	3090,7	0,96
P1A	9799,4	27890	2229,5	1,08
P1B/P1C	9799,4	27890	2170,3	1,13/1,15

Table 3.29: Ultimate predicted load according to equation (3.24) by Bonetti (2005), excluding the effect of the stirrups in confinement

Specimen	f_{lat} (kN/m^2)	m_r	a'/a	β	α	$P_{u,pred}$ (kN)	$P_{u,test}/P_{u,pred}$
P1	9799,4	3,62	0,59	0,19	1	3698,7	0,82
P1A	9799,4	2,26	0,59	0,19	1	2391,3	1,01
P1B/P1C	9799,4	2,21	0,59	0,19	1	2280,1	1,08/1,10

The average, standard deviation and coefficient of variation of the $P_{u,test}/P_{u,pred}$ ratio for specimens P1 for the analysed authors and cases, are presented in Table 3.30.

Table 3.30: Average, standard deviation and coefficient of variation of the $P_{u,test}/P_{u,pred}$ ratio for the analysed authors

	spiral + stirrups			spiral		
Author	μ	σ	C_v	μ	σ	C_v
Niyogi	0,60	0,12	0,19	0,96	0,19	0,19
Roberts	0,74	0,03	0,04	1,08	0,09	0,08
Bonetti	0,93	0,12	0,13	1,00	0,13	0,12

Figures 3.58 to 3.61 show the reinforcement strains along the height of the confined zone for the spiral and the stirrups, for specimens P1, P1A, P1B and P1C, respectively.

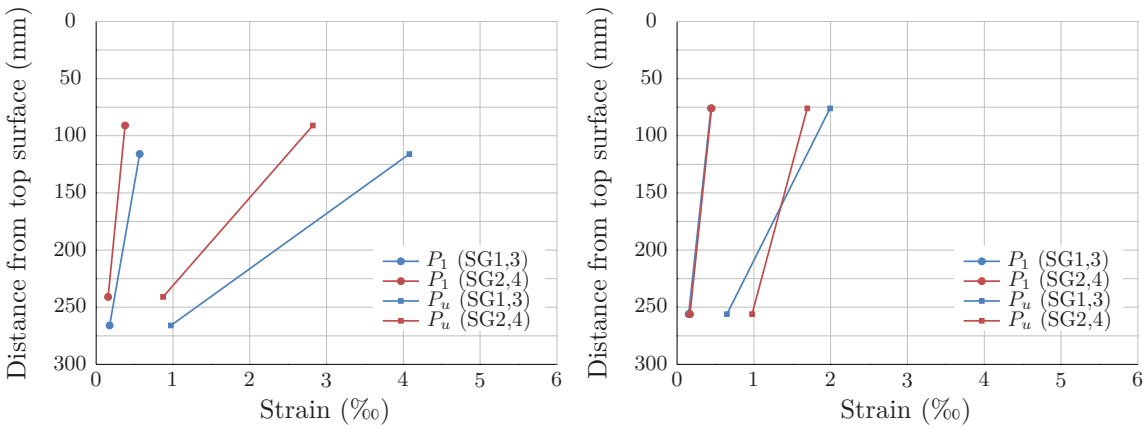

(a) Strain in the spiral

(b) Strain in the stirrups

Figure 3.58: Specimen P1 - Reinforcement strains along the height of the confined zone

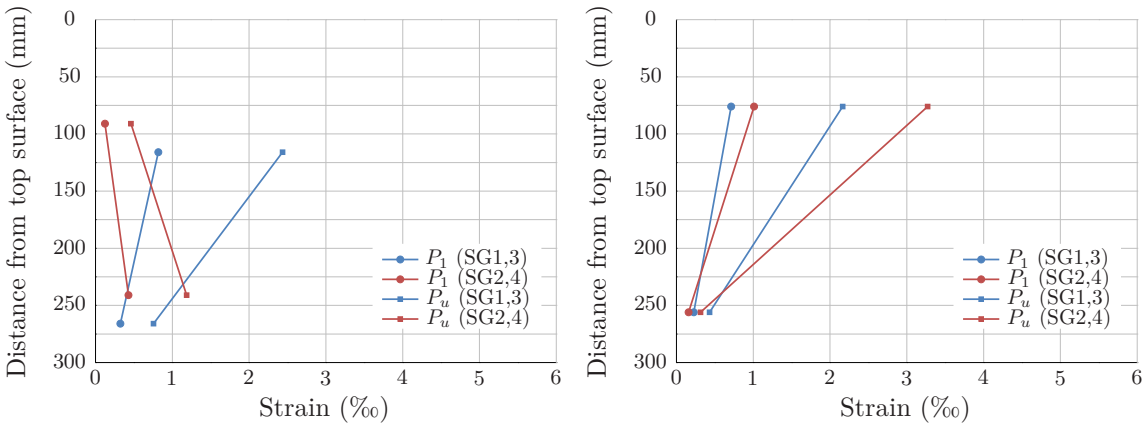

(a) Strain in the spiral **(b)** Strain in the stirrups

Figure 3.59: Specimen P1A - Reinforcement strains along the height of the confined zone

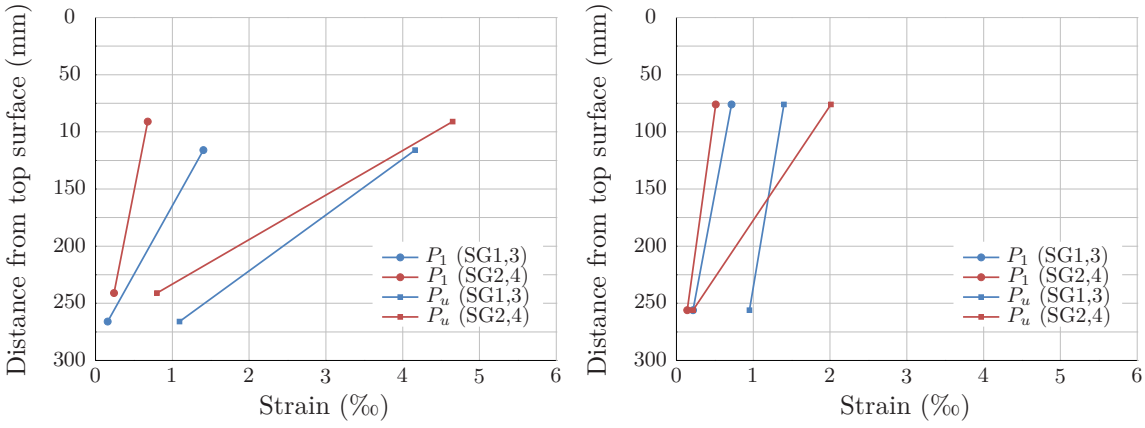

(a) Strain in the spiral **(b)** Strain in the stirrups

Figure 3.60: Specimen P1B - Reinforcement strains along the height of the confined zone

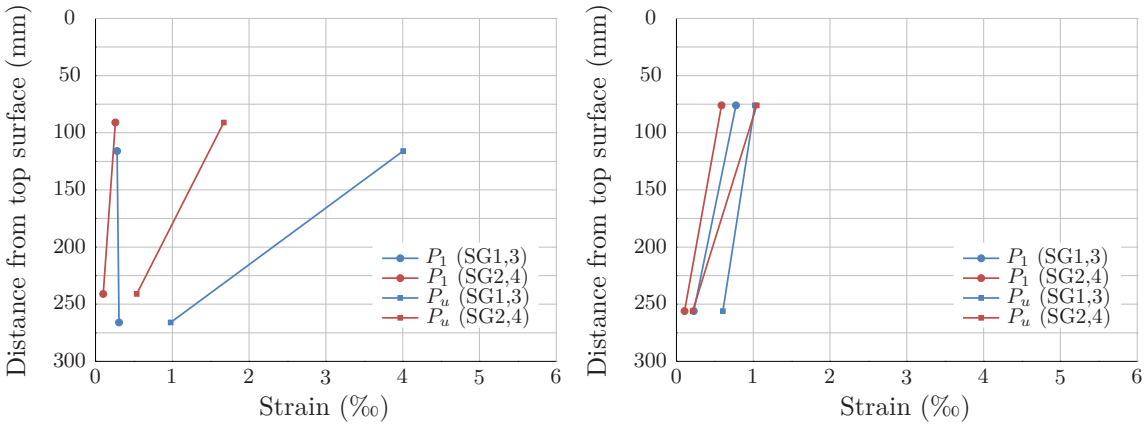

(a) Strain in the spiral **(b)** Strain in the stirrups

Figure 3.61: Specimen P1C - Reinforcement strains along the height of the confined zone

From the analysis of the figures above it can be concluded that in the case where there are, simultaneously, two types of confinement reinforcement, the outer reinforcement is not as effective as the inner one. In fact, the yield strain is only achieved for stirrups in the case of specimen P1A. Therefore, when calculating the bearing strength, the consideration of both spiral and stirrups in confinement can be against safety leading to higher loads, as can be observed in Tables 3.24, 3.25 and 3.26.

It should be noted that, even for the spiral reinforcement, the yield strain is not attained in the farthest zone from the anchorage.

Considering only the spiral confinement, the predicted failure loads given in Tables 3.27, 3.28 and 3.29 are closer to the results obtained from tests, and the only prediction against safety is the one from Niyogi (1975), as shown in Table 3.30.

Specimens P2

In the case of specimens P2, the predicted failure loads of the reinforced concrete specimens and the comparison with experimental values are presented in Tables 3.31, 3.32 and 3.33.

Table 3.31: Ultimate predicted load according to equation (3.16) by Niyogi (1975)

Specimen	a (mm)	a' (mm)	n_{plain} (kN)	p_l	K	$P_{u,pred}$ (kN)	$P_{u,test}/P_{u,pred}$
P2	305	180	2163,7	0,010	55	3327,8	0,78
P2A	305	180	1217,9	0,010	55	1873,2	1,13
P2B/P2C	305	180	1095,1	0,010	55	1684,3	0,89/0,93

Table 3.32: Ultimate predicted load according to equation (3.21) by Roberts (Breen et al., 1991)

Specimen	f_{lat} (kN/m^2)	A_{core} (mm^2)	$P_{u,pred}$ (kN)	$P_{u,test}/P_{u,pred}$
P2	6423,0	19172	2475,0	1,05
P2A	6423,0	19172	1613,8	1,31
P2B/P2C	6423,0	19172	1502,0	1,00/1,04

Table 3.33: Ultimate predicted load according to equation (3.24) by Bonetti (2005)

Specimen	f_{lat} (kN/m^2)	m_r	a'/a	β	α	$P_{u,pred}$ (kN)	$P_{u,test}/P_{u,pred}$
P2	6423,0	4,73	0,59	0,19	1	3200,1	0,81
P2A	6423,0	3,05	0,59	0,19	1	2163,7	0,98
P2B/P2C	6423,0	2,93	0,59	0,19	1	1975,9	0,76/0,79

As can be observed in the above tables, the value of the $P_{u,test}/P_{u,pred}$ ratio for speci-

men P2A presents a significant deviation from the average value in each case. Therefore, the results of this specimen were not included in the calculation of the average, standard deviation and coefficient of variation of the $P_{u,test}/P_{u,pred}$ ratio for specimens P2, presented in Table 3.34.

Table 3.34: Average, standard deviation and coefficient of variation of the $P_{u,test}/P_{u,pred}$ ratio for the analysed authors

Author	μ	σ	C_v
Niyogi	0,87	0,08	0,09
Roberts	1,03	0,03	0,03
Bonetti	0,79	0,03	0,04

Figure 3.62 presents the reinforcement steel strains along the height of the confined zone for specimens P2, P2A, P2B and P2C.

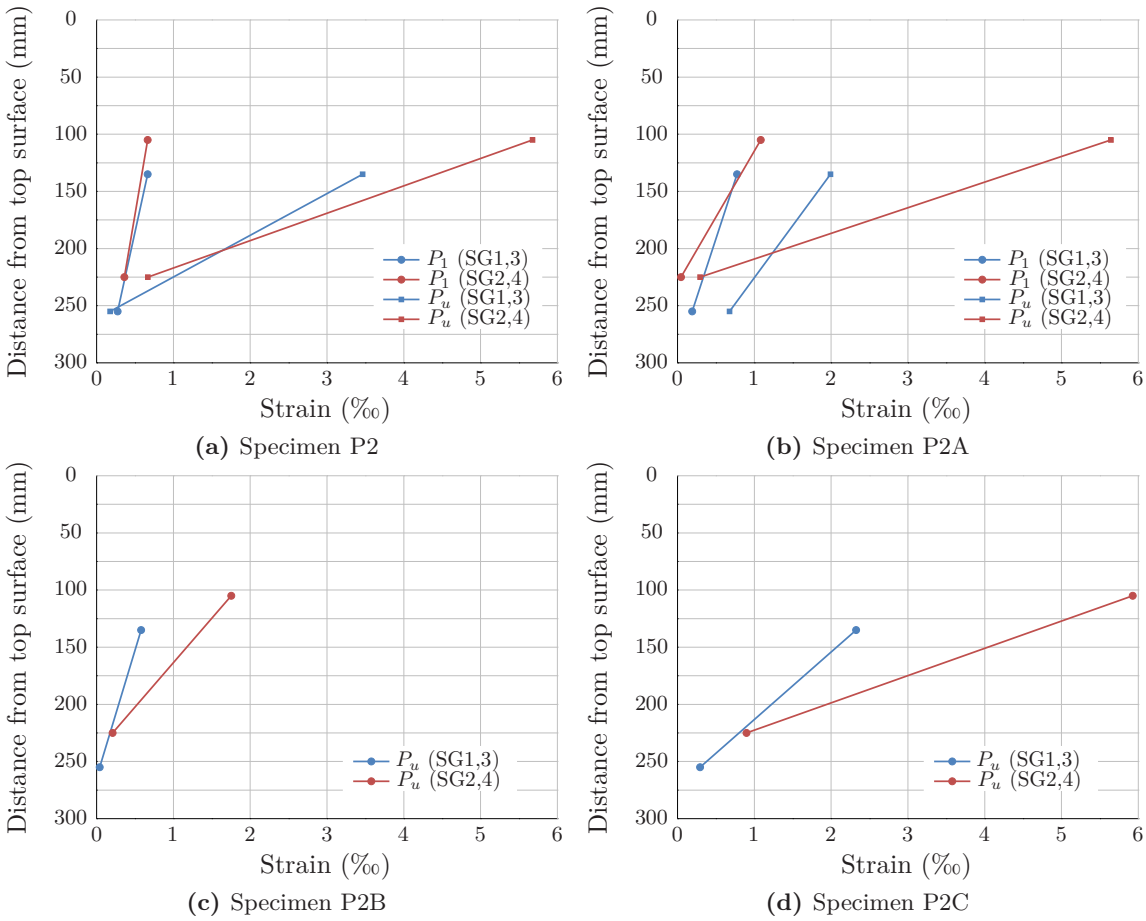

(a) Specimen P2 **(b)** Specimen P2A

(c) Specimen P2B **(d)** Specimen P2C

Figure 3.62: Reinforcement strains along the height of the confined zone

Regarding specimens P2, the only conservative prediction of the breaking load is cal-

culated by applying equation (3.21) by Roberts (Breen et al., 1991).

Also in this case it can be observed that, for the spiral reinforcement, the yield strain is not attained in the farthest zone from the anchorage.

Specimens P6

Tables 3.35, 3.36 and 3.37 present the predicted failure loads of specimens P6 and the comparison with experimental values.

Table 3.35: Ultimate predicted load according to equation (3.16) by Niyogi (1975)

Specimen	a (mm)	a' (mm)	n_{plain} (kN)	p_l	K	$P_{u,pred}$ (kN)	$P_{u,test}/P_{u,pred}$
P6	210	180	2924,4	0,009	55	4442,3	0,58
P6A/P6B	210	180	2546,8	0,009	55	3868,7	0,64/0,62

Table 3.36: Ultimate predicted load according to equation (3.21) by Roberts (Breen et al., 1991)

Specimen	f_{lat} (kN/m^2)	A_{core} (mm^2)	$P_{u,pred}$ (kN)	$P_{u,test}/P_{u,pred}$
P6	3357,2	14524	3120,4	0,83
P6A/P6B	3357,2	14524	2743,3	0,90/0,88

Table 3.37: Ultimate predicted load according to equation (3.24) by Bonetti (2005)

Specimen	f_{lat} (kN/m^2)	m_r	a'/a	β	α	$P_{u,pred}$ (kN)	$P_{u,test}/P_{u,pred}$
P6	1678,6	9,96	0,86	0,06	1	3781,0	0,69
P6A/P6B	1678,6	9,30	0,86	0,06	1	3380,0	0,73/0,71

Table 3.38: Average, standard deviation and coefficient of variation of the $P_{u,test}/P_{u,pred}$ ratio for the analysed authors

Author	μ	σ	C_v
Niyogi	0,61	0,03	0,05
Roberts	0,87	0,04	0,04
Bonetti	0,71	0,02	0,03

For specimens P6, P6A and P6B, the reinforcement strains along the height of the confined zone are illustrated in Figures 3.63, 3.64 and 3.65, respectively.

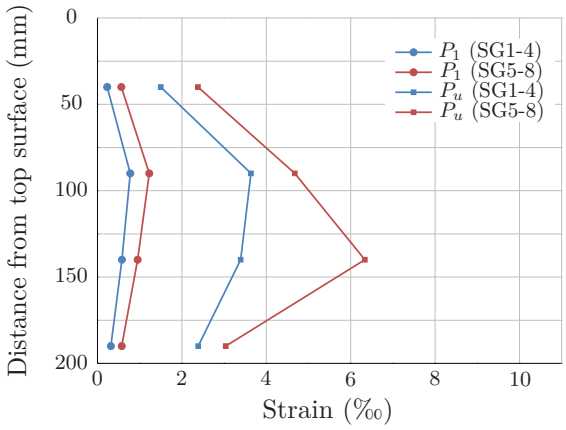

Figure 3.63: Specimen P6 - Reinforcement strains along the height of the confined zone

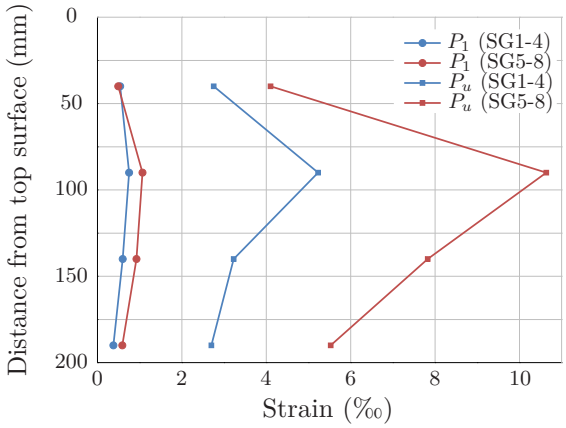

Figure 3.64: Specimen P6A - Reinforcement strains along the height of the confined zone

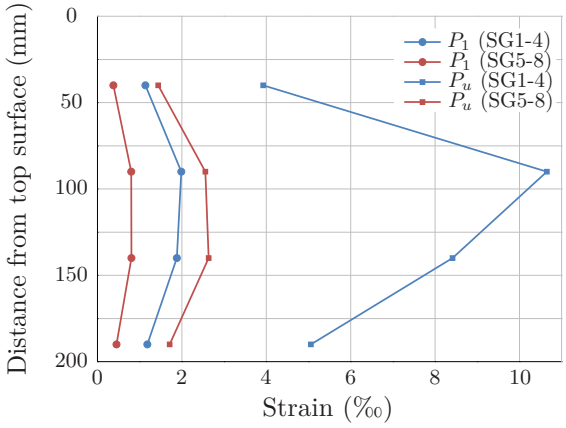

Figure 3.65: Specimen P6B - Reinforcement strains along the height of the confined zone

For the case of specimens P6, the predicted ultimate bearing strength for the analysed specimens is far from experimental values and is overestimated.

One of the causes of the observed differences could be related to the fact that the different confinement reinforcement levels have different strains along the height of the

confined zone, as shown in Figures 3.58 to 3.65, and just some of the reinforcing bars attained yielding. This may lead to non uniform confinement forces along the height, and smaller than the ones considered in the proposed equations.

Besides the confinement force, the use of special anchorage devices instead of simple plates also affects the results.

Thus, it is proposed in this case, to use equation (3.22) by Wollmann and Roberts-Wollmann (2000), for extrapolation of special bearing plate acceptance test results. Equation (3.22) is very similar to equation (3.21) but with a slight modification: the final strength is affected by a coefficient η that allows to adjust the values obtained on the basis of experimental results.

The calibration factor that best fits the experimental values is $\eta = 0{,}83$, lower than the values proposed by Wollmann and Roberts-Wollmann (2000).

3.5 Non-linear analysis

The finite element software ATENA (Cervenka et al., 2014) was used to simulate the behaviour of the prismatic test specimens, in order to assess the parameters to define the materials, for further application in the non-linear analysis of the anchorage blister models.

This software is based on the finite element method and can simulate the most significant non-linear properties of concrete for anchorage zones, such as crack propagation and confinement effect under multi-axial stress state. The reinforcement bars are modelled by truss elements embedded in concrete. The bond slip behaviour can be considered (Cervenka and Ganz, 2014). The concrete constitutive relations are described in Cervenka and Pappanikolaou (2008) and validations are presented in Cervenka and Cervenka (2010) and Cervenka et al. (2011).

3.5.1 Geometry of the models

The model is composed of concrete, steel reinforcement, post-tensioning anchorage (bearing plate and anchor head) and is supported at the bottom surface by a rigid steel base plate.

Taking advantage of the fold symmetry of the specimen, and in order to reduce the computation time, only one quarter of the model was considered and appropriate boundary conditions were adopted on symmetry planes. For this reason, the spiral reinforcement was simulated through quarters of circular levelled hoops.

The load was applied on the top of the anchor head by imposing a vertical displacement in increments of 0,05 mm.

The concrete, bearing plate and anchor head were modelled by volume macroelements, meshed independently in tetrahedra and brick volume elements of about 10 mm on the top of the model (that corresponds to the failure region) and gradually increased to 30 mm on the bottom, resulting in a total of 24443 elements in ORC specimens and 19942 elements in HPFRC specimens. Incompatible meshes are allowed on interfaces between macroelements. The kinematic relations between nodes of incompatible meshes are ensured by the master-slave method. The master-slave method also ensures that the discrete reinforcement bars are fixed to the surrounding solid element (Cervenka et al., 2014).

Figure 3.66 show the numerical models for ORC and HPFRC specimens, respectively.

(a) Specimens P1 and P2 **(b)** Specimens P5 and P6

Figure 3.66: Numerical models of prismatic specimens

3.5.2 Mechanical properties of materials

3.5.2.1 Concrete

ATENA software considers, for concrete, a fracture-plastic model that combines constitutive models for tensile (fracturing) and compressive (plastic) behaviour. In compression, the ascending branch is elliptical and its law is based on strains, while the descending branch is linear and based on displacements (Cervenka et al., 2014).

Table 3.39 presents the concrete mechanical properties used in ATENA models.

Table 3.39: Concrete mechanical properties used in the models

Specimens	Concrete type	f_{cm} (MPa)	f_{ctm} (MPa)	G_f (N/m)	E_{cm} (GPa)
P1	ORC	52,2	4,1	102,5	32,5
P1A	ORC	29,4	2,9	71,3	27,4
P1B and P1C	ORC	27,8	2,5	62,5	26,9
P2	ORC	52,2	4,1	102,5	32,5
P2A	ORC	29,4	2,9	71,3	27,4
P2B and P2C	ORC	26,4	2,3	58,1	26,5
P5	HPFRC	122,0	12,2	305,0	43,5
P5A and P5B	HPFRC	116,7	10,0	249,8	41,7
P6	HPFRC	112,3	8,6	216,0	44,6
P6A and P6B	HPFRC	97,8	7,9	198,0	41,9

The fracture energy of concrete (G_f) was determined using the equation (3.33), proposed by Vos (1983):

$$G_f = 0,000025 f_{ctm} \tag{3.33}$$

The modulus of elasticity of concrete (E_{cm}) was estimated from the compressive strength, using equation (3.34), recommended in EN 1992-1-1 (2004), reduced by 10% due to the use of limestone aggregates.

$$E_{cm} = 22 \left(\frac{f_{cm}}{10} \right)^{0,3} \tag{3.34}$$

Still concerning to concrete, Table 3.40 presents the other properties adopted.

Table 3.40: Concrete characteristics of the test specimens used in the models

Concrete type	ν	w_d (mm)	ε_{cp}	$r_{c,lim}$	S_F	e	β
ORC	0,20	-0,5	-1,5‰	0,8	-20,0	-0,52	0,40
HPFRC	0,20	-0,075	-3,5‰	0,8	-20,0	-0,52	0,70

In Table 3.40, and according to Cervenka et al. (2014),

ν is the Poisson's ratio;
w_d is the critical compressive displacement, i.e., the plastic displacement that defines the end point of the descending softening curve of the concrete constitutive law;
ε_{cp} is the plastic strain that corresponds to the compressive strength in the ascending curve of the concrete constitutive law;
$r_{c,lim}$ is the minimum value of the reduction of compressive strength due to cracks;
S_F is the crack shear stiffness factor, i.e., is a shear factor coefficient that defines a relationship between the normal and shear crack stiffness;
e is the failure surface eccentricity and defines the roundness of the failure surface;
β is the multiplier for the plastic flow direction (if $\beta < 0$ the material is being compacted during crushing, if $\beta = 0$ the material volume is preserved, and if $\beta > 0$ the material is dilating).

It was considered a fixed crack model coefficient of 1,00, that means that the crack direction is given by the principal stress direction at the moment of the crack initiation. During further loading this direction is fixed (Cervenka et al., 2014). The rotated cracks are only recommended for very large finite elements (shells) subjected to load of changing direction (Dobromil and Cervenka, 2015).

3.5.2.2 Steel reinforcement

The mechanical properties of the steel reinforcement considered in the numerical models are specified in Table 3.41.

Table 3.41: Steel reinforcement mechanical properties

Specimens	f_y (MPa)	f_u (MPa)	ε_u	E_s (GPa)
P1	542	657	10,9%	200
P2	561	673	11,4%	200
P6	564	667	11,6%	200

3.5.2.3 Bond-slip relations

The bond of reinforcement was considered, using the bond model recommended in the Model Code 2010 (2012). The relation between the bond stress (τ) and the slip (relative displacement of steel and concrete cross-section) is presented in Figure 3.67.

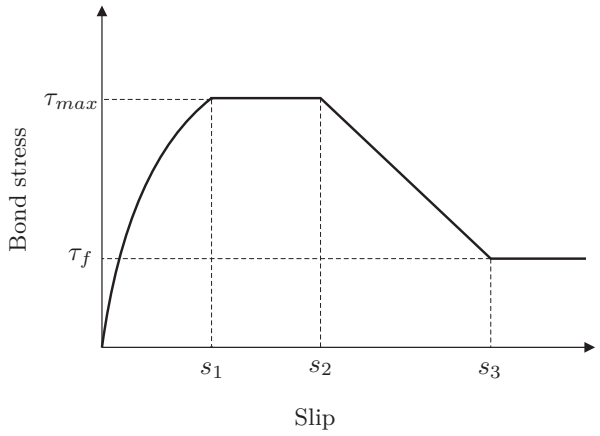

Figure 3.67: Analytical bond stress-slip relationship (Model Code 2010, 2012)

The relation presented above is defined by equation (3.35) and the parameters shown are given in Table 3.42.

$$\tau_0 = \tau_{max}(s/s_1)^{\alpha} \quad \text{for} \quad 0 \leq s \leq s_1 \tag{3.35a}$$

$$\tau_0 = \tau_{max} \quad \text{for} \quad s_1 \leq s \leq s_2 \tag{3.35b}$$

$$\tau_0 = (\tau_{max} - \tau_f)\,(s - s_2)\,(s_3 - s_2) \quad \text{for} \quad s_2 \leq s \leq s_3 \tag{3.35c}$$

$$\tau_f \quad \text{for} \quad s_3 < s \tag{3.35d}$$

Table 3.42: Parameters for defining the mean bond stress-slip relationship of deformed bars (Model Code 2010, 2012)

τ_{max}	s_1	s_2	s_3	α	τ_f
$2,5\sqrt{f_{ck}}$	1,0 mm	2,0 mm	c_{clear}	0,4	$0,40\tau_{max}$

In Table 3.42, above, c_{clear} is the clear distance between ribs of the reinforcement bars.

The values adopted for the parameters of the mean bond stress-slip relationship, are shown in Table 3.43.

Table 3.43: Parameters used in the definition of the mean bond stress-slip relationship

Specimen	f_{cm} (MPa)	τ_{max} (MPa)	τ_f (MPa)	ϕ_{long} (mm)	s_3 (mm)
P1	52,2	18,1	7,2	12	7,2
P1A	29,4	13,6	5,4	12	7,2
P1B and P1C	27,8	13,2	5,3	12	7,2
P2	52,2	18,1	7,2	10	6,5
P2A	29,4	13,6	5,4	10	6,5
P2B and P2C	26,4	12,8	5,1	10	6,5
P6	112,3	26,5	10,6	6	5,0
P6A and P6B	97,8	24,7	9,9	6	5,0

The mean bond stress-slip relationships considered are presented in Figures 3.68, 3.69 and 3.70, for specimens P1, P2 and P6, respectively.

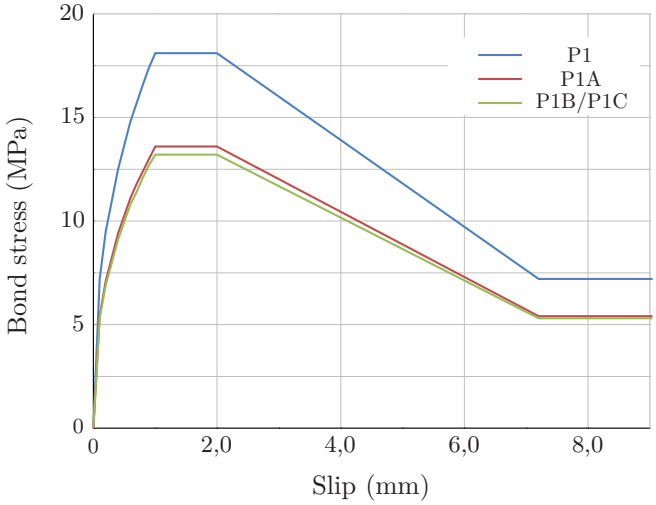

s	τ (MPa)		
(mm)	P1	P1A	P1B/P1C
0,0	0,0	0,0	0,0
0,2	9,6	7,1	6,9
0,4	12,5	9,4	9,1
0,6	14,8	11,1	10,8
1,0	18,1	13,6	13,2
2,0	18,1	13,6	13,2
7,2	7,2	5,4	5,3

Figure 3.68: Specimens P1 - mean bond stress-slip relationships

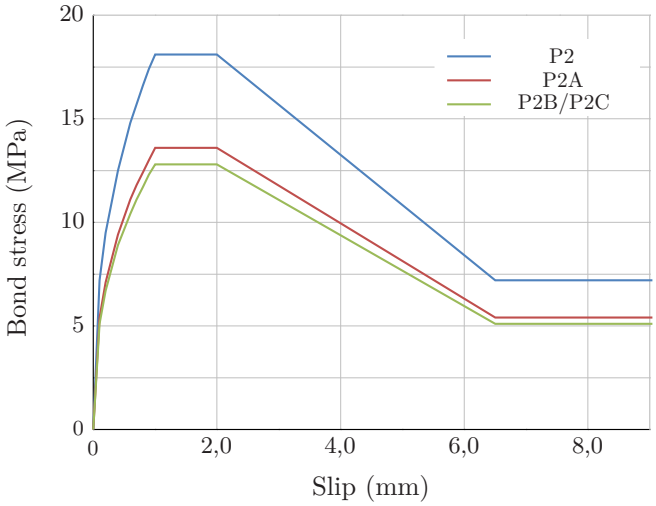

s	τ (MPa)		
(mm)	P2	P2A	P2B/P2C
0,0	0,0	0,0	0,0
0,2	9,6	7,1	6,7
0,4	12,5	9,4	8,9
0,6	14,8	11,1	10,4
1,0	18,1	13,6	12,8
2,0	18,1	13,6	12,8
6,5	7,2	5,4	5,1

Figure 3.69: Specimens P2 - mean bond stress-slip relationships

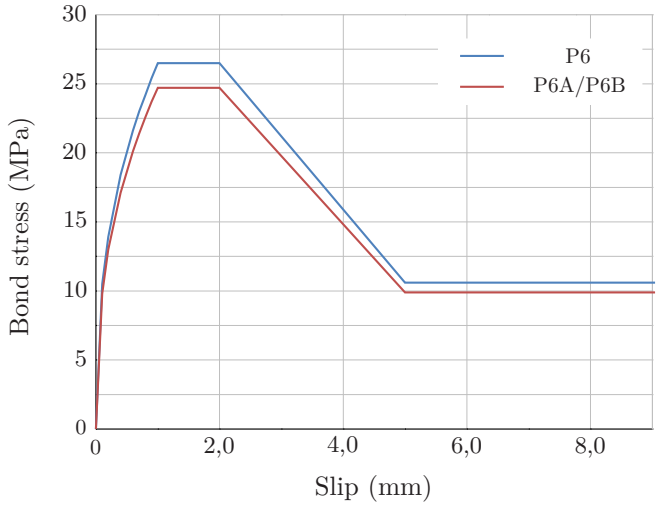

s	τ (MPa)	
(mm)	P6	P6A/P6B
0,0	0,0	0,0
0,2	13,9	13,0
0,4	18,4	17,1
0,6	21,6	20,1
1,0	26,5	24,7
2,0	26,5	24,7
5,0	10,6	9,9

Figure 3.70: Specimens P6 - mean bond stress-slip relationships

3.5.2.4 Anchorage steel

For modelling the anchor head a elastic-plastic material without hardening was chosen. The main properties considered are listed in Table 5.26.

Table 3.44: Characteristics of the anchorage steel

f_y (MPa)	E_s (GPa)	ν
250	210	0,30

3.5.2.5 Anchorage steel/concrete interface

The characteristics of the anchorage steel/concrete interface used in the models entails the following parameters whose values are presented in Table 3.45: normal stiffness (K_{nn}), tangential stiffness (K_{tt}), tensile strength ($f_{t,int}$), cohesion (c), friction coefficient (μ), minimum normal stiffness ($K_{nn,min}$) and minimum tangential stiffness ($K_{tt,min}$).

Table 3.45: Characteristics of the anchorage steel/concrete interface

K_{nn} (MN/m^3)	K_{tt} (MN/m^3)	$f_{t,int}$ (MPa)	c (GPa)	μ	$K_{nn,min}$ (MN/m^3)	$K_{tt,min}$ (MN/m^3)
200×10^6	200×10^6	1,0	1,0	0,2	200×10^3	200×10^3

3.5.3 Results of the numerical models

3.5.3.1 ORC Specimens

Figure 3.71 shows the comparison between the load-displacement relations of experimental and numerical models, for specimens P1.

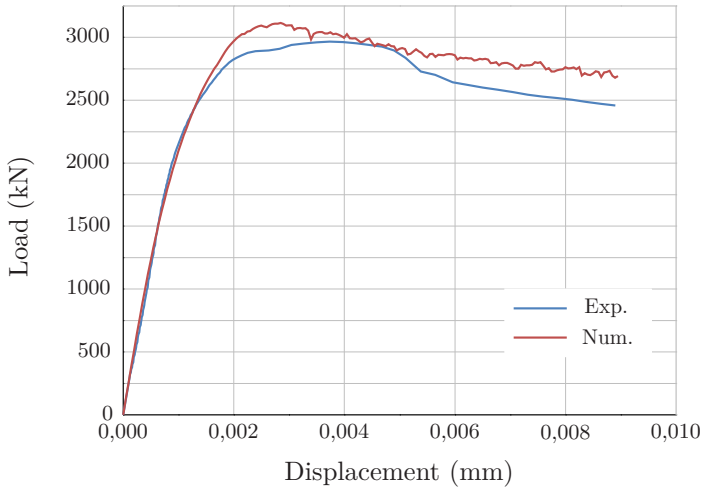

(a) Specimen P1

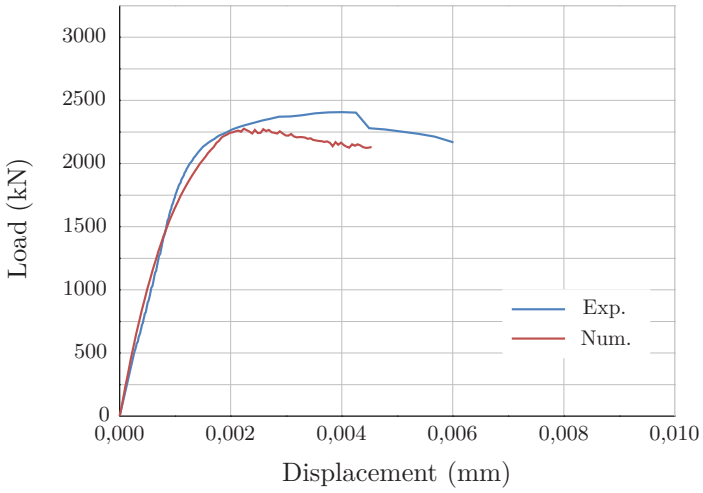

(b) Specimen P1A

Figure 3.71: Specimens P1 - Experimental and numerical load vs displacement relations

For specimens P1, the values obtained for the failure load in numerical models and his comparison with the experimental values are presented in Table 3.46.

Table 3.46: Comparison between the experimental and numerical failure load for specimens P1

Specimen	$P_{u,test}$ (kN)	$P_{u,num}$ (kN)	$P_{u,test}/P_{u,num}$
P1	2965,8	3114,8	0,95
P1A	2406,6	2275,6	1,06
P1B	2460,0	2266,8	1,09
P1C	2504,9	2266,8	1,11

In the case of specimens P2, the comparison between the load-displacement relations of experimental and numerical models, can be seen in Figures 3.71. Table 3.47 presents the comparison between the experimental and numerical failure load.

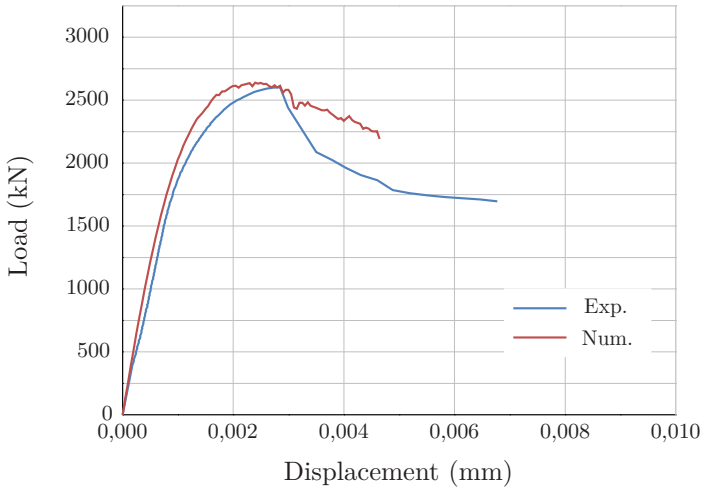

(a) Specimen P2

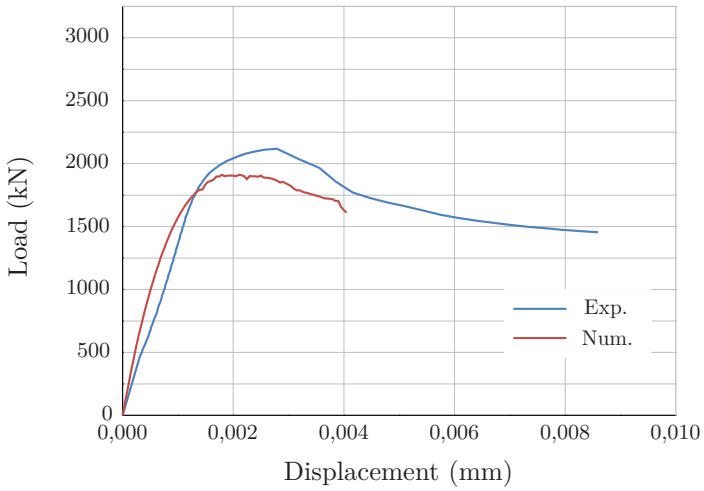

(b) Specimen P2A

Figure 3.72: Specimens P2 - Experimental and numerical load vs displacement relations

Table 3.47: Comparison between the experimental and numerical failure load for specimens P2

Specimen	$P_{u,test}$ (kN)	$P_{u,num}$ (kN)	$P_{u,test}/P_{u,num}$
P2	2604,3	2640,4	0,98
P2A	2118,3	1912,0	1,11
P2B	1495,8	1821,6	0,82
P2C	1563,5	1821,6	0,86

3.5.3.2 HPFRC Specimens

The comparison between the load-displacement relations of experimental and numerical models, for specimens P5, is presented in Figures 3.73a.

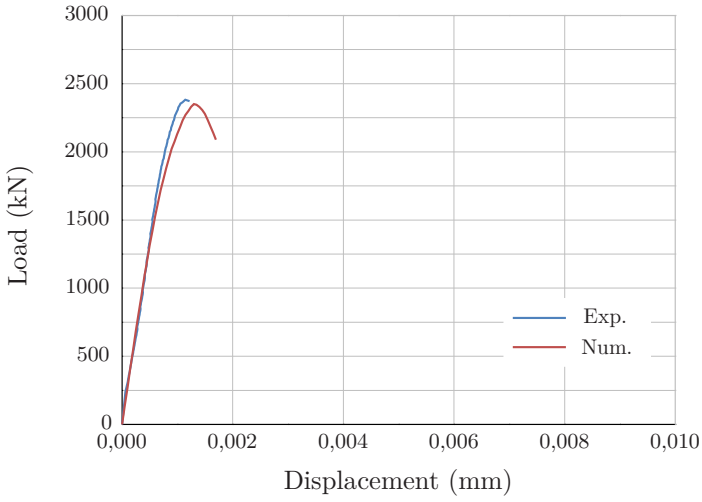

(a) Specimen P5

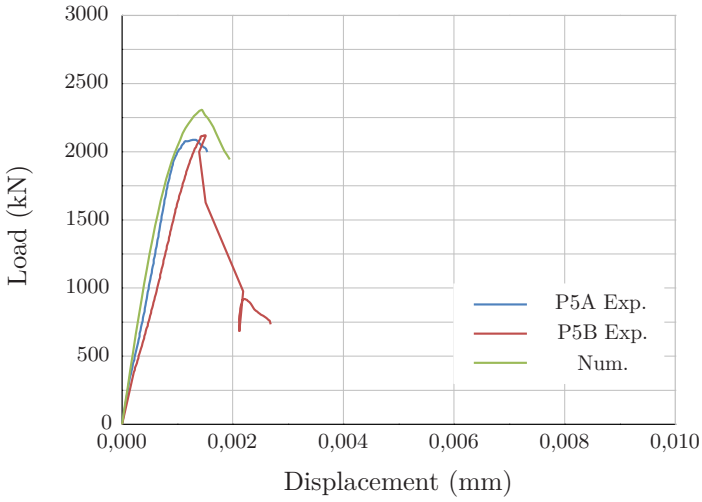

(b) Specimens P5A and P5B

Figure 3.73: Specimens P5 - Experimental and numerical load vs displacement relations

Table 3.48: Comparison between the experimental and numerical failure load for specimens P5

Specimen	$P_{u,test}$ (kN)	$P_{u,num}$ (kN)	$P_{u,test}/P_{u,num}$
P5	2367,0	2351,2	1,01
P5A	2087,9	2308,0	0,90
P5B	2117,4	2308,0	0,92

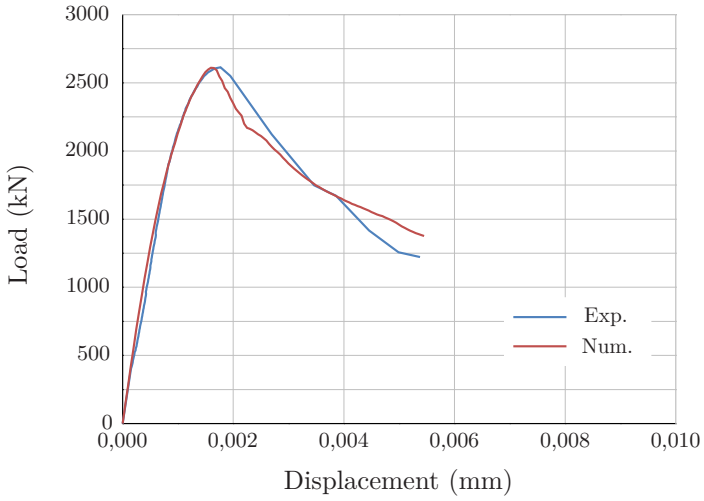

(a) Specimen P6

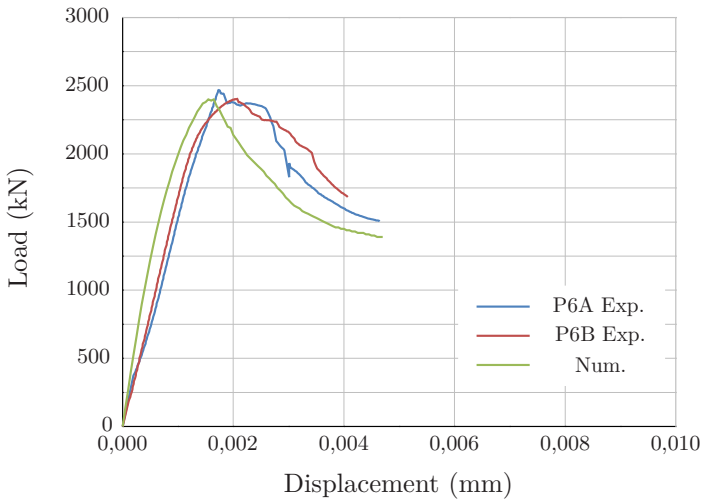

(b) Specimens P6A and P6B

Figure 3.74: Specimens P6 - Experimental and numerical load vs displacement relations

Table 3.49 presents the values obtained for the failure load in numerical models and his comparison with the experimental values, for specimens P6.

Table 3.49: Comparison between the experimental and numerical failure load for HPFRC specimens

Specimen	$P_{u,test}$ (kN)	$P_{u,num}$ (kN)	$P_{u,test}/P_{u,num}$
P6	2593,0	2610,4	0,99
P6A	2371,1	2400,4	0,99
P6B	2403,8	2400,4	1,01

3.5.3.3 Conclusions on the non-linear analysis

The calibration of the parameters shown in Table 3.40, in order to simulate the experimental tests, has proved to be an extremely slow process, given that the analysis running time of the models until failure was approximately four days for ORC specimens and two days for HPFRC specimens.

The values presented in Tables 3.46 and 3.47, show that the failure loads obtained in the non linear analysis of the ORC specimens are close to the experimental values. The proximity is greater for the case of specimens where the concrete strength is higher (specimens P1 and P2).

As shown in Figures 3.71 and 3.72, the initial stiffness obtained in the numerical models is similar to that obtained in the tests, except for specimen P2A.

For HPFRC specimens, the failure loads obtained in the non linear analysis are very close to the experimental tests, having a maximum difference of only 1% for specimens P6 (see Tables 3.48 and 3.49).

In this case, there is also a good approximation between the initial stiffness obtained by nonlinear analysis and by the experimental tests, as can be seen in Figures 3.73 and 3.74.

3.6 Conclusions

In this chapter, the experimental program carried out to assess both ultimate capacity and adequate serviceability of the local anchorage zone, using a high performance fibre reinforced concrete was described. A comparison of the experimental results with models found in the literature was presented and discussed. A non-linear analysis of the tested specimens was presented and the results were compared with the experimental tests.

Experimental program

Regarding the load transfer tests, from the analysis of the results it can be concluded that the failure load of the specimens increased and the crack width decreased with increasing concrete compressive and tensile strengths, for specimens with identical type and amount of reinforcement.

For the type of anchorage utilised, if the same concrete section is used as specified for the ordinary reinforced concrete specimens, the use of HPFRC allows the suppression of the confining reinforcement. The reduction of the concrete cross-section and of the confining reinforcement is also allowed if using HPFRC. The suppression of all the confining reinforcement is however not advisable, since the non-randomness of fibre orientation can lead to formation of cracks with unacceptable width.

The concrete tensile strength proved to be very important in the resistance of the local zone.

Comparison of the experimental results with models found in the literature

From the comparison of the results of the experimental tests with the models of Niyogi (1973), (Breen et al., 1991) and Bonetti (2005), for unreinforced concrete specimens, can be observed that the predicted failure loads were significantly higher than those obtained in laboratory tests. The main reason was the use of special anchorage devices instead of simple plates, for which the used equations were assessed.

The formulation proposed by Bonetti (2005) was the one that provided the most exact result which was obtained for specimen P4 without fibers in its composition and having consequently a very low tensile strength compared to the compressive strength.

Regarding specimens P5, Niyogi (1973) and Roberts (Breen et al., 1991) were the ones that were closer to the experimental results providing, however, non-conservative loads. It should be noted that the equation proposed by Niyogi (1973) does not take into account the existence of post-tensioning duct and the value of the concrete tensile strength.

For the reinforced concrete specimens, the models of Niyogi (1975), Roberts (Breen et al., 1991) and Bonetti (2005) were considered.

In the case where there were, simultaneously, two types of confinement reinforcement (specimens P1), the outer reinforcement was not as effective as the inner one. In fact, the yield strain was only achieved for stirrups in the case of specimen P1A. Therefore, when calculating the bearing strength, the consideration of both spiral and stirrups in confinement was against safety leading to higher loads. Considering only the spiral confinement,

the predicted failure loads were closer to the results obtained from tests, and the only prediction against safety was the one from Niyogi (1975).

Regarding specimens P2, the only conservative prediction of the breaking load was calculated by applying the formulation by Roberts (Breen et al., 1991). Also in this case it could be observed that, for the spiral reinforcement, the yield strain was not attained in the farthest zone from the anchorage.

For the case of specimens P6, the predicted ultimate bearing strength for the analysed specimens was far from experimental values and was overestimated.

One of the causes of the observed differences could be related to the fact that the different confinement reinforcement levels had different strains along the height of the confined zone, and just some of the reinforcing bars attained yielding. This may lead to non uniform confinement forces along the height, and smaller than the ones considered in the proposed equations. Besides the confinement force, the use of special anchorage devices instead of simple plates also affects the results.

In the case of reinforced HPFRC specimens (specimen P6) it is proposed to use equation (3.22) by Wollmann and Roberts-Wollmann (2000), for extrapolation of special bearing plate acceptance test results with a calibration factor of $\eta = 0{,}83$.

Non-linear analysis

The non-linear analysis was used to simulate the behaviour of the prismatic test specimens, in order to assess the parameters to define the materials, for further application in the non-linear analysis of the anchorage blister models.

The calibration of the parameters shown in Table 3.40 has proved to be an extremely slow process, given that the analysis running time of the models until failure was approximately four days for ORC specimens and two days for HPFRC specimens.

The failure loads obtained in the non linear analysis of the ORC specimens were close to the experimental values. The proximity was greater for the case of specimens where the concrete strength was higher (specimens P1 and P2). The initial stiffness obtained in the numerical models was similar to that obtained in the tests, except for specimen P2A.

For HPFRC specimens, the failure loads obtained in the non linear analysis were very close to the experimental tests, having a maximum difference of only 1% for specimens P6. In this case, there was also a good approximation between the initial stiffness obtained by nonlinear analysis and by the experimental tests.

Chapter 4

Design of the Anchorage Corner Blisters

4.1 Introduction

In order to study the behaviour of anchorage blisters regarding the transmission of stresses to the web and the bottom slab of the girder, as well as the feasibility of using high performance concrete only in the blister, two half scale models of the inferior corner of a box girder existing bridge were studied: a reference specimen of ordinary reinforced concrete (ORC) and a high performance fibre reinforced concrete (HPFRC) blister specimen.

The specimens were self-balanced with anchorages at both ends of the tendons and included a corner blister for two anchorages with a portion of the slab and the contiguous web. With exception of the dimensions of the anchorage blister, the two models had the same geometry. In the HPFRC blister specimen, the section of the blister was reduced.

The design of the reinforcement of the specimens was based in the tensile forces obtained with strut-and-tie models. The strut-and-tie models were developed taking into consideration the stress fields obtained from a linear-elastic analysis.

This chapter begins with a literature review on developments on strut-and-tie models.

Then, the studied models are described regarding the choice of geometry and layout of the prestressing tendons. The results of the elastic analysis are shown and the developed strut-and-tie models are presented and justified. Based on the strut-and-tie models the calculation of reinforcement is explained and detailed.

Finally, the models used on the non-linear analysis are presented and the results are discussed.

4.2 Literature review

4.2.1 Strut-and-tie models

The first truss structures were built of timber, probably during the early Bronze Age (about 2500 b.c.). Trusses were also usually used by ancient Greeks and Romans in roofing.

The first known written plans of timber trusses date back to the 15th and 16th centuries (Bamonte et al., 2001). Andrea Palladio, in his treatise "Il quattro libri dell'Architettura" (Palladio, 1570) describes a few timber bridges of his own design, as the Cismone river bridge shown in Figure 4.1, a 36 m span bridge that was actually built.

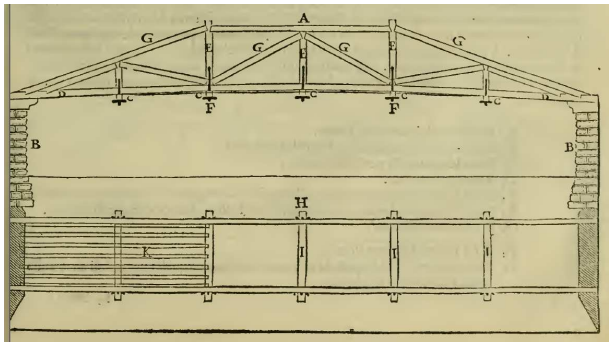

Figure 4.1: The Cismone River bridge (extracted from Palladio, 1570)

Figure 4.2 illustrates three more truss bridge plans presented by Palladio (1570) as "inventions" without any reference to a specific location.

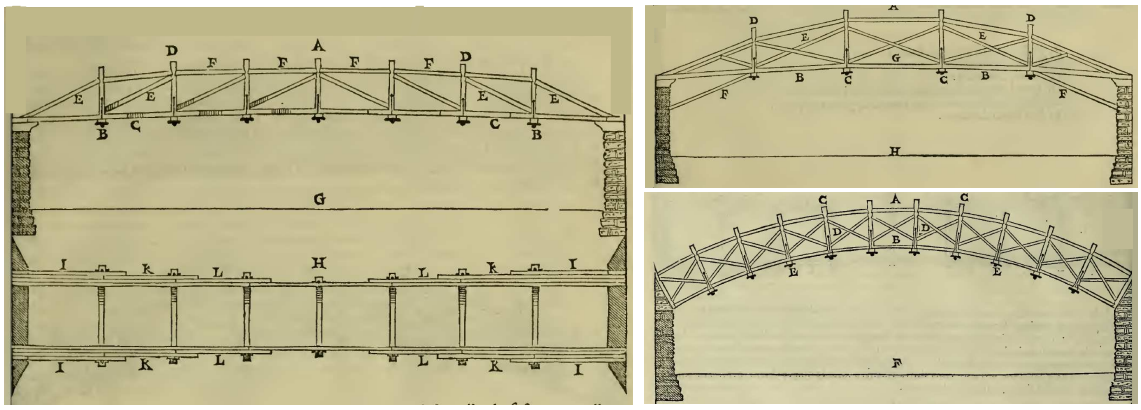

Figure 4.2: Drawings of Palladio's "inventiones" (extracted from Palladio, 1570)

Strut and tie models for shear design of reinforced concrete beams were initially introduced by Hennebique, based in his monolithic reinforced concrete construction system.

François Hennebique obtained a French Patent on 8 August 1892 (Hennebique, 1892), entitled "Combinaison particulière du métal et du ciment en vue de la création de poutraisons trés légères". In this patent, whose drawings are shown in Figure 4.3, Hennebique describes his construction system, whose main characteristic is the use of longitudinal plain round iron bars in the bottom of beams and slabs to provide tensile resistance, since concrete resisted compression on the top of the elements, and connection of compressed and tensile parts by stirrups (U-shaped metallic elements) which also provided shear resistance (LBA, 1901).

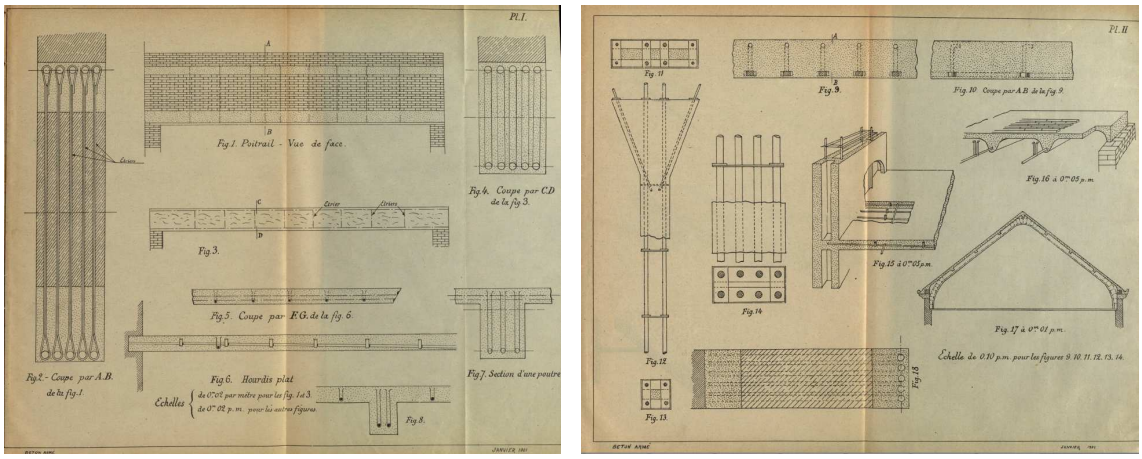

Figure 4.3: Hennebique patent on reinforced concrete (extracted from Hennebique, 1892)

The invention was improved with the complementary patents of 7 August 1893 (redefining the stirrup) and 18 December 1897 ("Dispositif de poutre continue sur plusieurs appuis"), the latter illustrated in Figure 4.4.

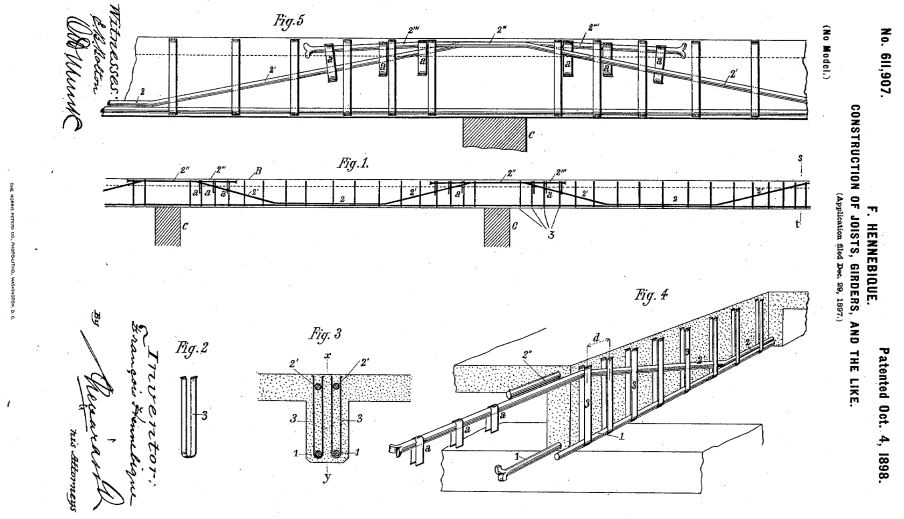

Figure 4.4: Hennebique's patent on continuous beams (extracted from Hennebique, 1897)

In January 1899, in the Third Congress of Reinforced Cement Concrete, Hennebique made the comparison between a reinforced concrete beam and a lattice girder: "Si l'on compare les 2 figures: il est facile de saisir la similitude de la composition des résistances et de la répartition du travail. La barre du bas et les étriers dans la poutre en béton armé sont tendues. Le béton de la partie supérieure de la poutre et le béton entre les étriers sont comprimés.(...) L'etrier avec la barre courbe ont pour mission de résister à l'effort tranchant." (extracted from LBA 1899a). At the same Congress, Hennebique also claimed that beam failures were characterised by the appearing of a inclined crack, with a maximum angle of 45°, near the inner edge of the support (LBA, 1899b).

In February 1899, W. Ritter (1899), professor at the École Polytechnique Fédérale de Zurich, published a paper entitled "Die Bauweise Hennebique" about Hennebique's monolithic reinforced concrete construction system. In this paper, the author describes the system and the inventor's calculation method for the design of reinforcement.

Concerning shear and, more specifically, stirrups design, Ritter affirms "Following Hennebique's intuition, the flat iron stirrups, which are placed around the rods, should absorb the shear forces. Here one usually assumes that the stirrups together with the rods and the concrete form a kind of truss (...), in which the stirrup represents the ties and the concrete, acting in the direction of the diagonal dotted lines, represents the struts. These lines are, according to the compression curves, assumed to be at an angle of 45°." (translated from Ritter, 1899) and presents the truss model, shown in Figure 4.5.

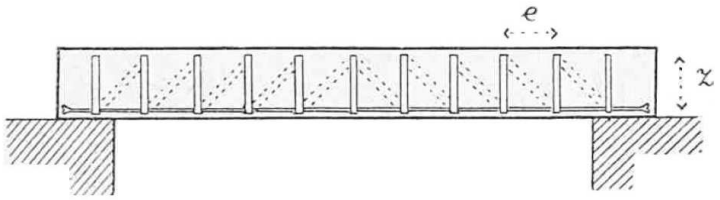

Figure 4.5: Hennebique's truss model (extracted from Ritter, 1899)

Ritter also presented the equation 4.1 derived from the truss model, that was used by Hennebique for stirrups design.

$$Q = 2 \cdot \sigma \cdot b \cdot d \tag{4.1}$$

where Q is the shear force and b and d the width and thickness of the flat steel bars of the stirrup.

According to the author, the factor 2 in the equation was based on the fact that each stirrup had two legs, despite the inventor's strange opinion in which half of the shear stresses were taken by the round bars.

In line with equation 4.1, Hennebique assumed that the diagonal compressive stresses would act at a 45° angle, ie the spacing e of the vertical ties and the lever arm z of the internal forces had the same value. So, Ritter proposed the general equation 4.2 to evaluate stirrups stresses:

$$\sigma = \frac{Q \cdot e}{2 \cdot b \cdot d \cdot z} \tag{4.2}$$

The author concludes: "That stirrups increase the carrying capacity of the beam in the vertical direction, it can hardly be denied, but to what extent the above formula reflects the reality, it may be difficult to determine theoretically. Experimental comparative tests would be necessary." (translated from Ritter, 1899).

In 1903, Emil Mörsch, in the service of the company Wayss & Freytag, performed a series of four tests on T-beams, shown in Figure 4.6, with the aim of clarifying the role of stirrups and the assumption of its replacement by appropriate arrangement of the main reinforcement.

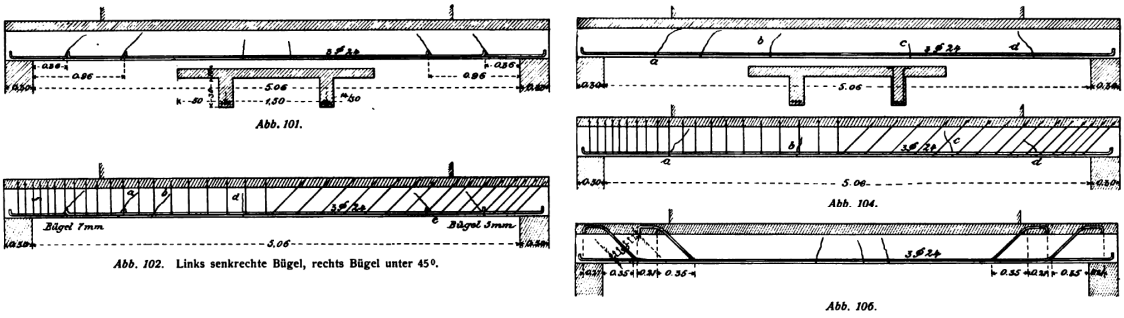

Figure 4.6: Mörsch first test specimens (extracted from Mörsch and Wayss & Freytag, AG, 1906)

Tests results were presented in 1906, in the second edition of *Der Eisenbetonbau: Seine Theorie und Anwendung* (Mörsch and Wayss & Freytag, AG, 1906). Mörsch concluded that with a convenient arrangement of the main reinforcement to resist shear stresses stirrups were not necessary, although, stirrups had the advantage of connecting the beam and the slab in case of any interruptions during casting. The author also concluded that test results demonstrated the importance of the bent longitudinal bar for the transfer of shear forces. Nevertheless, it was recognised the need for further shear tests (Mörsch and Wayss & Freytag, AG, 1906, p. 133).

In April 1907, Mörsch published the results of one more series of experimental tests on T-beams performed near the end of 1906 with the aim of studying the action of stirrups (Mörsch, 1907a, Mörsch, 1907b, Mörsch, 1907c). The beams where designed to fail by shear in the rib. Figures 4.7, 4.8, 4.9 and 4.10 illustrate the tested specimens as well as the cracks representation of the specimens after tests.

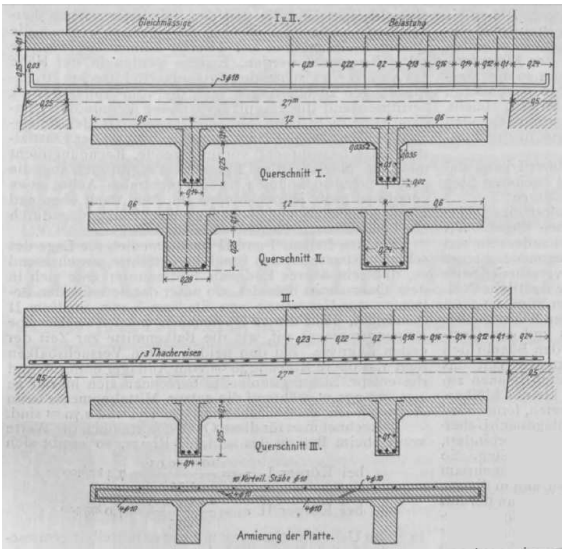

(a) Test specimens definition

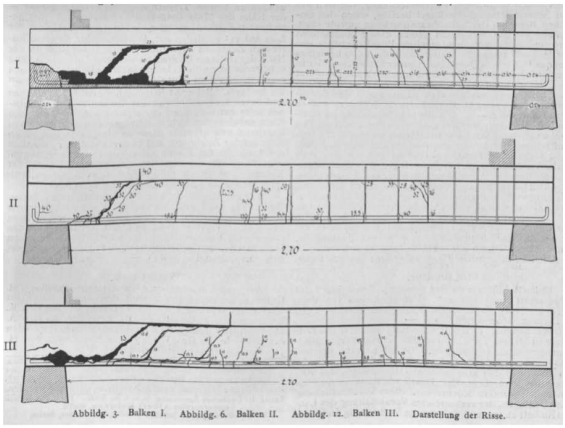

(b) Specimens after test (cracks representation)

Figure 4.7: Mörsch 1906 test specimens I, II and III (extracted from Mörsch, 1907a)

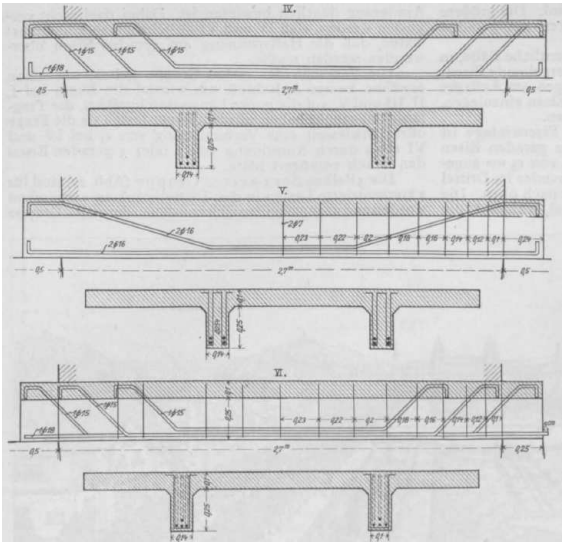

(a) Test specimens definition

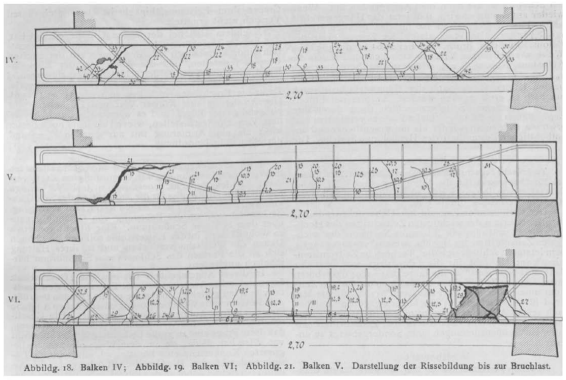

(b) Specimens after test (cracks representation)

Figure 4.8: Mörsch 1906 test specimens IV, V and VI (extracted from Mörsch, 1907b)

These tests were also presented in the third edition of *Der Eisenbetonbau: Seine Theorie und Anwendung* (Mörsch, 1908).

According to the author, the reinforced concrete beams could be considered as trusses with single or double strut systems, as shown in Figure 4.11, where the diagonal concrete strips represented the continuous field of diagonal compression (Mörsch, 1907b, p. 224).

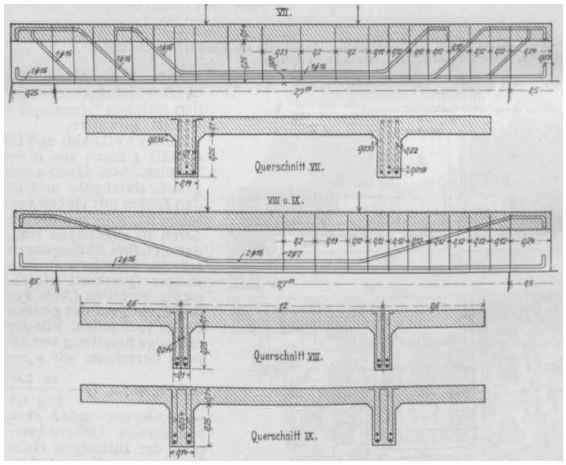

(a) Test specimens definition

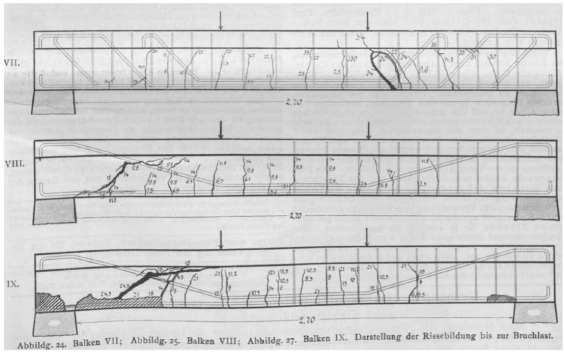

(b) Specimens after test (cracks representation)

Figure 4.9: Mörsch 1906 test specimens VII, VIII and IX (extracted from Mörsch, 1907b)

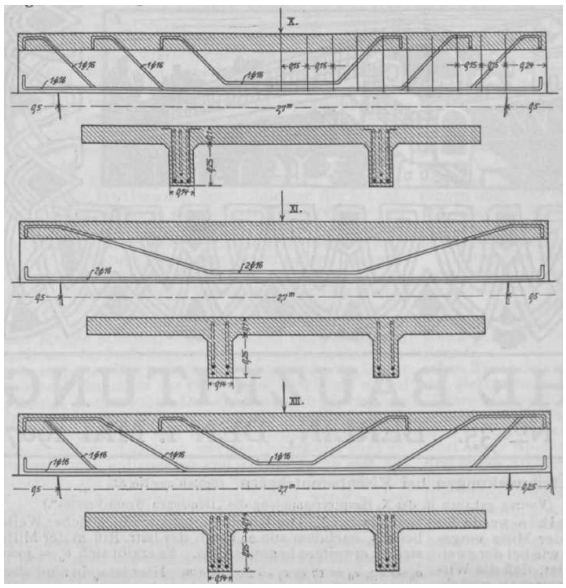

(a) Test specimens definition

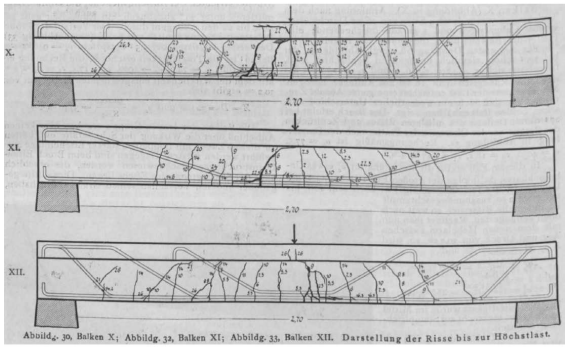

(b) Specimens after test (cracks representation)

Figure 4.10: Mörsch 1906 test specimens X, XI and XII (extracted from Mörsch, 1907c)

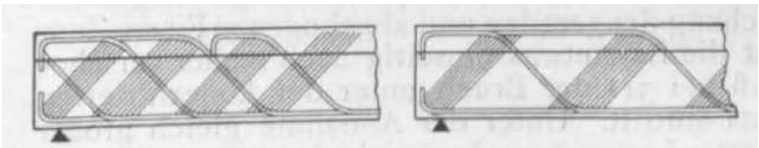

Figure 4.11: Mörsch truss model (extracted from Mörsch, 1907b)

From test results, Mörsch concluded "With respect to the stirrup I reconfirmed my formerly expressed opinion that, with proper arrangement of the main reinforcement,

stirrup have no special static task anymore. However, they can not be dispensed with, because they increase the safety, protection against accidents, ensure the connection of beam and slab and act in the central beam portion, where the bent iron is missing. In particular, it has been shown that the truss-reinforcement is deficient without stirrup and allows premature failure at the end of the beam." (translated from Mörsch, 1907c, p. 242).

Despite that, in the third edition of *Der Eisenbetonbau: Seine Theorie und Anwendung* (Mörsch, 1908, p. 159), and referring to test results of specimens I, II and III (shown in Figure 4.7b), the author emphasises the favourable influence of stirrups, since cracks also formed where the stirrups existed, most inclined near the supports, but they did not open as widely as in the other halves.

Between 1906 and 1909 experimental testing in the United States showed that the truss models produced very conservative estimates of strength.

During the summer of 1906 (Withey, 1907), and the spring and summer of 1907 (Withey, 1908), at the University of Wisconsin, M. O. Withey performed several test series on reinforced concrete beams. One of the series was designed to study the deformations along stirrups in reinforced concrete beams. Withey noticed that the stirrups tensile stresses given by Hennebique's model were too high when compared with the values from the tests results. The author also found that, in beams with inclined rods, a considerable portion of the diagonal tension was taken up by the rods (Withey, 1908, p. 130).

Talbot (1909), based on tests performed in 1907 and 1909 concluded that the stress developed in stirrups was less than the one given by the truss models and that part of the shear was carried through the concrete of the top of the beam. Talbot recommends the use of two-thirds of the external vertical shear instead of the full amount for the calculation of tension and bond in stirrups (Talbot, 1909, p. 72).

With the aim of studying the effect of the application of a concentrated load on top of a cuboid, Mörsch (1924) first introduced the strut-and-tie model shown in Figure 4.12.

From the 60s, strut-and-tie models experienced new developments, with researchers working to extend the application of strut-and tie models, as Kupfer (1964) that developed an extension of the truss-analogy of Mörsch using the principle of minimum strain energy, or Leonhardt (1965) that, with basis on the shear tests performed between 1961 and 1963 in Stuttgart, derived a method for reducing the shear reinforcement in reinforced concrete beams, using the truss analogy to explain the mechanism of failure at ultimate shear load.

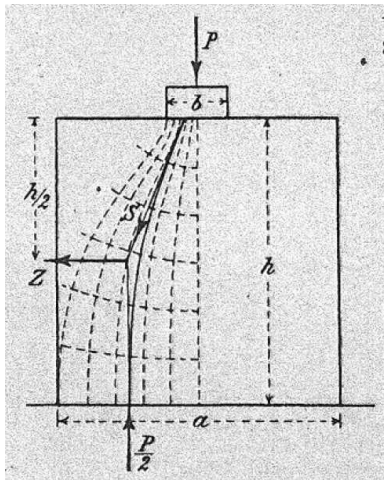

Figure 4.12: Mörsch's strut-and tie model for a concentrically loaded member (Mörsch, 1924)

Meanwhile, several researchers worked to apply the truss analogy to shear, torsion and bending, highlighting the work of Lampert and Thürlimann (1971), Mitchell and Collins (1974), Grob and Thürlimann (1976), Müller(1976a, 1976b, 1978) and Thürlimann (1979) among others.

Schlaich and Schäfer (1984) first introduced the division in B (B for bending or Bernoulli) and D regions (discontinuity regions) and generalized strut-and-tie models for application to other reinforced concrete structures besides beams.

In 1985, Marti proposed the use of basic tools to reinforced concrete beam design. Basic tools included struts and ties, nodes, fans, and arches. According to the author, the distribution and the details of the reinforcement could be determined by developing truss models and stress fields corresponding to possible equilibrium systems of the internal forces in the concrete and in the reinforcement under ultimate loads Marti (1985a). Marti (1985b) presents three design examples illustrating the practical application of truss models.

Vecchio and Collins (1986) presented the Modified Compression-Field Theory for reinforced concrete elements subjected to shear. This model considered tensile stresses in the concrete between the cracks, and used experimentally verified average stress-average strain relationships for the cracked concrete.

In 1988, Muttoni et al. published a book entitled "Design and construction of reinforced concrete structures with stress fields" in German (Muttoni et al., 1988) where the consistency of stress field models in the design concept was shown. In 1997 an improved version was published in English (Muttoni et al., 1997).

Rogowsky and Marti (1996) published a report about design and detailing of anchorage zones of post-tensioning tendons. The design was based on strut-and-tie models.

4.3 Reference model

4.3.1 Specimens definition

4.3.1.1 General

The Lezíria Bridge, over the Tagus River, was used as a prototype for the reference model considered in this study. A half-scale model of the inferior corner of the box girder was considered.

In order to not constrain the laboratory test site and the geometry of the model with regard to the relative position and distance between the tendons, a self-balanced model with anchorages at both ends of the tendons was chosen, as shown in Figure 4.13. The model includes a corner blister for two anchors, with a portion of the slab and the contiguous web.

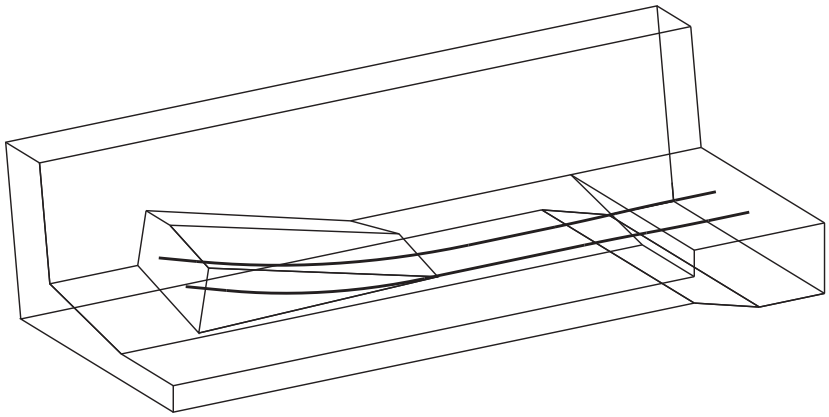

Figure 4.13: View of the reference model

4.3.1.2 Model length

In order to assess the specimen length, in particular slab length behind the blister and distance between anchorage zones (i.e. prestressing tendons length), a linear elastic analysis using a 3D finite element model of shell elements, which simulated the slab, the web and the blister of the specimen was carried out. A number of different dimensions for each one of the parameters listed above were studied.

For the case of the slab length to be considered behind the blister, the maximum tensile force immediately behind anchor, parallel to the tendon axis, of each case (F_T) was evaluated and compared with the value obtained for the maximum assumed length of 3000 mm ($F_{T,3000}$). The results for the application of a 1000 kN force in each anchorage

are summarised in Table 4.1.

Table 4.1: Evaluation of the maximum tensile force immediately behind the anchors

L (mm)	F_T (kN/m)	$F_T/F_{T,3000}$
3000	863,53	1,00
1500	857,50	0,99
1000	813,44	0,94
750	744,70	0.86
500	605,81	0,70

For the case of the distance to consider between anchorage zones, in order to assess the distance required to distribute the stresses to the web of the specimen, the overall slab compression force, parallel to the tendon axis, of each case was evaluated in two cross sections between anchors (F_1 and F_2) and compared with the value obtained for maximum length of 6000 mm ($F_{1,6000}$ and $F_{2,6000}$). The results for the application of a 1000 kN force in each anchorage are summarised in Table 4.2. It should be noted that sections 1 and 2 listed in Table 4.2 refer to cross sections that are at a distance of 1500 mm of intermediate and end anchors, respectively.

Table 4.2: Evaluation of the overall compression force between anchorages

L (mm)	F_1 (kN)	$F_{1,6000}/F_1$	F_2 (kN)	$F_{2,6000}/F_2$
6000	-1222,23	1,00	-1196,22	1,00
4500	-1224,01	1,00	-1199,70	1,00
4000	-1228,77	0,99	-1207,03	0,99
3500	-1244,66	0.98	-1227,56	0,97
3000	-1290,53	0,95	-1290,53	0,93

The dimensions taken, not only reflect the underlying analysis, but also the optimisation of dimensions to obtain the smallest model.

As shown in Figure 4.14, behind the blister, a slab length of 500 mm was adopted, despite the 30% difference that exists between the maximum tensile force behind anchor, parallel to the tendon axis, and the value obtained for maximum length. In this particular case, the distance could be minimised, because the problem of cracking behind intermediate anchorages has been subjected to a large number of studies (Wollmann, 1992).

Between anchorages it was adopted a distance of 3500 mm, since in this case was intended to provide enough space for the dissipation of compressive stresses.

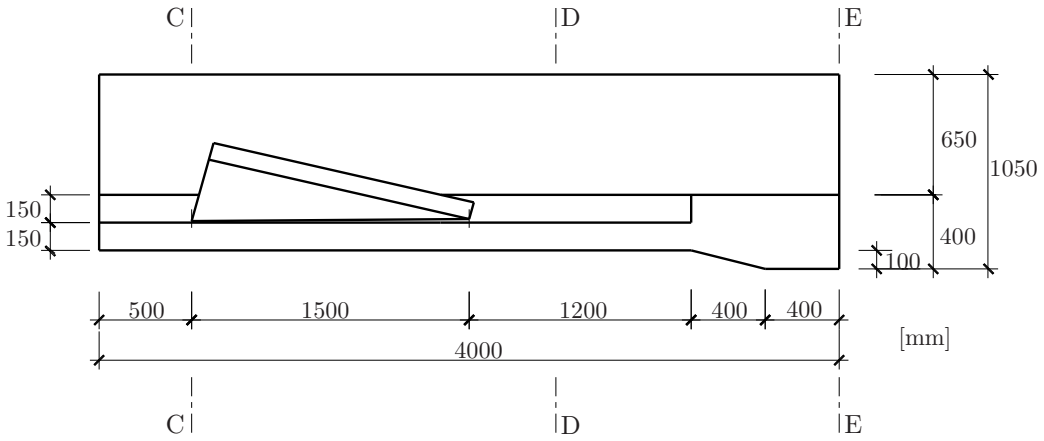

Figure 4.14: Reference model - Elevation

4.3.1.3 Typical cross-section

The specimen typical cross-section is presented in Figure 4.15 and was defined based on the dimensions of the prototype. The width and height of the cross-section were chosen to ensure an adequate distribution of the prestressing force, taking into account the position of the prestressing tendons.

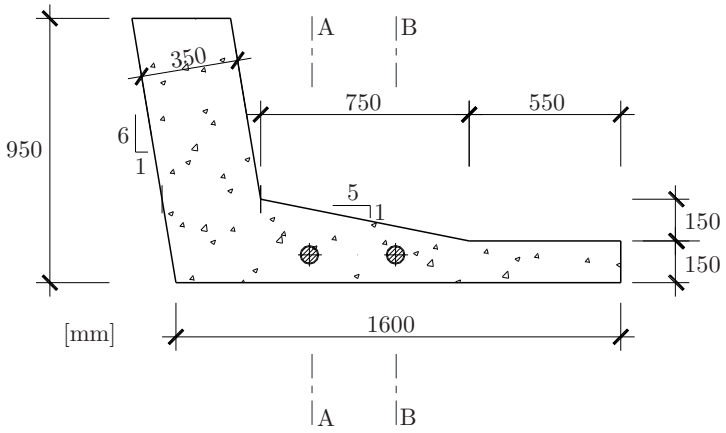

Figure 4.15: Typical cross-section of the models (cross section D-D)

4.3.1.4 Geometry of the anchorage corner blister

The geometry of the blister is based mainly on detailing considerations. Minimum edge distances for the anchor body and minimum radius of tendon curvature should be respected. Besides, the geometry should provide sufficient clearance for the stressing jack (Rogowsky and Marti, 1996).

It was initially adopted a length of 1500 mm (see Figure 4.14), which proved to be

sufficient to meet both the minimum radius of tendon curvature and to ensure adequate concrete cover, when the tendons begin the way up to the anchorage.

Seeking the optimisation of the dimensions and size of the blister, in the plane of the anchor head, perpendicular to the tendons, the minimum edge distances for the anchor body were adopted, always seeking for the simplification of the blister geometry.

Regarding the reference model and considering both minimum centre distance and edge distance of anchorages, recommended by VSL International (2012) for the type of anchorage used, and adopting the necessary distances from anchorages to bottom slab and web in order to allow the tendon's tensioning without conflicts between these elements and the hydraulic jack, the geometry of the blister resulted in that shown in Figure 4.16.

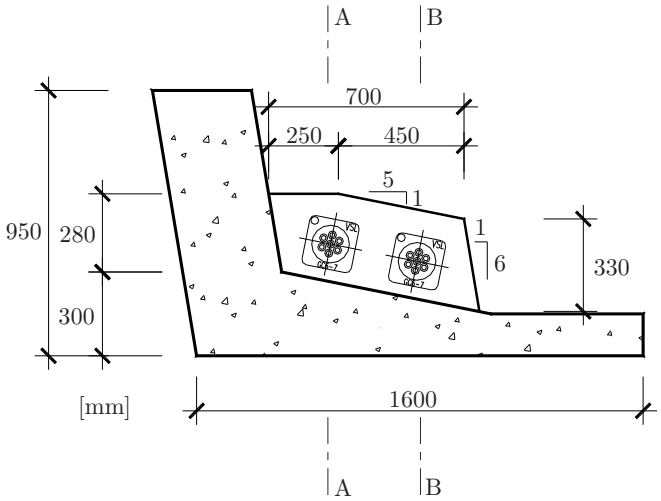

Figure 4.16: Reference model - Cross section C-C

4.3.1.5 Layout of the post-tensioning tendons

The tendons layout was set to minimise the post-tension friction losses and the size of the anchorage blister.

In the extremity of the anchorage blister (section C-C), the tendon's height and the location of the anchorage closer to the web of the girder were imposed by the hydraulic jack dimensions, as it was necessary to adopt the necessary distances to allow the tendon's tensioning without conflicts between the hydraulic jack and the bottom slab and web. Between the two anchors was adopted the required distance to avoid crushing of the concrete at the time of tensioning.

On the opposite edge (section E-E), given that it is an end anchorage and there is no space conditioning, a tendon's straight profile was adopted in order to minimise the post-tension friction losses. The distance between the two anchorages was imposed by the

hydraulic jack dimensions, as both tendons were intended to be prestressed simultaneously from this extremity.

Figures 4.17 and 4.18 show the tendons profile and plan layout, respectively.

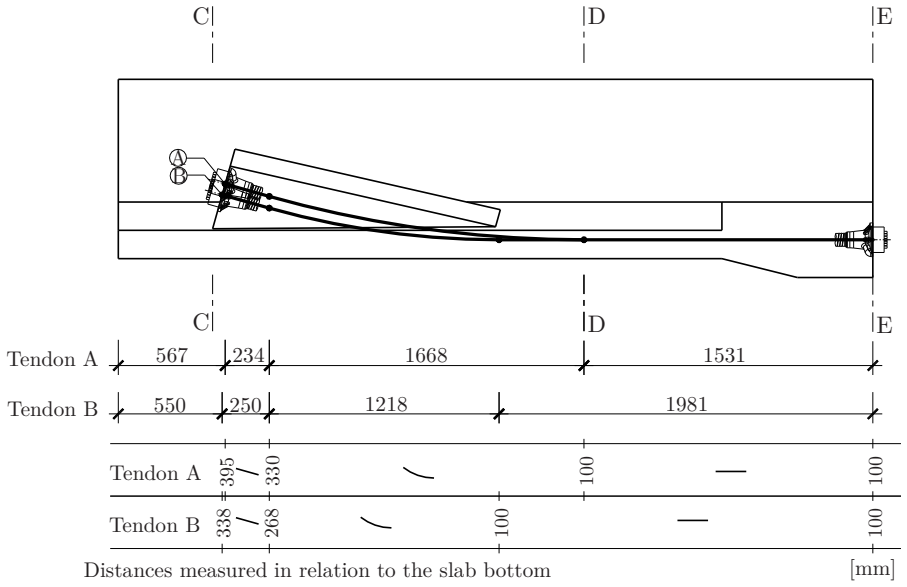

Figure 4.17: Reference model post-tensioning tendons layout - profile

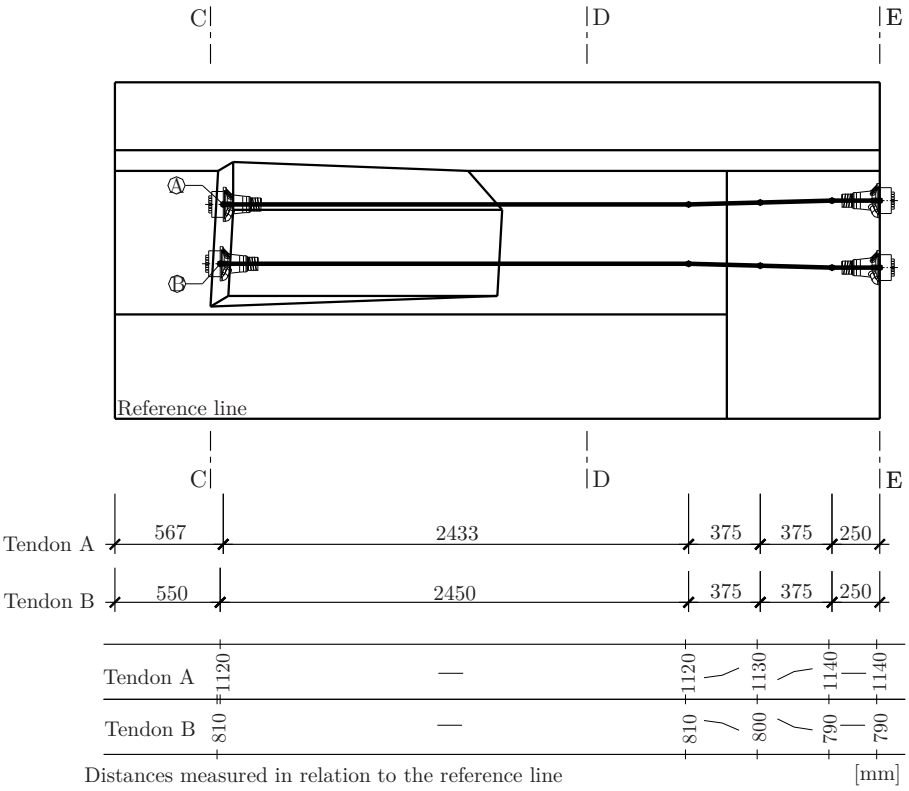

Figure 4.18: Reference model post-tensioning tendons layout - plan view

4.3.2 Elastic analysis

In order to determine the linear elastic stress distribution in the reference model a 3D finite element model of solid elements, whose discretization is presented in Figure 4.19, was used.

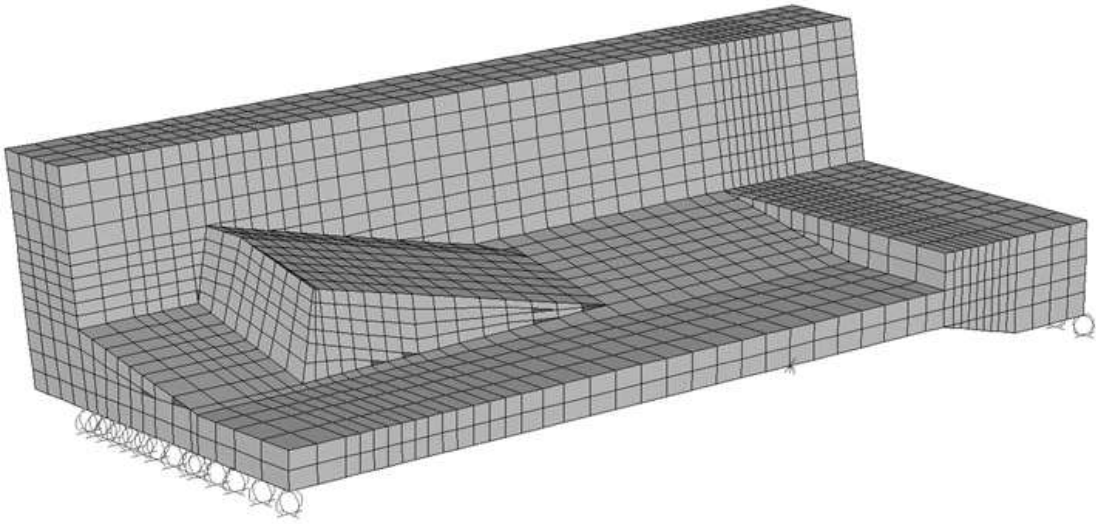

Figure 4.19: View of the 3D finite element model of the reference model

The prestressing effect was simulated by applying equivalent uniformly distributed loads in fictitious bars along the tendons path, and in the solid faces in the anchorage zones, as shown in Figure 4.20. The losses of the prestressing force due to friction effect was neglected.

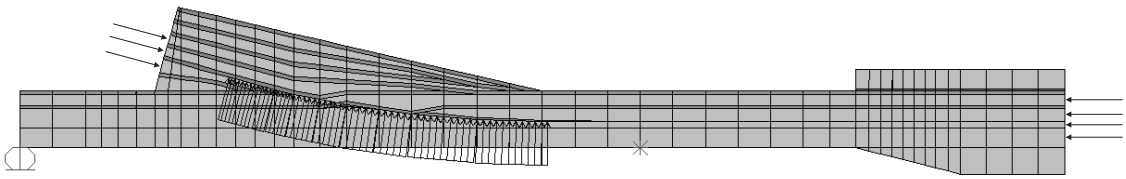

Figure 4.20: Equivalent uniformly distributed loads in a tendon's path, in the reference model

The model was analysed using the program SAP2000 (CSI Computers and Structures Inc., 2007). The results provided helped to identify the critical regions (with higher stresses) and the load paths, serving as a basis for the development of strut-and-tie models.

Figures 4.21a, 4.21b and 4.21c show the stresses due to a prestressing force of 1000 kN in the longitudinal, transversal and vertical directions, respectively, obtained from the linear elastic analysis of the reference model.

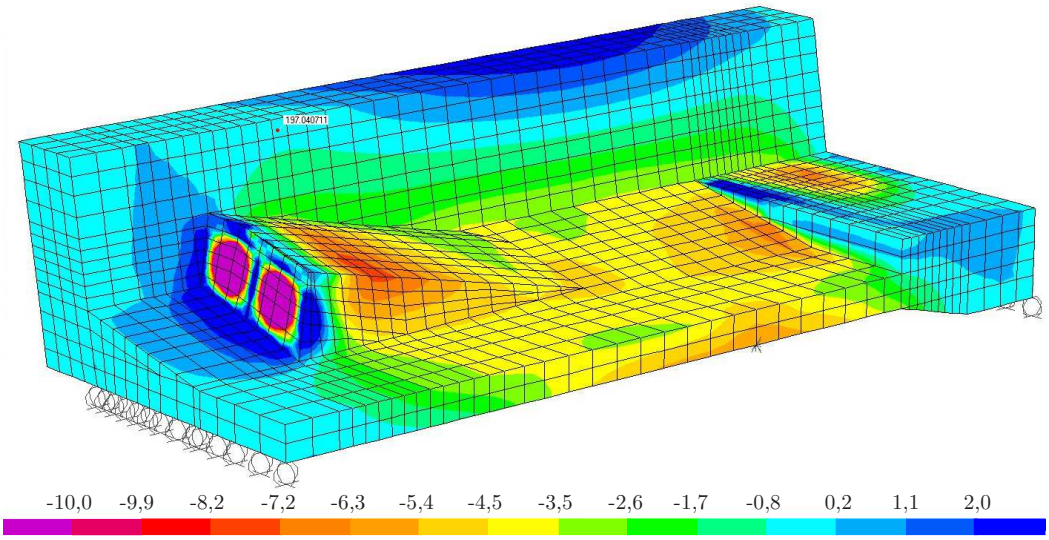

(a) Longitudinal direction

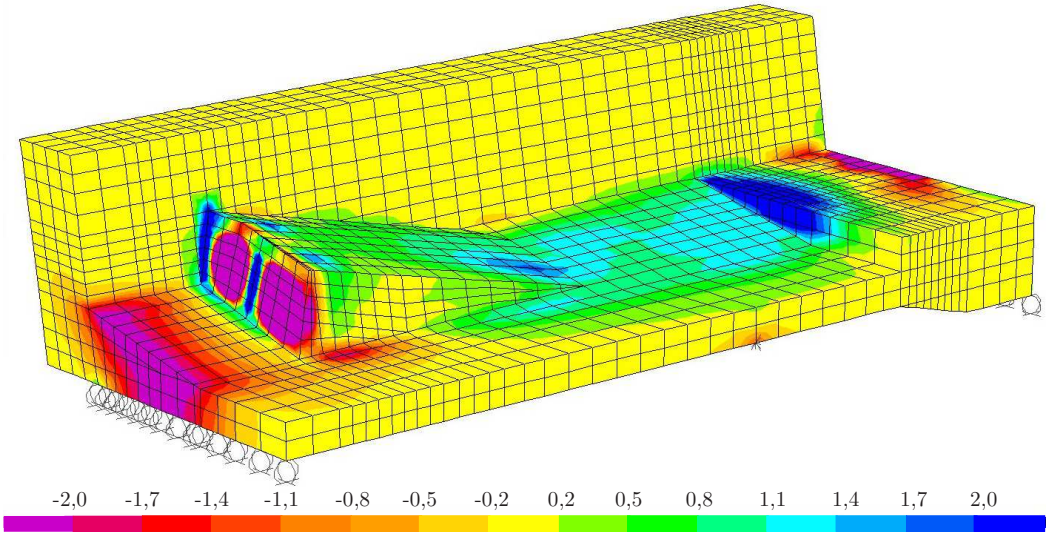

(b) Transversal direction

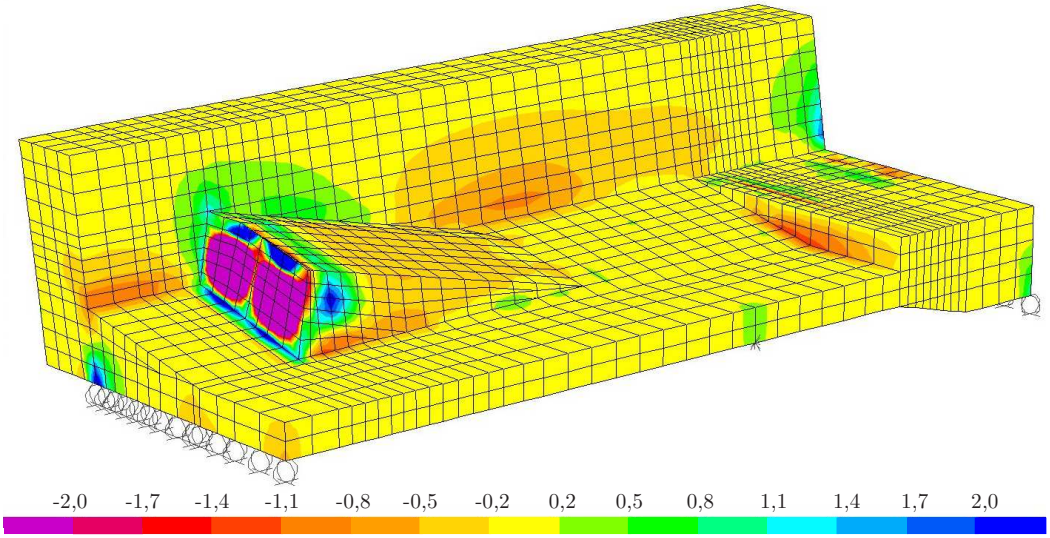

(c) Vertical direction

Figure 4.21: Stresses in the reference model (in MPa)

4.3.3 Strut-and-tie models

The strut-and-tie models were developed taking into account the stress trajectories, the distributions obtained from the linear-elastic analysis and the need to keep the equilibrium with the applied loads in the ultimate limit state. The action of radial forces due to tendon curvature, both in longitudinal section and in plan, were considered. In the choice of the ties adopted position and direction has been taken into account the fact that the ties should coincide with the corresponding reinforcement. The principles adopted in the conception of each strut-and-tie model are indicated below.

Longitudinal sections

Figures 4.22a and 4.22b show the stresses due to the prestressing force in the vertical and longitudinal directions, respectively, obtained from the linear elastic analysis of the reference model in a longitudinal section, along the alignment of a prestressing tendon.

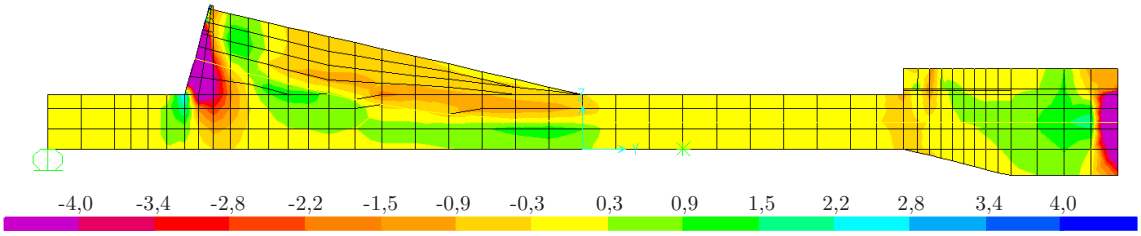

(a) Vertical direction

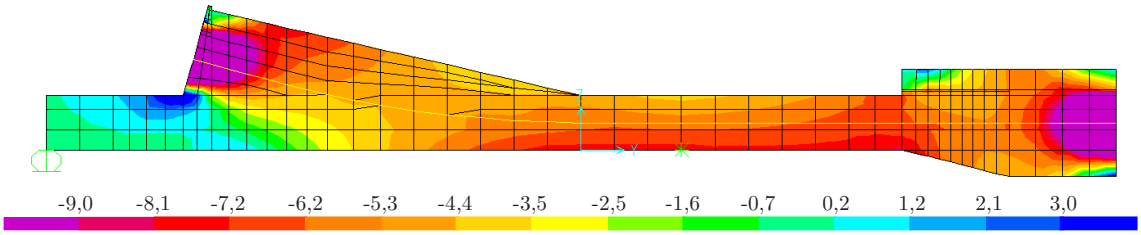

(b) Longitudinal direction

Figure 4.22: Stresses in the reference model (in MPa) - Longitudinal section

The strut-and-tie models adopted in the longitudinal sections are shown in Figures 4.23 and 4.24, for each tendon.

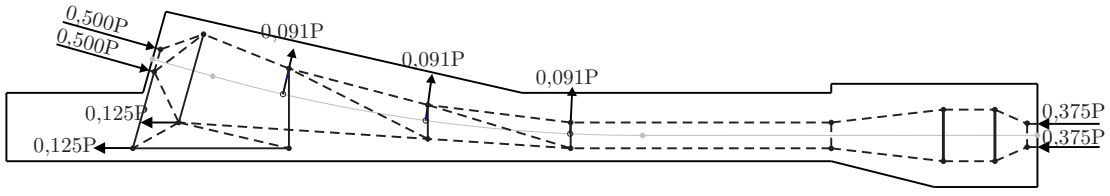

Figure 4.23: Strut and tie model - Section A-A (tendon A)

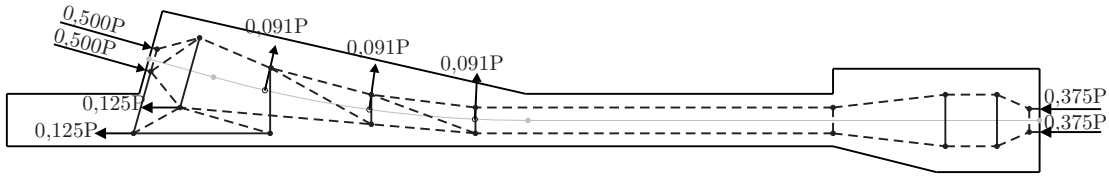

Figure 4.24: Strut and tie model - Section B-B (tendon B)

In the longitudinal sections, due to the dispersion of the concentrated prestressing force over the cross-section, it was assumed that the reinforcement needed should be parallel to the front face of the blister (perpendicular to the applied force). The resultant tie force was located in the theoretical section where the compression stress field, due to the dispersion of the concentrated force, intersects the upper face of the blister.

In the slab between anchorages, the compression was considered to be uniformly distributed along the full slab thickness (for this purpose, and for simplification, the variation of the slab thickness at the junction with the web was discarded). So that, two equal struts located at one quarter and three quarters of the regular slab thickness were adopted.

According to Rogowsky and Marti (1996), a tie back force of 25% of the prestressing force was assumed, uniformly distributed along the full slab thickness.

The transverse ties were designed to resist to half of the radial forces due to tendon curvature. The other half was resisted by the concrete struts that converge in each top node. The orientation of the left strut of each node was determined by the establishment of the equilibrium at the node.

The details of the strut-and-tie models in the blister anchorage zones are presented in Figures 4.25 and 4.26 for tendons A and B, respectively.

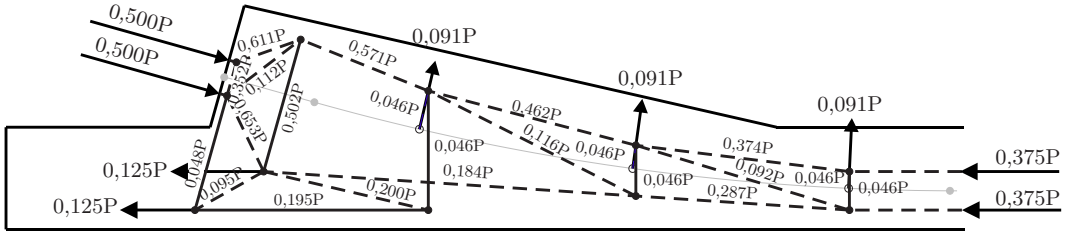

Figure 4.25: Strut and tie model - Section A-A (detail of the anchorage zone)

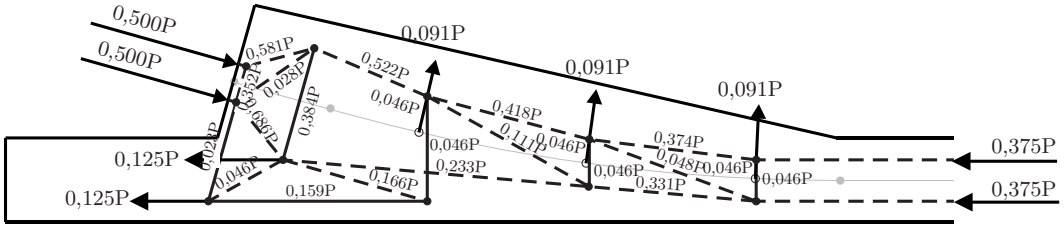

Figure 4.26: Strut and tie model - Section B-B (detail of the anchorage zone)

Plan view

For each specimen, two models were considered in the horizontal plan: a top plan where the effect of force distribution between prestressing anchorages was analysed (Figure 4.27), and a lower plan that represents the effect of the tie back force in front of the blister and its equilibrium in the model (Figures 4.28).

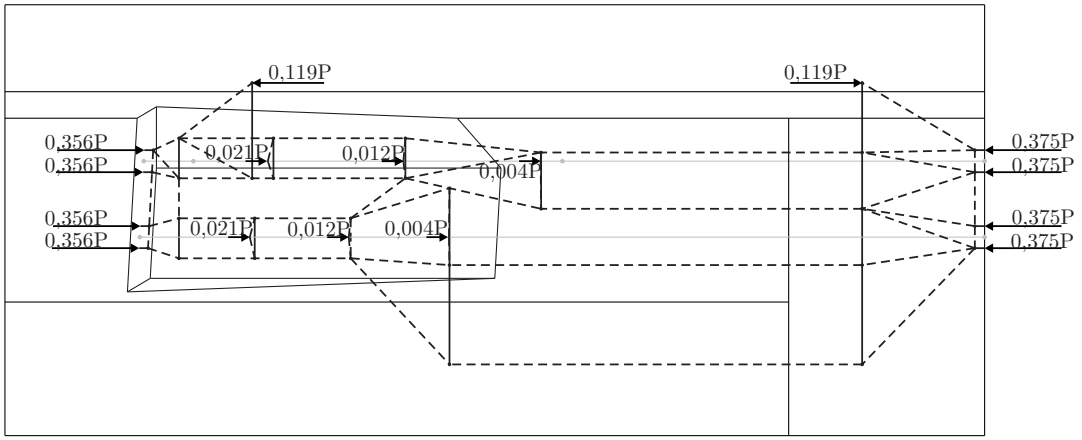

Figure 4.27: Strut and tie model - Top plan view

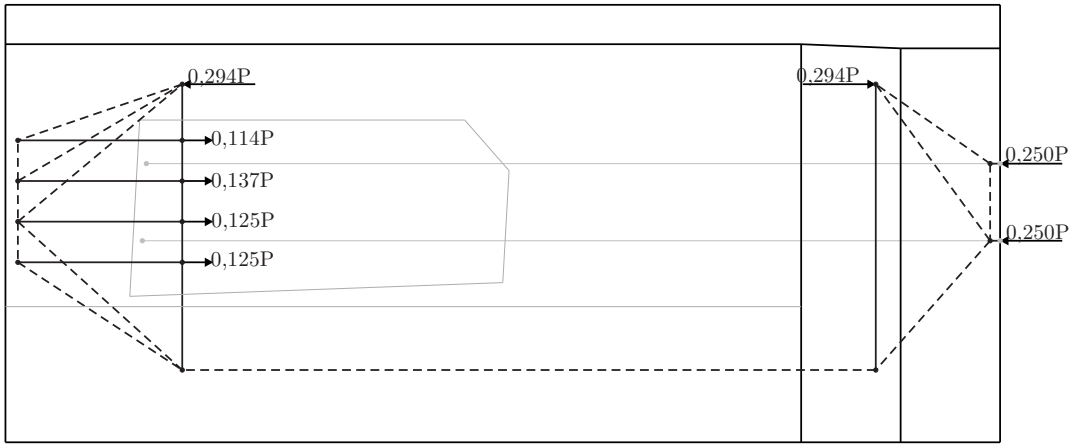

Figure 4.28: Strut and tie model - Bottom plan view

In the top plan (Figure 4.27), immediately after the anchorage, the dispersion of the prestressing force in the blister and web of the section was considered . After the section where the primary stress field reaches the level of the slab, the dispersion extends also to the slab width.

Regarding the lower plan (Figures 4.28), the tie back force was applied considering the force distribution achieved on the top plan.

The detail of anchorage zone, regarding the top plan, is shown in the Figure 4.29, presented below.

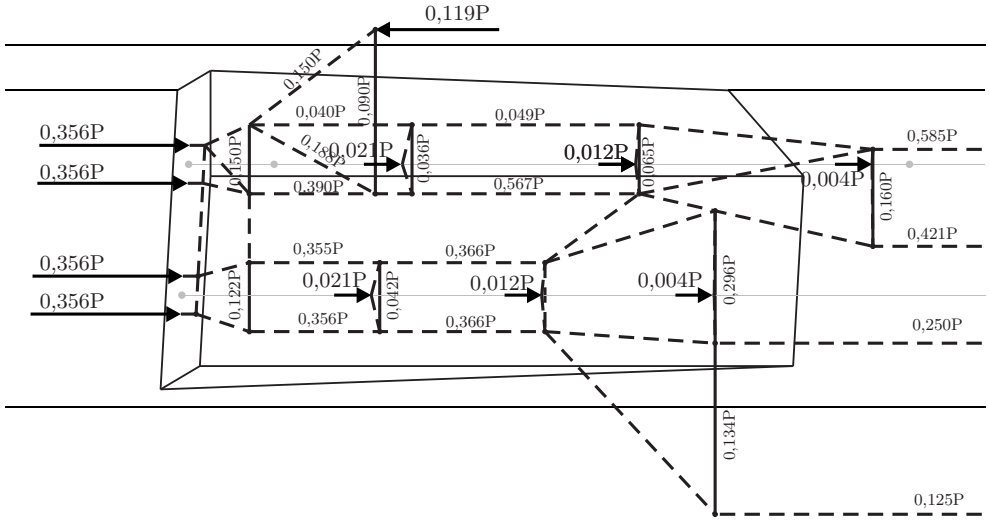

Figure 4.29: Strut and tie model - Top plan view (detail of the anchorage zone)

Web

Regarding the web of the section, Figures 4.30 and 4.31 show the distribution of tensile and compressive stresses given by the elastic model.

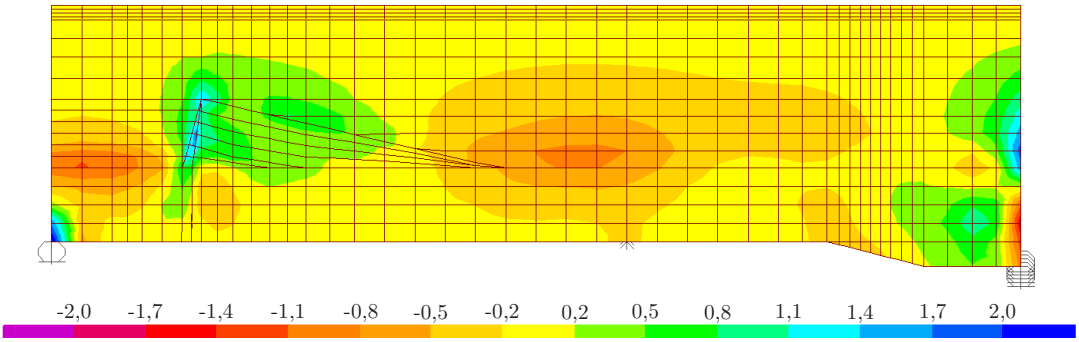

Figure 4.30: Reference model web - Stresses in the vertical direction (in MPa)

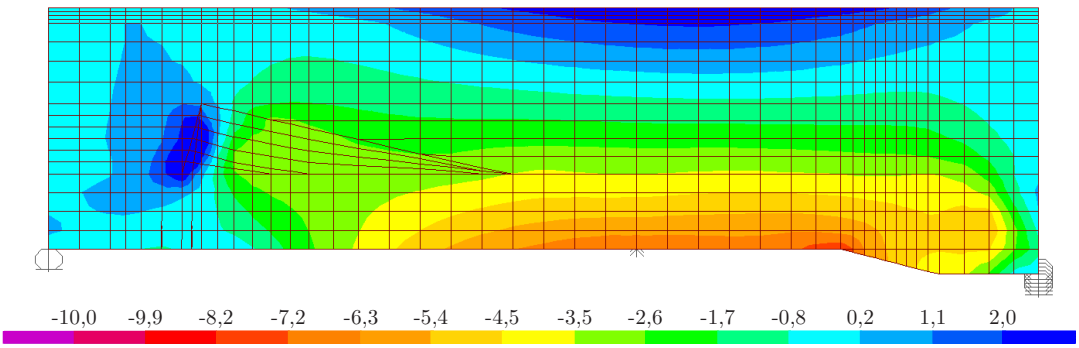

Figure 4.31: Reference model web -Stresses in the longitudinal direction (in MPa)

The strut-and-tie model presented in Figure 4.32 was developed taking into account the dissipation of the prestressing force to the web, whose resultant was obtained in plan models, and the distribution of tensile and compressive stresses presented above.

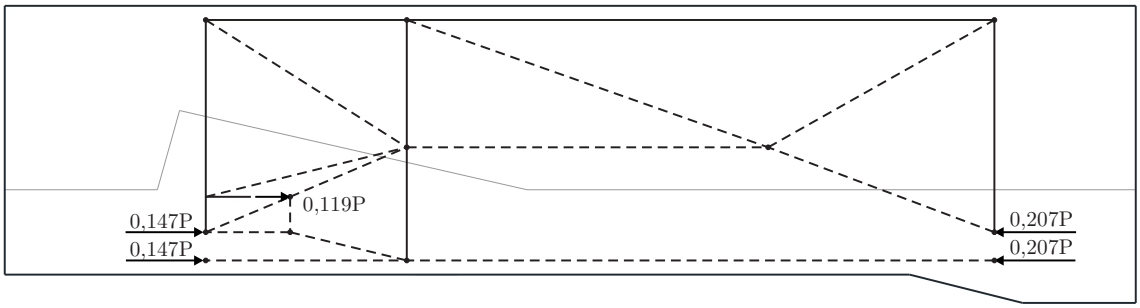

Figure 4.32: Strut and tie model - Web

4.3.4 Specimens design

The design of the specimens reinforcement was made based in the tensile forces obtained with the strut-and-tie models previously presented.

By the fact that the force applied during the test was limited to the failure load of the prestressing tendons and assuming that concrete failure was not relevant, the steel reinforcement used in the blister zone was intentionally undersized with the purpose of trying to reach the failure of the model during the test. So, the reinforcement was designed considering a post-tensioning force of half of the specified characteristic value of 0,1% proof force ($F_{p0,1k}$) for seven strands type 0,6" (with a maximum nominal area of 150 mm^2) and a reinforcing steel tensile strength of 600 MPa, since the reinforcing steel grade that was planned to use would be an A500NR SD.

Longitudinal sections

Considering the longitudinal models presented in Figures 4.25 and 4.26, for tendons A and B, respectively, Table 4.3 presents the tensile force considered for each tie, the corresponding steel reinforcement area and the reinforcement adopted in each case. The identification of the ties used in Table 4.3 is shown in Figure 4.33.

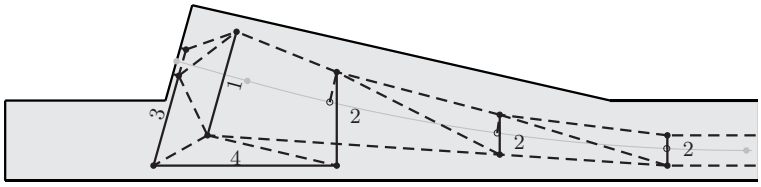

Figure 4.33: Identification of ties

Table 4.3: Reinforcement calculation based on the longitudinal strut-and-tie models

	Tendon A			Tendon B		
Tie	F_t (kN)	A_s (cm^2)	Adopted reinf.	F_t (kN)	A_s (cm^2)	Adopted reinf.
1	422,0	7,03	7 stirrups ϕ8//0,05	322,4	5,37	7 stirrups ϕ8//0,05
2	38,3	0,64	stirrups ϕ6//0,20	38,3	0,64	stirrups ϕ6//0,20
3	40,6	0,68	2ϕ8	19,6	0,33	2ϕ8
4	163,7	2,73	5ϕ8[a]	133,6	2,23	5ϕ8

[a] The contribution of the slab reinforcement was also considered

Top plan view

Regarding the strut-and-tie model presented in Figure 4.27, Table 4.4 presents the tensile force considered for each tie (according to Figure 4.34) and the corresponding steel reinforcement area.

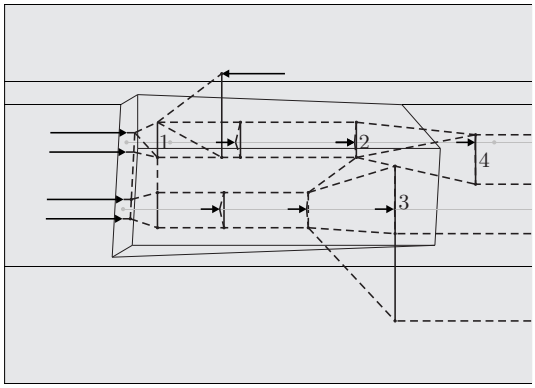

Figure 4.34: Identification of ties

Table 4.4: Reinforcement obtained based on the top plan strut-and-tie model

Tie	F_t (kN)	A_s (cm^2)
1	125,7	2,09
2	54,4	0,91
3	248,6	4,14
4	134,7	2,25

The contribution of the top reinforcement of the blister and of the top and bottom reinforcement of the slab was considered, so no additional reinforcement was adopted.

Bottom plan view

In the case of the bottom plan view strut-and-tie model previously presented in Figure 4.28, the reinforcement determination is presented in Table 4.5, according to Figure 4.35.

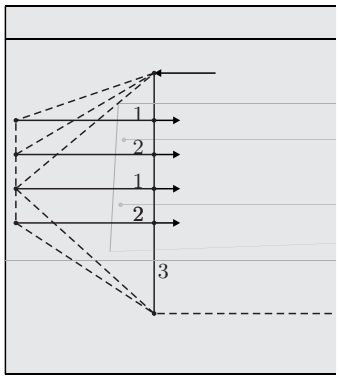

Figure 4.35: Identification of ties

Table 4.5: Reinforcement obtained based on the bottom plan strut-and-tie model

Tie	F_t (kN)	A_s (cm^2)	Adopted reinf.
1+2	130,5	2,17	-
3	210,0	3,50	$5\phi8$[a]

[a] The contribution of the slab bottom reinforcement was also considered

4.3.5 Specimens reinforcement detailing

The reinforcement detailing is presented in Figures 4.36, 4.37 and 4.38.

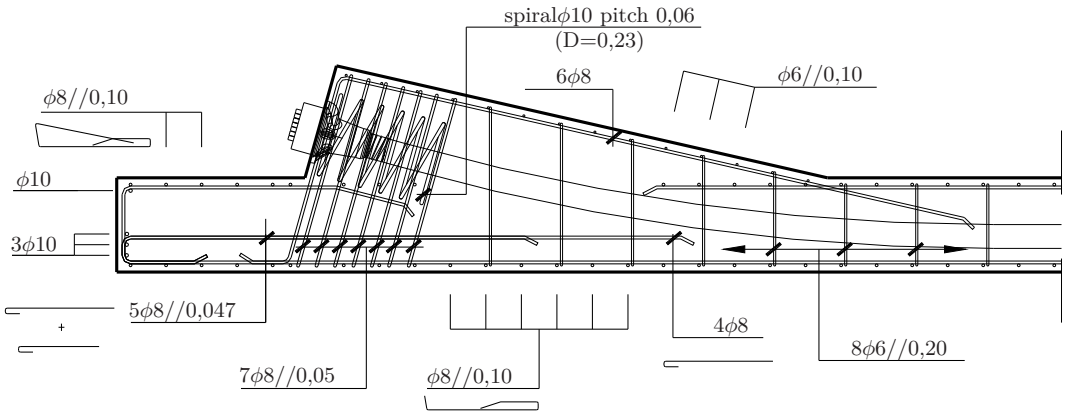

Figure 4.36: Reinforcement in the blister anchorage zone for tendon A

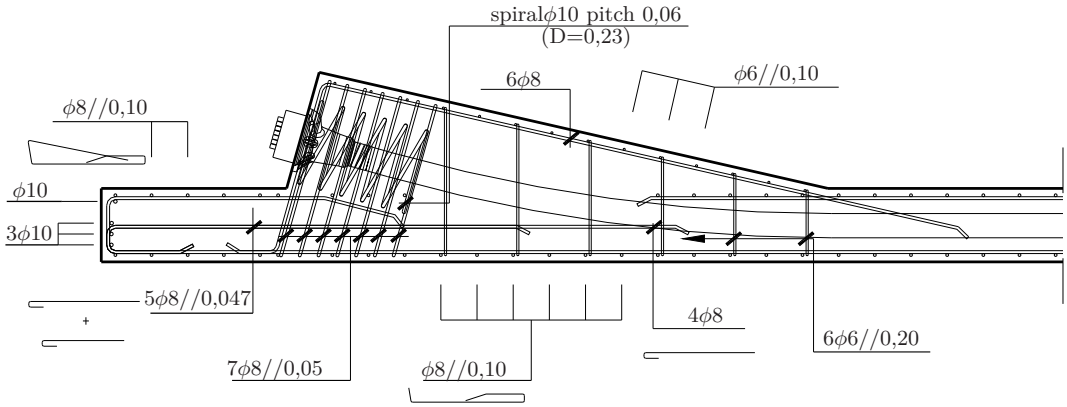

Figure 4.37: Reinforcement in the blister anchorage zone for tendon B

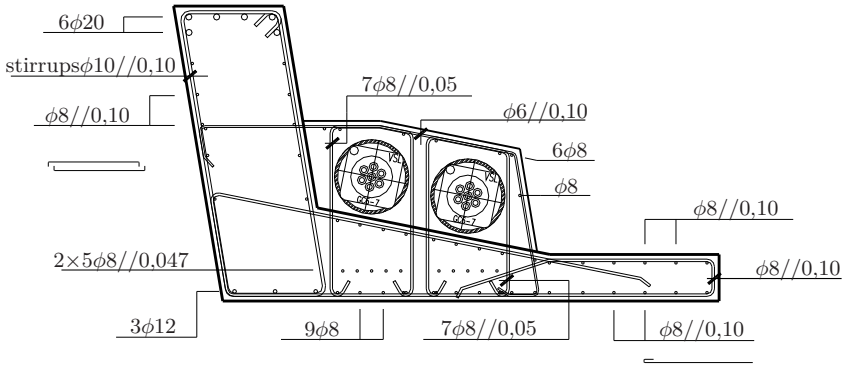

Figure 4.38: Reinforcement in the blister anchorage zone - Cross section

4.4 HPFRC blister model

4.4.1 Specimens definition

4.4.1.1 General

The geometry of the HPFRC blister model is the same as the reference model with the exception of the anchorage blister whose dimensions were reduced.

4.4.1.2 Geometry of the anchorage corner blister

Also in this case, the optimisation of the dimensions and size of the blister, in the plane of the anchor head, perpendicular to the tendons was the main concern. The adopted centre distance and edge distance of anchorages were those assessed through tests of pris-

matic models presented in Chapter 3. In this case it was also necessary to consider the required distances from anchorages to bottom slab and web in order to allow the tendon's tensioning. The adopted geometry is presented in Figures 4.39 and 4.40.

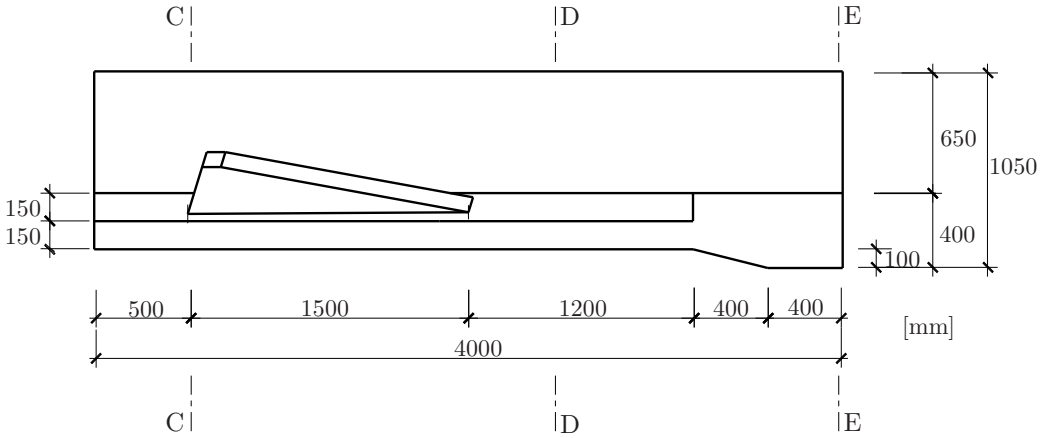

Figure 4.39: HPFRC blister model - Elevation

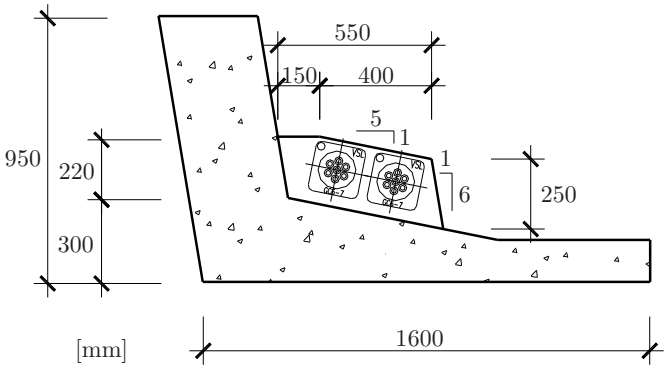

Figure 4.40: HPFRC blister model - Cross section C-C

As can be seen in Figure 4.39, by the fact that HPFRC is a self-compacting concrete it was necessary to provide in the anchorage blister, a horizontal surface to allow casting, since all the inclined surfaces of the blister would have to have formwork.

4.4.1.3 Layout of the post-tensioning tendons

As described above for the case of the reference model, the position of the anchorages of the prestressing tendons was conditioned by the hydraulic jack dimensions in order to allow the tendon's tensioning.

The tendons profile and plan view are shown in Figures 4.41 and 4.42, respectively.

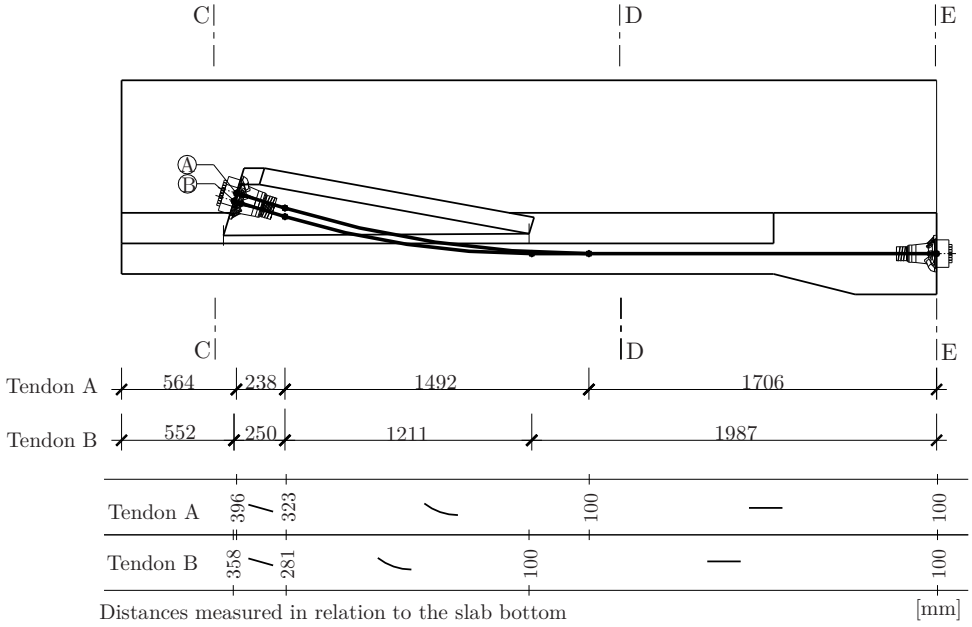

Figure 4.41: HPFRC blister model post-tensioning tendons layout - profile

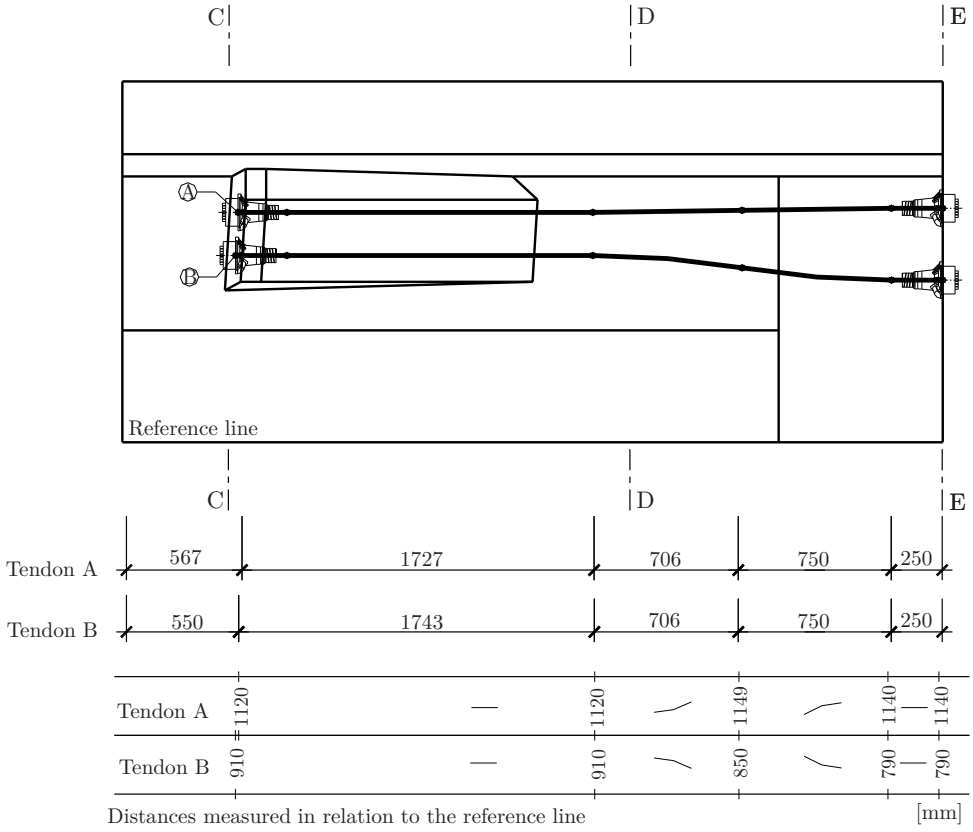

Figure 4.42: HPFRC blister model post-tensioning tendons layout - plan view

4.4.2 Elastic analysis

The discretization of the 3D finite element models of solid element for the HPFRC blister model is presented in Figure 4.43.

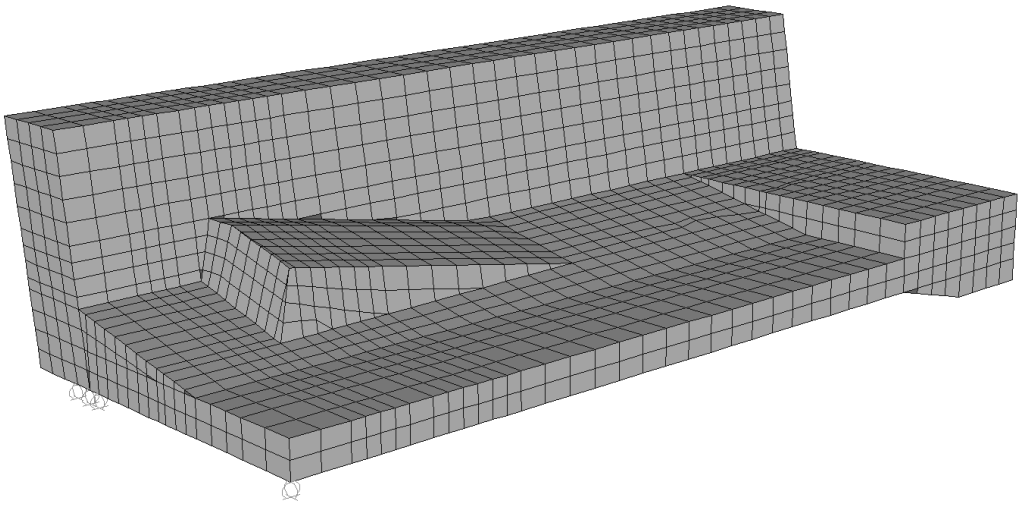

Figure 4.43: View of the 3D finite element model of the HPFRC blister model

The stresses attained for the HPFRC blister model for the introdution of the pre-stressing force, using the program SAP2000 (CSI Computers and Structures Inc., 2007), are presented in Figures 4.44, 4.45 and 4.46 for the longitudinal, transversal and vertical directions, respectively. From the analysis of the diagrams it can be concluded that there are no significant differences between the location of the critical regions in both models.

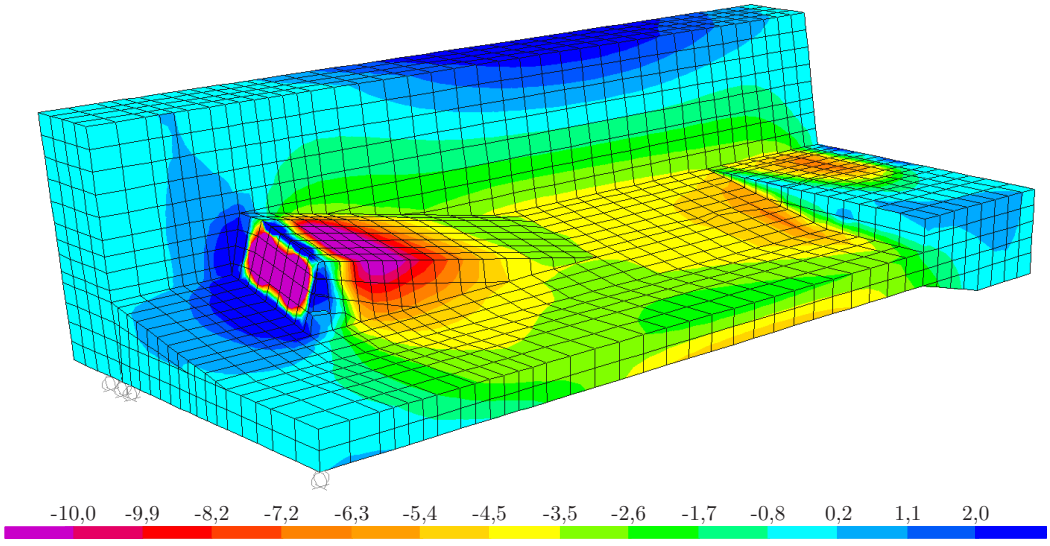

Figure 4.44: Stresses in the longitudinal direction of the HPFRC blister model (in MPa)

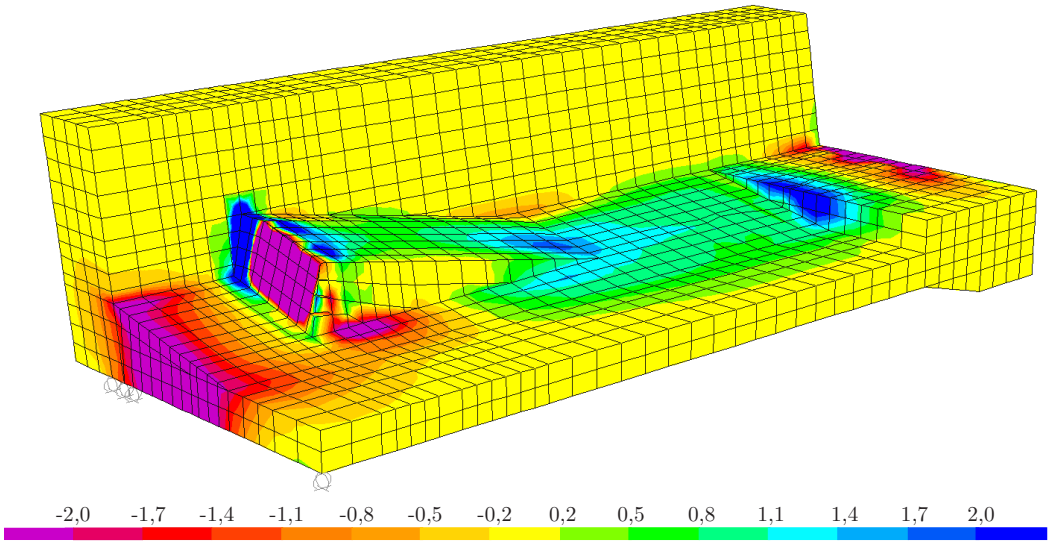

Figure 4.45: Stresses in the transversal direction of the HPFRC blister model (in MPa)

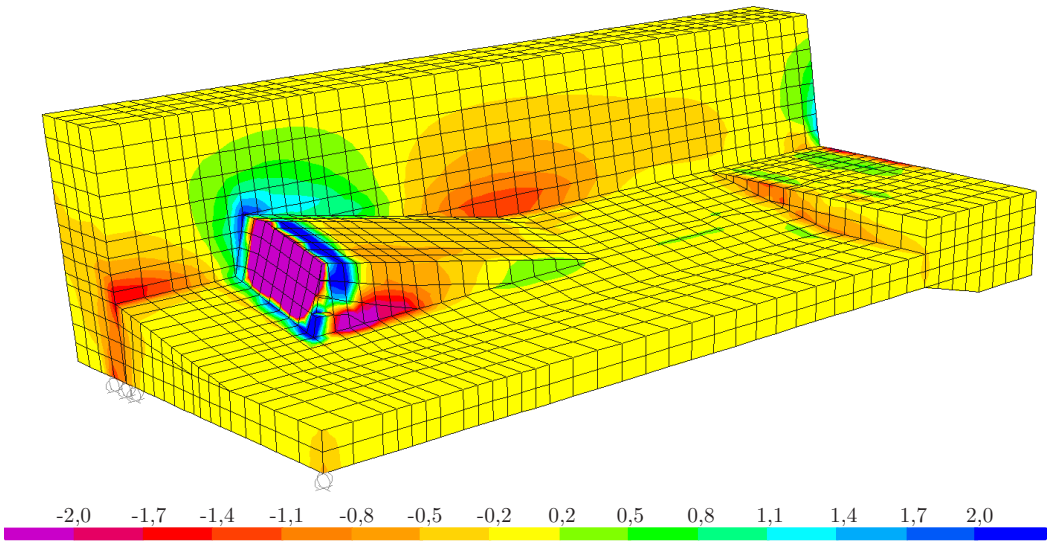

Figure 4.46: Stresses in the vertical direction of the HPFRC blister model (in MPa)

As mentioned previously, these results helped to identify the critical regions (with higher stresses) and the load paths, serving as a basis for the development of strut-and-tie models.

4.4.3 Strut-and-tie models

Longitudinal sections

Figures 4.47a and 4.47b show the stresses due to the prestressing force in the vertical and longitudinal directions, respectively, obtained from the linear elastic analysis of the

reference model in a longitudinal section, along the alignment of a prestressing tendon, in the blister zone.

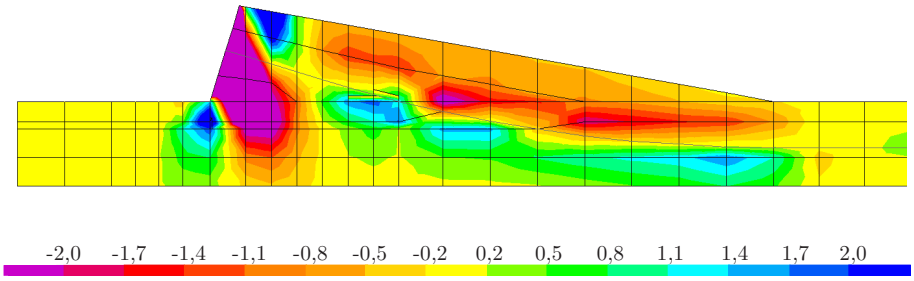

(a) Vertical direction

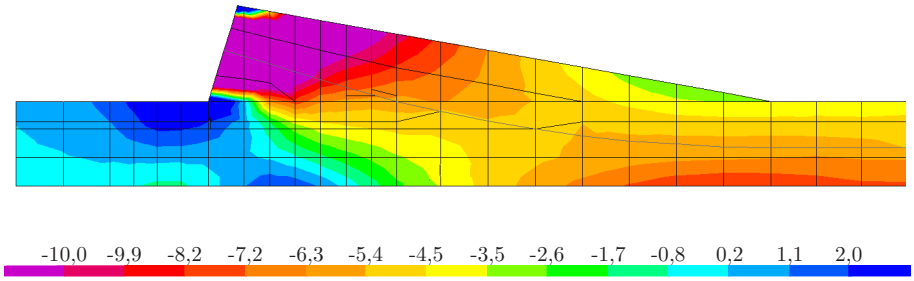

(b) Longitudinal direction

Figure 4.47: Stresses in the HPFRC blister model (in MPa) - Longitudinal section

Based on the same principles indicated for the reference model, the strut-and-tie models adopted in the longitudinal sections for the HPFRC blister model are shown in Figures 4.48 and 4.49, for each tendon.

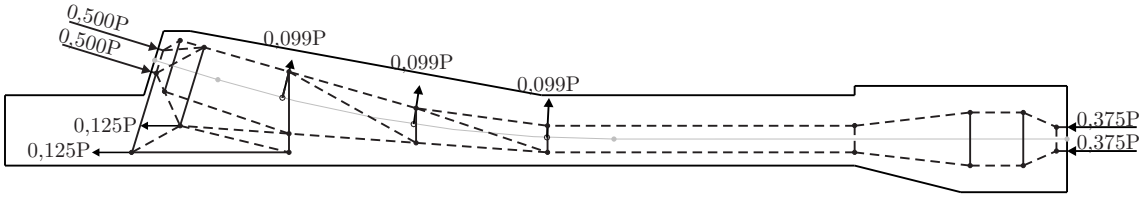

Figure 4.48: Strut and tie model - Section A-A

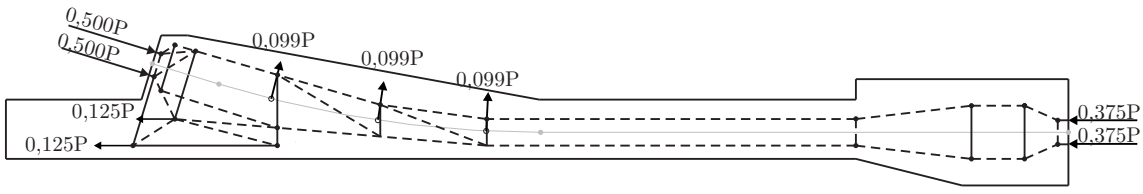

Figure 4.49: Strut and tie model - Section B-B

The details of the strut-and-tie models in the blister anchorage zones are presented in Figures 4.50 and 4.51 for tendons A and B, respectively.

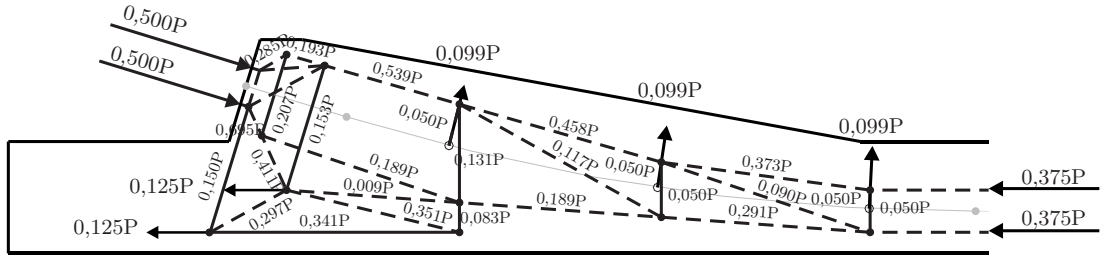

Figure 4.50: Strut and tie model - Section A-A (detail of the anchorage zone)

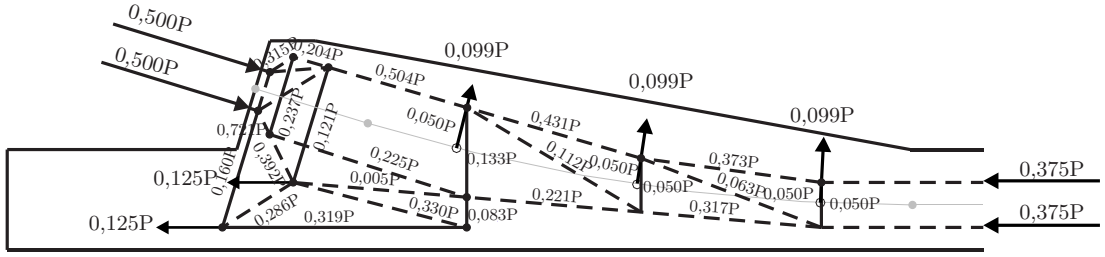

Figure 4.51: Strut and tie model - Section B-B (detail of the anchorage zone)

Plan view

For the HPFRC blister model, the strut-and-tie models for the top and bottom plans are shown in Figures 4.52 and 4.53, respectively.

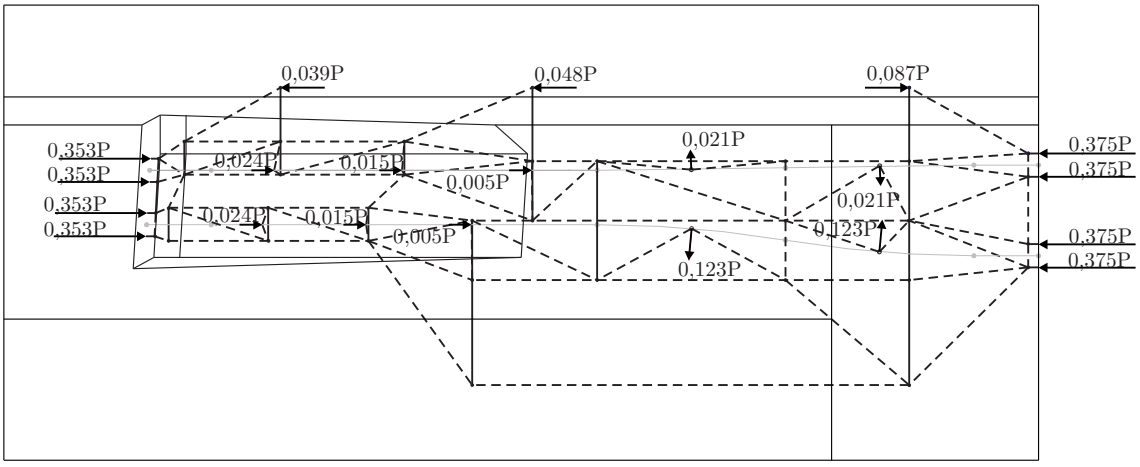

Figure 4.52: Strut and tie model - Top plan view

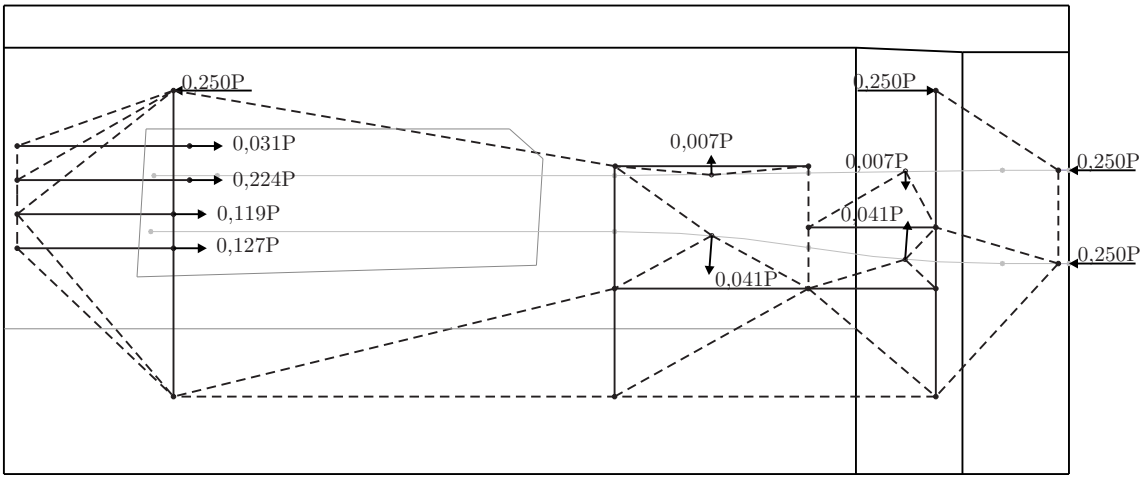

Figure 4.53: Strut and tie model - Bottom plan view

The detail of anchorage zone, regarding the top plan, is shown in the Figure 4.54, presented below.

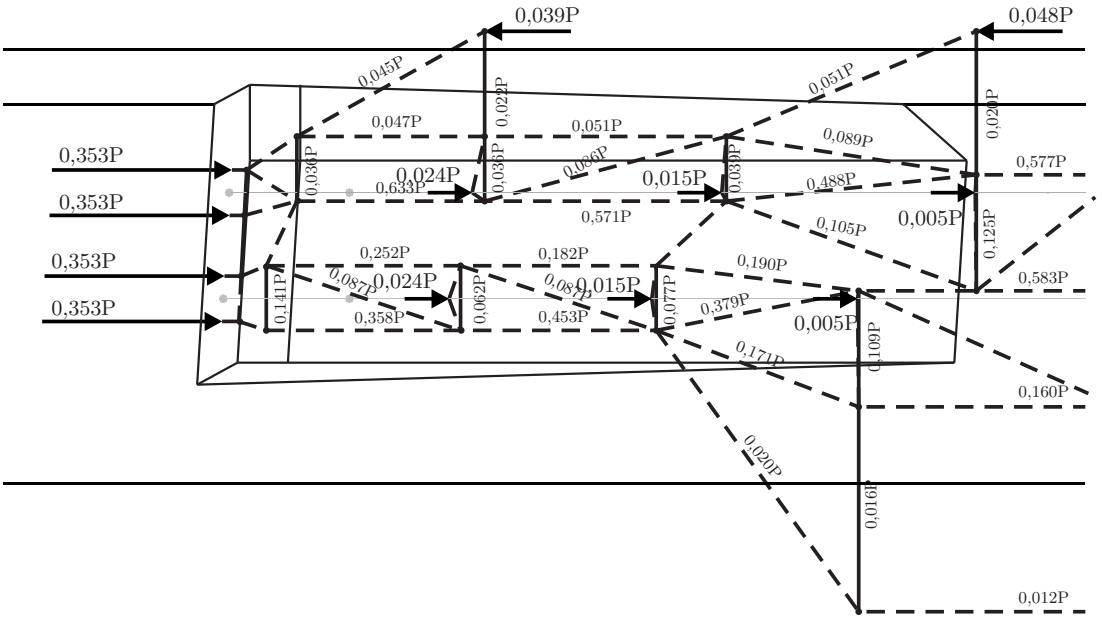

Figure 4.54: Strut and tie model - Top plan view (detail of the anchorage zone)

Web

The strut-and-tie model considered in the web of the section is presented in Figure 4.55.

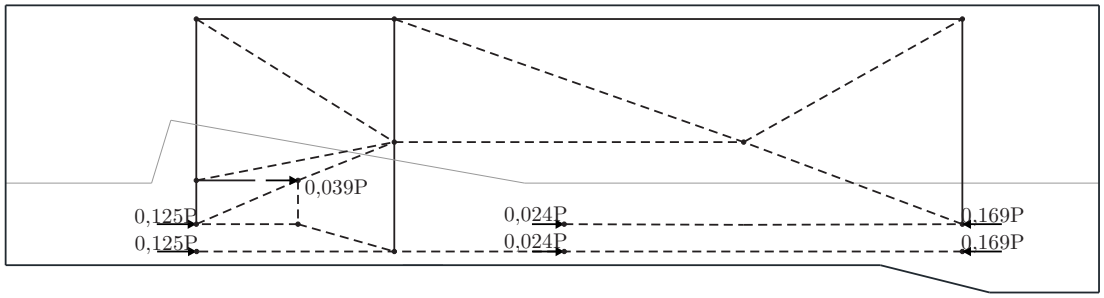

Figure 4.55: Strut and tie model - Web

4.4.4 Specimens design

The design of the specimens reinforcement was made based in the tensile forces obtained on the strut-and-tie models previously presented.

Similarly to what has been assumed for the reference model, and with the purpose of trying to reach the failure of the model during the test, the reinforcement was designed considering a post-tensioning force of half of the specified characteristic value of 0,1% proof force ($F_{p0,1k}$) for seven strands type 0,6" (with a maximum nominal area of 150 mm^2) and a reinforcing steel tensile strength of 600 MPa. Thus, the steel reinforcement used in the blister zone was intentionally undersized.

Longitudinal sections

Considering the longitudinal models presented in Figures 4.48 and 4.49, for tendons A and B, respectively, Table 4.6 presents the tensile force considered for each tie, the corresponding steel reinforcement area and the reinforcement adopted in each case. The identification of the ties used in Table 4.6 is shown in Figure 4.56.

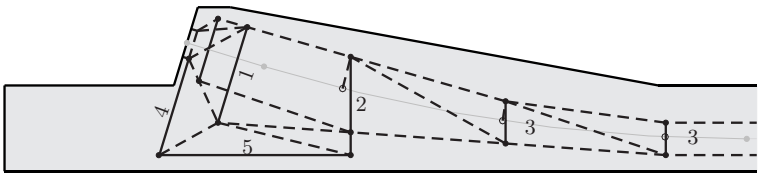

Figure 4.56: Identification of ties

Regarding the unidentified tie parallel to tie 1 and closer to the anchor heads, no reinforcement was considered, since the load transfer tests of the HPFRC prismatic specimens showed that no specific reinforcement was needed in the local zone. Besides, the tensile stress related with this tie is smaller than the concrete tensile strength.

Table 4.6: Reinforcement calculation based on the longitudinal strut-and-tie models

	Tendon A			Tendon B		
Tie	F_t (kN)	A_s (cm^2)	Adopted reinf.	F_t (kN)	A_s (cm^2)	Adopted reinf.
1	128,8	2,15	4 stirrups ϕ6//0,05	101,2	1,69	4 stirrups ϕ6//0,05
2	109,8	1,83	stirrups ϕ6//0,10	111,6	1,86	stirrups ϕ6//0,10
3	41,6	0,69	stirrups ϕ6//0,20	41,6	0,69	stirrups ϕ6//0,20
4	126,0	2,10	3ϕ10	134,4	2,24	3ϕ10
5	286,5	4,78	4ϕ10[a]	268,2	4,47	4ϕ10

[a] The contribution of the slab reinforcement was also considered

Top plan view

Regarding the strut-and-tie model presented in Figure 4.52, Table 4.7 presents the tensile force considered for each tie (according to Figure 4.57) and the corresponding steel reinforcement area.

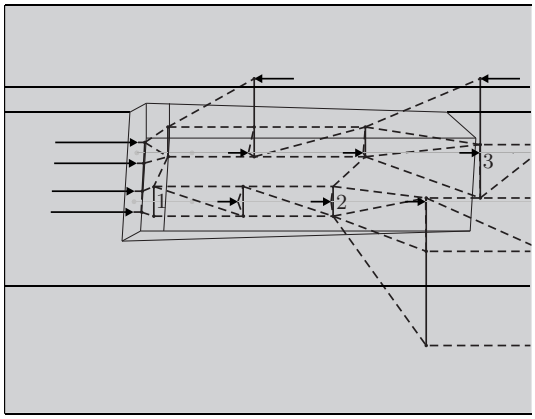

Figure 4.57: Identification of ties

Table 4.7: Reinforcement obtained based on the top plan strut-and-tie model

Tie	F_t (kN)	A_s (cm^2)
1	118,8	1,98
2	65,0	1,08
3	105,0	1,75

The contribution of the top reinforcement of the blister and of the top and bottom reinforcement of the slab was considered, so there was no need to adopt additional reinforcement.

Bottom plan view

In the case of the bottom plan view strut-and-tie model previously presented in Figure 4.53, the reinforcement determination is presented in Table 4.8, according to Figure 4.58.

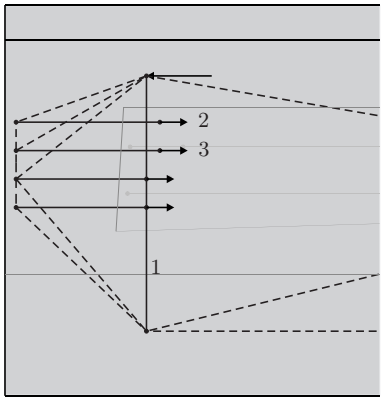

Figure 4.58: Identification of ties

Table 4.8: Reinforcement obtained based on the top plan strut-and-tie model

Tie	F_t (kN)	A_s (cm^2)	Adopted reinf.
1+2	213,9	3,57	$4\phi10$[a]
3	157,2	2,62	-

[a] The contribution of the slab bottom reinforcement was also considered

4.4.5 Specimens reinforcement detailing

The reinforcement detailing is presented in Figures 4.59, 4.60 and 4.61.

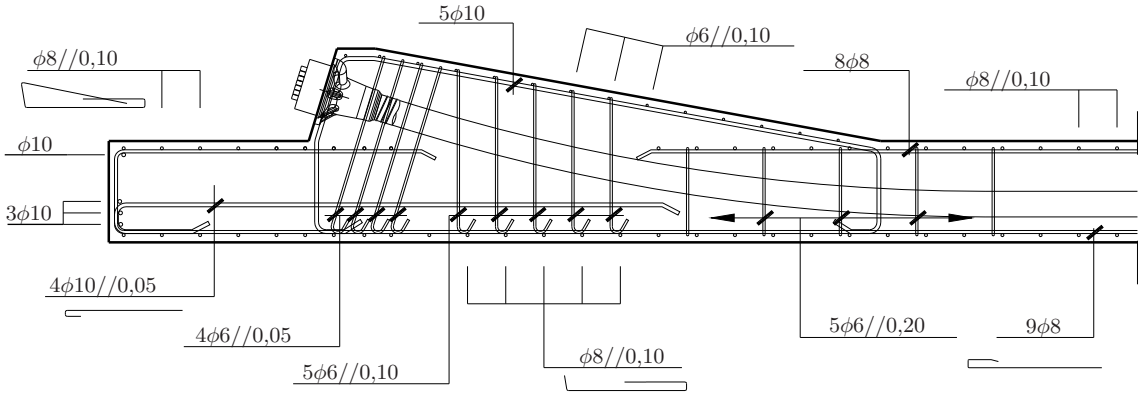

Figure 4.59: Reinforcement in the blister anchorage zone for tendon A

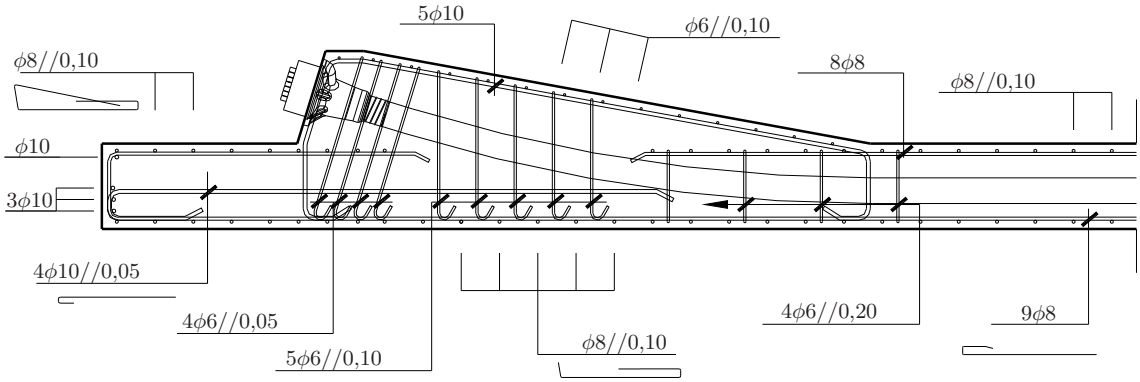

Figure 4.60: Reinforcement in the blister anchorage zone for tendon B

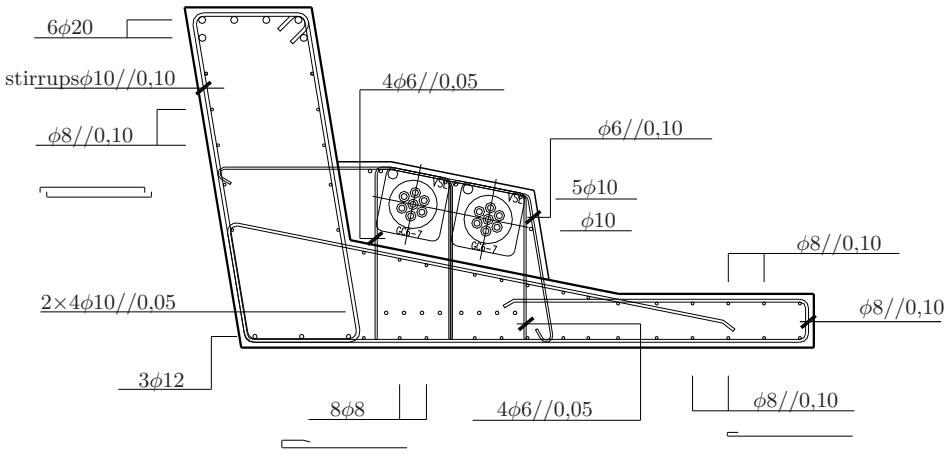

Figure 4.61: Reinforcement in the blister anchorage zone - Cross section

4.5 Comparison between the reinforcement of the ORC and HPFRC blister models

Table 4.9 presents the steel reinforcement weight for the ties considered in the strut-and-tie models presented early in this chapter, for each tendon of the ORC blister model. The identification of ties is shown in Figure 4.62.

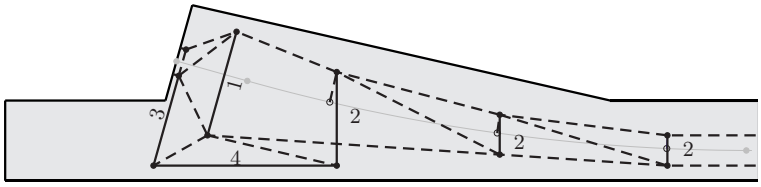

Figure 4.62: Identification of ties of the reference model

Table 4.9: Steel reinforcement weight for considered ties (reference model)

Tie	Adopted reinforcement	Steel reinforcement weight (N)	
		Tendon A	Tendon B
1	7 stirrups ϕ8//0,05	37,4	35,1
2	stirrups ϕ6//0,20	17,0	12,7
3	2ϕ8	28,7	27,9
4	5ϕ8	33,7	33,7
spiral	ϕ10	26,4	26,4

For the HPFRC blister model, the steel reinforcement weight corresponding to the considered ties is presented in Table 4.10. The identification of ties is shown in Figure 4.63.

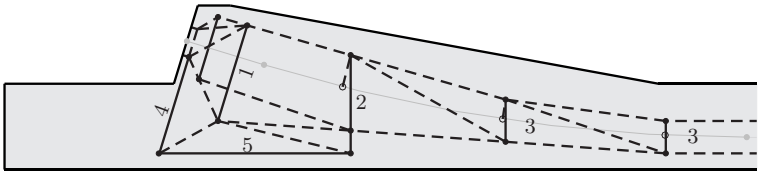

Figure 4.63: Identification of ties of the HPFRC blister model

Table 4.10: Steel reinforcement weight for the considered ties (HPFRC blister model)

Tie	Adopted reinforcement	Steel reinforcement weight (N)	
		Tendon A	Tendon B
1	4 stirrups ϕ6//0,05	10,5	9,9
2	5 stirrups ϕ6//0,10	16,2	16,1
3	stirrups ϕ6//0,20	8,6	6,0
4	3ϕ10	41,1	39,6
5	4ϕ10	41,3	41,3

Table 4.11 shows, for each model, the blister volume and the total steel reinforcement weight for the ties considered above.

Table 4.11: Blister volume and steel reinforcement weight for the considered models

Model	Blister volume (m^3)	Steel Reinforcement weight (N)
ORC blister model	0,158	279,1
HPFRC blister model	0,102	230,6

As can be seen, the volume of the HPFRC blister is approximately 65% of the volume of the ORC blister. Regarding the steel reinforcement, the difference is smaller, but the adoption of HPFRC results into a reduction of approximately 17% of the value obtained for the ORC blister.

The great advantage of adopting HPFRC in the anchorage blister, in addition to saving materials, was the decreased of the steel reinforcement density near the local anchorage zone, with the obvious improvements in concrete quality.

Chapter 5

Analysis of the Anchorage Corner Blisters

5.1 Introduction

An experimental program was carried out to study the transmission of prestressing force to the slab and web of the section, assess the models used in design and to study the feasibility of using reinforced high performance concrete in the blister, either with casting in situ, either with precast solutions.

The experimental program included three half scale models of the inferior corner of a box girder bridge: a reference specimen of ordinary reinforced concrete and two high performance fibre reinforced concrete (HPFRC) blister specimens. The three specimens had the same geometry, except for the anchorage blisters whose dimensions were reduced in the HPFRC blister specimens, and included a corner blister for two anchors, with a portion of the slab and the contiguous web. The design of the specimens was based on constructive considerations and the design of the reinforcement was made based in the tensile forces obtained from the strut-and-tie models, as described in the previous chapter.

ATENA (Cervenka et al., 2014), the non-linear finite element analysis software, was used to reproduce the experimental test of the anchorage blister models, in order to reach the failure of the models and therefore establish the load and failure mode, which was not possible to achieve in the laboratory.

This chapter begins by illustrating the execution of the anchorage blister specimens, presenting the monitoring equipment and the test procedure. After, the results of the tests are given and discussed. Afterwards, the non-linear analysis of the tested specimens is presented and the results are compared. Finally, recommendations for the design of anchorage blisters are proposed.

5.2 Experimental program

5.2.1 Ordinary reinforced concrete blister model - Reference model

5.2.1.1 Specimen execution

The specimens were produced in the precast company CONCREMAT - Préfabricação e Obras Gerais. The concrete strength class requested was a C30/37 and the reinforcing steel grade was an A500NR SD (f_{yk} = 500 MPa; ductility class C).

The reference blister model execution is shown in the figures below.

Figures 5.1 and 5.2 present the specimen reinforcement, as designed in the previous chapter and drawn in Figures 4.36 to 4.38.

(a) Front view **(b)** Side view

Figure 5.1: Reinforcement of the reference model anchorage blister

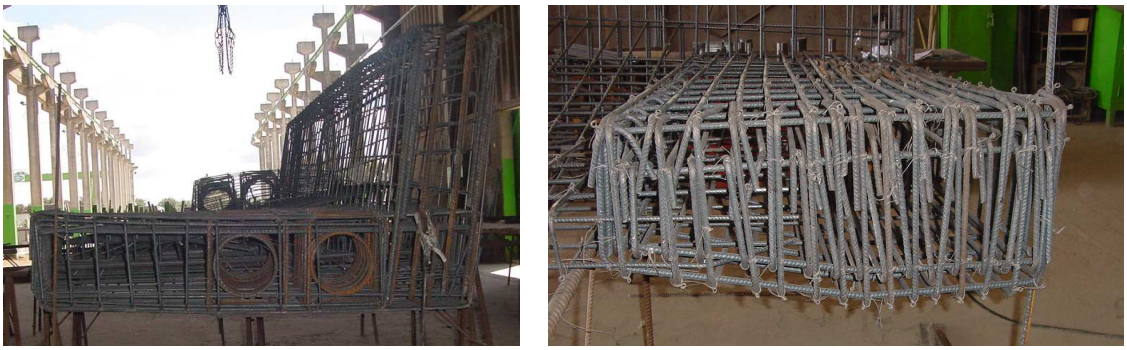

(a) Front view **(b)** Side view

Figure 5.2: Reinforcement of the reference model anchorage end block

Figure 5.3 shows the casting and surface finish of the specimen.

Additionally, for the determination of concrete strength at the date of the test, 150 mm width cubic specimens were cast.

Figure 5.3: Casting and surface finish of the reference blister specimen

5.2.1.2 Monitoring equipment

Before casting, a total of 66 strain gauges (model TML type FLA-5-11-5L), were affixed to diametrically opposite sides of selected reinforcing bars, whose position is indicated in Figures 5.5, 5.6, 5.7 and 5.8. Figure 5.4 shows the location of the sections presented in the aforementioned figures.

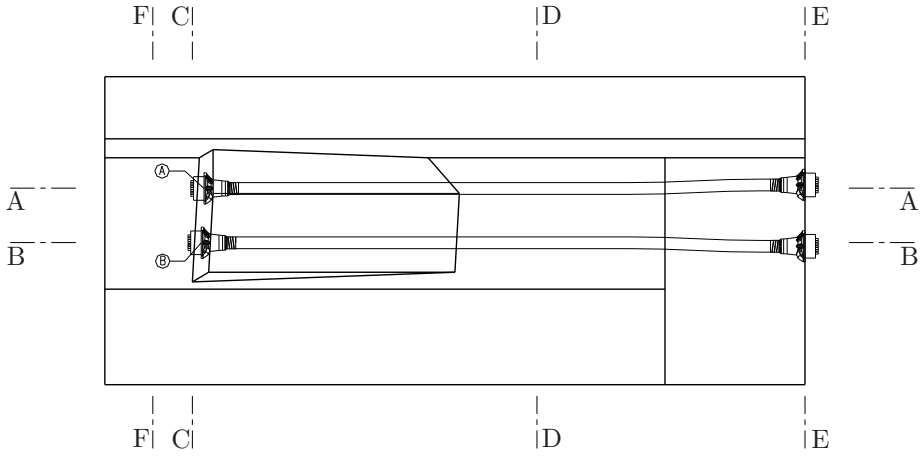

Figure 5.4: Position of the sections considered

It is noteworthy that the numbering shown in the figures below refers to pairs of strain gauges.

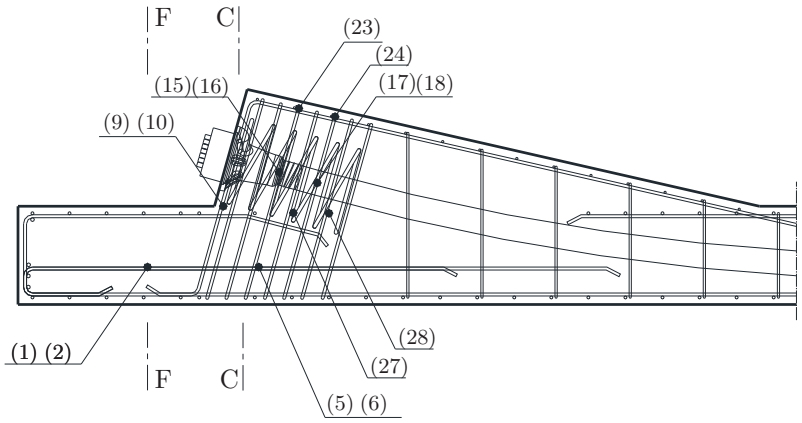

Figure 5.5: Strain gauges on the anchorage blister reinforcement (Section A-A)

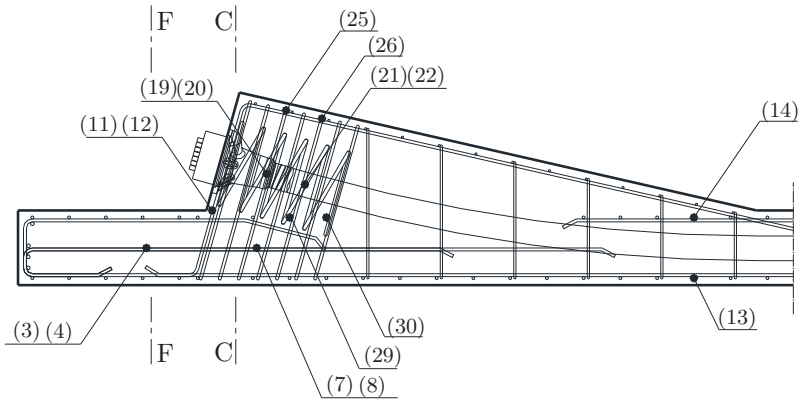

Figure 5.6: Strain gauges on the anchorage blister reinforcement (Section B-B)

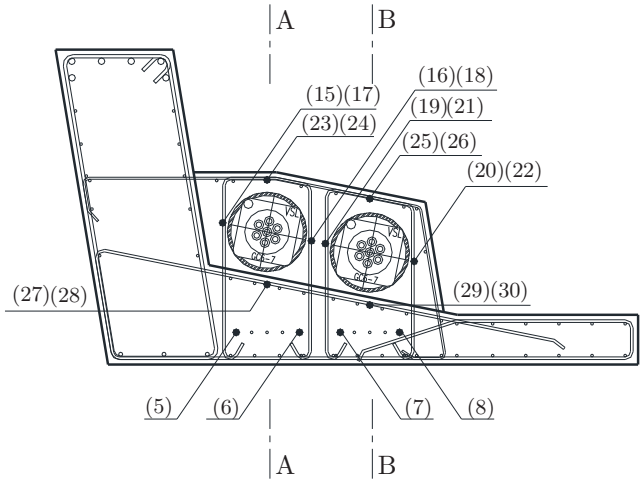

Figure 5.7: Strain gauges on the anchorage blister reinforcement (Section C-C)

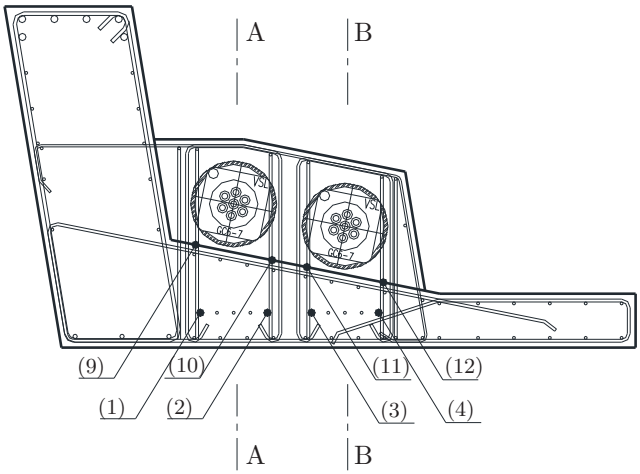

Figure 5.8: Strain gauges on the anchorage blister reinforcement (Section F-F)

Figure 5.9 presents some details and the positioning of the strain gauges used.

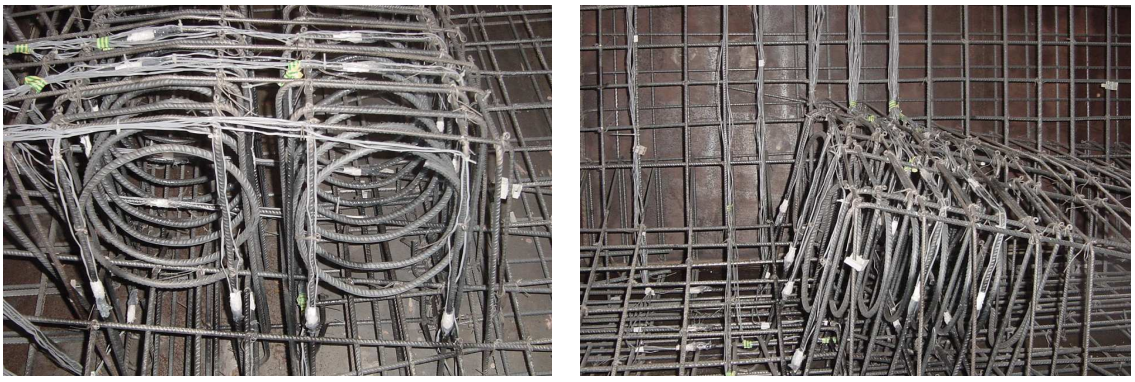

(a) Front view **(b)** Side view

Figure 5.9: Strain gauges on the anchorage blister reinforcement

The concrete surface strains were measured with relative displacement transducers TML type PI-2-50, PI-2-150 and PI-2-200 on the locations given in Figures 5.10, 5.11 and 5.12. These positions correspond to the zones of the surface of the specimen with the highest tensile stresses.

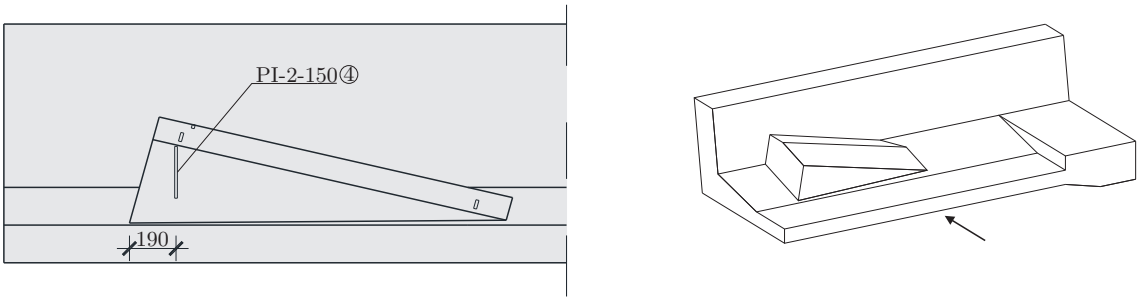

Figure 5.10: Identification and location of the relative displacement transducers (lateral view)

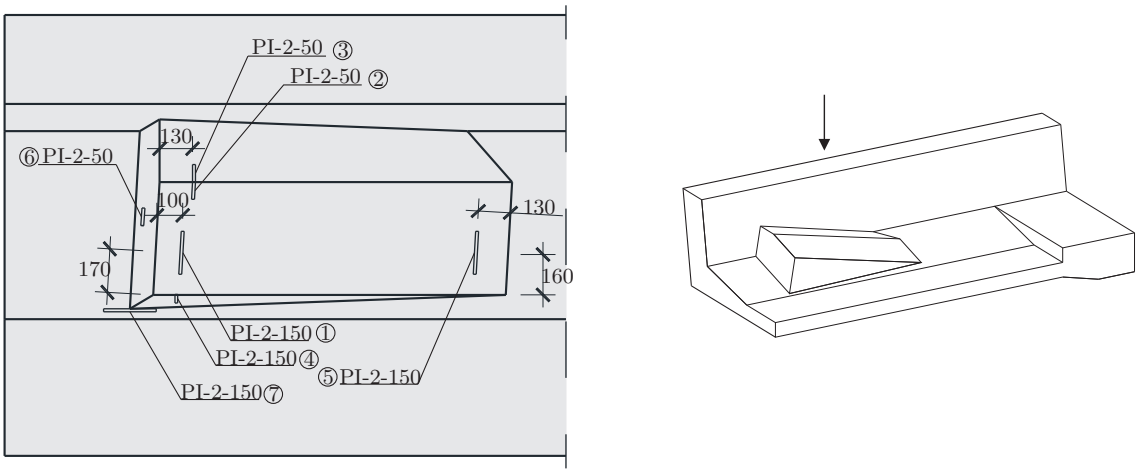

Figure 5.11: Identification and location of the relative displacement transducers (top view)

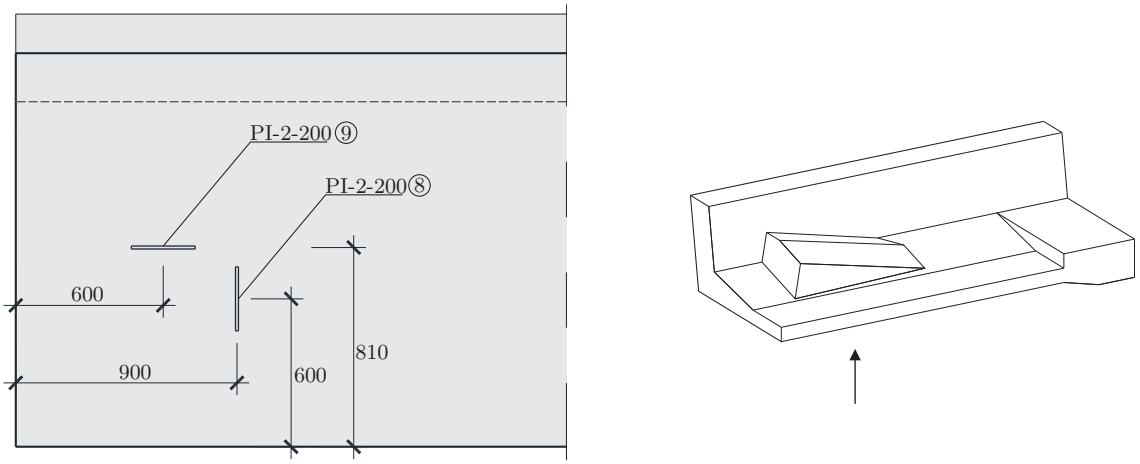

Figure 5.12: Identification and location of the relative displacement transducers (bottom view)

The displacement of the anchorage blister in relation to the bottom slab and web was

measured using two CDP-50 TML displacement transducers (transducers 1 and 2) and one CDP-100 TML displacement transducer (transducer 3), respectively, whose position and identification is shown in Figure 5.13.

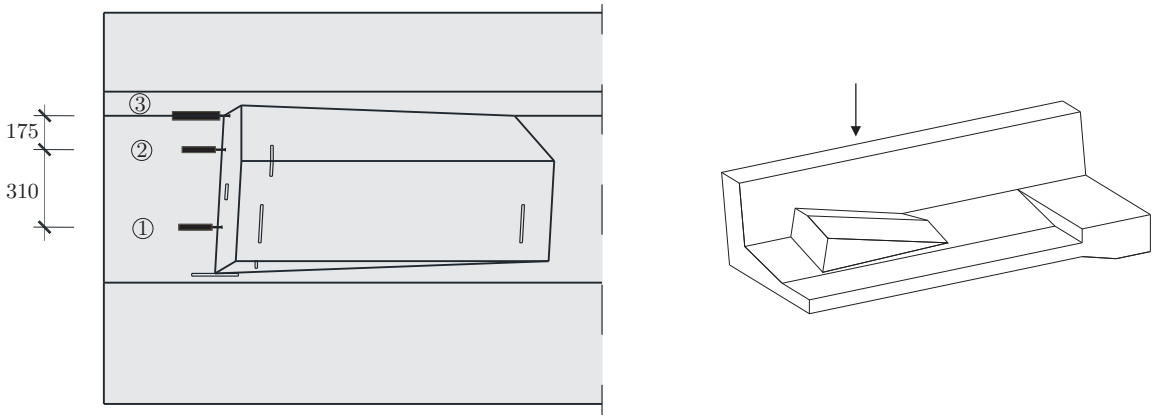

Figure 5.13: Identification and location of the displacement transducers (top view)

The elongation of the prestressing tendons was also measured using displacement transducers coupled to the hydraulic jacks (see Figures 5.16 and 5.17).

In order to quantify the value of the prestressing force in the anchorage blister for each tendon , two TML KCM-2MNA load cells with 2000 kN capacity were used.

The data acquisition was performed by a datalogger type HBM Centipede 100.

The monitoring equipment in the anchorage blister is shown in Figure 5.14.

Figure 5.14: Detail of the monitoring equipment in the anchorage blister

5.2.1.3 Test procedure and measurements

The bottom surface of the specimen was not levelled so the test was performed with the specimen rotated in relation to the actual position, as shown in Figure 5.15.

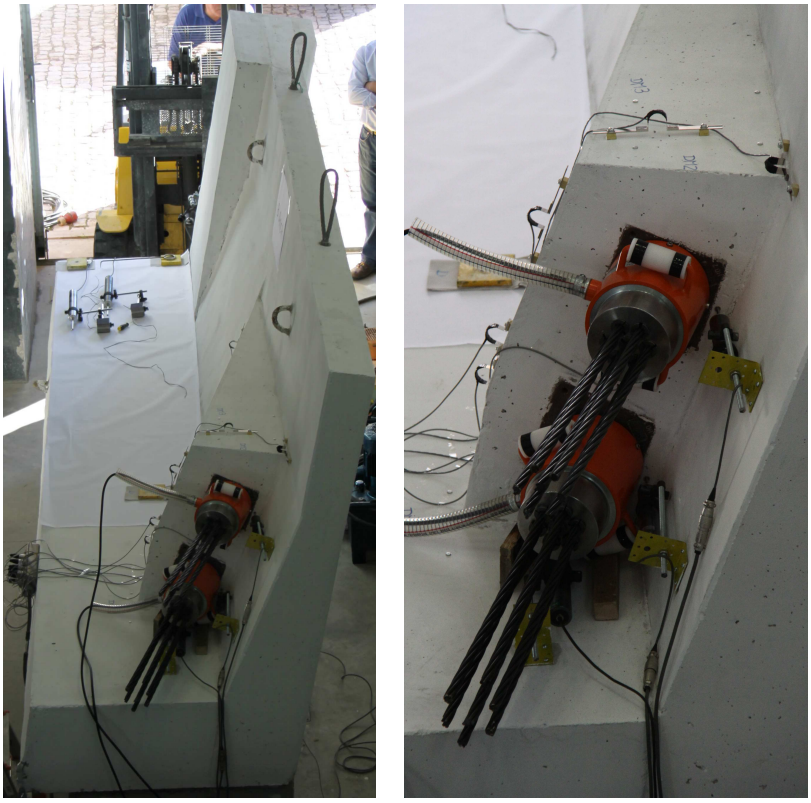

(a) General view of the specimen **(b)** Detail of the anchorage blister

Figure 5.15: Reference model before testing

Since the adoption of larger diameter ducts or anchorage bearing plates for a larger number of strands would misrepresent the behaviour of the specimen, the elements adopted were the ones usually used for seven strand tendons. Obviously, this decision limited the test since the force that can be applied is dependent on the failure force of the prestressing strands.

Thus, in a first phase of the test, two tendons with 7 strands of 0,6" type prEN 10138-3(2006) Y1860S7 with a nominal cross-section of 150 mm^2 each were used. The tendons were prestressed to 87% of the tensile strength. Given that for the maximum tensioning force of the tendons the model was far from failure, it was decided to perform a second phase, using 9 strands of the same type in each duct. The strands were prestressed to 80% of the tensile strength. A sudden malfunction in the oil pump prevented further testing.

In the first phase of the test, the tendons were tensioned with a VSL hydraulic jack type ZPE12-St2, as shown in Figure 5.16.

Figure 5.16: Detail of the VSL stressing jacks

The prestressing force was applied in increments of 154,7 kN, corresponding to a pressure increment of 50 bar in the hydraulic jack, up to 1701,7 kN, as shown in Table 5.1. All the readings of the monitoring equipment were recorded at intervals of 2 seconds.

Table 5.1: Loading steps in the first phase of the reference model test

Loading step	Pressure (bar)	P_0 (kN)	Loading step	Pressure (bar)	P_0 (kN)
1	50	154,7	7	350	1082,9
2	100	309,4	8	400	1237,6
3	150	461,1	9	450	1392,3
4	200	618,8	10	500	1547,0
5	250	773,5	11	550	1701,7
6	300	928,2			

In the second phase of the test, the tendons were tensioned with a STRONGHOLD hydraulic jack type G-200, as shown in Figure 5.17.

Figure 5.17: Detail of the STRONGHOLD stressing jacks

In this phase of the test, it was necessary to use an adapter made with welded steel plates for the transition between an originally intended anchorage bearing plate for 7 strands to an anchor head or hydraulic jack for 9 strands. Figures 5.18a and 5.18b show the adapters used for the live and dead-end extremities, respectively.

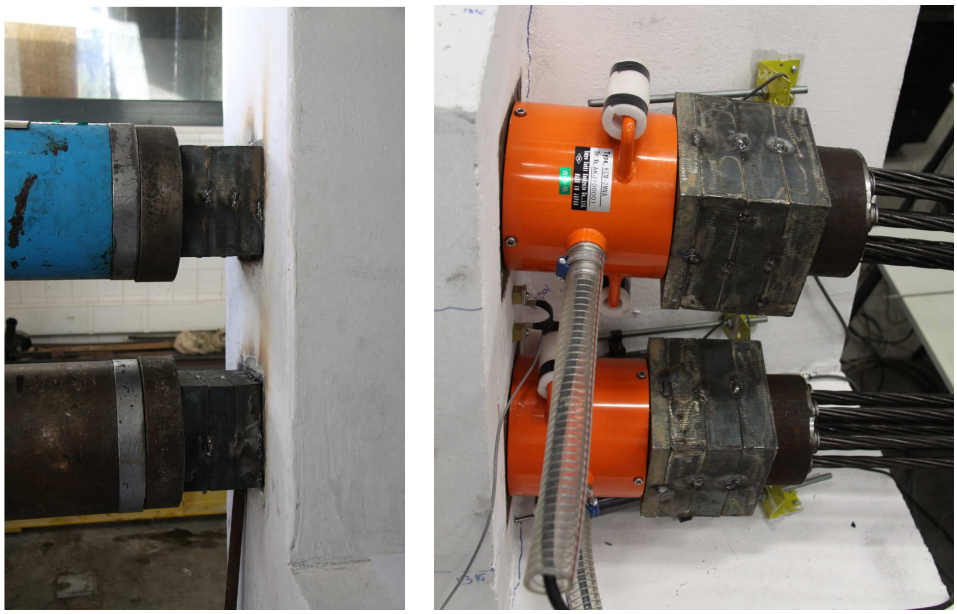

(a) Live-end **(b)** Dead-end

Figure 5.18: Steel adapters used in the second phase of the test

In this case, the prestressing force was applied in increments of 133,6 kN, which corresponds to a pressure increment of 50 bar in the hydraulic jack, up to 1870,4 kN. The loading steps are defined in Table 5.2.

Table 5.2: Loading steps in the second phase of the reference model test

Loading step	Pressure (bar)	P_0 (kN)	Loading step	Pressure (bar)	P_0 (kN)
1	50	133,6	8	400	1068,8
2	100	267,2	9	450	1202,4
3	150	400,8	10	500	1336,0
4	200	534,4	11	550	1469,6
5	250	668,0	12	600	1603,2
6	300	801,6	13	650	1736,8
7	350	935,2	14	700	1870,4

All the readings of the monitoring equipment were recorded at intervals of 2 seconds.

5.2.1.4 Experimental results

Evolution of cracking during the test

First phase of the test

The first cracks appeared in the anchorage blister and have been detected in the ninth load level, as shown in Figures 5.19 and 5.20.

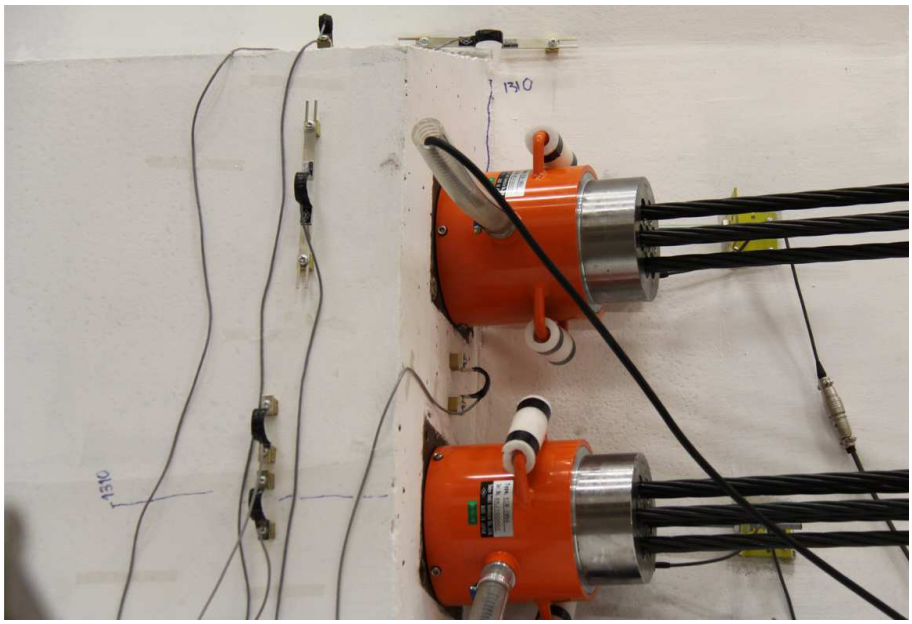

Figure 5.19: General view of cracking on the anchorage blister at the ninth load level

(a) Relative displacement transducer 3 **(b)** Relative displacement transducer 4

Figure 5.20: Detail of cracking on the anchorage blister at the ninth load level

At the tenth load step, a longitudinal crack appeared on the upper surface of the slab, on the alignment of one of the prestressing tendons, between the blister and the end block (see Figure 5.21) and, after, on the underside of the bottom slab (see Figure 5.22).

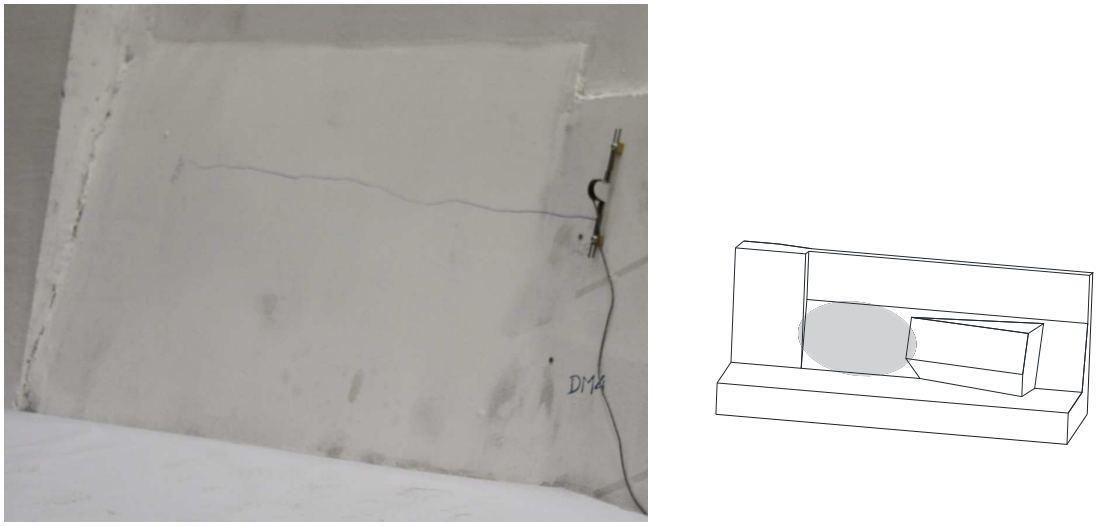

Figure 5.21: Cracking between the blister and the end block at the tenth load level

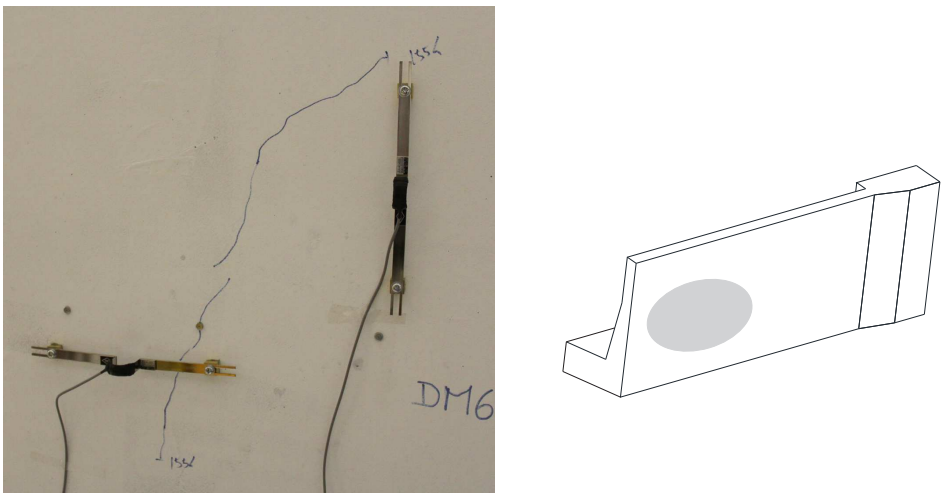

Figure 5.22: Cracking on the underside of the bottom slab at the tenth load level

Second phase of the test

In this second phase, new cracks were detected on the underside of the bottom slab at the eighth load increase, as shown in Figure 5.23.

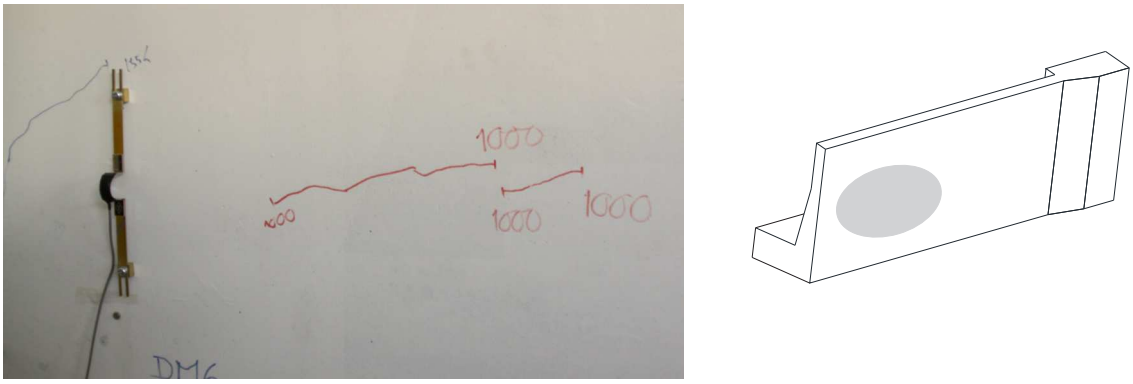

Figure 5.23: Cracking at the underside of the bottom slab in the eighth load level

At the twelfth load step a longitudinal crack appeared on the upper face of the slab, along the alignment of the other prestressing tendon, between the blister and the end block (see Figure 5.24).

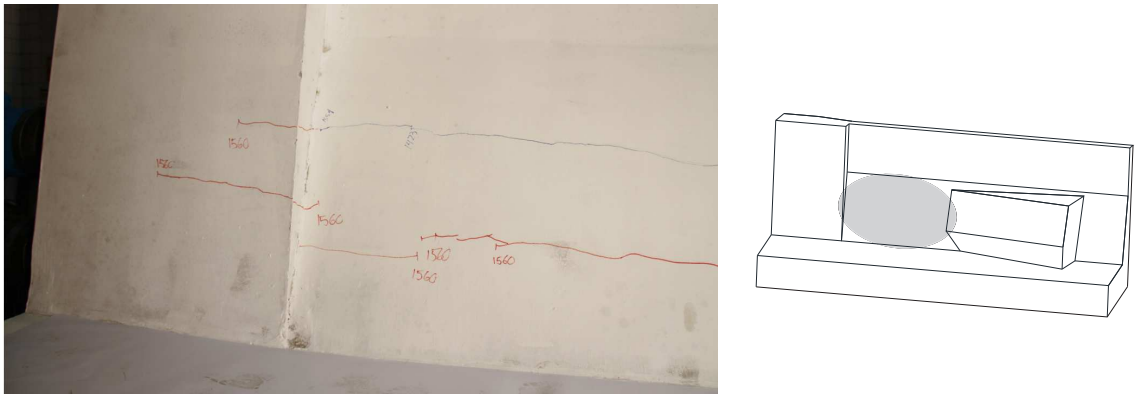

Figure 5.24: Cracking between the blister and the end block at the twelfth load level

Cracking increased also on the anchorage blister, as shown in Figure 5.25.

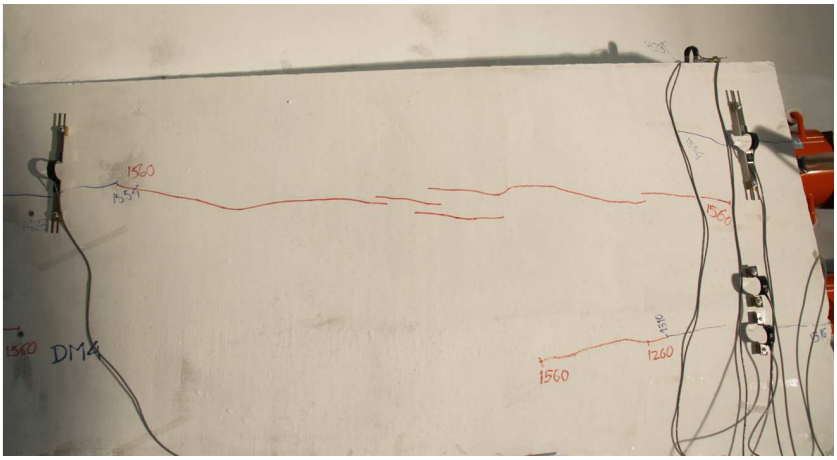

Figure 5.25: Cracking on the anchorage blister

On the upper face of the web, cracking was also detected at this load step (Figure 5.26).

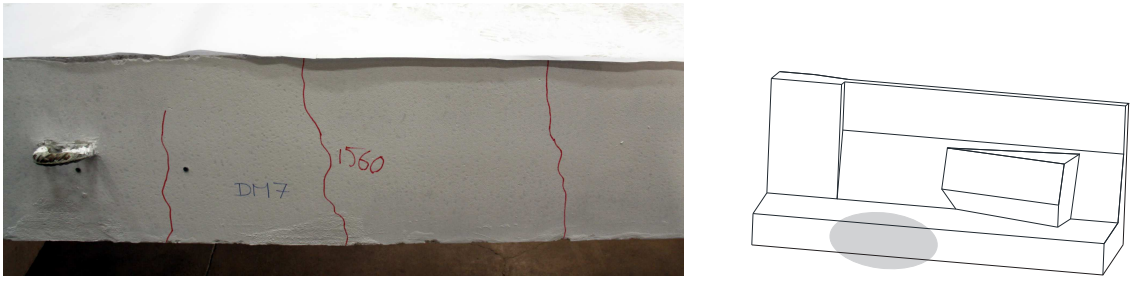

Figure 5.26: Cracking on the top surface of the web

Figures 5.27 and 5.28 show the appearance of the blister and underside of the bottom slab at the end of the test.

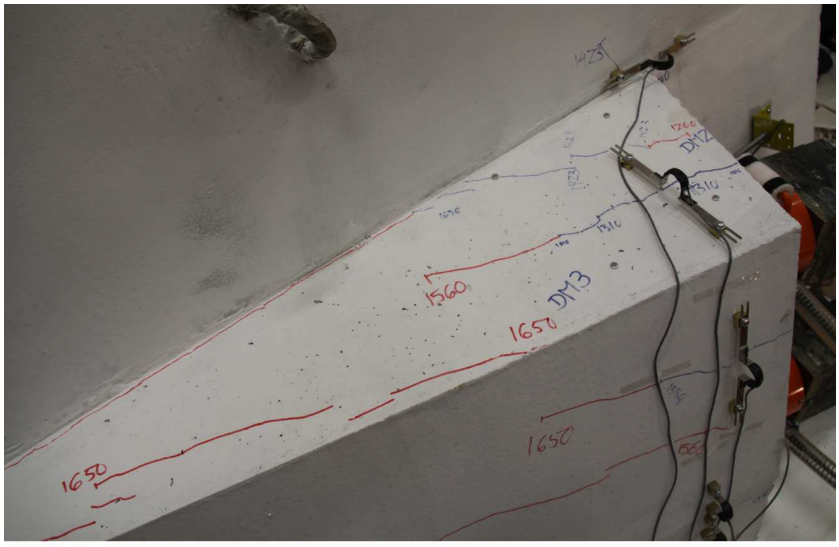

Figure 5.27: Cracking on the anchorage blister

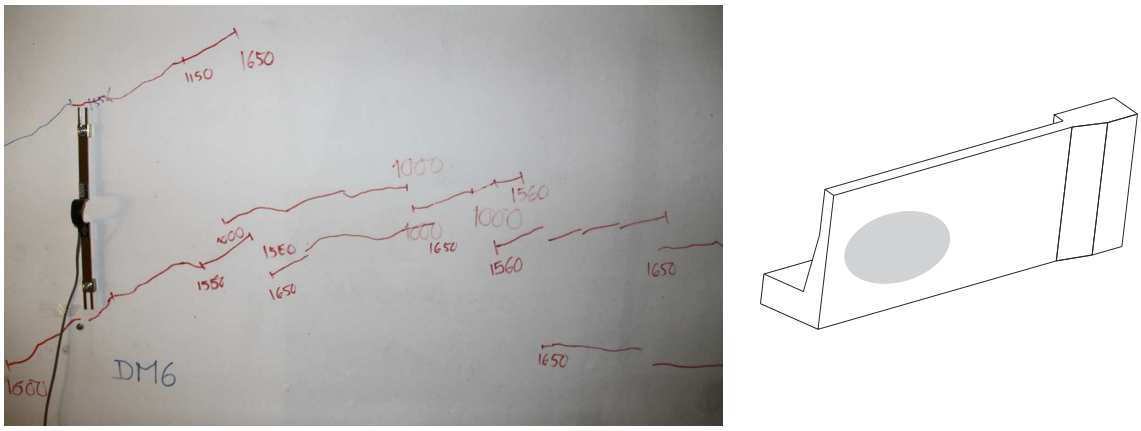

Figure 5.28: Cracking on the underside of the bottom slab at the end of the test

As can be seen in Figures 5.19 to 5.28 above, the main cracks opened in the relative displacement transducers area, denoting a good agreement between the elastic 3D finite element analysis and the experimental results.

Results of parameters recorded throughout the test

Figures 5.29a and 5.29b show the evolution of the measured load with time, for the first and second phases of the test, respectively.

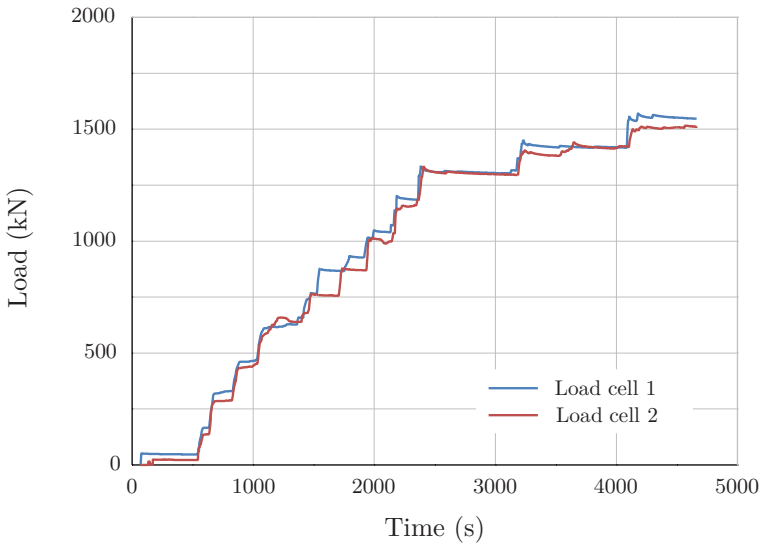

(a) First phase of the test

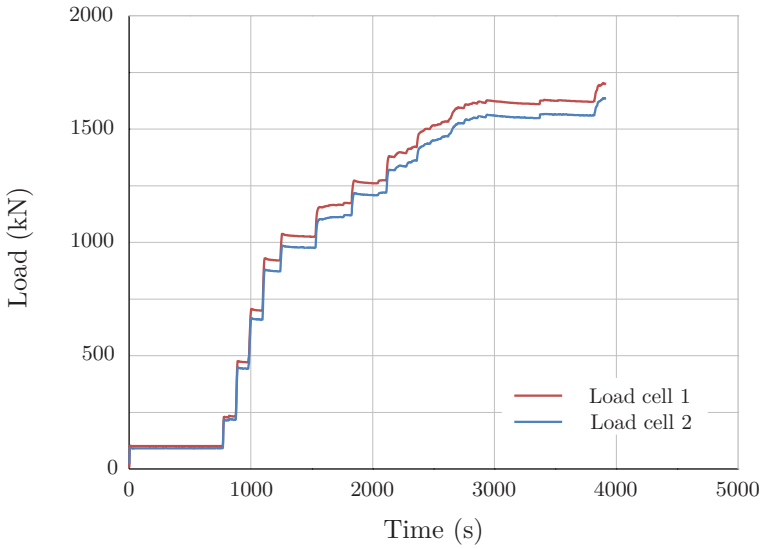

(b) Second phase of the test

Figure 5.29: Evolution of the measured load with time

It should be noted that the applied load, presented in Tables 5.1 and 5.2, does not correspond to the measured load because the load cells were located in the anchorage blister and the post-tensioning was applied at the opposite end. The difference between the two corresponds to the loss of prestressing force by friction.

As shown in Figures 5.29a and 5.29b above, at the ninth and tenth loading steps for the first phase of the test and eleventh and twelfth loading steps for the second phase of test, the loading was kept constant for about 15 minutes for observation and crack tracking. This fact caused some creep in the specimen, as will be seen in the figures below.

Since there are significant residual values of displacements and strains at the end of the first phase of the test, the results of the two phases will be presented on the same graphs.

The evolution of the blister displacements with the average measured load is presented in Figure 5.30.

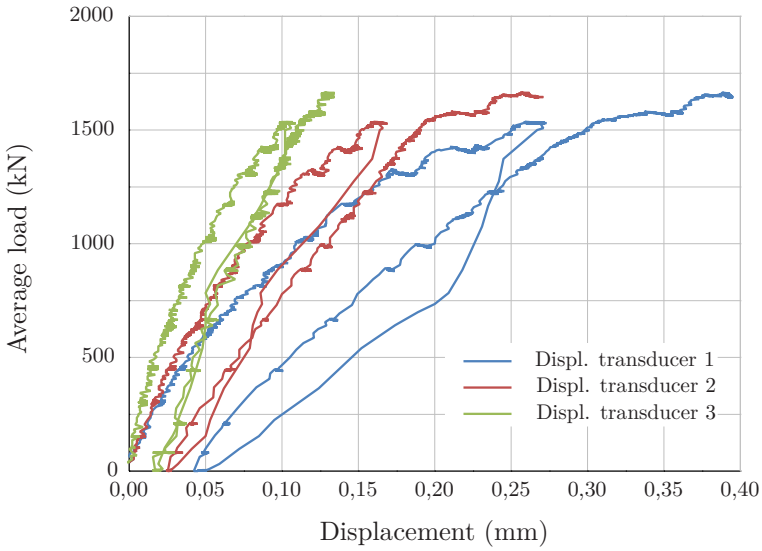

Figure 5.30: Evolution of the blister displacements with the average load

As can be seen, the measured displacements are smaller as closer to the web the transducer is. There is a residual displacement at the end of the first phase of the test.

The evolution of the relative displacements in the concrete surface with the average measured load is illustrated in Figure 5.31.

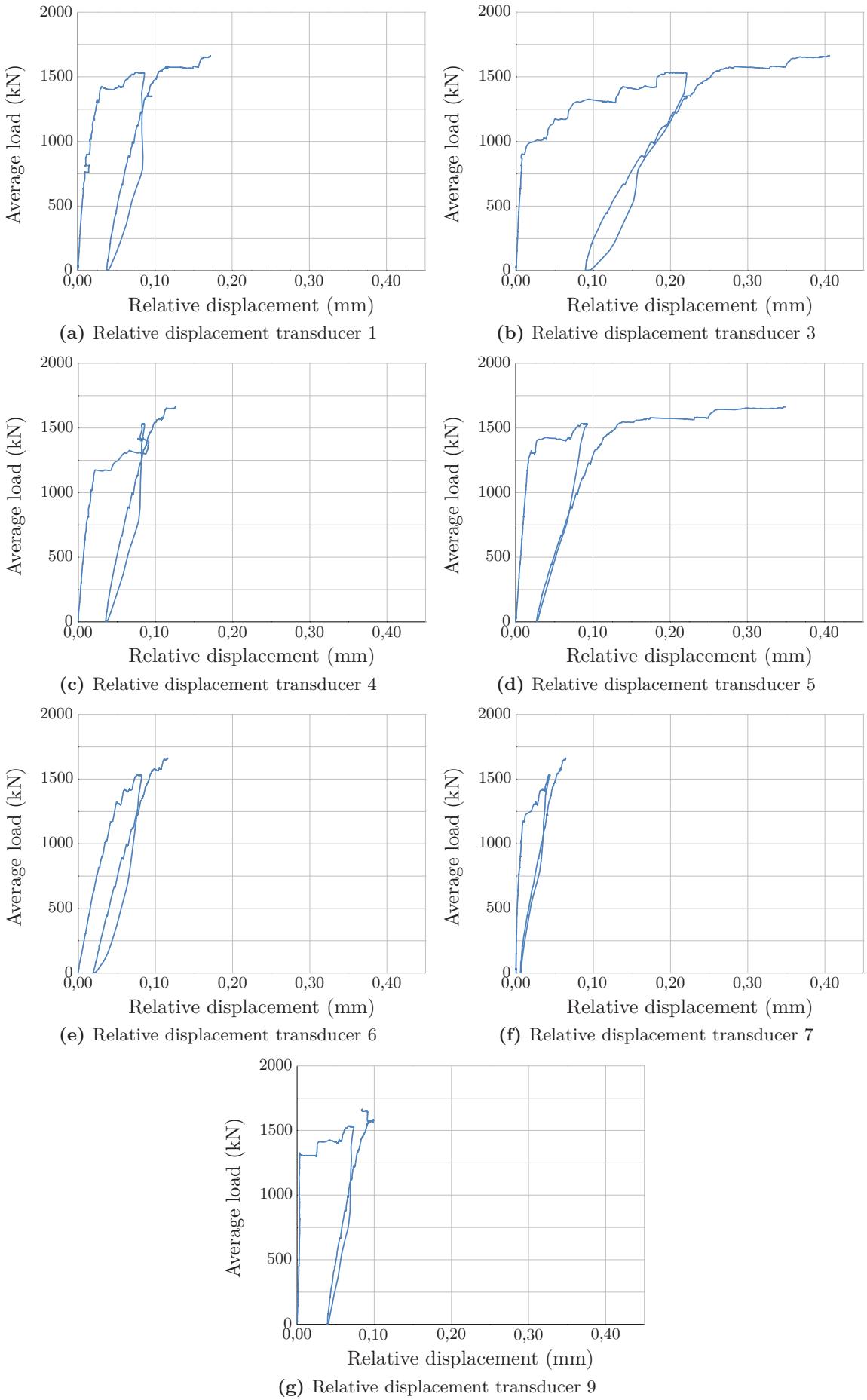

(a) Relative displacement transducer 1

(b) Relative displacement transducer 3

(c) Relative displacement transducer 4

(d) Relative displacement transducer 5

(e) Relative displacement transducer 6

(f) Relative displacement transducer 7

(g) Relative displacement transducer 9

Figure 5.31: Concrete surface relative displacements vs average load

The relative displacement transducers 3 and 5 (Figure 5.11) show displacement values greater than 0,3 mm, denoting large crack openings that can be seen in Figures 5.25 and 5.24, respectively.

Figure 5.32 shows the evolution of the strains of the reinforcing steel with the average measured load. The strains shown are the average of the obtained extensions of the two diametrically opposite placed strain gauges and are all below the steel yielding strain.

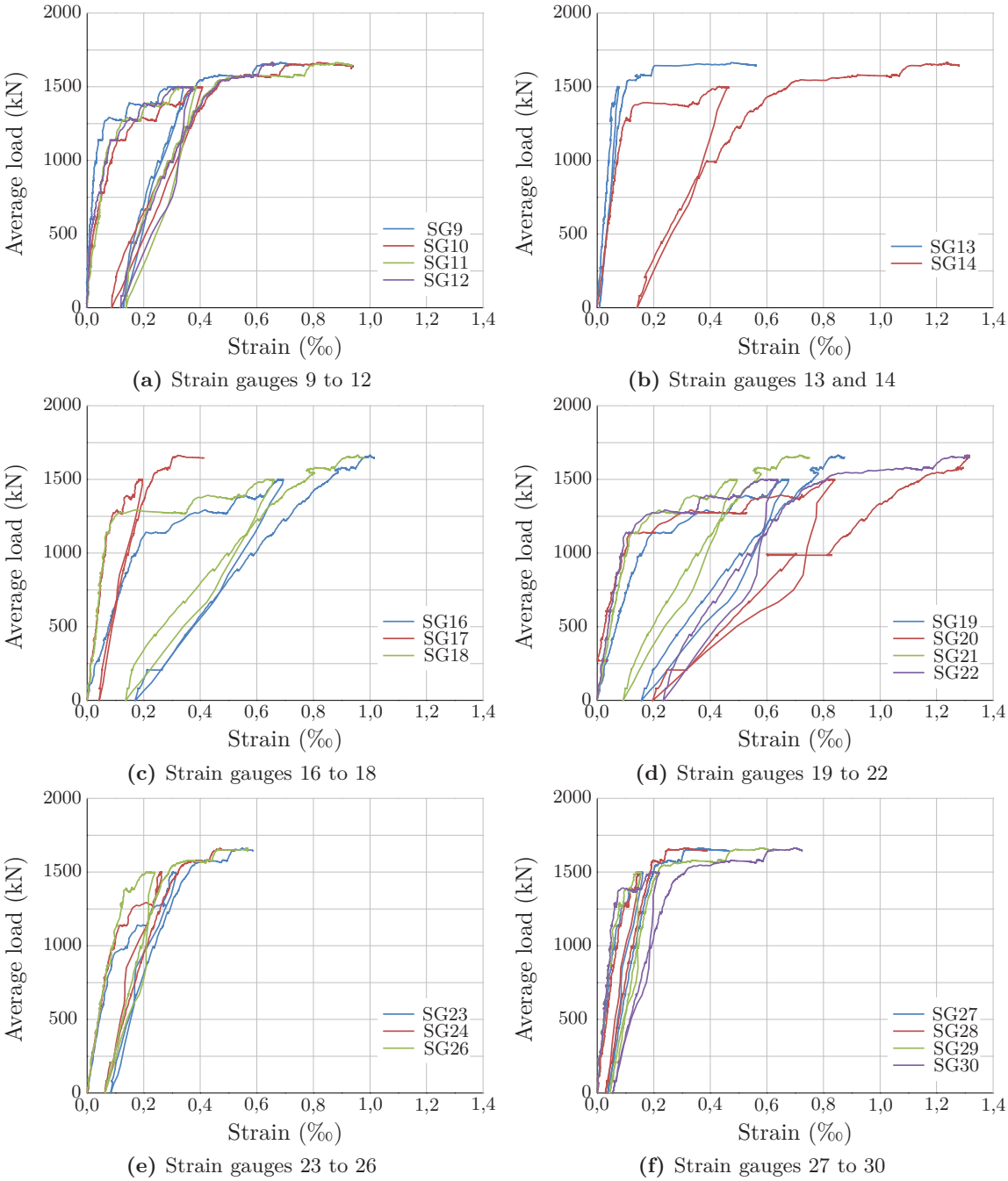

(a) Strain gauges 9 to 12

(b) Strain gauges 13 and 14

(c) Strain gauges 16 to 18

(d) Strain gauges 19 to 22

(e) Strain gauges 23 to 26

(f) Strain gauges 27 to 30

Figure 5.32: Strain of the reinforcing steel vs average measured load

The results for strain gauges 5 to 7 and 15 are not presented because there was an

error in the data acquisition. Strain gauges 1 to 4, 8 and 25 were damaged during the casting of the specimen.

From the analysis of the evolution of the reinforcing steel strains with the measured load, for the second phase of the test (Figure 5.32) it can be observed that strain gauges 14, 16 and 18 present lower stiffness than the strain gauges that showed similar behaviour in the previous test phase. Analysing its behaviour in the first phase of the test, in all cases for a certain load level, the strain has a significant increase without incrementing the load, which can be justified by the formation of a crack in the region of the strain gauge. In the particular case of strain gauge 14, the crack formation can be seen in Figure 5.31d.

Although the strain values are not directly related to the tensile force on the ties of the strut and tie models used in design, but with the steel reinforcement stress, it can be seen that:

- Strain gauges 16 to 22 have large strains because they are located in the reinforcement that corresponds to tie 1 of the strut and tie longitudinal models (see Figures 5.7 and 4.33), which is the one with larger tensile force. In this case, the ratio between the adopted and the required reinforcement is 1,0 and 1,3 for tendons A and B, respectively.
- Strain gauges 20 and 22 have the highest strains as they are located near the crack that can be observed in Figure 5.20b.
- Strain gauges 16, 18, 19 and 21 present similar strains because they are located in the legs of the stirrups between the two tendons. Among these, the strain gauges 19 and 21 have the largest strain, since they are located in the reinforcement that corresponds to tie 1 of tendon A (see Figures 5.7 and 4.33), which is the one with larger tensile force and smaller ratio between the adopted and the required reinforcement.
- Strain gauges 9 to 12 are located in the reinforcement that corresponds to tie 3 of the longitudinal strut and tie models (Figure 4.33). Among these, the strain gauges 10 and 11 present the largest strain because they are located in the reinforcement between the two tendons.

In the second phase of the test, the effect of creep is notorious for the eleventh and twelfth load steps. For these load steps, there is a significant increase of the relative displacement for transducers 1, 3 and 5 (Figures 5.31a, 5.31b and 5.31d, respectively) and of the strains in all cases (Figure 5.32).

Materials Characterisation

Ordinary concrete

The compressive strength of the concrete used in the ordinary reinforced concrete blister model was evaluated through uniaxial compression tests. These tests were performed

in accordance with EN 12390-3 (2001), except that the application of loading was performed under displacement control condition with a displacement speed of 0,02 mm/s until failure. Cubic specimens with 150 mm width were used. The geometry of the specimens is in accordance with the recommendations of EN 12390-1 (2000).

The values of the mean compressive strength and characteristic compressive strength for 150 mm cubic specimens are presented in Table 5.3.

Table 5.3: Compressive strength of cubic specimens of 150 mm at the age of the test

Number of specimens	$f_{cm,cube}$ (MPa)	δ	$f_{ck,cube}$ (MPa)
3	34,6	2,1%	33,4

The coefficient of variation (δ) was determined using equation (2.1) presented in Chapter 2. The characteristic compressive strength of concrete (f_{ck}) was obtained from the values of the mean compressive strength achieved in the tests assuming the normal distribution equation (2.2) (see Chapter 2).

Tensile splitting tests were performed in accordance with EN 12390-6 (2000), except that the application of loading was done under displacement control condition with a displacement speed of 0,02 mm/s until failure. Table 5.4 presents the values of the tensile splitting strength and mean axial tensile strength for the concrete used.

Table 5.4: Tensile splitting strength of cylindrical specimens at the age of the test

Number of specimens	$f_{ct,sp}$ (MPa)	δ	f_{ctm} (MPa)
6	2,7	29,5%	2,4

The mean value of the axial tensile strength (f_{ctm}) was calculated according to EN 1992-1-1 (2004), based on the value of the tensile splitting strength (see Chapter 2).

Reinforcing steel

The mechanical characteristics of the reinforcing steel were obtained by performing direct tensile tests according to EN 10002-1 (2001). Three test specimens of each diameter were tested using a tensile testing machine INSTRON 1343 with a 250 kN load capacity.

Table 5.5 presents the mean values of the yield stress f_y, maximum strength f_u and strain of steel reinforcement at maximum load ε_u. The modulus of elasticity of the steel has not been determined experimentally. The typical value of 200 GPa was adopted. The stress-strain diagrams obtained during the tests are presented in Figure 5.33.

Table 5.5: Steel reinforcement characteristics

Bar diameter (mm)	f_y (MPa)	f_u (MPa)	ε_u (%)
6	564	667	11,6
8	535	643	15,1
10	542	662	14,1
12	557	668	13,6
20	546	659	11,3

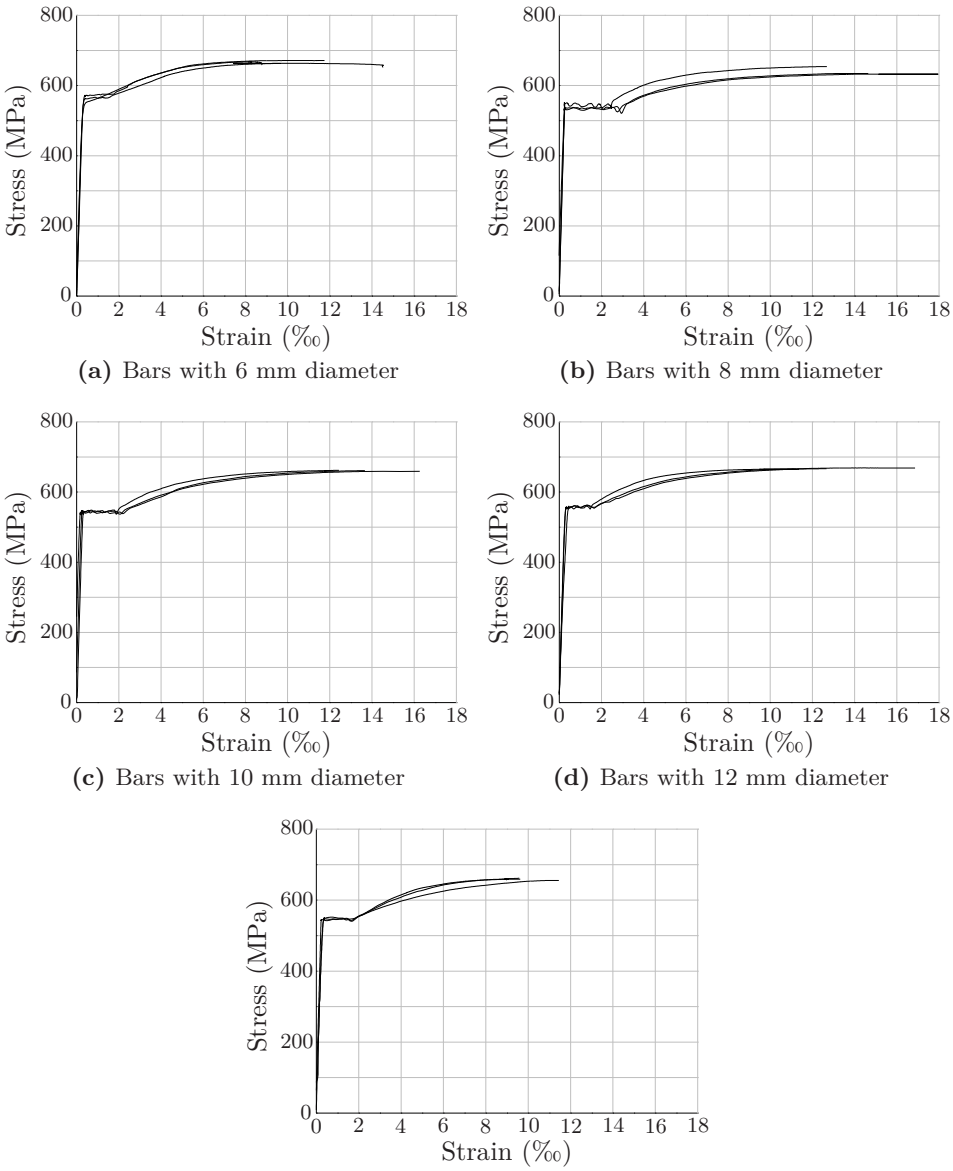

(a) Bars with 6 mm diameter

(b) Bars with 8 mm diameter

(c) Bars with 10 mm diameter

(d) Bars with 12 mm diameter

(e) Bars with 20 mm diameter

Figure 5.33: Steel reinforcement stress-strain diagrams

5.2.2 High Performance Fibre Reinforced Concrete blister model

5.2.2.1 Specimen execution

In the case of the HPFRC blister model, only the blister was cast with HPFRC. The remaining elements (bottom slab, web and end block) were cast with ordinary concrete. The strength class requested was a C30/37, i.e., the same as the reference model. The reinforcing steel grade was an A500NR SD (f_{yk} = 500 MPa; ductility class C).

Figure 5.34 presents the specimen reinforcement in the blister zone, as designed in the previous chapter and drawn in Figures 4.59 to 4.61. The reinforcement in the end block is similar to the one presented for the reference model.

(a) Front view **(b)** Side view

Figure 5.34: Reinforcement of the HPFRC blister model

In order to be able to cast the anchorage blister with a different concrete from the web and bottom slab, it was necessary to use an open mesh metal sheet, type hy-rib (BBA, 1993), at the interface of the two elements. Figure 5.35 shows the casting of the specimen in the blister zone.

(a) General view in the blister zone **(b)** Detail of metal sheet formwork

Figure 5.35: Casting of the HPFRC blister model

5.2.2.2 Monitoring equipment

Before casting, eight strain gauges (model TML type FLA-5-11-5L), were affixed to diametrically opposite sides of selected reinforcing bars, whose position is indicated in Figures 5.37 to 5.40. Figure 5.36 shows the location of the sections presented in the aforementioned figures.

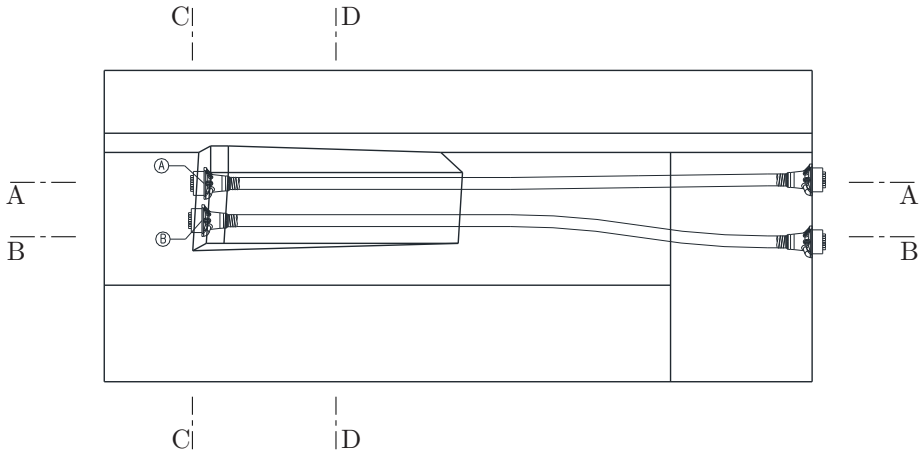

Figure 5.36: Position of the sections considered

In this case, each number shown in the figures below refers to a single strain gauge.

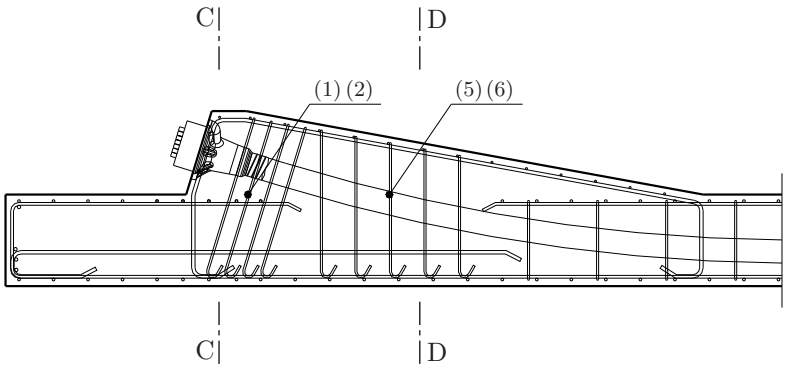

Figure 5.37: Strain gauges on the anchorage blister reinforcement (Section A-A)

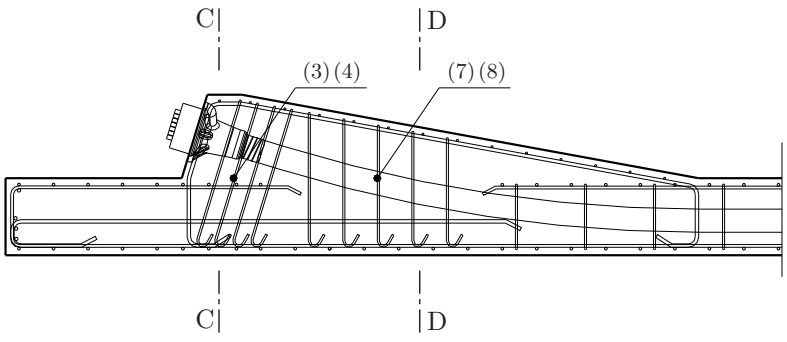

Figure 5.38: Strain gauges on the anchorage blister reinforcement (Section B-B)

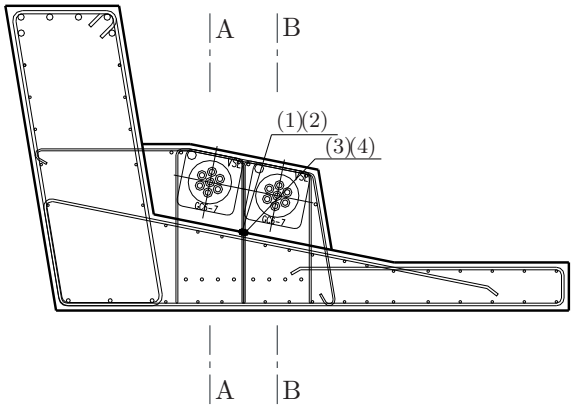

Figure 5.39: Strain gauges on the anchorage blister reinforcement (Section C-C)

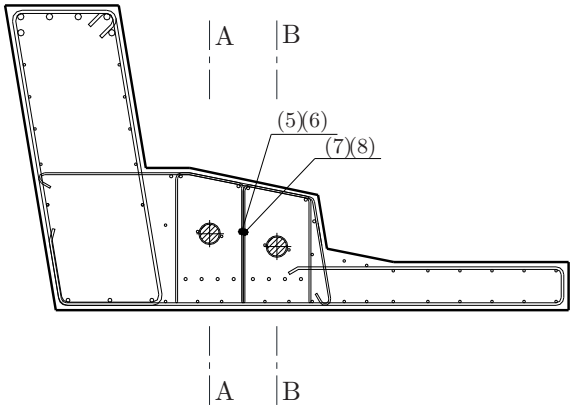

Figure 5.40: Strain gauges on the anchorage blister reinforcement (Section D-D)

The location and identification of the relative displacement transducers TML type PI-2-50, PI-2-150 and PI-2-200, used to measure the surface strains, is given in Figures 5.41, 5.42 and 5.43. As already mentioned, these positions correspond to the zones of the surface with the highest tensile stresses.

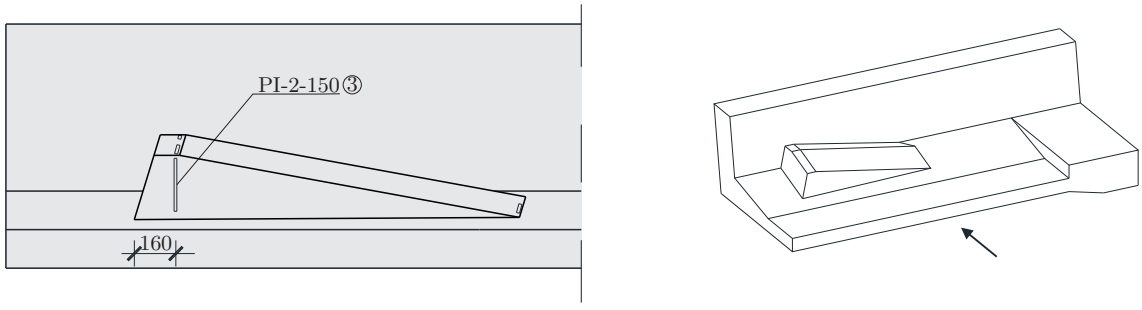

Figure 5.41: Identification and location of the relative displacement transducers (lateral view)

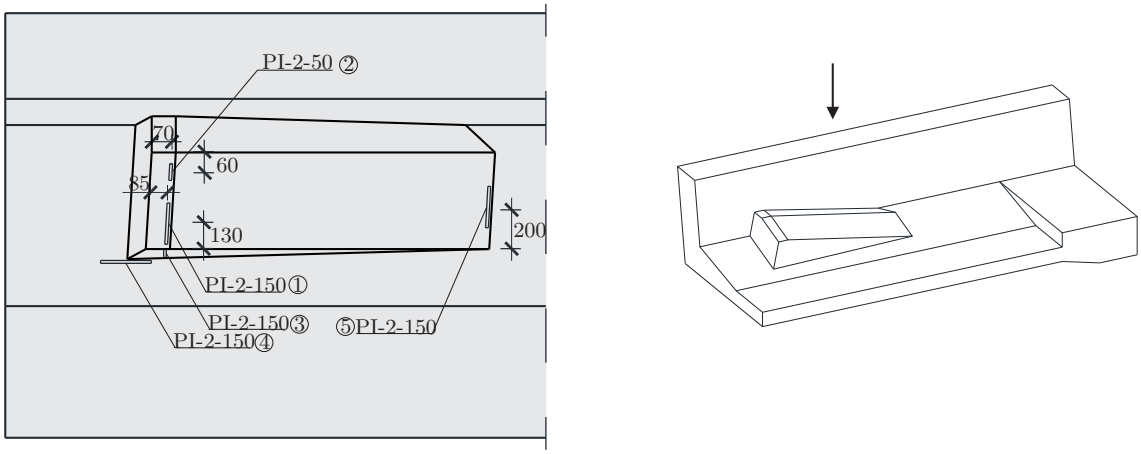

Figure 5.42: Identification and location of the relative displacement transducers (top view)

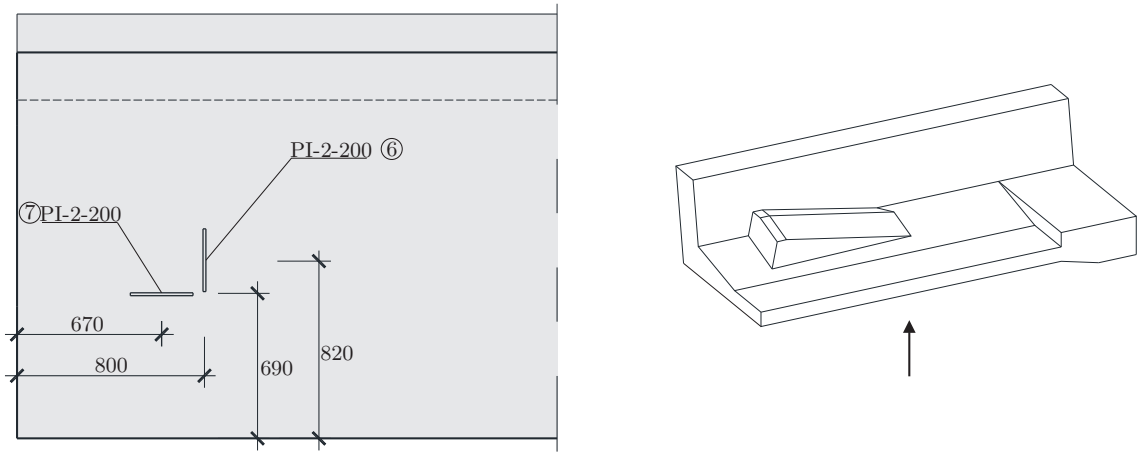

Figure 5.43: Identification and location of the relative displacement transducers (bottom view)

To measure the displacement of the anchorage blister in relation to the bottom slab, three CDP-50 TML displacement transducers were used. Its position and identification is shown in Figure 5.44, .

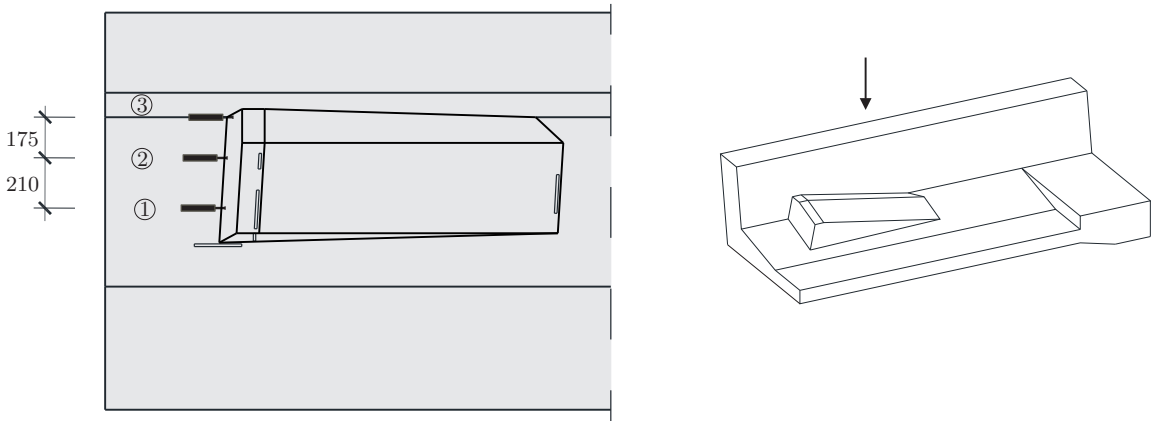

Figure 5.44: Identification and location of the displacement transducers

Two TML KCM-2MNA load cells with 2000 kN capacity were used to quantify the value of the prestressing force in the extremity of the anchorage blister for each tendon.

The data acquisition equipment used was composed by three HBM Spider8, with eight measurement channels per basic device, connected in series.

The monitoring equipment in the anchorage blister is shown in Figure 5.45.

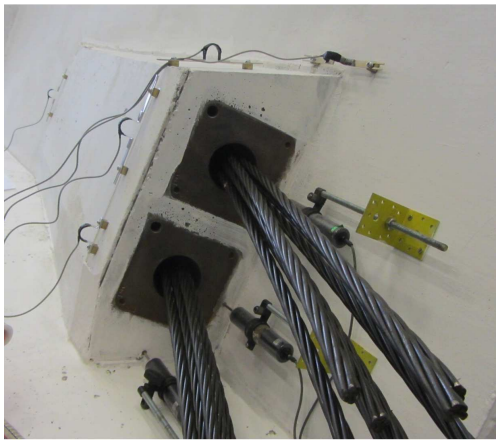

Figure 5.45: Detail of the monitoring equipment in the anchorage blister

5.2.2.3 Test procedure and measurements

As the reference model, this model was also tested rotated in relation to the actual position, as shown in Figure 5.46.

Figure 5.46: HPFRC blister model before testing

Based on the experience of the the first test, in this case it was decided to use 9 strands of 0,6" type prEN 10138-3(2006) Y1860S7 in each tendon from the beginning. The strands

were prestressed to 83,7% of the tensile strength, value that corresponded to the failure of the first strand.

A VSL hydraulic jack type ZPE19 was used, as shown in Figure 5.47.

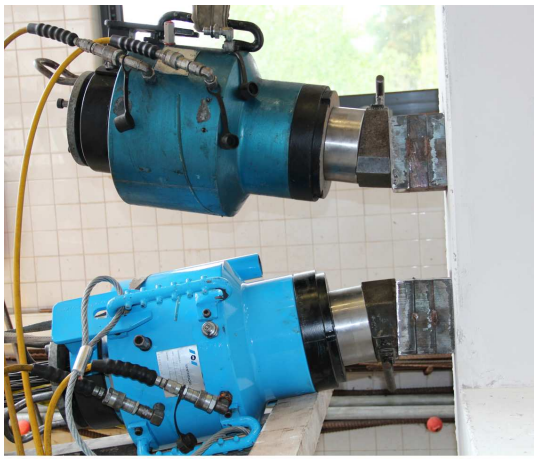

Figure 5.47: View of the VSL stressing jacks

As can be seen in Figure 5.47, in this test, besides being necessary to use the adapters made with welded steel plates for making the transition between an originally intended anchorage bearing plate for 7 strands to an anchor head or hydraulic jack to 9 strands, used previously, was also necessary to use curved extensions. Since the diameter of the hydraulic jacks that were available for testing was higher than the spacing between anchorages, the curved extensions intended to deviate the hydraulic jacks and thereby allow tensioning the two tendons simultaneously.

The prestressing force was applied in increments of 125,1 kN, corresponding to a pressure increment of 25 bar in the hydraulic jack, up to approximately 2101,3 kN, as shown in Table 5.6.

Table 5.6: Loading steps in the HPFRC blister model test

Loading step	Pressure (bar)	P_0 (kN)	Loading step	Pressure (bar)	P_0 (kN)
1	25	125,1	10	250	1250,8
2	50	250,2	11	275	1375,8
3	75	375,2	12	300	1500,9
4	100	500,3	13	325	1626,0
5	125	625,4	14	350	1751,1
6	150	750,5	15	375	1876,1
7	175	875,5	16	400	2001,2
8	200	1000,6	17	420	2101,3
9	225	1125,7			

All the readings of the monitoring equipment were recorded at intervals of 1 second.

5.2.2.4 Experimental results

Evolution of cracking during the test

The first cracks appeared on the underside of the bottom slab and on the anchorage blister, and have been detected at the eleventh load level, as shown in Figures 5.48 and 5.49, respectively.

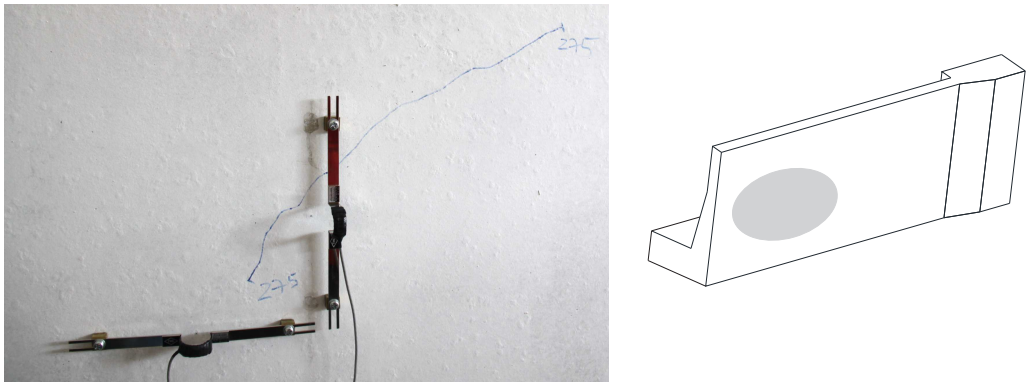

Figure 5.48: Cracking on the underside of the bottom slab at the eleventh load step

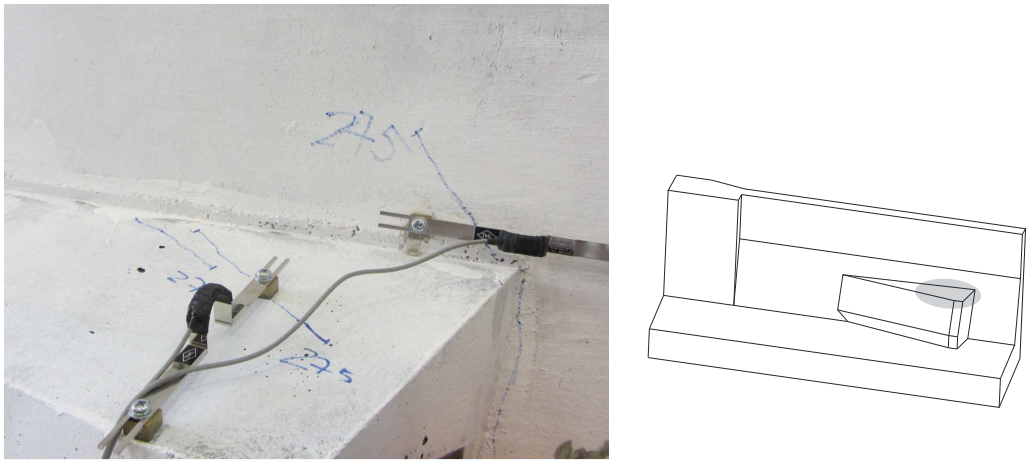

Figure 5.49: Cracking on the anchorage blister at the eleventh load step

In the fourteenth load step, a longitudinal crack appeared along the interface between the slab and the blister, as shown in Figure 5.50.

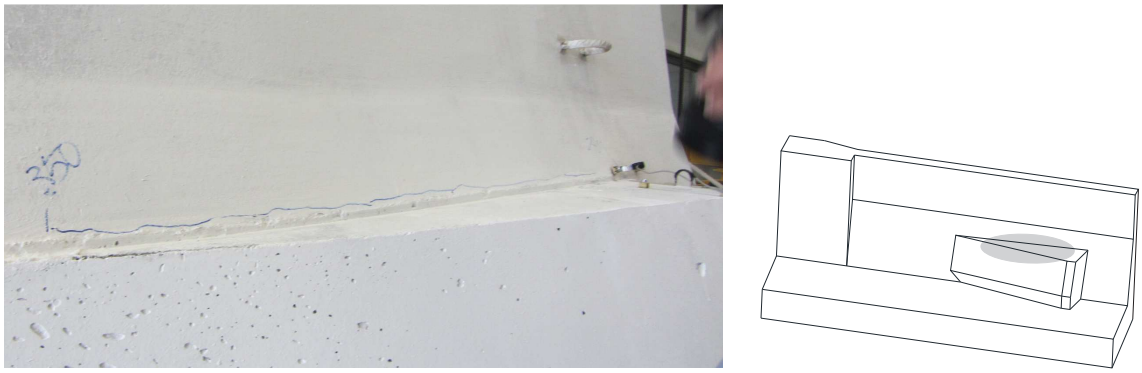

Figure 5.50: Cracking in the interface slab/blister at the fourteenth load step

In the fifteenth load step, a longitudinal crack appeared in the upper surface of the slab, on the alignment of one of the prestressing tendons, between the blister and the end block (see Figure 5.51).

Figure 5.51: Cracking between the blister and the end block at the fifteenth load step

Figures 5.52 and 5.53 present the appearance of the blister and the underside of the bottom slab at the end of the test.

Figure 5.52: Cracking on the anchorage blister

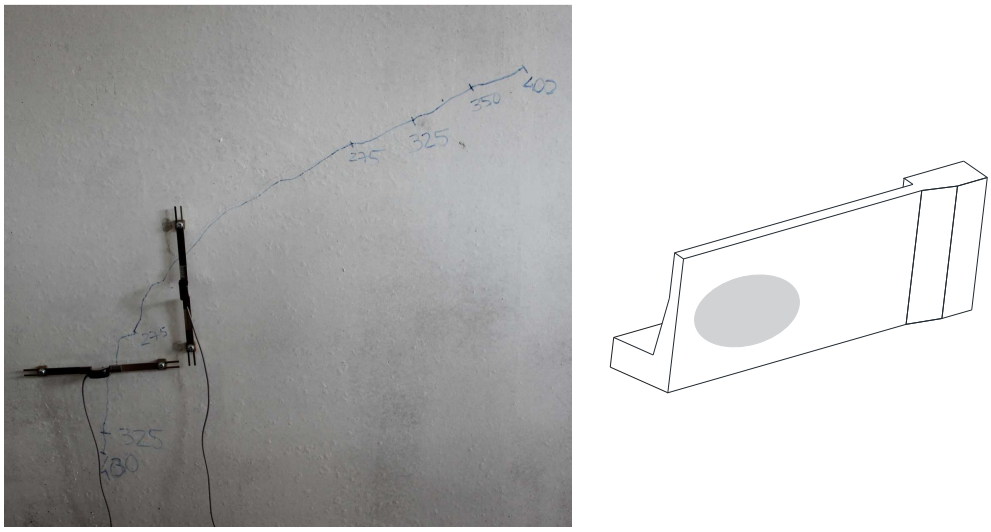

Figure 5.53: Cracking on the underside of the bottom slab at the end of the test

Figure 5.54 shows the strands that failed in the test.

Figure 5.54: Detail of the broken strands

Results of parameters recorded throughout the test

Figure 5.55 shows the evolution of the measured load with time, for the HPFRC blister model.

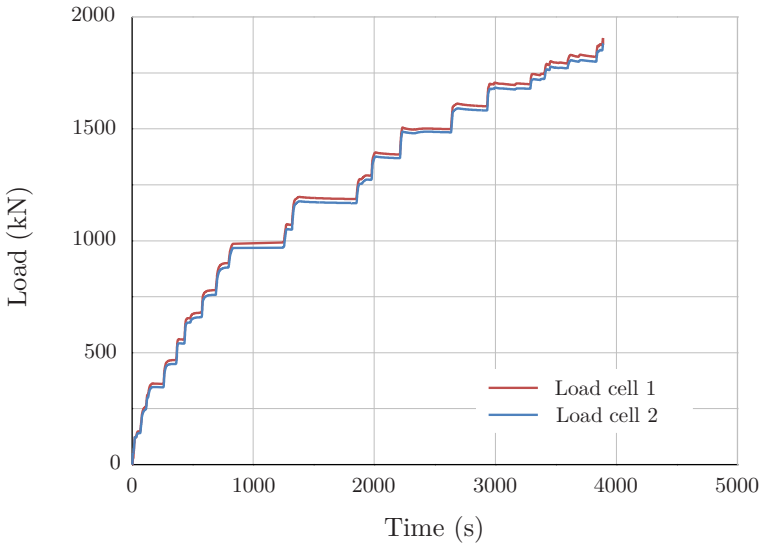

Figure 5.55: Evolution of the measured load with time

The evolution of the blister displacements with the average measured load is presented in Figure 5.56.

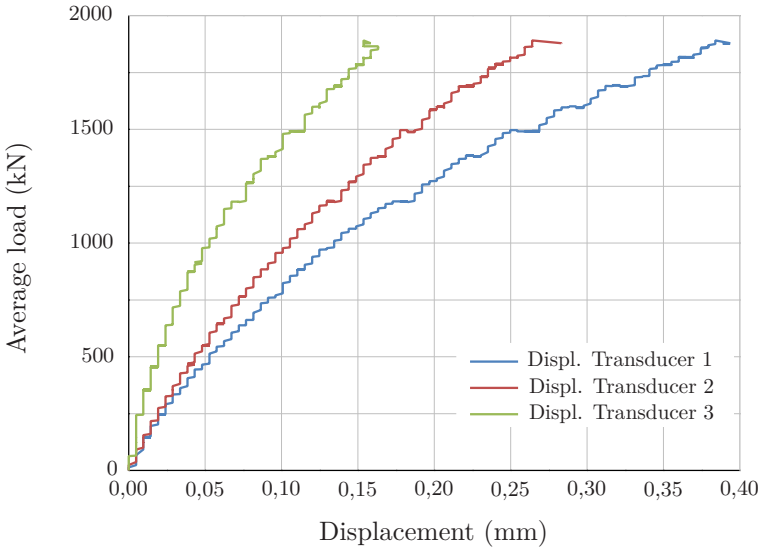

Figure 5.56: Evolution of the blister displacements with the average measured load

Figure 5.57 presents the evolution of the concrete surface relative displacements with the average measured load, for the transducers used in the test.

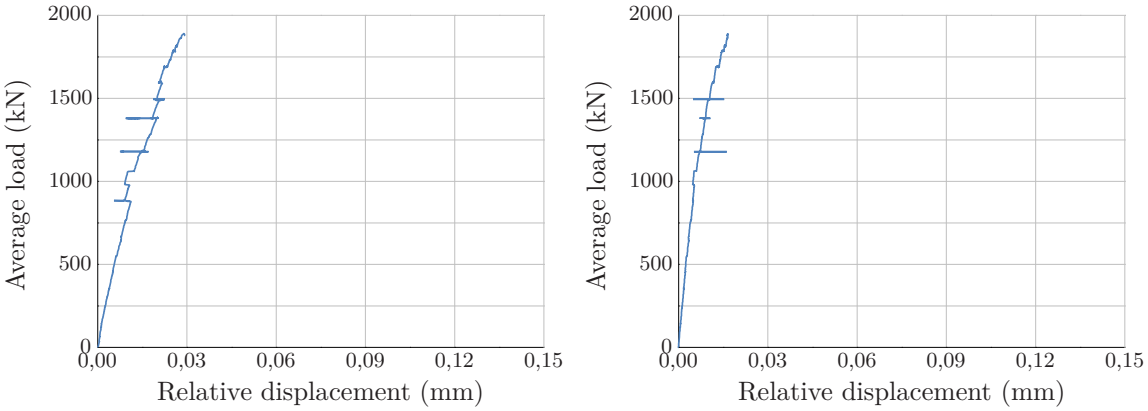

(a) Relative displacement transducer 1

(b) Relative displacement transducer 2

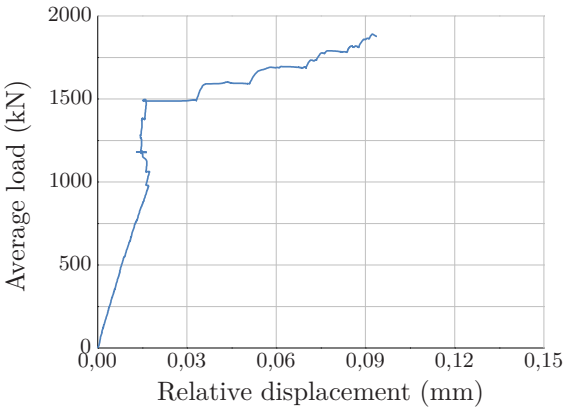

(c) Relative displacement transducer 3

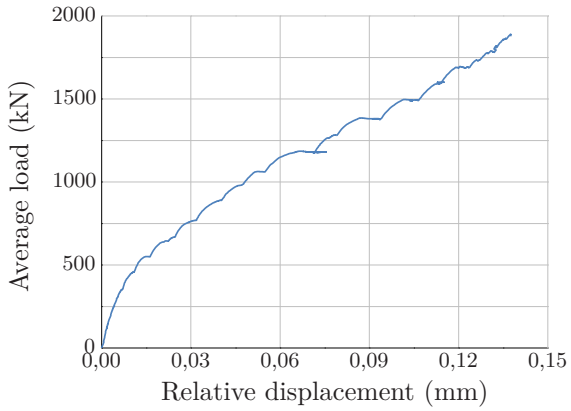

(d) Relative displacement transducer 4

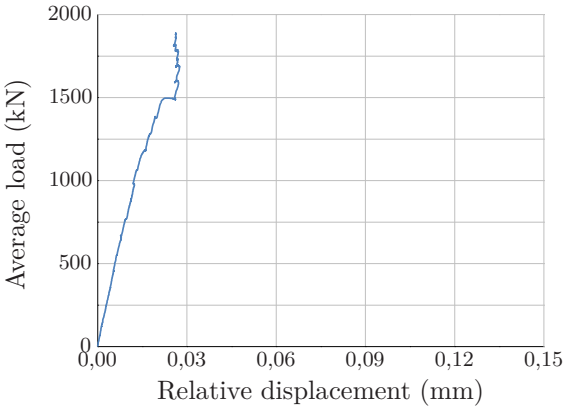

(e) Relative displacement transducer 5

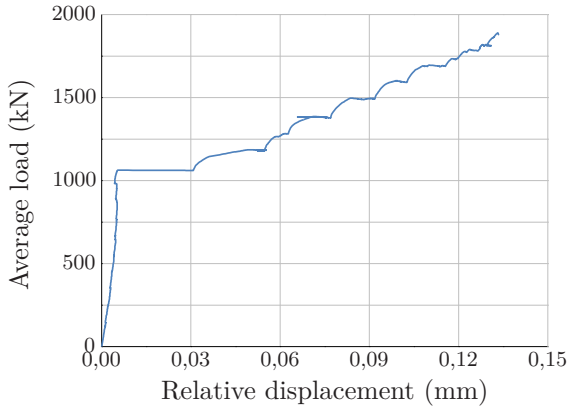

(f) Relative displacement transducer 6

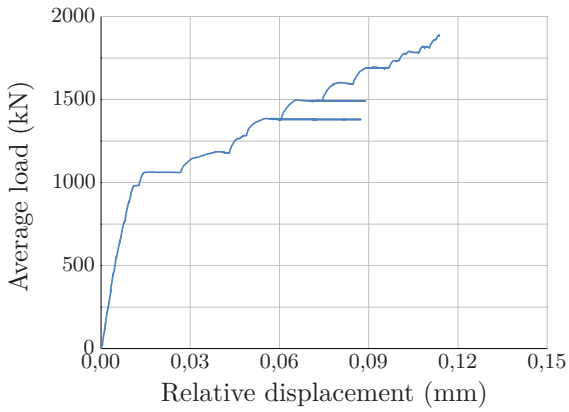

(g) Relative displacement transducer 7

Figure 5.57: Concrete surface relative displacements vs average measured load

Figure 5.58 shows the evolution of the strains of the reinforcing steel with the average measured load.

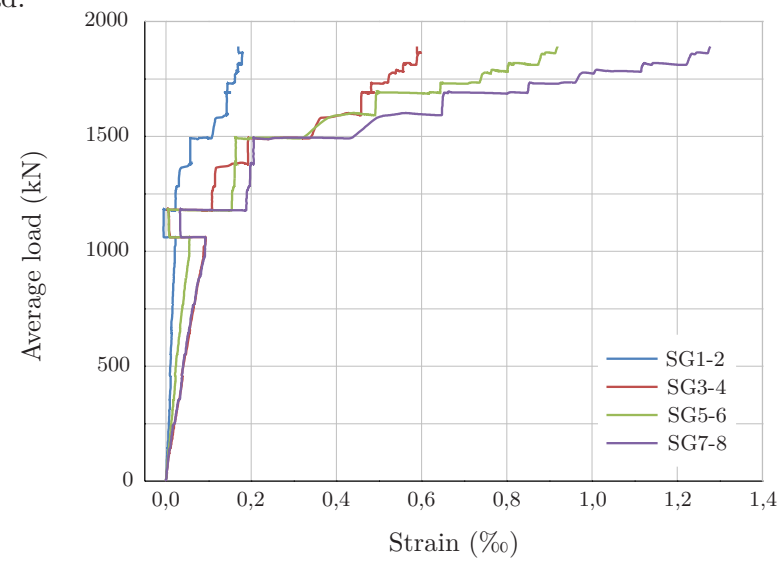

Figure 5.58: Strain of the reinforcing steel vs average measured load

A malfunction of the strain gauges occurred between load values of 1125 kN and 1250 kN. The highest strain values were measured in strain gauges 7 and 8, which correspond to tie 2 in the strut and tie model presented in Figure 4.56.

Materials Characterisation

Ordinary concrete

In accordance with the procedure adopted for the concrete characterisation of the ordinary reinforced concrete blister model, the compressive strength of the ordinary concrete used in the HPFRC blister model was evaluated through uniaxial compression tests, performed in accordance with EN 12390-3 (2001) using three cubic specimens with 150 mm width. Also in this case, the load application was performed under displacement control condition with a displacement speed of 0,02 mm/s until failure. The specimens geometry is in accordance with the recommendations of EN 12390-1 (2000).

The values of the mean compressive strength and characteristic compressive strength for the 150 mm cubic specimens, at the age of the test (87 days), are presented in Table 5.7. Table 5.7 also presents the mean value of the axial tensile strength.

Table 5.7: Mechanical properties of the ordinary concrete at the age of the test

Number of specimens	$f_{cm,cube}$ (MPa)	δ	$f_{ck,cube}$ (MPa)	f_{ctm} (MPa)
3	46,1	2,3%	44,4	3,3

The coefficient of variation (δ) was determined using equation (2.1) presented in Chapter 2.

The characteristic compressive strength of concrete (f_{ck}) was obtained from the values of the mean compressive strength achieved in the tests assuming the normal distribution equation (2.2) (see Chapter 2).

The mean value of the axial tensile strength (f_{ctm}) was calculated according to EN 1992-1-1 (2004), based on the value of the characteristic compressive strength referred to cylinder specimens, using equation (3.32) presented in Chapter 3).

HPFRC

The compressive strength of the HPFRC was evaluated through uniaxial compression tests, performed in accordance with EN 12390-3 (2001) in cubic specimens with 150 mm width and cylinders.

The values of the mean compressive strength and characteristic compressive strength for the 150 mm cubic specimens and cylinders, at the age of 87 days, are presented in Tables 5.8 and 5.9, respectively.

Table 5.8: HPFRC compressive strength for 150 mm cubic specimens at the age of the test

Number of specimens	$f_{cm,cube}$ (MPa)	δ	$f_{ck,cube}$ (MPa)
6	117,1	5,3%	107,9

Table 5.9: HPFRC compressive strength for cylinder specimens at the age of the test

Number of specimens	f_{cm} (MPa)	δ	f_{ck} (MPa)
3	97,8	4,1%	92,4

The concrete tensile strength was assessed by tensile splitting tests, performed in accordance with EN 12390-6 (2000), except that the application of loading was done under displacement control condition with a displacement speed of 0,02 mm/s until failure.

According to EN 1992-1-1 (2004), and based on the value of the tensile splitting strength, an approximate value of the mean value of axial tensile strength (f_{ctm}) was obtained using equation (3.32), presented in Chapter 2.

Table 5.10 presents the values of the tensile splitting strength and mean axial tensile strength for the HPFRC mixture at the age of the test (87 days).

Table 5.10: HPFRC tensile splitting strength and related mean tensile strength for cylinder specimens at the age of the test

Number of specimens	$f_{ct,sp}$ (MPa)	δ	f_{ctm} (MPa)
6	13,0	22,2%	11,7

Reinforcing steel

Table 5.5 presents the mechanical characteristics of the reinforcing steel used. The stress-strain diagrams obtained during the tests are presented in Figure 5.33.

5.2.3 High Performance Fibre Reinforced Concrete precast blister model

In the case of the HPFRC precast blister model, the blister was cast before the slab and web of the specimen.

To allow the precast blister to settle in the reinforcement of the bottom slab, simplifying its positioning during the casting of the remaining model, it was considered its dimension plus 15 mm corresponding to the concrete cover of the web and bottom slab, as shown in Figures 5.59 and 5.60. Also the opposite region to the anchorage zone was chamfered to get a minimum thickness of 50 mm and avoid fractures (see Figure 5.59).

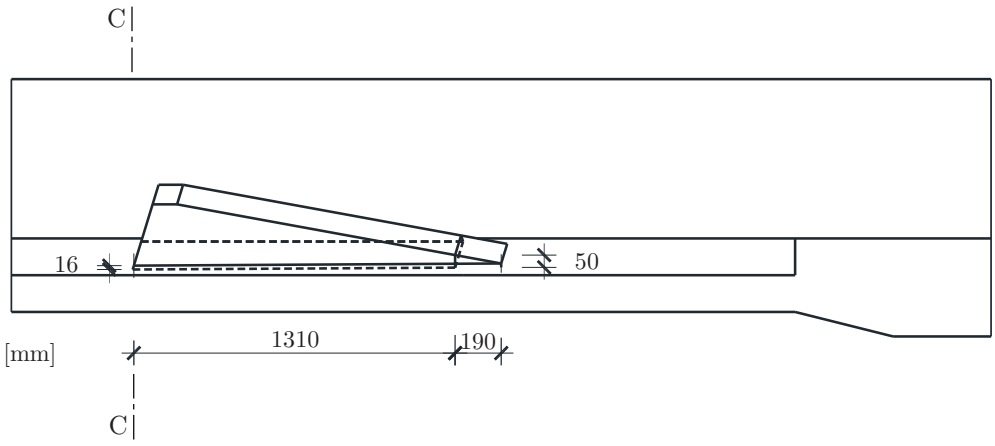

Figure 5.59: HPFRC precast blister model - Elevation

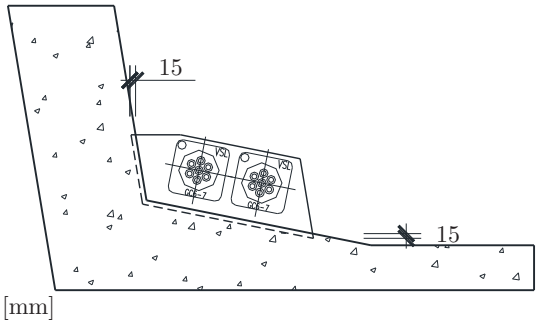

Figure 5.60: HPFRC precast blister model - Section C-C

5.2.3.1 Specimen execution

Blister execution

The HPFRC blister was cast upside down, with the surface that will connect the slab at the top, as shown in the figures below, because there was the need to leave the reinforcement of the anchorage blister in standby to make the subsequent connection to the bottom slab and web of the model.

Figure 5.61 shows the location of the sections presented in the aforementioned figures.

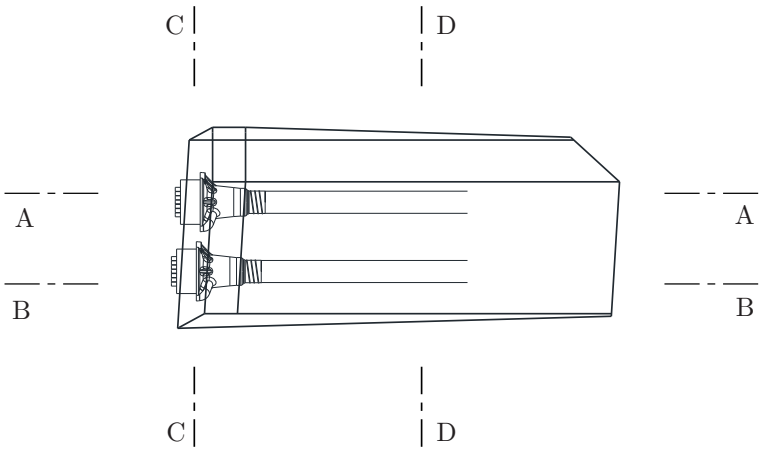

Figure 5.61: Position of the sections considered

Figures 5.62 and 5.63 present the drawings of the reinforcement of the precast anchorage blister.

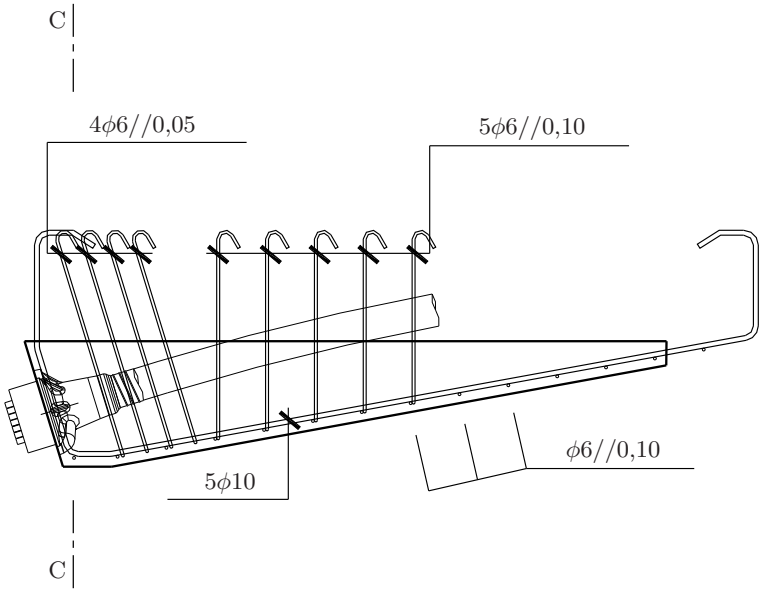

Figure 5.62: Section A-A

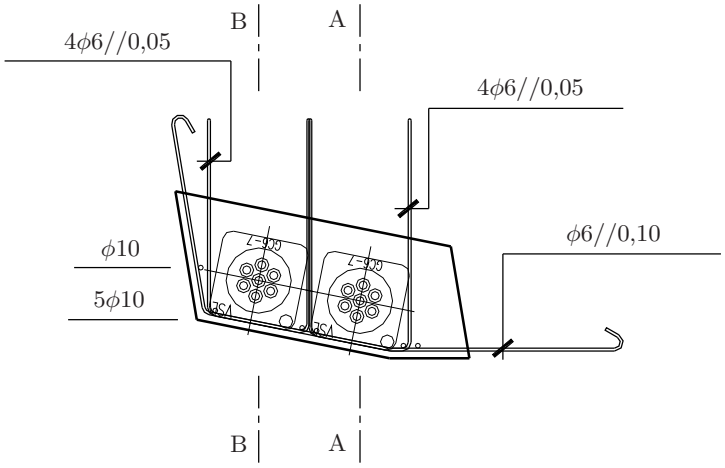

Figure 5.63: Section C-C

It should be noted that, for this specimen, the design of the reinforcement was based on the strut-and-tie models used for the HPFRC blister model.

Pictures of the reinforcement of the blister are shown in Figure 5.64.

(a) Side view **(b)** Front view

Figure 5.64: Reinforcement of the precast blister

In the casting of the overall model it was necessary to ensure the complete filling of the area under the anchorage blister. Thus, vertical pipes were left in the blister (as shown in Figure 5.65) to allow any air accumulated to be expelled, thereby minimising the formation of air pockets in the surface between the bottom slab and the blister.

Figure 5.65: Anchorage blister ready to be cast

The casting of the blister is shown in Figure 5.66.

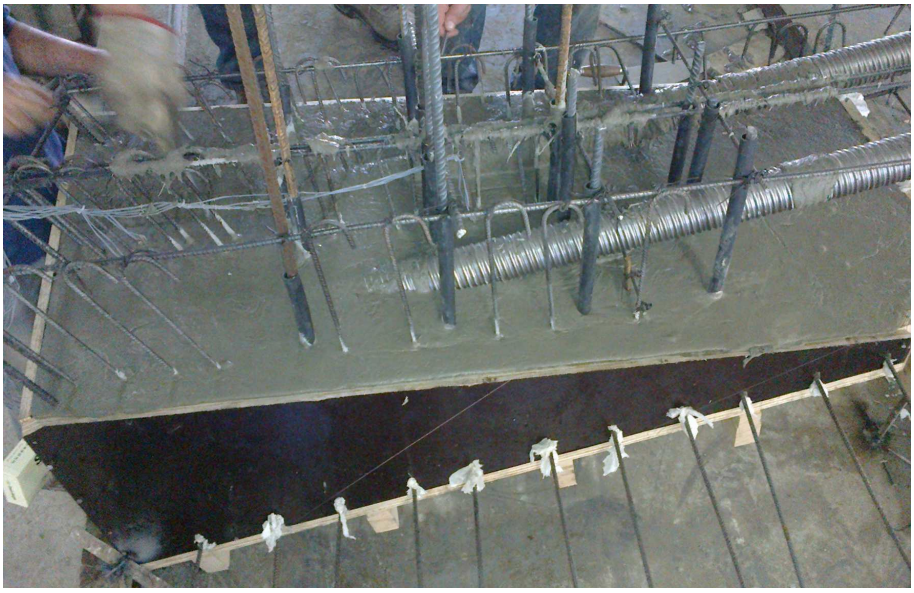

Figure 5.66: Casting of the anchorage blister

The surfaces in contact with the bottom slab and web were a free surface and a surface cast against plywood formwork, respectively. To increase bond at the interface between the two concretes, these surfaces were intentionally roughened with a pneumatic chipping hammer, as shown in Figure 5.67a. Figure 5.67b shows concrete surface after preparation.

(a) Concrete surface preparation

(b) Concrete surface after preparation

Figure 5.67: Concrete surface preparation

Overall specimen execution

The bottom slab, web and end block of the specimen were cast with ordinary concrete. The strength class requested was a C30/37, i.e., the same of the reference model. The reinforcing steel grade was an A500NR SD.

Figure 5.68 shows the reinforcement of the bottom slab, web and end block

Figure 5.68: Reinforcement of the bottom slab, web and end block

The casting of the overall specimen, with the precast blister in position, is illustrated in Figure 5.69. The casting took place 118 days after the casting of the precast HPFRC blister.

Figure 5.69: Casting of the overall specimen

The holes left in the blister to allow the air to be released during the casting of the overall model were filled with epoxy resin before testing, as can be seen in Figure 5.71.

5.2.3.2 Monitoring equipment

The monitoring equipment used was the same that was utilised on the HPFRC blister test, as described in Section 5.2.2.

5.2.3.3 Test procedure and measurements

As the previous models, this model was also tested rotated in relation to the actual position, as shown in Figure 5.70. In this case 9 strands of 0,6" type prEN 10138-3(2006) Y1860S7 with a nominal cross-section of 150 mm^2 in each tendon were also used, prestressed to 89,7% of the tensile strength, corresponding to the failure of the first strand.

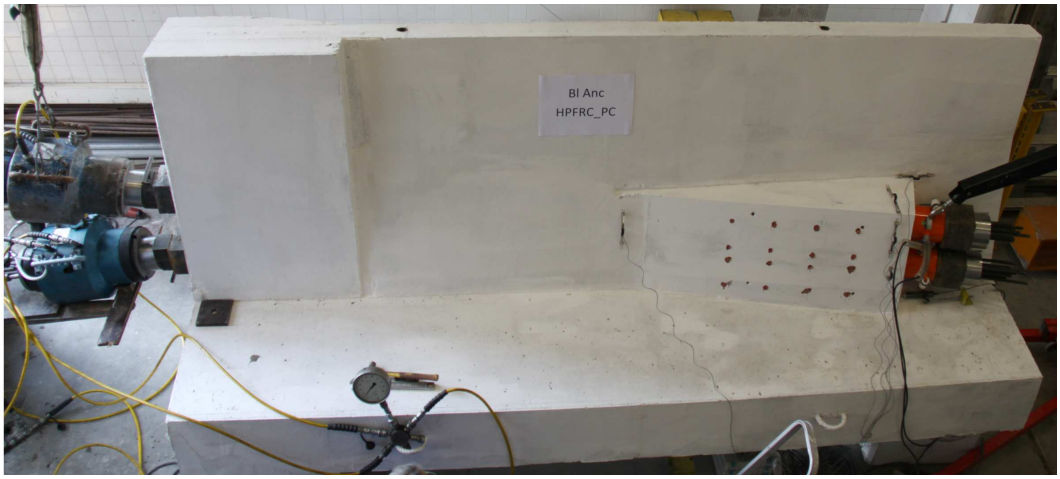

Figure 5.70: HPFRC blister model before testing

Figure 5.71 shows a detail of the blister before testing.

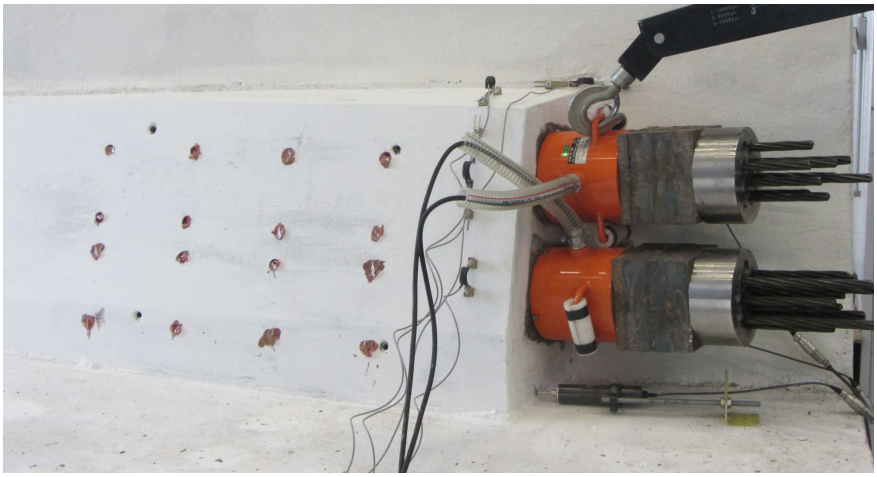

Figure 5.71: Detail of the HPFRC blister before testing

The procedure of this test was the same of the previous one, regarding stressing equipment and adapters. The prestressing force was applied in increments of 125,1 kN, corresponding to a pressure increment of 25 bar in the hydraulic jack, up to approximately 2251,4 kN, as shown in Table 5.11.

Table 5.11: Loading steps in the HPFRC precast blister model test

Loading step	Pressure (bar)	P_0 (kN)	Loading step	Pressure (bar)	P_0 (kN)
1	25	125,1	10	250	1250,8
2	50	250,2	11	275	1375,8
3	75	375,2	12	300	1500,9
4	100	500,3	13	325	1626,0
5	125	625,4	14	350	1751,1
6	150	750,5	15	375	1876,1
7	175	875,5	16	400	2001,2
8	200	1000,6	17	425	2126,3
9	225	1125,7	18	450	2251,4

All the readings of the monitoring equipment were recorded at intervals of 1 second.

5.2.3.4 Experimental results

Evolution of cracking during the test

The first cracks appeared on the anchorage blister and on the underside of the bottom slab, and have been detected at the thirteenth load level, as shown in Figures 5.72 and 5.73.

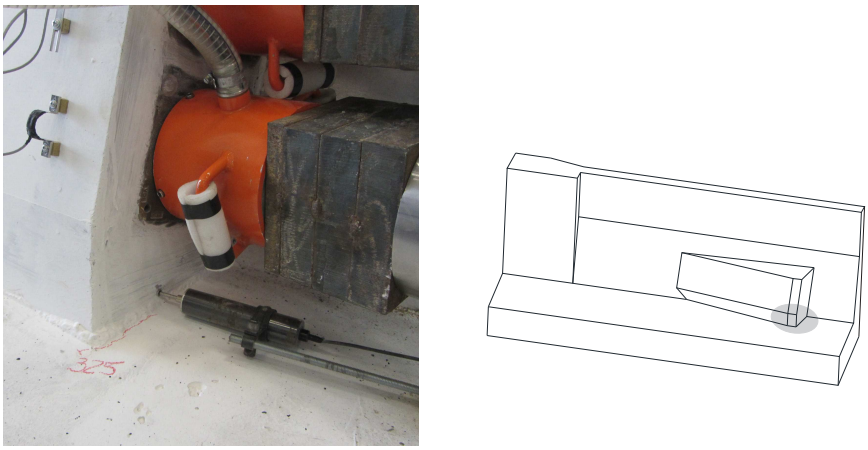

Figure 5.72: Cracking on the anchorage blister at the thirteenth load step

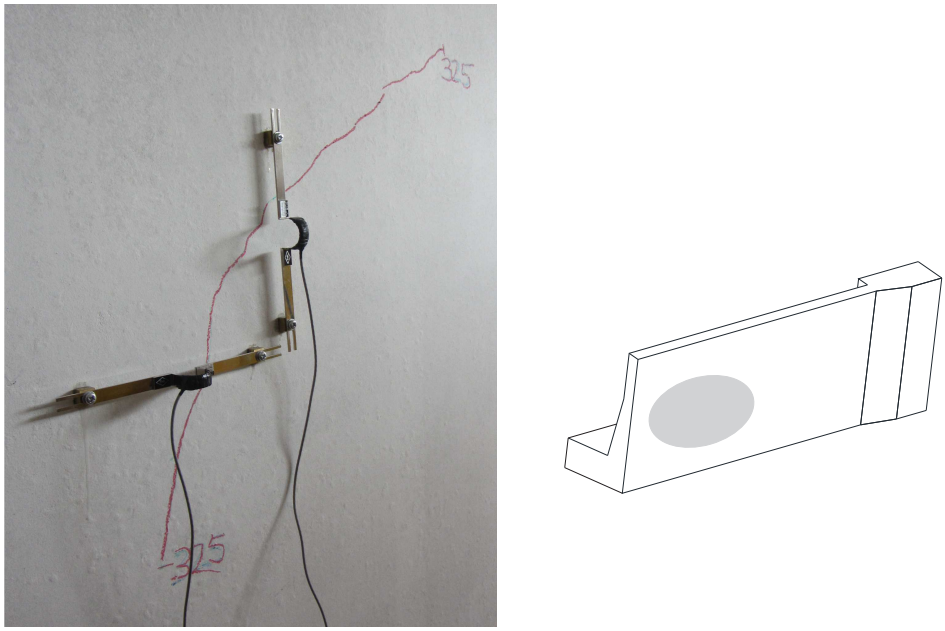

Figure 5.73: Cracking on the underside of the bottom slab at the thirteenth load step

At the fourteenth load step, a longitudinal crack appeared along the interface between the slab and the blister, as shown in Figure 5.74.

Figure 5.74: Cracking on the interface slab/blister

Figures 5.75 and 5.77 show cracking in the subsequent load steps.

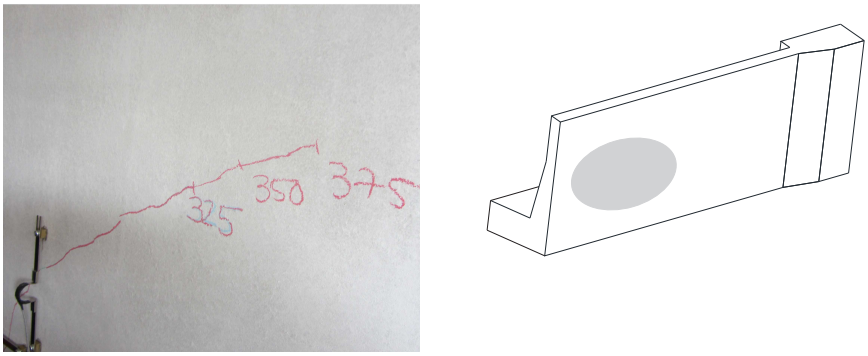

Figure 5.75: Cracking on the underside of the bottom slab at the fourteenth load step

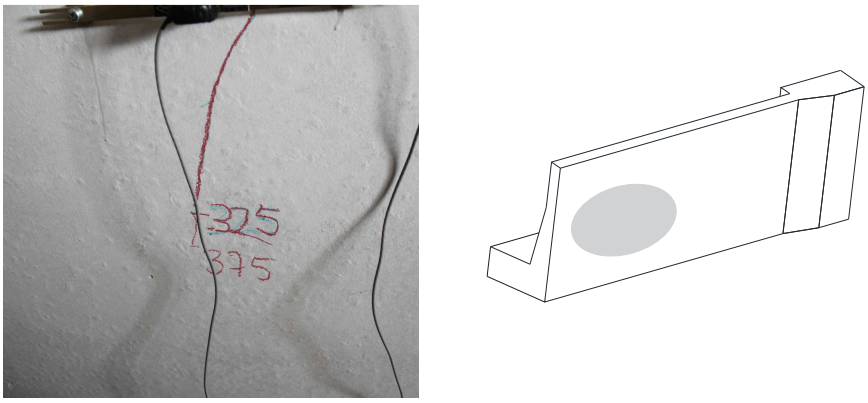

Figure 5.76: Cracking on the underside of the bottom slab at the fourteenth load step

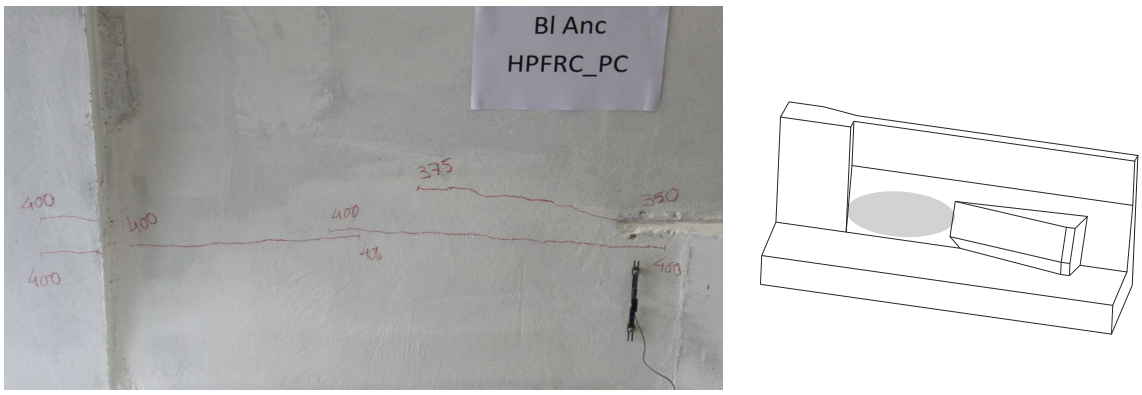

Figure 5.77: Cracking between the blister and the end block

Results of parameters recorded throughout the test

The evolution of the measured load with time for the HPFRC precast blister model is shown in Figure 5.78.

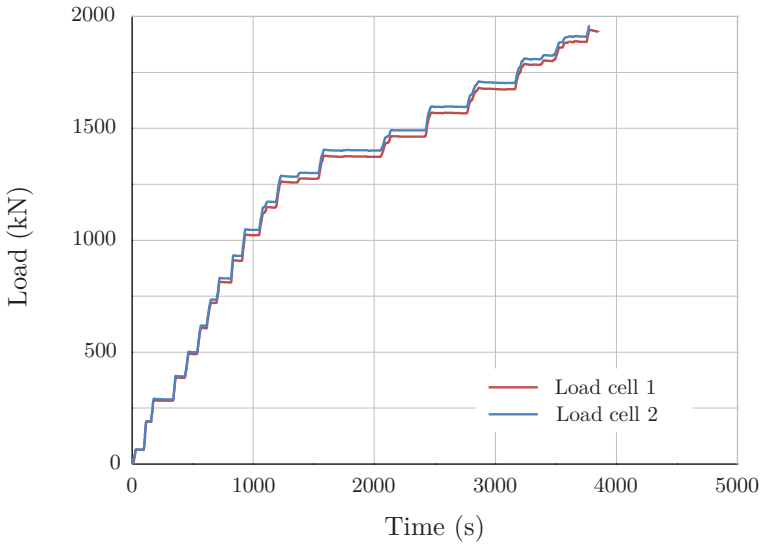

Figure 5.78: Evolution of the measured load with time

The evolution of the blister displacements with the average measured load is illustrated in Figure 5.79.

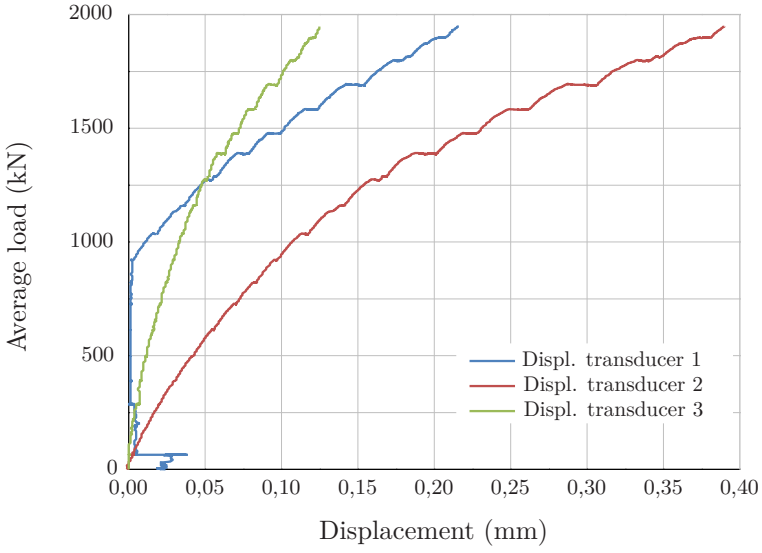

Figure 5.79: Evolution of the blister displacements with the average measured load

Apparently, transducer 1 did not work properly up to the load of 875 kN.

Figure 5.80 presents, for the various relative displacement transducers used, the variation of the concrete surface relative displacements with the average measured load.

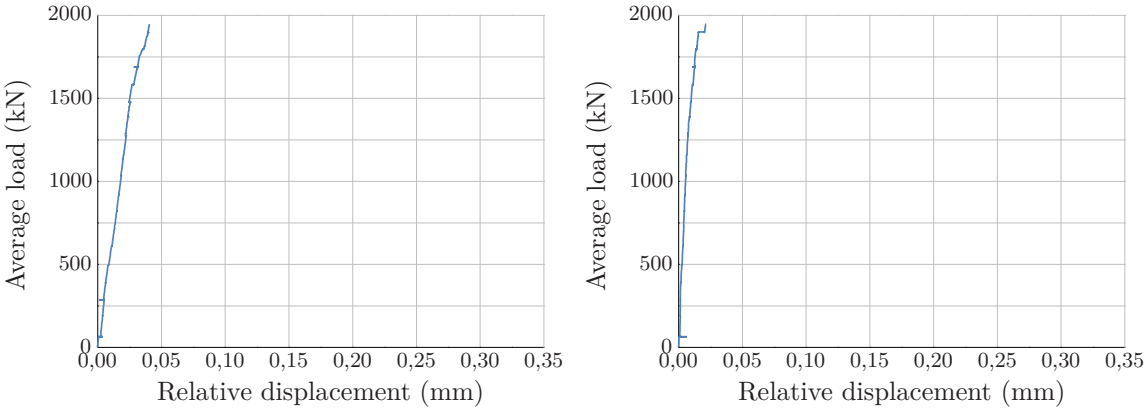

(a) Relative displacement transducer 1

(b) Relative displacement transducer 2

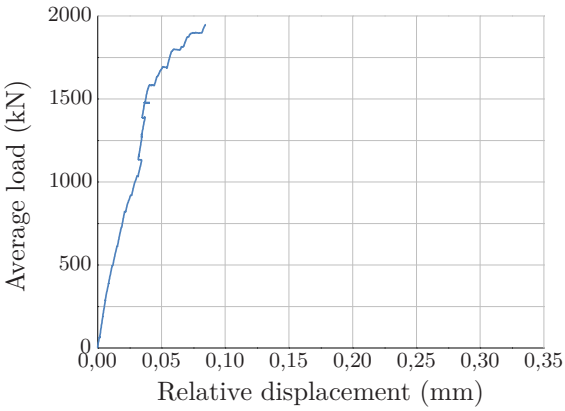

(c) Relative displacement transducer 3

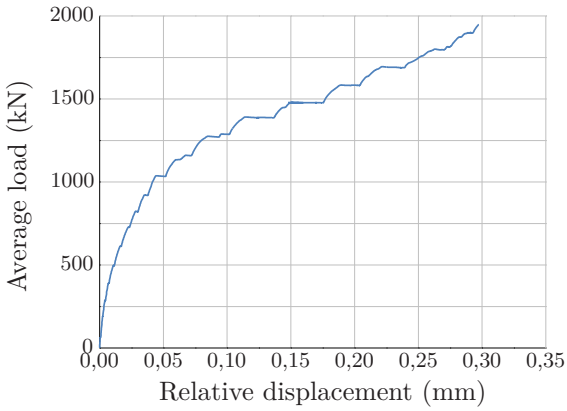

(d) Relative displacement transducer 4

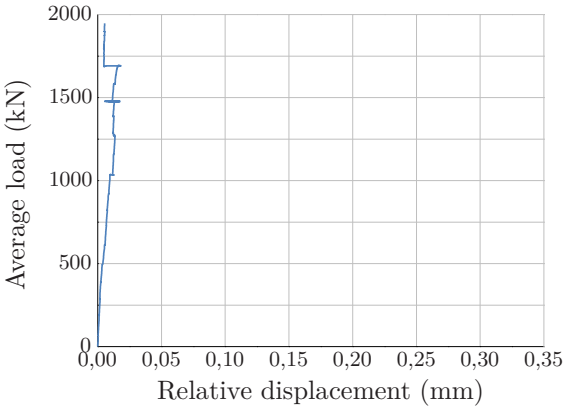

(e) Relative displacement transducer 5

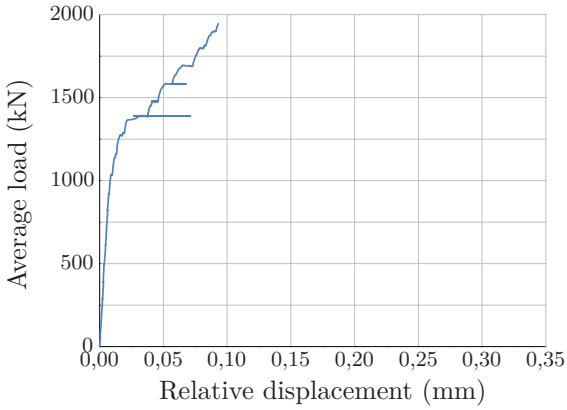

(f) Relative displacement transducer 6

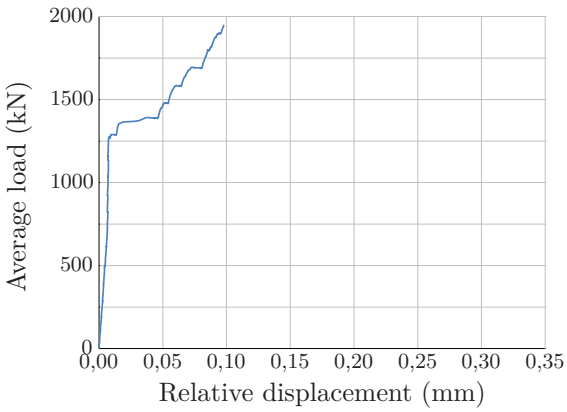

(g) Relative displacement transducer 7

Figure 5.80: Concrete surface relative displacements vs average measured load

It should be noted that, in the tests of the HPFRC blister models, the horizontal scale of the graphs showing the relation between the concrete surface relative displacements with the average measured load is different.

As can be seen in Figure 5.80d, the relative displacement measured by transducer 4 (see Figure 5.42) nearly reached to 0,3 mm, denoting a slip of the HPFRC blister.

Figure 5.81 shows the evolution of the strains of the reinforcing steel with the average measured load.

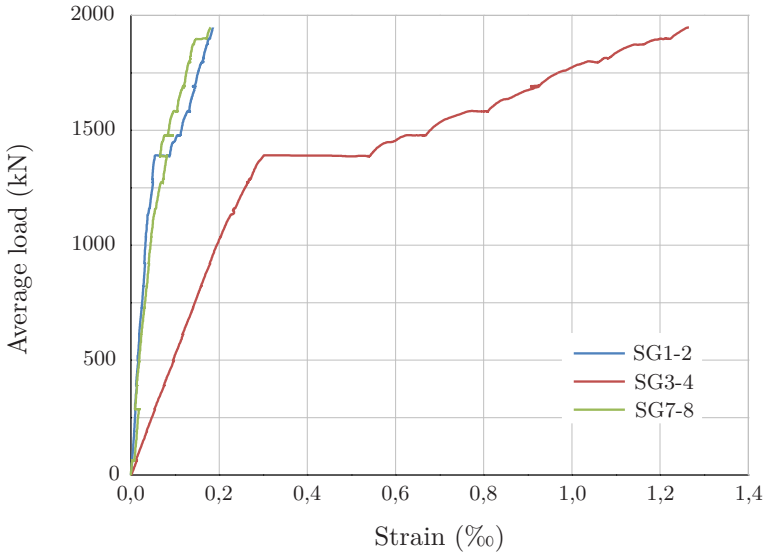

Figure 5.81: Strain of the reinforcing steel vs average measured load

Materials Characterisation

Ordinary concrete

The compressive strength of the ordinary concrete used in the HPFRC precast blister model was evaluated using the procedure already described for the previous models.

The values of the mean compressive strength and characteristic compressive strength for the 150 mm cubic specimens, at the age of the test (28 days), are presented in Table 5.12. Table 5.12 also presents the mean value of the axial tensile strength.

Table 5.12: Mechanical properties of the ordinary concrete at the age of the test

Number of specimens	$f_{cm,cube}$ (MPa)	δ	$f_{ck,cube}$ (MPa)	f_{ctm} (MPa)
6	49,2	2,5%	47,2	3,4

The coefficient of variation (δ) was determined using equation (2.1) presented in Chapter 2.

The characteristic compressive strength of concrete (f_{ck}) was obtained from the values of the mean compressive strength achieved in the tests assuming the normal distribution equation (2.2) (see Chapter 2).

The mean value of the axial tensile strength (f_{ctm}) was calculated according to EN 1992-1-1 (2004), based on the value of the characteristic compressive strength referred to cylinder specimens, using equation (3.32) presented in Chapter 3.

HPFRC

The average compressive strength, the coefficient of variation and the characteristic compressive strength of the HPFRC for 150 mm cubic specimens, at the age of 143 days, are presented in Table 5.13.

Table 5.13: HPFRC compressive strength for 150 mm cubic specimens at the age of the test

Number of specimens	$f_{cm,cube}$ (MPa)	δ	$f_{ck,cube}$ (MPa)
6	126,7	5,1%	116,2

The concrete tensile strength was assessed by tensile splitting tests, performed according to the procedure described for the previous specimens, and is presented in Table 5.14 for the HPFRC mixture at the age of the test (87 days).

Table 5.14: HPFRC tensile splitting strength and related mean tensile strength for cylinder specimens at the age of the test

Number of specimens	$f_{ct,sp}$ (MPa)	δ	f_{ctm} (MPa)
6	12,6	19,7%	11,3

Reinforcing steel

The mechanical characteristics of the reinforcing steel are the same as for the reference model, and are presented in Table 5.5.

Characterisation of the interface between the precast blister and the web and bottom slab

In order to study the strength of the interface between the precast blister and the web and bottom slab, a second model with a precast HPFRC blister was built (pull-off model). The geometry of the specimen is presented in Figures 5.82 and 5.83.

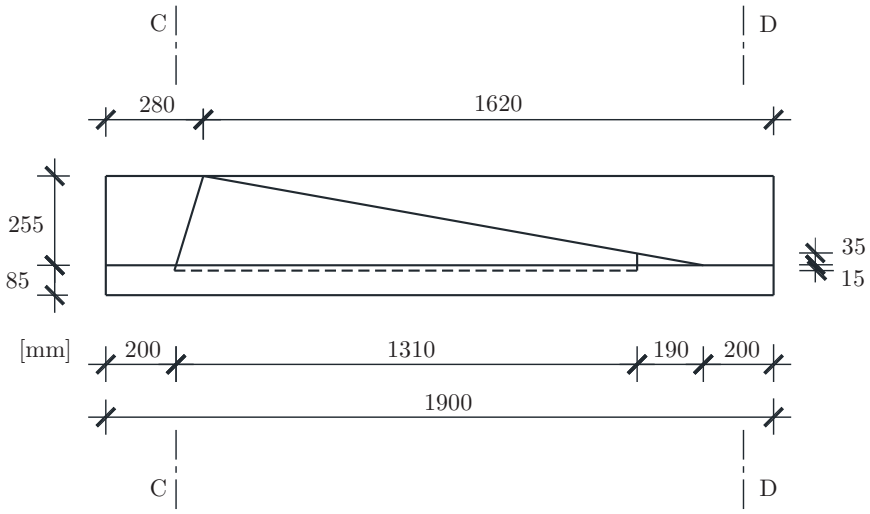

Figure 5.82: Pull-off model - Elevation

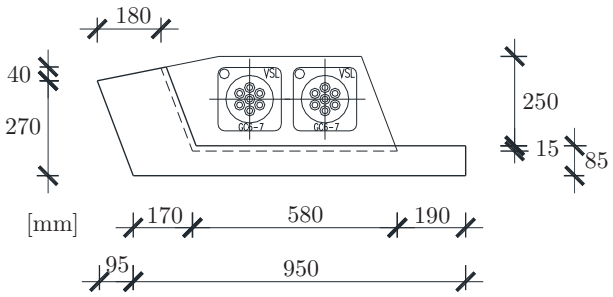

Figure 5.83: Pull-off model - Cross section C-C

The two precast blister models were cast in the same day, and the portion of web and bottom slab was cast with the same concrete mixture of the overall model. Figure 5.84 shows the casting of the portion of web and bottom slab, with the precast blister in position.

Figure 5.84: Casting of the pull-off model

Characterisation of the concrete surface roughness

The surface roughness for both blisters was evaluated with a discrete geometric measurement using a CDP-50 TML displacement transducer, as shown in Figure 5.85.

(a) General view of the equipment used **(b)** Transducer

Figure 5.85: Equipment used to evaluate the surface roughness

Figures 5.86 and 5.87 show the measured roughness profile after the surface treatment for both blisters. Blister 1 and blister 2 are the blisters of the HPFRC precast blister model and pull-off model, respectively.

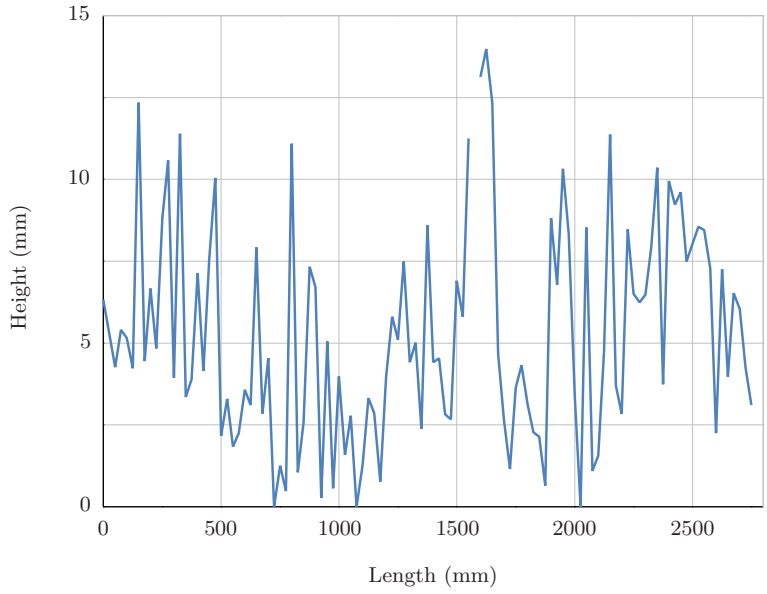

Figure 5.86: Surface roughness profile of blister 1

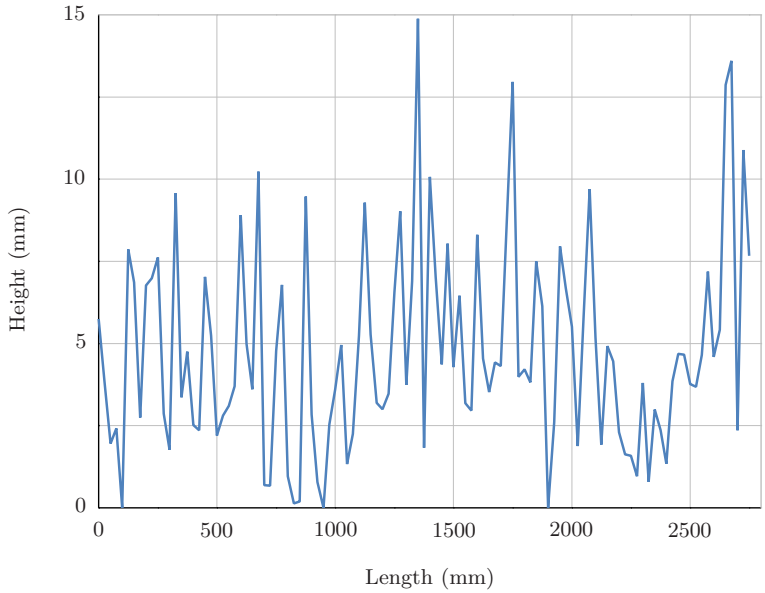

Figure 5.87: Surface roughness profile of blister 2

The roughness parameters, presented below, were determined according to the expressions presented by Santos et al. (2007) and Santos and Júlio (2013), based in Mummery (1992), and by the Model Code 2010 (2012).

- Mean Roughness (R_m)

  The mean roughness or average roughness is the most common roughness parameter referred in the literature because of its simplicity, and is defined as the average deviation of the profile in relation to its mean line, as stated in equation 5.1.

$$R_m = \frac{1}{l_m}\int_0^{l_m} |y(x) - \overline{y}|dx \approx \frac{1}{n}\sum_{i=1}^{n} |y_i - \overline{y}| \tag{5.1}$$

  where,

  l_m is the evaluation length;
  $y(x)$ is the profile height, at position x;
  $\overline{y}$ is the mean profile height;
  n is the number of discrete measurements;
  y_i is the amplitude of each measurement.

  The mean line can be determined using equation (5.2).

$$\overline{y} = \frac{1}{l_m}\int_0^{l_m} y(x)dx \approx \frac{1}{n}\sum_{i=1}^{n} y_i \tag{5.2}$$

- Root Mean Square Roughness (R_q)

  The root mean square roughness is a parameter more sensitive to peaks and valleys and it is given by:

$$R_q = \sqrt{\frac{1}{l_m}\int_0^{l_m}(y(x)-\overline{y})^2 dx} \approx \sqrt{\frac{1}{n}\sum_{i=1}^{n}(y_i-\overline{y})^2 dx} \tag{5.3}$$

- Mean peak height (R_t)

  The mean peak height is the average of the maximum peak hight from each sampling length and can be determined using equation (5.4):

$$R_t = \frac{1}{5}\sum_{j=1}^{5} p_j \tag{5.4}$$

  where p_j is the maximum peak height in each sampling length.

  The sampling length (s_L) is considered as the evaluation length divided into five equal parts.

  The maximum peak height can be determined using equation (5.5):

$$p_j = max\,[y_i - \overline{y}]_0^{s_{L_j}} \tag{5.5}$$

- Mean valley depth (R_{vm})

  The mean valley depth is the average of the maximum valley depth from each sampling length. This parameter is given by equation (5.6):

$$R_{vm} = \frac{1}{5}\sum_{j=1}^{5} v_j \tag{5.6}$$

  where v_j is the maximum valley depth in each sampling length and can be determined using equation (5.7):

$$v_j = max\,[\overline{y} - y_i]_0^{s_{L_j}} \tag{5.7}$$

- Mean peak-to-valley height (R_z)

  The mean peak-to-valley height is the average of the maximum peak-to-valley height from each sampling length and can be calculated using equation (5.8):

$$R_z = \frac{1}{5}\sum_{j=1}^{5}(p_j + v_j) \tag{5.8}$$

Table 5.15 presents the roughness parameters obtained for the two analysed specimens.

Table 5.15: Roughness parameters

Specimen	R_m (mm)	R_q (mm)	R_t (mm)	R_{vm} (mm)	R_z (mm)
Blister 1	2,7	3,3	6,7	4,3	11,0
Blister 2	2,4	3,1	7,5	4,2	11,7

According to Model Code 2010 (2012), for the values of the mean peak height (R_t) obtained (above 3 mm), the surface can be classified as *very rough*.

For the quantification of the bond strength, the coefficients of friction μ and cohesion c were determined, using the design approach proposed by Santos and Júlio (2014). According to this formulation, both coefficients of friction and cohesion can be determined from the mean valley depth coefficient, using equations (5.9) and (5.10), respectively.

$$\mu_d = \frac{1,376{R_{vm}}^{0,04}}{\gamma_{fr}} \tag{5.9}$$

$$c_d = \frac{1,06{R_{vm}}^{0,15}}{\gamma_{coh}} \tag{5.10}$$

For the partial safety factors γ_{fr} and γ_{coh} the maximum values of 1,2 and 2,6, respectively, can be adopted.

Table 5.16 presents the coefficients of friction and cohesion obtained.

Table 5.16: Roughness parameters

Specimen	μ_d	c_d	μ_m	c_m
Blister 1	1,2	0,5	1,4	1,3
Blister 2	1,2	0,5	1,4	1,3

For the calculation of the mean values of the coefficients of friction and cohesion (μ_m and c_m), the partial safety factors were not considered.

The Model Code 2010 (2012) recommends friction coefficients between 1,0 and 1,4 for very rough surfaces, which is consistent with the values obtained.

Determination of the bond strength of the interface

In order to determine the bond strength of the interface between the precast blister and the web and bottom slab, pull-off tests were carried out, using the test setup shown in Figure 5.88.

Figure 5.88: Pull-off test setup

The test consisted of the pullout of a 150 mm square steel plate, bonded to the concrete surface with epoxy resin. The increase in the area of the test steel plate was due to the need to dissipate the vibrations caused by the isolation of the concrete specimens after the casting of the elements using electric saws, whose vibration causes premature rupture of the interface (Ramos et al., 2014).

For the pullout test, the system described in Ramos et al. (2014) was used, consisting of a reaction system capable of levelling the whole set and adapt to the irregularities of the supporting material.

Table 5.17 presents the tensile bond strength (f_b) determined from the tests, assuming a uniform tension distribution in the contact area, and the coefficient of variation (δ).

Table 5.17: Bond strength of the interface

Number of specimens	f_b (MPa)	δ
5	1,36	8,6%

5.2.4 Comparison between the experimental results of the three tested models

The tests on anchorage blister models were conditioned by the limitation of the value of force that could be applied. As already mentioned, the ducts and anchorage bearing plates adopted were designed for 7 strands, to not misrepresent the behaviour of the specimen. Despite the fact of being possible to use 9 strands in a duct of 7 strands, which increased the value of force that could be applied, it was not sufficient to achieve the failure of the models. Despite this limitation, the design value of the load was achieved with acceptable levels of cracking for a serviceability situation.

The HPFRC blister and the HPFRC precast blister models showed a very similar behaviour during the test. No significant difference regarding cracking was observed, except for the crack formed in the connection between the blister and the bottom slab (relative displacement transducer 7 - Figure 5.11 - for the ORC blister model and transducer 4 - Figure 5.42 - for the HPFRC blister models - Figures 5.31f, 5.57d and 5.80d). The evolution of the concrete surface relative displacements for the mentioned relative displacement transducers is summarised in Figure 5.89 for the ordinary reinforced concrete blister model (ORC BM), HPFRC blister model (HPFRC BM) and HPFRC precast blister model (HPFRC PBM).

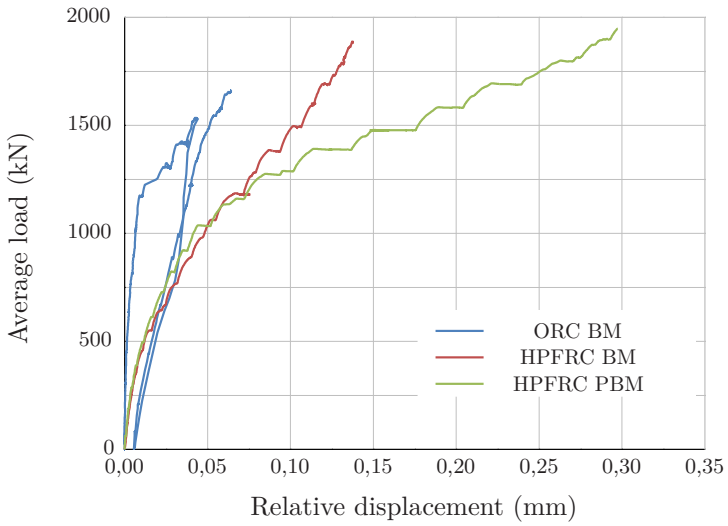

Figure 5.89: Evolution of the concrete surface relative displacements near the blister, with the post-tensioning average measured load

The Figure 5.89 above shows that the measured relative displacement is higher for the HPFRC blister models, and become considerably higher for the precast blister model from the 10th load step (aprox. 1250 kN). Anyway, the crack width does not exceed 0,3 mm for the maximum load achieved in the test.

For the three specimens, the main cracks opened in the relative displacement transducers area, denoting a good agreement between the elastic 3D finite element analysis and the experimental results.

Regarding the blister displacements, the behaviour of the three specimens is similar, as can be seen in Figures 5.90a, 5.90b and 5.90c. In all cases, the measured displacements are smaller as closer to the web the transducer is.

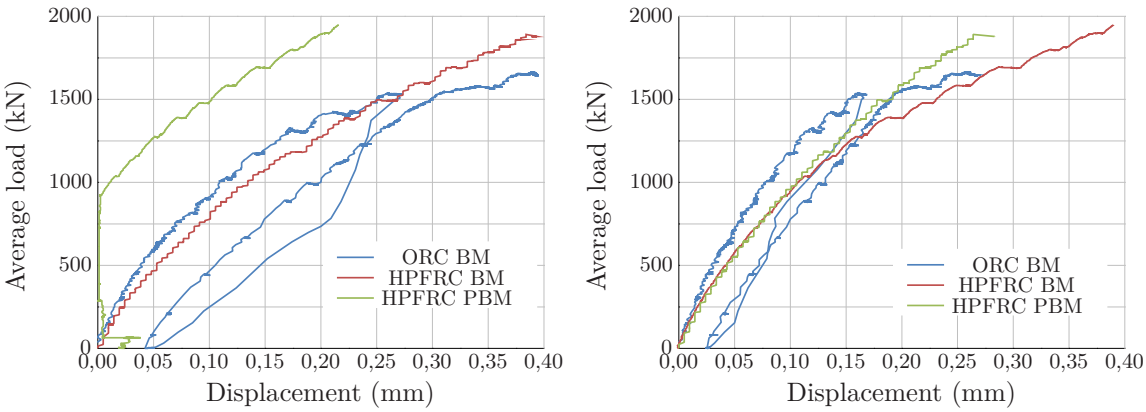

(a) Displacement transducer 1

(b) Displacement transducer 2

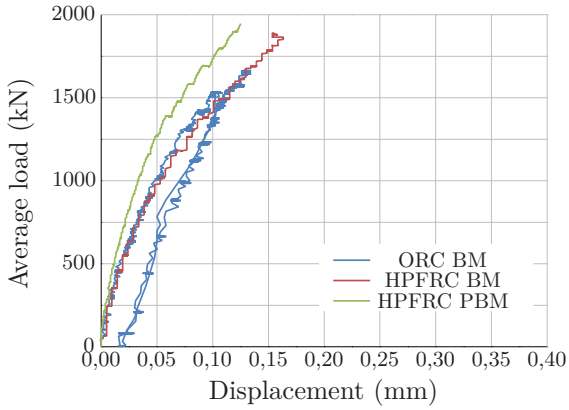

(c) Displacement transducer 3

Figure 5.90: Evolution of the blister displacements with the average measured load

Regarding the steel reinforcement strains, the measured values are all below the steel yielding strain.

Although the strain values are not directly related to the tensile force on the ties of the strut and tie models used in design, but with the steel reinforcement tension, it can be seen that in most cases the larger strains were measured in the strain gauges located in the reinforcement that corresponded to the ties with larger tensile force.

In conclusion, the HPFRC precast blister can be a very interesting solution, since it

can reduce the execution time and facilitate casting without harming local resistance and behaviour in serviceability conditions.

5.3 Non-linear analysis of the anchorage blister models

In order to find the failure load of the models, which was not possible to achieve in the laboratory tests, the non-linear finite element analysis software ATENA (Cervenka et al., 2014) was used to reproduce the experimental test of the anchorage blister specimens.

Regarding the HPFRC blister models, the one with the precast blister was not analysed. As the only difference between the two specimens is the characteristics of the interface between the blister and the slab and web, the models have a very high number of elements and high computation time, and due to the difficulty of the accurate simulation of the mechanisms that contribute to the shear strength of the interface, in particular the dowel action of reinforcement, the interface resistance was evaluated by another method that will be described in due course.

5.3.1 Geometry of the models

The models of the anchorage blister specimens are composed of concrete, steel reinforcement, post-tensioning steel and steel plates to simulate, in a simplified way, the bearing plates of the post-tensioning anchorages.

The concrete and the steel plates were modelled by volume macroelements, meshed independently in tetrahedra and brick volume elements of about 40 mm in the anchorage blister, and gradually increased to 100 mm in the most distant areas, resulting in a total of 34430 elements in the ORC blister model, and a total of 47159 elements in the HPFRC blister model.

Incompatible meshes are allowed on interfaces between macroelements. The kinematic relations between nodes of incompatible meshes are ensured by the master-slave method. The master-slave method also ensures that the discrete reinforcement bars are fixed to the surrounding solid element (Cervenka et al., 2014).

In this case, it was decided to simplify the modelling of the anchorage bearing plate, considering a steel plate only. Not only the modelling of the casting would excessively complicate the geometry and discretization of the blister in that area, but also it was considered that the interaction between the bearing plate and the concrete was not a conditioning factor for the model behaviour.

Figures 5.91 and 5.92 show the geometry and finite element mesh of the numerical

model for the ORC blister specimen, respectively.

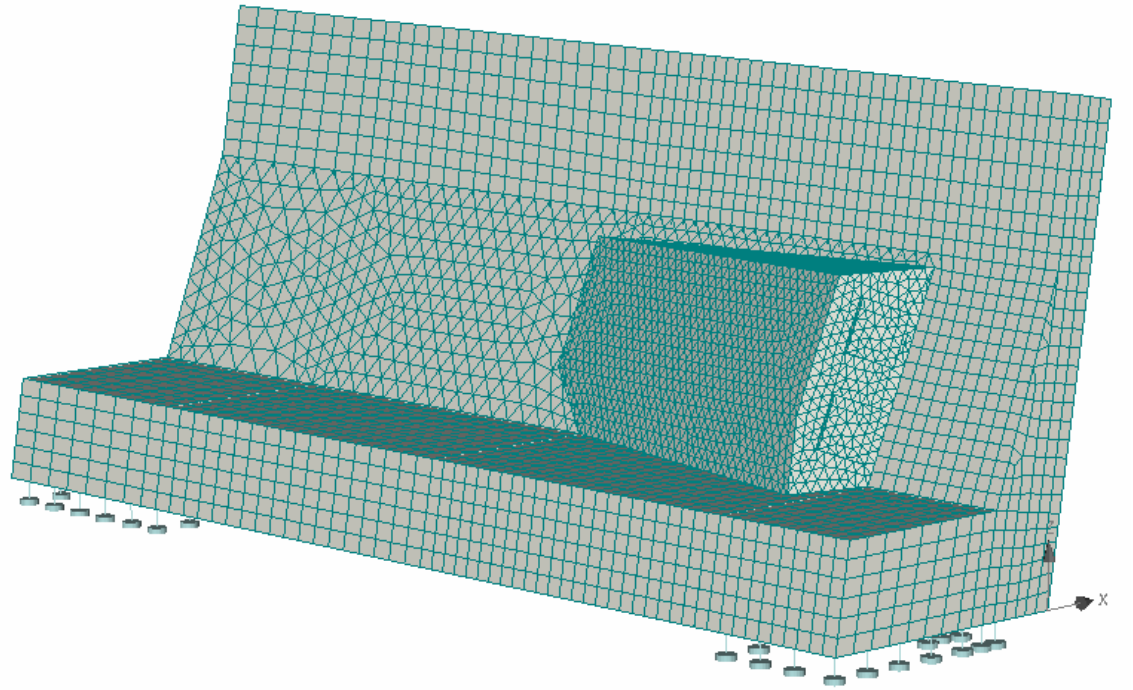

Figure 5.91: Geometry of the numerical model of the ORC blister specimen

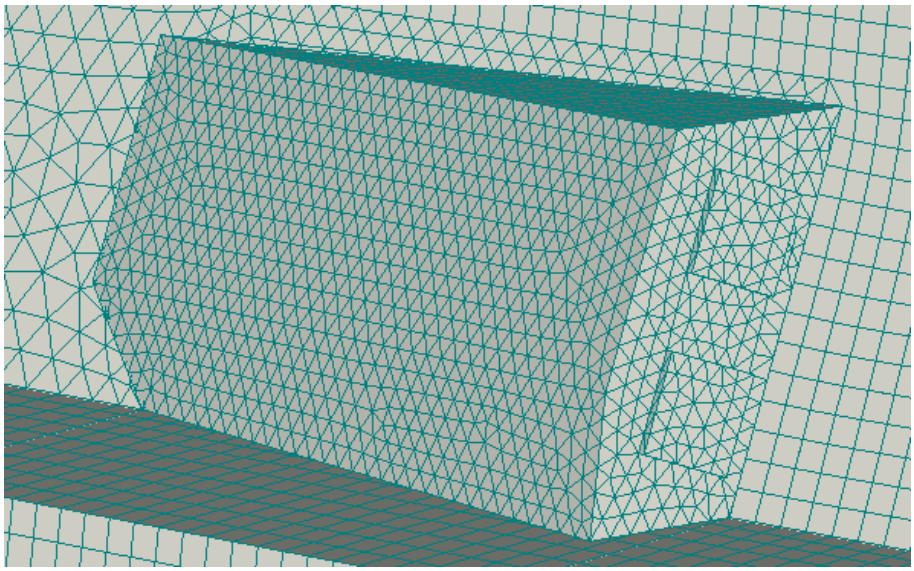

Figure 5.92: Numerical model of the ORC blister specimen - Detail of the blister

The reinforcement bars were modelled by truss elements embedded in concrete. The bond of the steel reinforcement was considered. The prestressed tendons were simulated as external prestressing cables and the loss of the prestressing force due to friction was considered.

Figures 5.93 and 5.94 show the reinforcement and prestressing tendons (lines in green) of the numerical model for the ORC blister specimen.

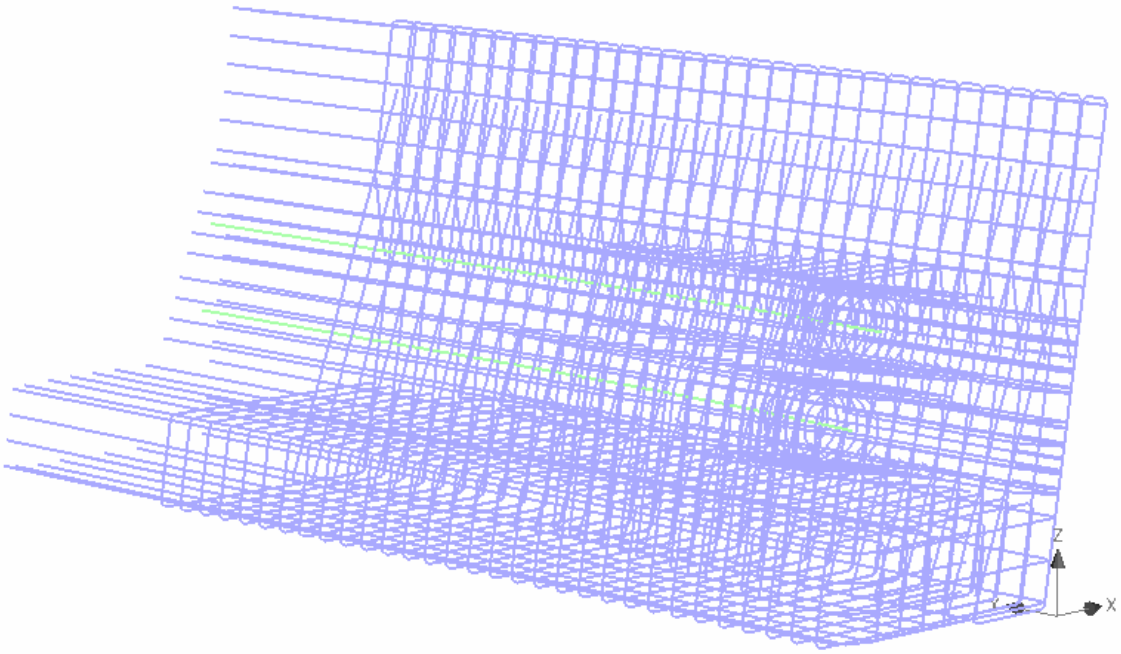

Figure 5.93: Reinforcement of the numerical model of the ORC blister specimen

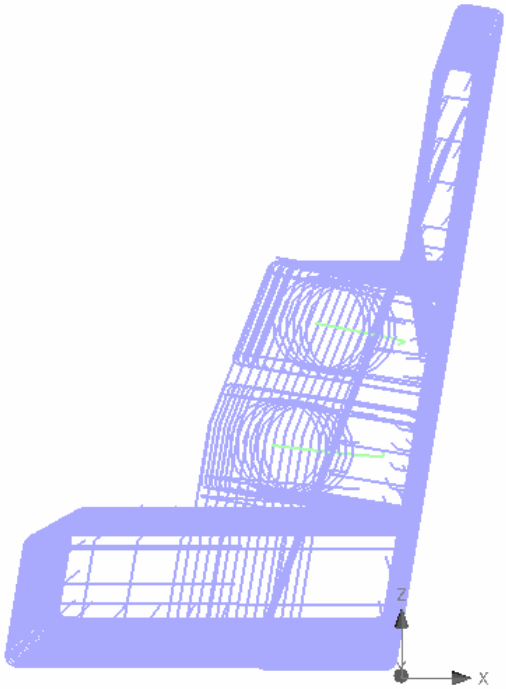

Figure 5.94: Reinforcement of the numerical model of the ORC blister specimen - Lateral view

The geometry and discretization of the numerical model for the HPFRC blister specimen is presented in Figures 5.95 and 5.96.

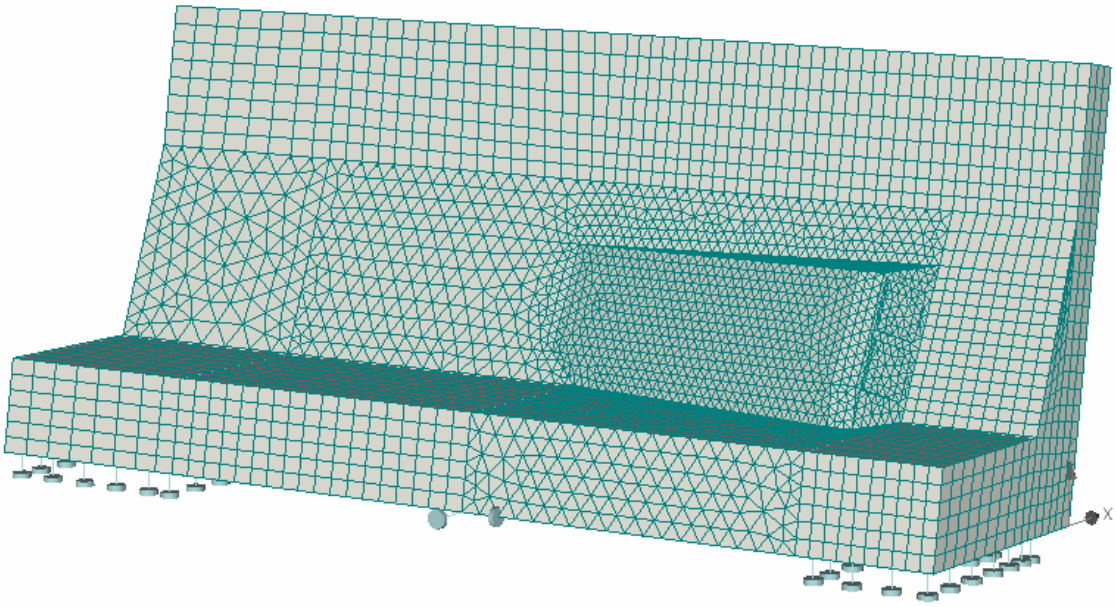

Figure 5.95: Geometry of the numerical model of the HPFRC blister specimen

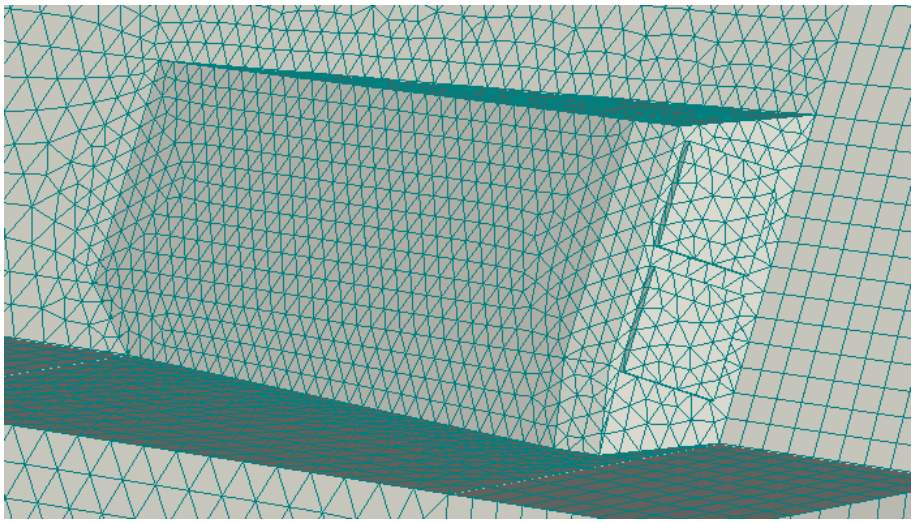

Figure 5.96: Numerical model of the HPFRC blister specimen - Detail of the blister

Figures 5.97 and 5.97 show the reinforcement and prestressing tendons (lines in green) of the numerical model for the HPFRC blister specimen.

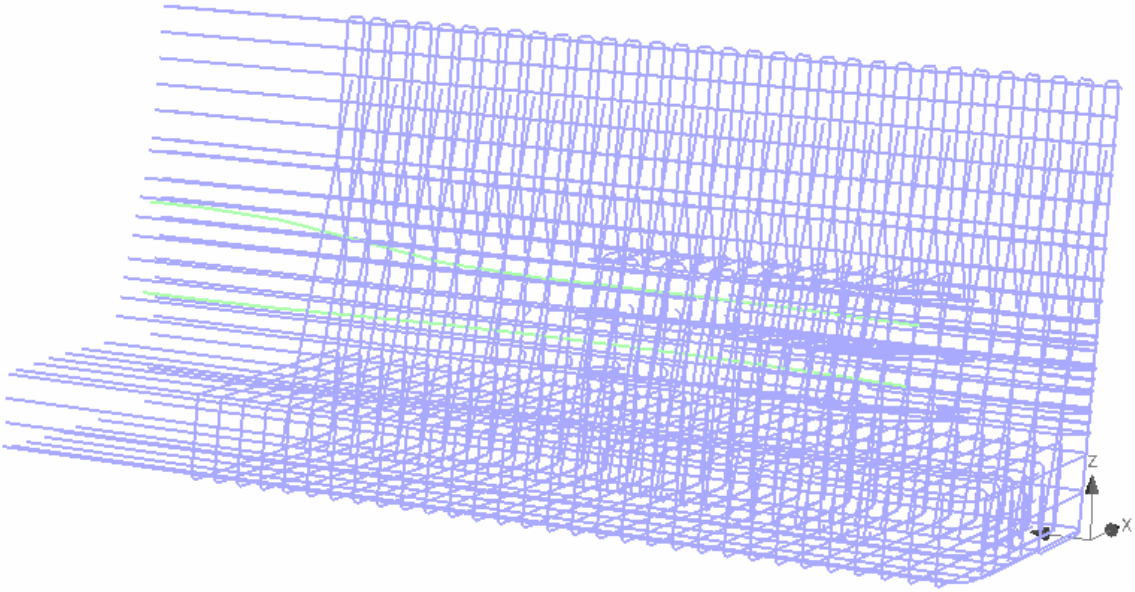

Figure 5.97: Reinforcement of the numerical model of the HPFRC blister specimen

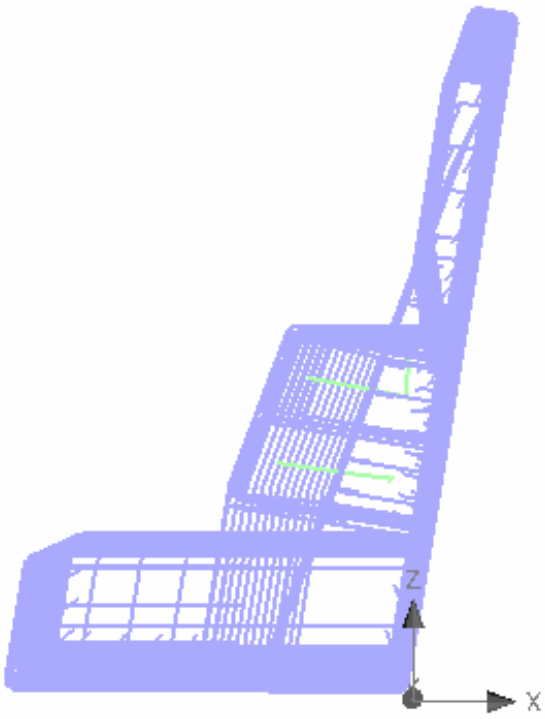

Figure 5.98: Reinforcement of the numerical model of the HPFRC blister specimen - Lateral view

5.3.2 Mechanical properties of materials

5.3.2.1 Concrete

Tables 5.18 and 5.19 present the OC and HPFRC mechanical properties used in ATENA models, respectively.

Table 5.18: OC mechanical properties

Specimen	f_{cm} (MPa)	f_{ctm} (MPa)	G_f (N/m)	E_{cm} (GPa)
ORC blister model	27,7	2,4	60,0	26,9
HPFRC blister model	36,9	3,3	82,5	29,3

Table 5.19: HPFRC mechanical properties

Specimen	f_{cm} (MPa)	f_{ctm} (MPa)	G_f (N/m)	E_{cm} (GPa)
HPFRC blister model	97,8	11,7	292,5	44,3

In Table 5.18, the cylinder mean compressive strength (f_{cm}), the tensile strength (f_{ctm}) and the modulus of elasticity of concrete (E_{cm}) were determined using equations (3.30), (3.32) and (3.34), respectively, presented in Chapter 3.

The values of the fracture energy (G_f) shown in Tables 5.18 and 5.19 were determined using equation (3.33), presented in Chapter 3.

The HPFRC modulus of elasticity was calculated through equation (2.7), presented in Chapter 2.

Still concerning to concrete, the other properties adopted, that were defined and assessed in Chapter 3, are given in Table 5.20.

Table 5.20: Concrete characteristics of the test specimens

Concrete type	ν	w_d (mm)	ε_{cp}	$r_{c,lim}$	S_F	e	β
OC	0,20	-0,5	-1,5‰	0,8	-20,0	-0,52	0,40
HPFRC	0,20	-0,075	-3,5‰	0,8	-20,0	-0,52	0,70

It was considered a fixed crack model coefficient of 1,00.

5.3.2.2 Reinforcing steel

The mechanical properties of the steel reinforcement considered in the numerical models are specified in Table 5.5. For the modulus of elasticity E_s was considered the value of 200 GPa.

5.3.2.3 Bond-slip relations

The bond of reinforcement was considered, using the bond model recommended in the Model Code 2010 (2012) and presented in Figure 3.67, from Chapter 3, and defined by equation (3.35).

The bond stress values required to define the bond slip relations for the tested models are presented in Table 5.21. Although the blister reinforcement bars are embedded partly in ordinary concrete and partly in HPFRC, as a simplification the bond-slip relation was defined considering only the ordinary concrete characteristics.

Table 5.21: Definition of the bond stress values required to define the bond stress-slip relations

Specimen	f_{cm} (MPa)	τ_{max} (MPa)	τ_f (MPa)
ORC blister model	27,7	13,2	5,3
HPFRC blister model	36,9	15,2	6,1

The bond slip relations are presented in Figures 5.99 and 5.100 for the ORC and HPFRC blister models, respectively.

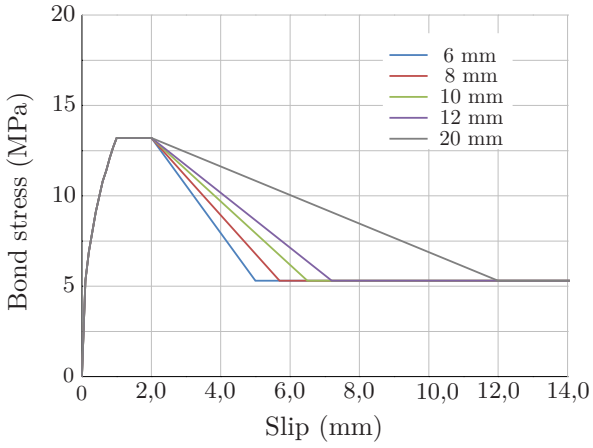

s (mm)	τ (MPa)
0,0	0,0
0,2	6,9
0,4	9,1
0,6	10,8
0,8	12,1
1,0	13,2
2,0	13,2
s_3	5,3

Figure 5.99: ORC blister model - mean bond stress-slip relationships

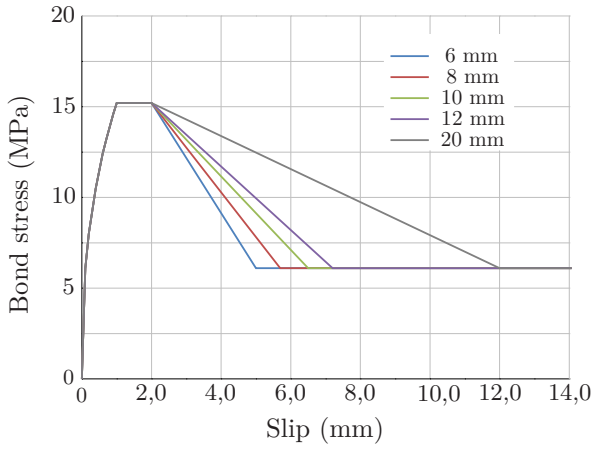

s (mm)	τ (MPa)
0,0	0,0
0,2	8,0
0,4	10,5
0,6	12,4
0,8	13,9
1,0	15,2
2,0	15,2
s_3	6,1

Figure 5.100: HPFRC blister model - mean bond stress-slip relationships

The slip value s_3 is given in Table 5.22 for each bar diameter.

Table 5.22: Definition of the mean bond stress-slip relationship used for the specimens

ϕ (mm)	6	8	10	12	20
s_3 (mm)	5,0	5,7	6,5	7,2	12,0

5.3.2.4 Anchorage steel

For modelling the anchor head an elastic-plastic material without hardening was chosen. The main properties considered are listed in Table 5.26.

Table 5.23: Characteristics of the anchorage steel

f_y (MPa)	E_s (GPa)	ν
250	210	0,30

5.4 Comparison between the experimental tests and the non-linear analysis

In the following sections the comparison between the experimental and numerical models will be presented, namely the appearance of cracks that have formed over the various load steps and the evolution of the blister displacements with the applied load.

5.4.1 ORC blister model

5.4.1.1 Evolution of cracking

Figures 5.101 and 5.102 presents the comparison of cracking in the anchorage corner blister at the ninth load level of the first phase of the test (aprox. 1390 kN).

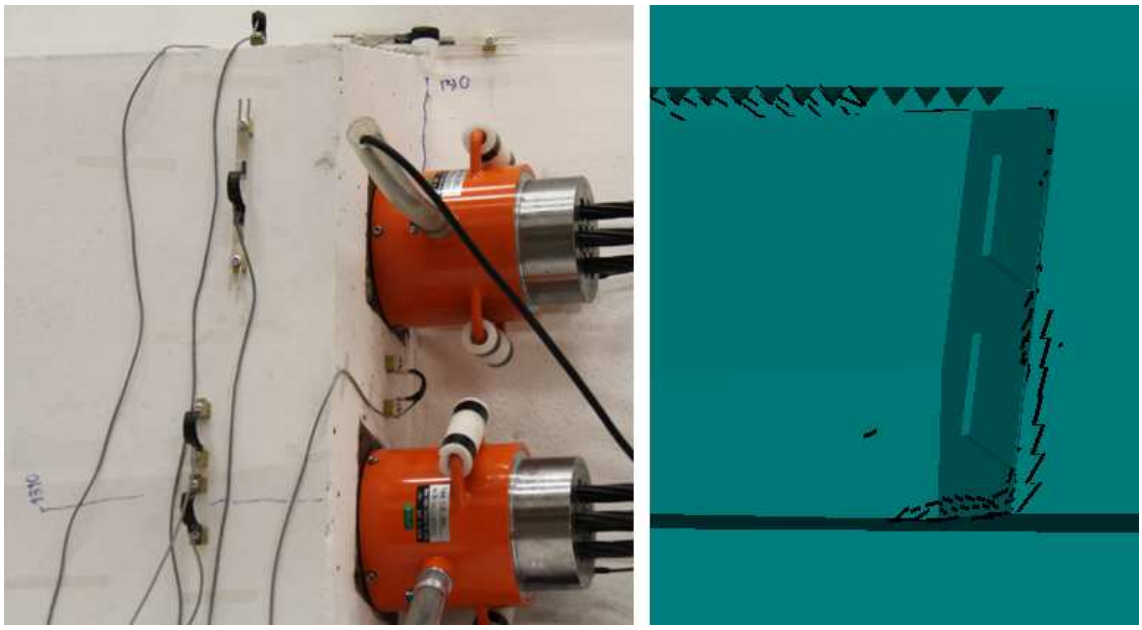

Figure 5.101: Comparison of cracking on the anchorage blister at the ninth load level of the first phase of the test

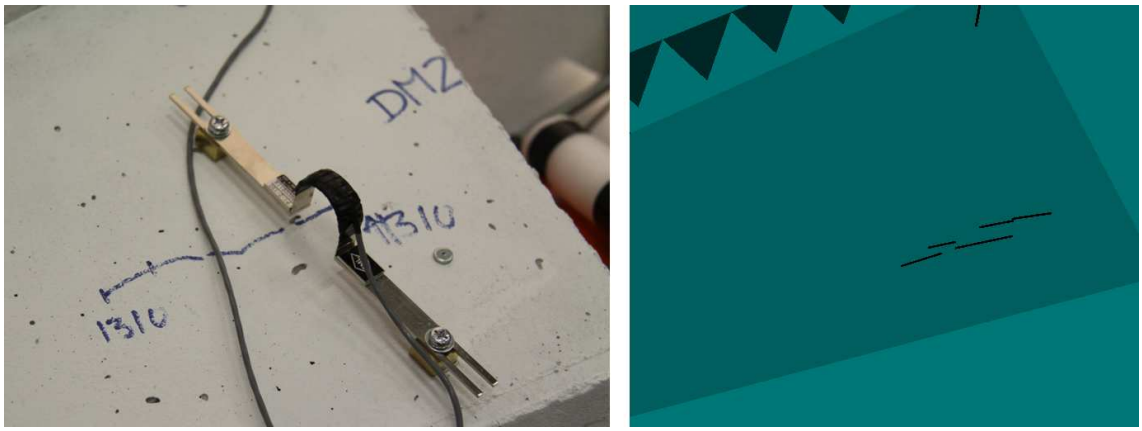

Figure 5.102: Comparison of cracking on the anchorage blister at the ninth load level of the first phase of the test

The cracking at the underside of the bottom slab at the tenth load level of the first phase of the test (aprox. 1550 kN) is presented in Figure 5.103.

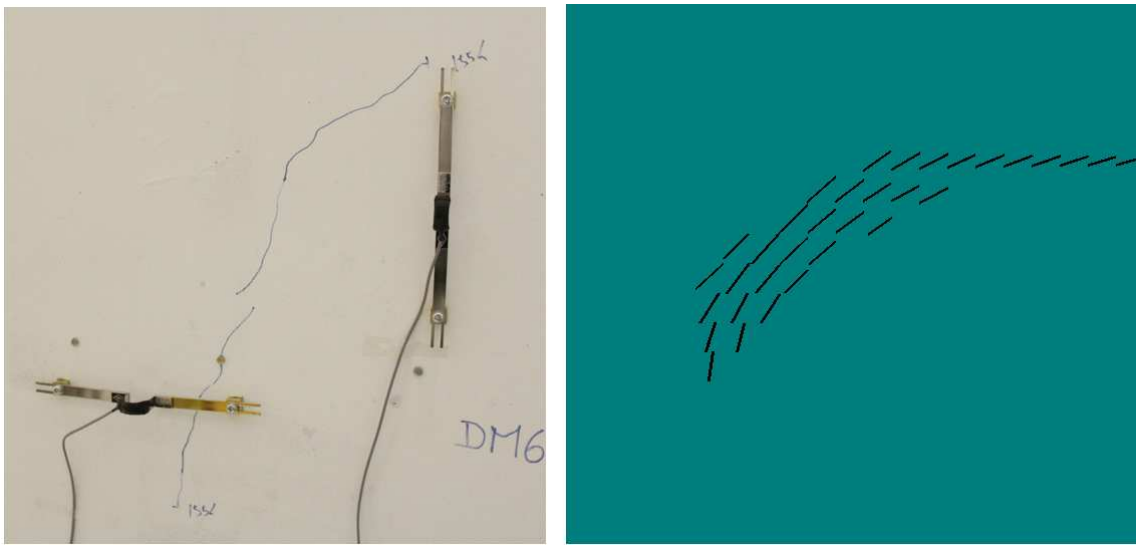

Figure 5.103: Comparison of cracking on the underside of the bottom slab at the tenth load level of the first phase of the test

At the twelfth load step of the second phase of the test (aprox. 1600 kN) the cracking on the top surface of the web can be seen in Figure 5.104.

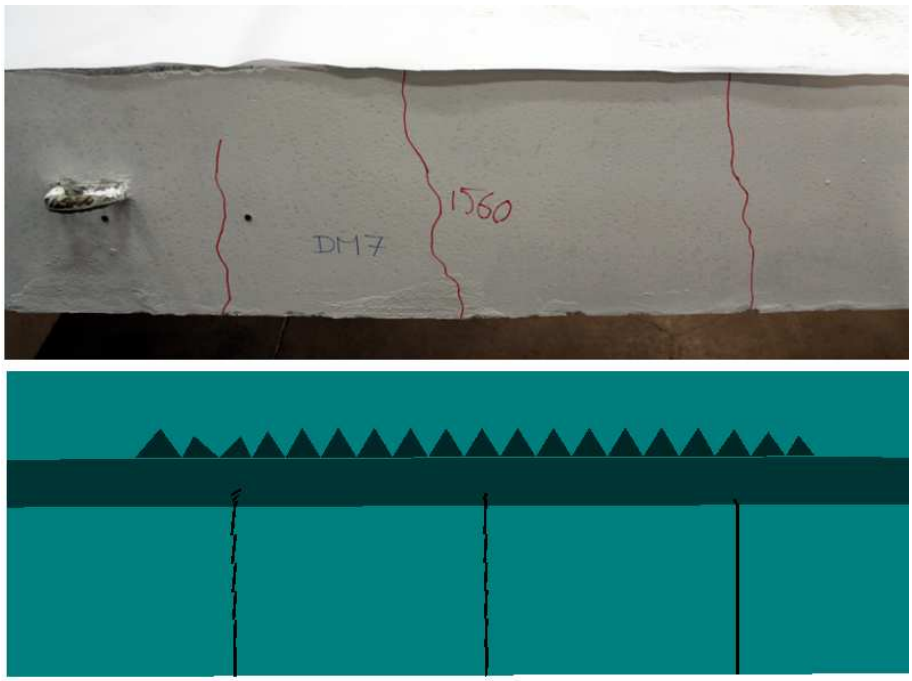

Figure 5.104: Comparison of cracking on the top surface of the web at the twelfth load step of the second phase of the test

At the end of the second phase of the test, for a load of approximately 1870 kN, the comparison of cracking on the blister and on the underside of the bottom slab is presented in Figures 5.105 and 5.106, respectively.

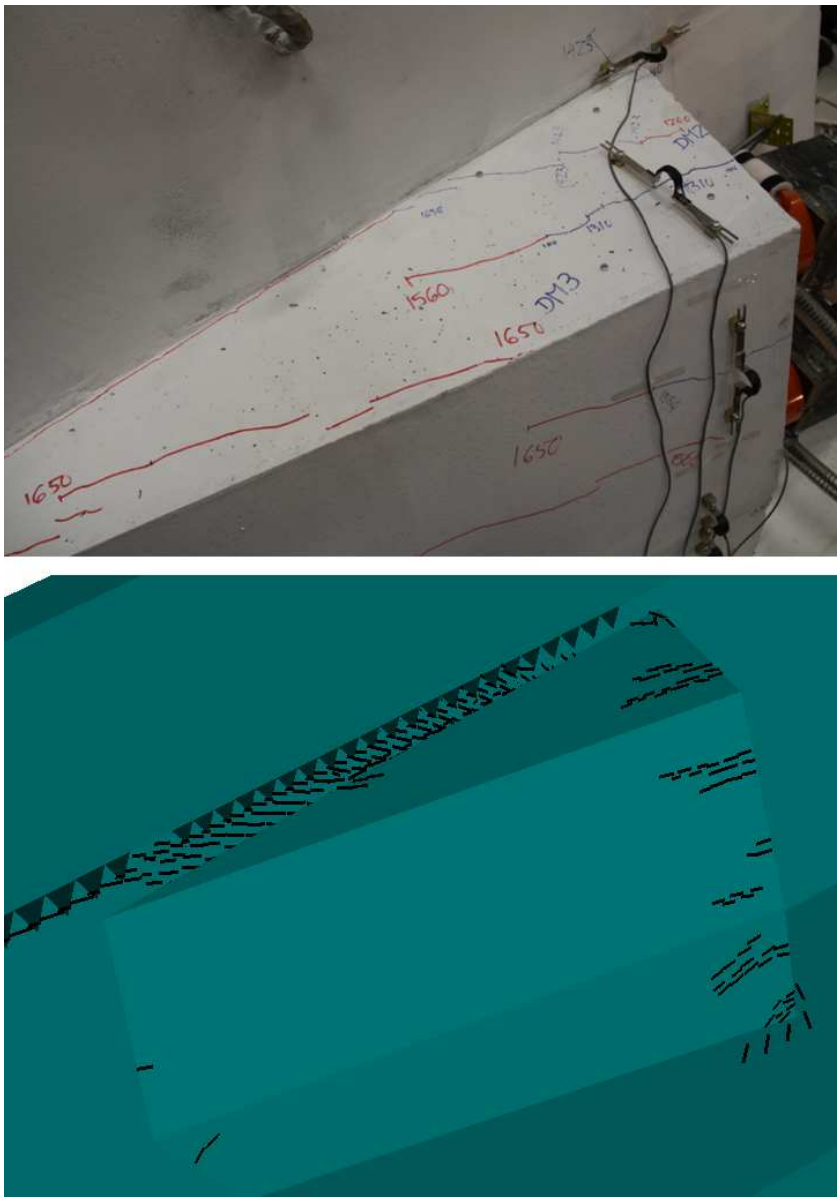

Figure 5.105: Comparison of cracking on the blister at the end of the second phase of the test

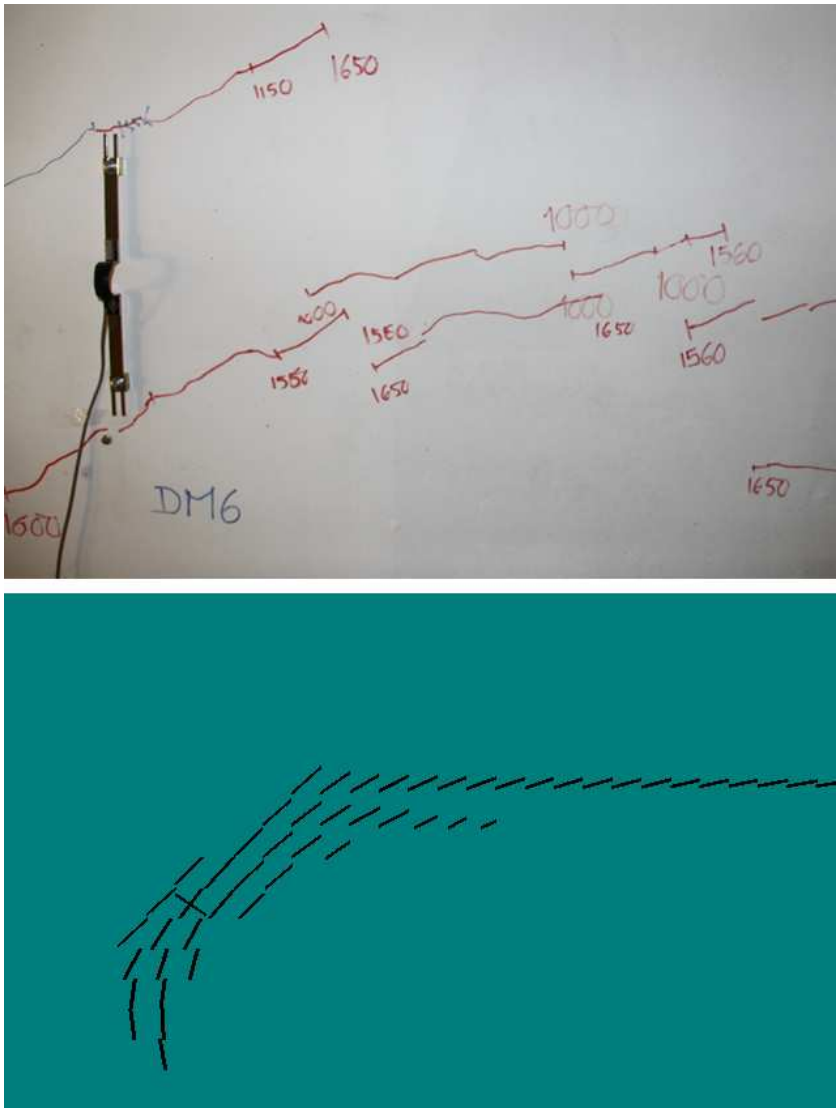

Figure 5.106: Comparison of cracking on the underside of the bottom slab at the end of the second phase of the test

In the figures presented above the similarity between the crack pattern obtained in numerical simulation and on the experimental test can be observed.

5.4.1.2 Discussion of the results of parameters recorded throughout the test

Figure 5.107 shows the comparison between the evolution of the blister displacements with the average load for the experimental and numerical models. Regarding the experimental curve, only the first phase of the test is represented.

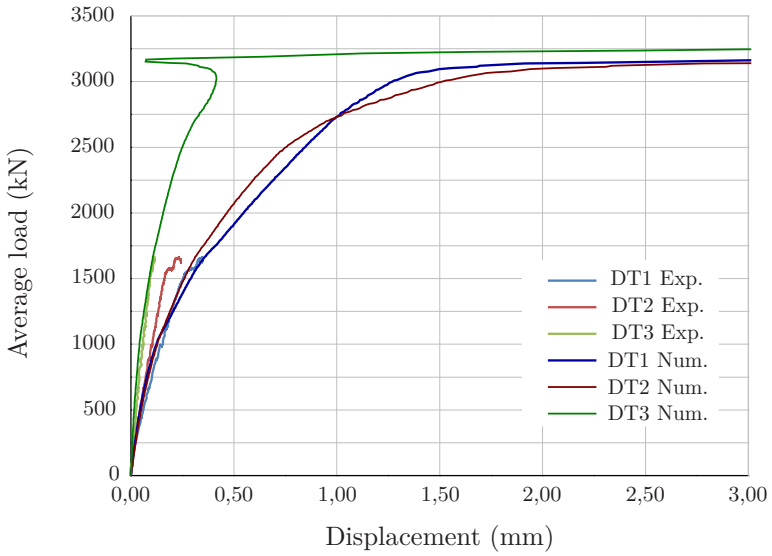

Figure 5.107: Evolution of the blister displacements with the average load

Figure 5.108 shows an amplification of the load-displacement curves within the range of loading covered by the test.

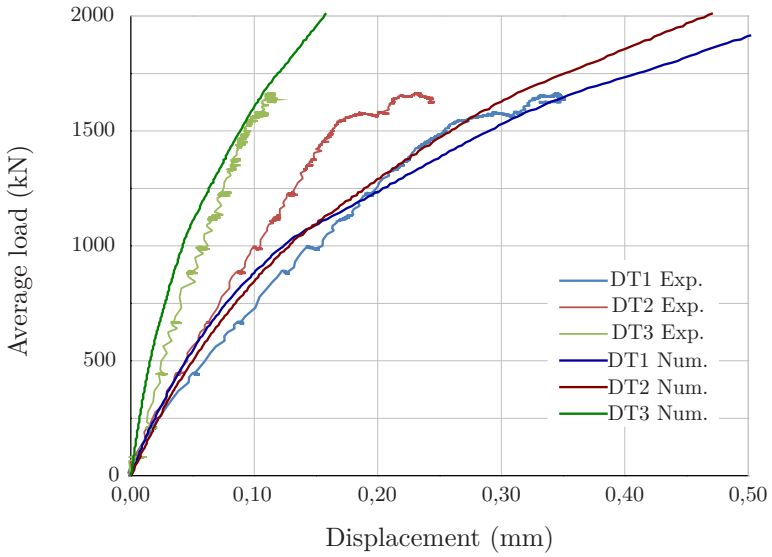

Figure 5.108: Evolution of the blister displacements with the average load

As can be observed in the figures above, there is a good agreement between the experimental and numerical curves. Near failure, the numerical analysis shows that the steel reinforcement achieved high strain values, but the failure of the model was governed by concrete crushing.

The average failure load was 3304,8 kN, which corresponds to a ratio between the

average failure load and the design load of 3,9, and a ratio between the average failure load and the breaking load of a tendon with 7 strands of 1,7.

5.4.2 HPFRC blister model

The comparison between the appearance of cracks that have formed until the eleventh load level (aprox. 1380 kN) on the anchorage blister, in the experimental test and in the non-linear analysis, is presented in Figure 5.109, for the HPFRC blister model.

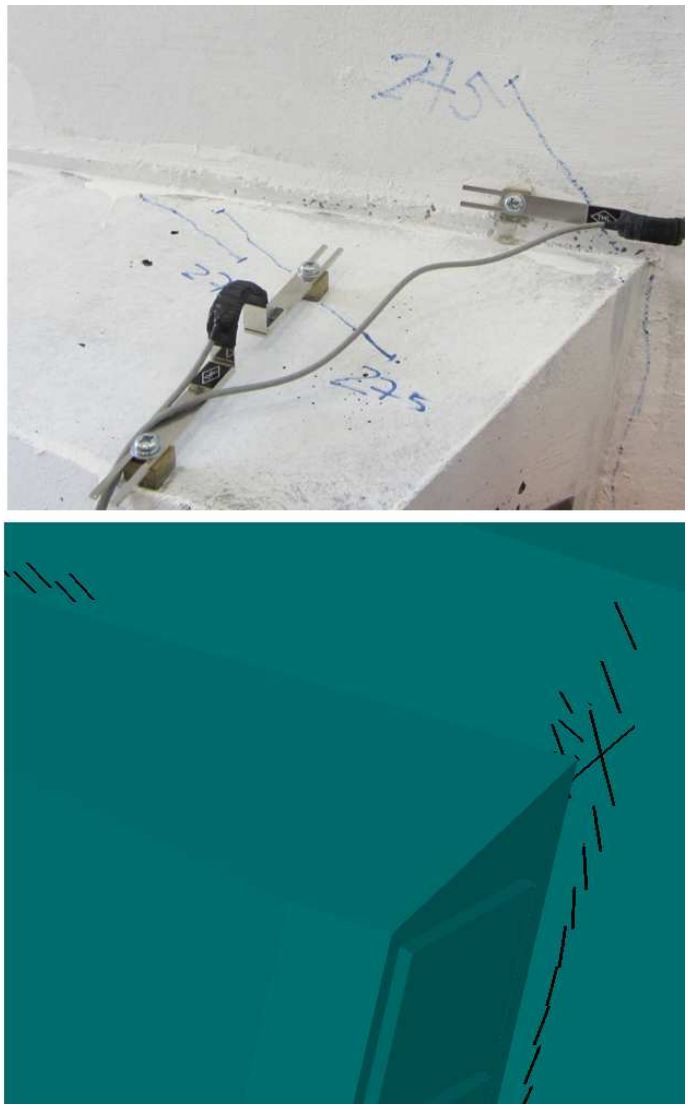

Figure 5.109: Comparison of cracking on the anchorage blister at the eleventh load level

At the fourteenth load step (aprox. 1750 kN), the cracking on the interface slab/blister is presented in Figure 5.110 for the experimental and numerical models.

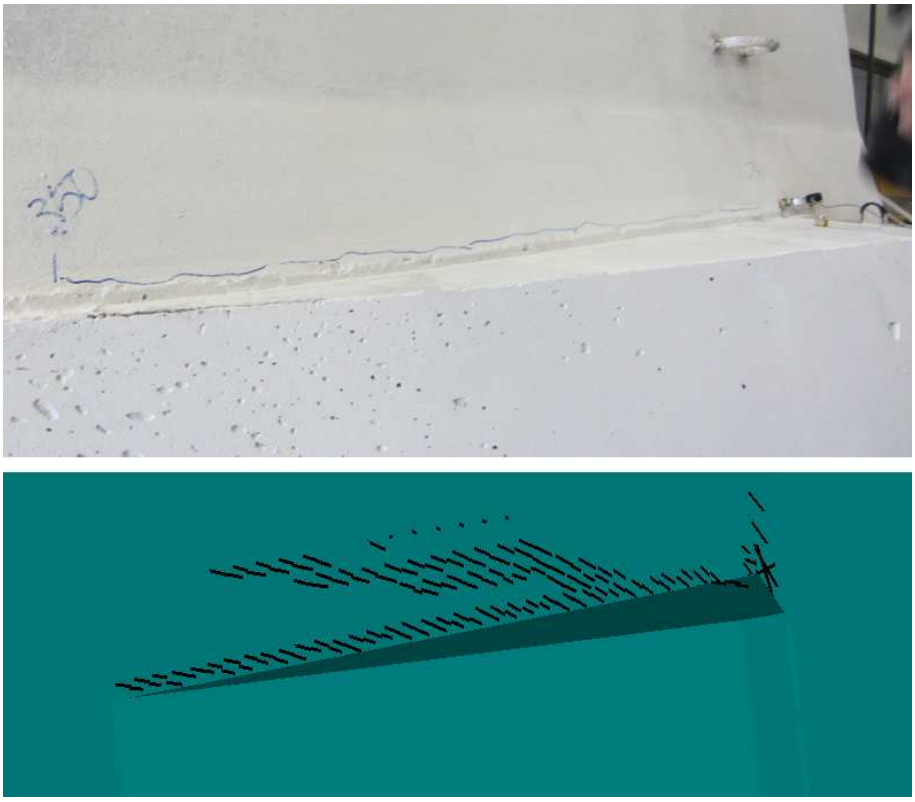

Figure 5.110: Comparison of cracking on the interface slab/blister at the fourteenth load step

At the end of the experimental test, for a load of approximately 2100 kN, the comparison of the crack pattern on the underside of the bottom slab and on the anchorage blister is presented in Figures 5.111 and 5.112, respectively.

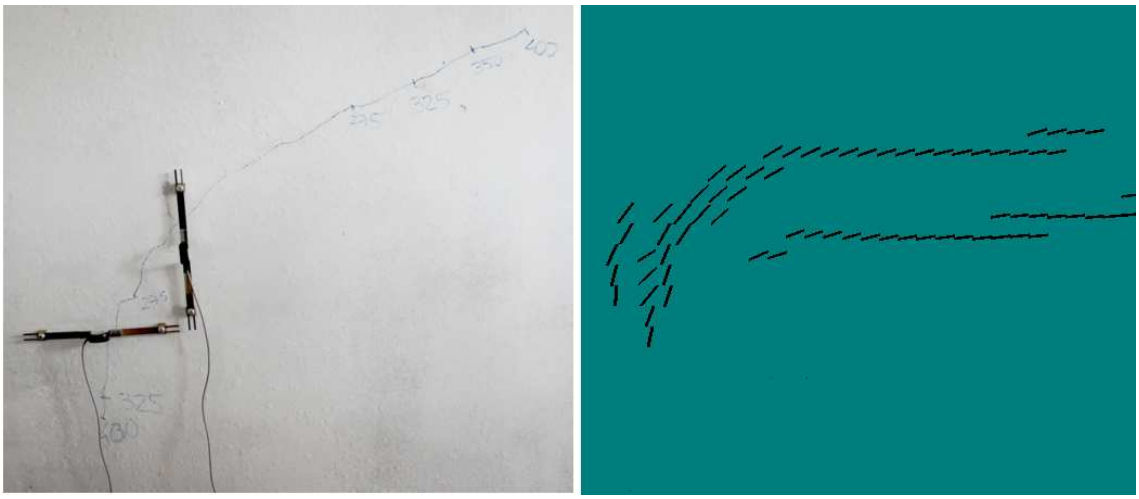

Figure 5.111: Comparison of cracking on the underside of the slab at the end of the experimental test

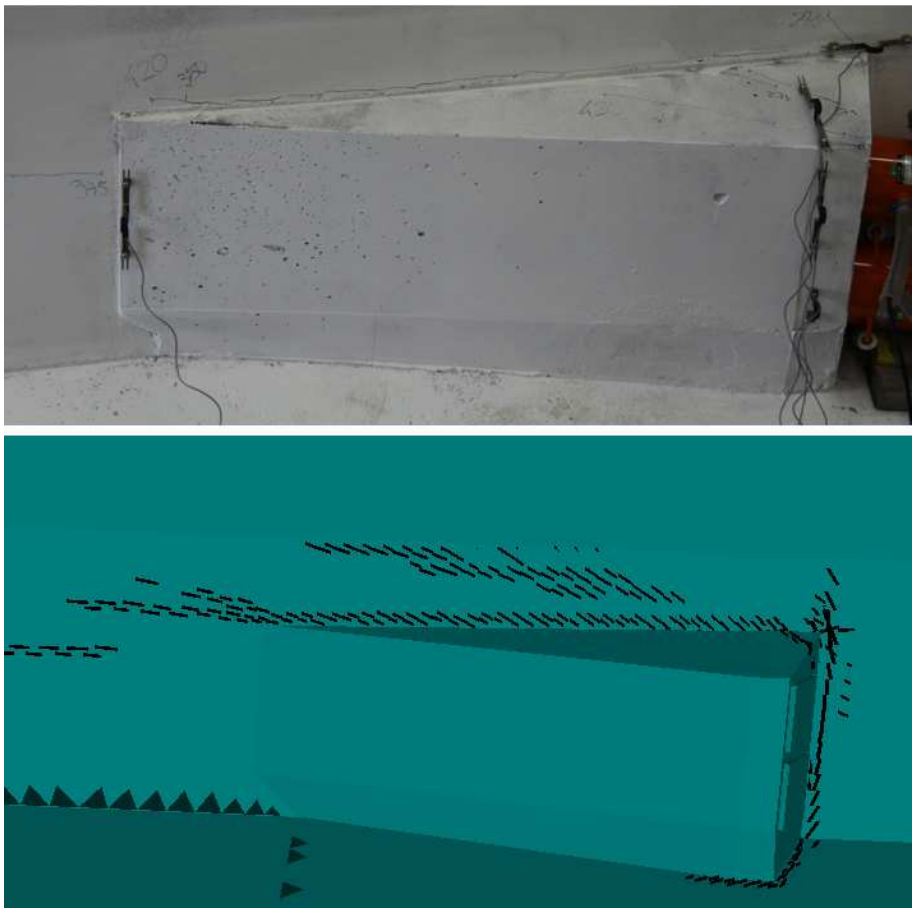

Figure 5.112: Comparison of cracking on the anchorage blister at the end of the experimental test

As in the case of the reference model, the crack pattern obtained in numerical simulation and on the experimental test for the HPFRC blister model is very similar. There are, however, some small differences regarding the cracking on the anchorage blister: in the numeric model almost no cracking was observed in the anchorage blister for the level of load attained in the experimental test, analogously to what was observed in the experimental test of the HPFRC precast blister model.

5.4.2.1 Discussion of the results of parameters recorded throughout the test

Figure 5.113 presents the comparison between the evolution of the blister displacements with the average load for the experimental and numerical models. An amplification of the load-displacement curves within the range of loading covered by the test is shown in Figure 5.114.

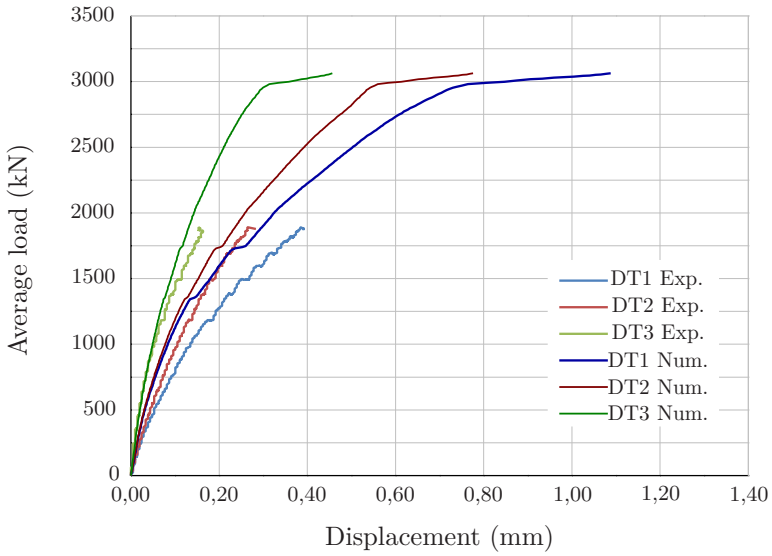

Figure 5.113: Evolution of the blister displacements with the average load

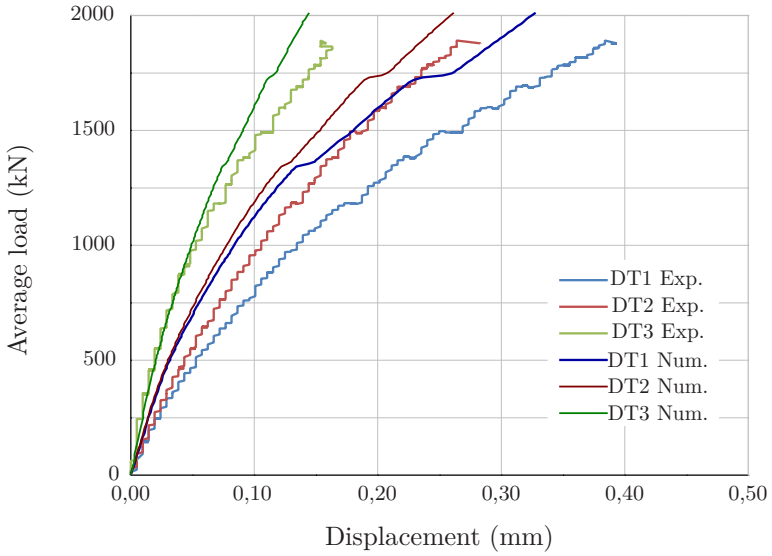

Figure 5.114: Evolution of the blister displacements with the average load

In the HPFRC blister model, the load-displacement curves obtained in the numerical model show a slightly more rigid behaviour for transducers 1 and 2. Beyond that, there is a good agreement between the experimental and numerical curves.

The average failure load was 3063,2 kN, which corresponds to a ratio between the average failure load and the design load of 3,6, and a ratio between the average failure load and the breaking load of a tendon with 7 strands of 1,6.

5.5 Design and detailing recommendations

5.5.1 Resistance of the interface between the HPFRC precast blister and the slab and web of the model

The resistance of the interface between the HPFRC precast blister and the slab and web of the model was evaluated using the formulation proposed by the Model Code 2010 (2012), based in Randl (2013), and presented in equation (5.11).

$$\tau_u = c_r \cdot f_{c,cube}^{1/3} + \mu(\rho k_1 f_y + \sigma_n) + k_2 \rho \sqrt{f_y f_{c,cube}} \tag{5.11}$$

where,

τ_u is the ultimate shear friction capacity;
c_r is the coefficient for aggregate interlock effects at rough interfaces;
ρ is the degree of reinforcement crossing the interface ($\rho = A_s/A_c$);
k_1 is a coefficient that addresses the fact that the tensile force in the reinforcement may be limited due to simultaneous bending and/or reduced anchorage of the bars;
σ_n is the compressive stress due to external normal force;
k_2 is the coefficient that considers the interaction of bending and axial stress in the connector and also the fact that interface shear failure may already occur at low slip values.

The equation (5.11) explicitly includes the influence of mechanical interlocking and adhesive bonding, friction due to external compression forces perpendicular to the interface and due to the clamping effect caused by reinforcement, and dowel action of the reinforcement that crosses the interface.

Since, in this case, there are two interfaces with different characteristics, equation (5.12) will be used for the determination of the ultimate load (V_u).

$$V_u = c_r \cdot f_{c,cube}^{1/3} \cdot A_c + \mu(A_s k_1 f_y + P_n) + k_2 A_s \sqrt{f_y f_{c,cube}} \tag{5.12}$$

where P_n is the compressive external normal force.

The calculation of the contribution of each of the aforementioned mechanisms is presented below.

5.5.1.1 Definition of the interfaces

In the present case, as shown in Figure 5.115, there are two different interfaces between the HPFRC precast blister and the slab and web of the model.

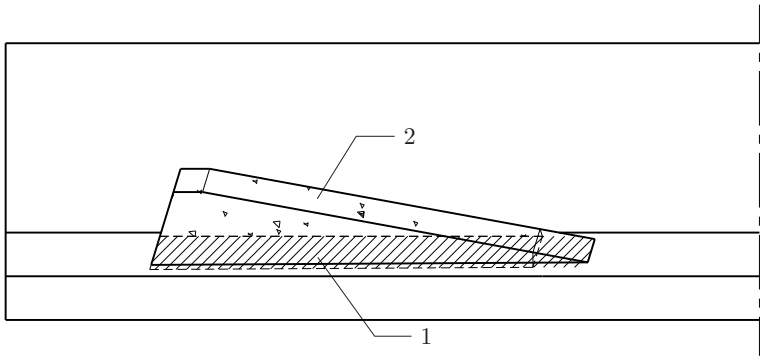

Figure 5.115: HPFRC blister model - Elevation

It should be noted that it was considered that Interface 1 also includes the adjacent surface at the end of the precast blister, given that in order to have slippage of the blister, failure of this surface must occur.

The area of the different interfaces is given in Table 5.24.

Table 5.24: Geometric characteristics of the considered interfaces

Interface	A_c (m^2)
1	0,810
2	0,184
Total	0,994

5.5.1.2 Mechanical interlocking

Table 5.25 presents the values considered for the determination of the contribution of the mechanical interlocking and adhesive bonding part for the shear strength.

Table 5.25: Resistance of the interface due to mechanical interlocking

$f_{c,cube}$ (MPa)	c_r	A_c (m^2)	$c_r \cdot f_{c,cube}^{1/3} \cdot A_c$ (kN)
49,2	0,4	0,994	1456,9

The value adopted for the coefficient c_r corresponds to the value indicated by Randl (2013), for very rough surfaces, not including the safety factor.

5.5.1.3 Friction

Friction due to external compression forces perpendicular to the interface blister/slab

The interface blister/slab is compressed by the applied prestressing force (P). So, the friction due to external compression forces perpendicular to the interface blister/slab depends on the value of the component of the prestressing force that is perpendicular to the interface (P_n), as shown in Table 5.26.

Table 5.26: Resistance of the interface due to external compression forces perpendicular to the interface

Interface	μ	P_n (kN)	μP_n (kN)
1	1,4	P sin16,72	0,40 P

The value considered for the coefficient of friction was obtained by equation (5.9), from Santos and Júlio (2014), and is presented in Table 5.16.

Friction due to clamping effect caused by the reinforcement

Figures 5.116 and 5.117 show the reinforcement in the blister anchorage zone.

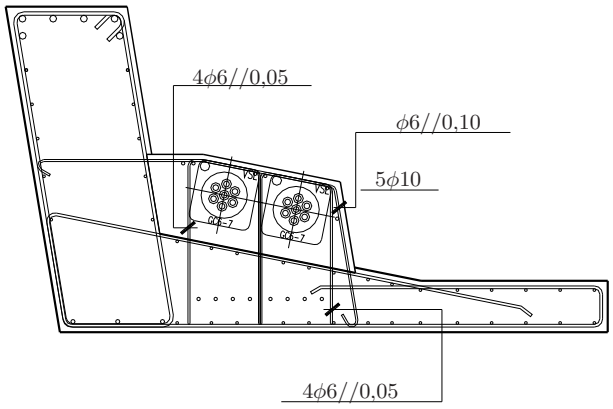

Figure 5.116: Reinforcement in the blister anchorage zone - Cross section

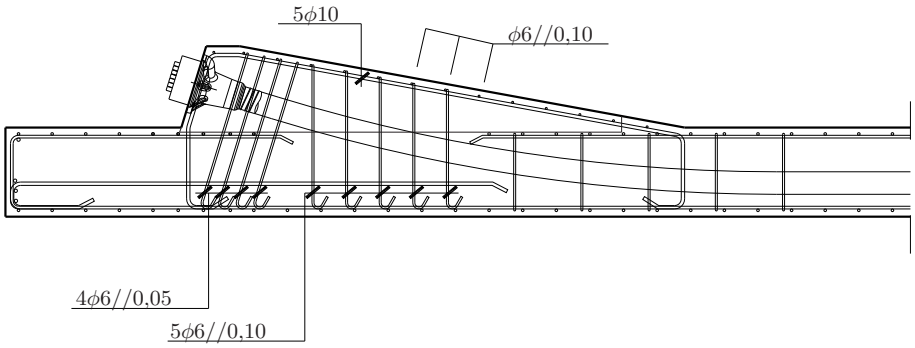

Figure 5.117: Reinforcement in the blister anchorage zone for tendons A and B

As can be seen in the figures above, the steel reinforcing bars are not perpendicular to the interface. Thus, it was considered only the contribution of the reinforcement perpendicular to the interface. The determination of the effective area of steel reinforcement crossing the interface is shown in Table 5.27.

Table 5.27: Effective area of steel reinforcement crossing the interface

Interface	Reinforcement	A_s (cm^2)	α_L (°)	α_T (°)	$A_s sin\alpha$ (cm^2)
1	4φ6//0,05	4,52	73,0	78,7	4,24
1	5φ6//0,10	5,65	90,0	78,7	5,54
1	14φ6	3,96	90,0	69,2	3,70
1	10φ10	7,86	90,0	78,7	7,71
2	14φ6	3,96	90,0	80,5	3,91

The indicated angles α_L and α_T are the angles between the reinforcing bars and the concrete surface, on the longitudinal and transversal direction, respectively.

Table 5.28 presents the calculation of the resistance of the interface due to clamping effect caused by the reinforcement and the values adopted for the parameters involved.

Table 5.28: Resistance of the interface due to clamping effect caused by the reinforcement

Interface	$A_s sin\alpha$ (cm^2)	Bar diameter (mm)	f_y (MPa)	μ	k_1	$\mu(A_s sin\alpha)k_1 f_y$ (kN)
1	13,48	6	564	1,4	0,5	532,2
1	7,71	10	542	1,4	0,5	292,5
2	3,91	6	564	1,4	0,5	154,4
Total						979,1

For the coefficient k_1 was adopted the recommended value for very rough surfaces (Randl, 2013).

The contribution of the steel reinforcement in the direction of the interface was neglected.

5.5.1.4 Dowel action

The determination of the shear strength due to dowel action is shown in Table 5.29.

Table 5.29: Dowel action

Interface	$A_s sin\alpha$	Bar diameter	f_y	$f_{c,cube}$	k_2	$k_2(A_s sin\alpha)\sqrt{f_y f_{c,cube}}$
	cm^2	(mm)	(MPa)	(MPa)		(kN)
1	13,48	6	564	49,2	0,9	202,1
1	7,71	10	542	49,2	0,9	113,3
2	3,91	6	564	49,2	0,9	58,6
Total						374,0

Also for the coefficient k_2 was adopted the value recommended by Randl (2013) for very rough surfaces.

5.5.1.5 Failure load of the interface

The failure load of the interface, and consequently the maximum prestressing force (P_u), presented in Table 5.30 was determined using equation (5.12).

Table 5.30: Failure load of the interface

$c_r \cdot f_{c,cube}^{1/3} \cdot A_c$	μP_n	$\mu(A_s sin\alpha)k_1 f_y$	$k_2(A_s sin\alpha)\sqrt{f_y f_{c,cube}}$	V_u	P_u
(kN)	(kN)	(kN)	(kN)	(kN)	(kN)
1456,9	0,40 P_u	979,1	374,0	P_u cos16,72	5038,4

The average failure load is 2519,2 kN, which corresponds to a ratio between the average failure load and the design load of 3,0, and a ratio between the average failure load and the breaking load of a tendon with 7 strands of 1,3.

5.5.2 Design recommendations

Although the existence of simplified methods for the design of anchorage zones, the design of anchorage corner blisters presents some peculiarities, not only because they are intermediate eccentric anchorages (i.e. the tendons do not extend over the full length of the bridge, so they have to be anchored at intermediate locations along the girder) but also because these anchorages are located in blisters (outside the webs), so the prestressing force has to be transferred from the blister to the bottom slab and the web of the girder. Thus, the following effects must be taken into account in design and safety assessment:

- bearing pressures in the local anchorage zone;
- corbel action and local bending (due to the eccentricity of the tendon);
- blister bursting (due to the distribution of the concentrated post-tensioning force);
- tendon deviation (due to the tendon curvature);
- transfer of forces into the slab and web.

For the bearing pressures, the safety verification is typically carried out indirectly through geometrical considerations specified by the post-tensioning system supplier, such as the imposition of minimum permissible anchorage spacing and minimum permissible edge distances, for certain levels of concrete resistance to compression. In cases where this information is not provided, the expressions referred in Chapter 3 (in particular equation (3.22) by Wollmann and Roberts-Wollmann (2000) with a calibration factor of $\eta = 0{,}83$ for HPFRC) can be used, not forgetting that the adequate serviceability of the local anchorage zone is not assured.

Regarding the other effects that require steel reinforcement, it is possible to consider them separately but generally this option leads to solutions with high amounts of reinforcement with the consequent problems in concrete casting *in situ*. The results are zones with low concrete compacity, which may lead to concrete crushing failures under the anchor plates. The need for optimisation, to reduce steel reinforcement density, can justify the use of more elaborated/sofisticated methods with the combined integration of all the effects.

One option could be the use of a linear-elastic analysis but, in the case of anchorage corner blisters, it requires the use of 3D finite elements, with the inherent difficulties in model definition and quantification of results for the design of steel reinforcement.

Another valid and more rational alternative can include the development of strut-and-tie models. These models provide a conservative design based on equilibrium conditions and material strength limitations for the elements of the model. In more complex cases, the use of linear-elastic models can be very useful to find the load paths and to identify the regions with higher stresses (critical regions), serving as a basis for the development of strut-and-tie models.

Principles for the development of a corner blister strut-and-tie model

The strut-and-tie models must be developed taking into consideration the stress trajectories, the distributions obtained from the linear-elastic analysis and the need to keep the equilibrium with the applied loads in the ultimate limit state. In the choice of the ties adopted position and direction has to be taken into account the fact that the ties should coincide with the corresponding reinforcement. Figure 5.118 shows the example of a strut and tie model, where the mentioned effects that have to be taken into account in anchorage blisters, are shown.

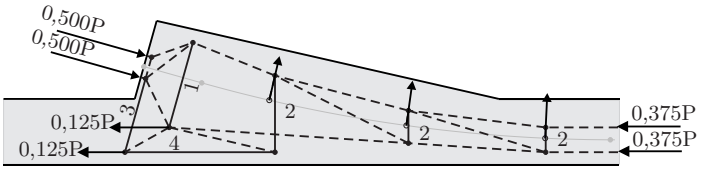

Figure 5.118: Example of a strut-and-tie model

Regarding the post-tensioning anchorage force, it is usually sufficient to replace the anchorage with two statically equivalent forces (P/2 acting at the quarter points of the anchorage). The action of radial forces due to tendon curvature, both in longitudinal section and in plan, can be considered.

In the longitudinal sections, due to the dispersion of the concentrated prestressing force over the cross-section, it can be assumed that the reinforcement needed should be parallel to the front face of the blister (perpendicular to the applied force) - ties 1 and 3 of Figure 5.118. The resultant tie force can be located in the theoretical section where the compression stress field, resulting from the dispersion of the concentrated force, intersects the upper face of the blister. Depending on the dimensions of the anchorage blister, the layout of the strut-and-tie model near the anchorage can be slightly different, as shown in Figure 4.50 for the HPFRC blister with smaller dimensions.

In the slab between anchorages, the compression can be considered as uniformly distributed along the full slab thickness (for this purpose, and for simplification, the variation of the slab thickness at the junction with the web can be discarded). As such, two equal struts located at one quarter and three quarters of the regular slab thickness can be adopted (see Figure 5.118).

A tie back force of 25% of the prestressing force is sufficient to control cracking and can be assumed uniformly distributed along the full slab thickness.

The transverse ties (tie 2 of Figure 5.118) can be designed to resist to half of the radial forces derived from tendon curvature being the other half held by the concrete struts that

converge in each top node. In this case, the orientation of the left strut of each node should be determined through the equilibrium at the node.

Although the case of an anchorage corner blister is three dimensional, the decomposition in several 2D models is always possible.

5.5.3 Detailing recommendations

The compression strut and node forces should be resisted by concrete, and can be checked. This verification usually is not determining, since the concrete stresses at the end of the local zone and the beginning of the general zone are controlled by the local zone design to acceptable values (Rogowsky and Marti, 1996).

Reinforcement must be designed to resist to the tensile forces of the ties of the strut-and-tie model, not forgetting that the ties of the model are resultants of stress fields, therefore the centroid and the direction of the reinforcement should be similar to the ties of the model. In anchorage zones it is recommended to limit the reinforcement design strength to 250 MPa to control the crack width (EN 1992-2, 2005).

The adoption of U-shaped ties must be preferential over closed loops to simplify the steel reinforcement assembly, regarding that shall be provided adequate anchorage of the bars (if possible, the bars should be extended to the bottom face of the slab, even for the precast blister solutions), specially for precast blister solutions.

Close spacing of the ties is recommended at the bursting zone. The spacing must not exceed the distance of the anchorage to the edge or 150 mm (Wollmann, 1992). In the remaining zone of the anchorage blister, the spacing of ties shall be restricted regarding crack control.

For the cases of precast blisters solutions, special attention shall be given to the shape of the steel reinforcement that is left in standby, in order to simplify its positioning on the reinforcement of the bottom slab. The treatment of the surfaces in contact with the bottom slab and web is highly recommended, in order to increase bond between the blister and the remaining adjacent elements. The reinforcement that crosses the interface between the two concretes shall also be designed to resist the shear force in the interface (see section 5.5.1)

"Finally, don't be overly conservative. Not only it is wasteful, but also leads to more congested details and more difficult construction which can in turn result in an inferior structure. Properly placed and consolidated concrete is far more important than extra reinforcement" (Rogowsky and Marti, 1996).

5.6 Conclusions

In this chapter, the experimental program in corner anchorage blister specimens was described, and the results of the tests were given and discussed. A non-linear analysis of the tested specimens was presented and the results were compared with the ones obtained in the experimental tests. At last, recommendations for the design and detailing of anchorage blisters were proposed.

The tests on anchorage blisters were conditioned by the limitation of the value of the force that could be applied, since the anchorage bearing plate and duct adopted were the ones for 7 strands to not misrepresent the behaviour of the specimens. Despite the fact of have being used 9 strands in a duct of 7 strands, the increase of the force value was not sufficient to achieve the failure of the specimens. Despite this limitation, in the HPFRC blister specimens the design value of the load was achieved with acceptable levels of cracking for a serviceability situation.

For the three specimens, the main cracks opened in the relative displacement transducers area, denoting a good agreement between the elastic 3D finite element analysis and the experimental results.

Comparing the test results of the HPFRC blister specimens, the two models showed a very similar behaviour during the test. No significant difference regarding cracking was observed, except for the crack formed in the connection between the blister and the bottom slab. Measurements of the relative displacement transducers in that zone showed that the relative displacement become higher for the precast blister model from a load value of approximately 1250 kN. Anyway, the crack width did not exceed 0,3 mm for the maximum load achieved in the test.

Regarding the steel reinforcement, although the strain values are not directly related to the tensile force on the ties of the strut-and-tie models used for design but with the steel reinforcement stress, in most cases the larger strains were measured in the strain gauges located in the reinforcement that corresponded to ties with larger tensile force. The measured values were all below the steel yielding strain.

In order to find the failure load of the specimens, the experimental tests were reproduced with the non-linear finite element analysis software ATENA. Because of the similarity between the HPFRC blister models and due to the difficulty of the accurate simulation of the mechanisms that contribute to the shear strength of the interface, it was decided not to analyse the model with the precast blister.

Regarding the blister displacements and the crack patterns, it was observed a good agreement between the experimental tests and the non-linear analysis.

For the ORC blister model, the average failure load was 3304,8 kN, which corresponds to a ratio between the average failure load and the design load of 3,9, and a ratio between the average failure load and the breaking load of a tendon with 7 strands of 1,7. In the case of the HPFRC blister model, the average failure load was 3063,2 kN, which corresponds to a ratio between the average failure load and the design load of 3,6, and a ratio between the average failure load and the breaking load of a tendon with 7 strands of 1,6.

Besides the fact of the steel reinforcement used in the blister zone had been intentionally undersized with the purpose of trying to reach the failure of the models during the test, as referred in Chapter 4, the failure loads obtained in the non-linear analysis have large safety factors. This may be due to the existence or secondary reinforcement which also contributes to the resistance and for neglecting the concrete tensile strength in the strut-and-tie models.

The resistance of the interface between the HPFRC precast blister and the web and slab of the model was evaluated using the formulation proposed by the Model Code 2010 (2012), based in Randl (2013). An average failure load of 2519,2 kN was obtained, which corresponds to a ratio between the average failure load and the design load of 3,0, and a ratio between the average failure load and the breaking load of a tendon with 7 strands of 1,3.

In conclusion, the use of HPFRC in anchorage corner blisters is a very interesting solution regarding the saving of materials and the reduction of the steel reinforcement density near the local anchorage zone, with the obvious advantages in concrete quality.

The adoption of solutions with HPFRC precast blisters avoids the production and casting with two different concretes on site. This solution can be advantageous with regard to quality control in the execution of HPFRC blisters.

Chapter 6

Conclusions and future developments

In the previous chapters, the conclusions concerning the various subjects were presented. In this sixth chapter, the main aspects mentioned throughout the work, and a summary of the main conclusions and recommendations arising from this study are shown.

6.1 Summary overview

The first chapter presented the history of the first post-tensioning structures and a brief historical background of the analysis methods of anchorage zones.

In the second chapter, a short literature review of the first developments of fiber reinforced concrete and the description of different high performance and ultra high performance concretes were presented. The composition of the HPFRC mixture was provided and the constituent materials characterised. The results of fresh concrete tests were presented and justified, and HPFRC workability analysed. The results of mechanical tests were analysed and followed by shrinkage measurements.

Chapter 3 started with a literature review on the research carried out on the bearing strength of concrete (plain, reinforced and reinforced high performance), and on load transfer tests regarding the test specimen, test procedure and acceptance criteria, according to three different guiding documents (FIP Recomendation, 1993, AASHTO, 2002 and European Organisation for Technical Approvals, 2002). The experimental program performed to assess both the ultimate capacity and the adequate serviceability of the local anchorage zone was presented. This program was based on load transfer tests specified in Guideline ETAG 013 (European Organisation for Technical Approvals, 2002). After, the

experimental program regarding test specimens, test procedure and experimental results was described. A comparison of the experimental results with models in the literature was then presented and discussed. At last, a non-linear analysis of the tested specimens was presented and the results were compared with the experimental tests.

Chapter 4 presented the design of half-scale anchorage blister models used to investigate the behaviour of anchorage blisters regarding the transmission of stresses to the web and the bottom slab of the girder and the feasibility of using high performance concrete in the blister only. Since it was intended to design the steel reinforcement of the test specimens using strut-and-tie models, the chapter began with a short literature review on developments on these type of models. Then, the specimens were described regarding the choice of geometry and layout of the prestressing tendons. The results of the elastic analysis were shown and the developed strut-and-tie models were presented and justified. Based on the strut-and-tie models the calculation of reinforcement was explained and detailed.

The experimental program regarding the models designed in Chapter 4 was presented in Chapter 5. To study the transmission of prestressing force to the slab and web of the section, assess the models used in design and to study the feasibility of using high performance concrete only in the blister, either with casting in situ, or with precast solutions, three half scale models of the inferior corner of a box girder bridge were tested: a reference specimen of ordinary reinforced concrete and two specimens with blisters of high performance fibre reinforced concrete (HPFRC). The three specimens had the same geometry, except for the anchorage blisters whose dimensions were reduced in the HPFRC blister specimens, and included a corner blister for two anchorages, with a portion of the slab and the web contiguous. Chapter 5 began by showing the execution of the anchorage blister specimens. The monitoring equipment and the test procedure was described and the results of the tests were presented and discussed. The non-linear finite element analysis of the anchorage blister models was presented and the results were compared with the ones obtained in the experimental tests. Then, the resistance of the interface between the HPFRC precast blister and the slab and web of the model was determined using the the formulation proposed by the Model Code 2010 (2012), based in Randl (2013). At last, design and detailing recommendations were provided and the conclusions were presented.

6.2 Conclusions

A summary of the main conclusions and recommendations of the study carried out is presented below.

6.2.1 High performance fibre reinforced concrete

The production of HPFRC in large scale was a challenge, since the mixture was extremely sensitive to the moisture content of the sand and to the ambient temperature. Regarding water content, in large scale production it was neither possible to dry the sand nor to accurately measure its moisture content, making it difficult to correct the amount of water to add to the mixture. The moisture content of the sand at its surface and the one below the surface differed. Concerning air temperature, and for temperatures higher than 25°C, it was not possible to achieve adequate workability without requiring the addition of significant amounts of water. The workability of the HPFRC mixture was assessed using the slump flow test and v-funnel test.

According to the mechanical characterisation tests carried out at the age of 28 days, the HPFRC presented an average compressive strength of 107,4 MPa, 113,5 MPa and 107,3 MPa for 150 mm and 100 mm cubic specimens and cylindrical test specimens, respectively.

Regarding the evolution with time of the mean compressive strength for three mixtures of HPFRC, referred to 150 mm cubes, it can be concluded that all mixtures presented a 7-day strength between 83% and 89% of the 28-day strength. With 14 days, the strength range between 91% and 94% of the strength at 28 days.

For the average of the mean value of the concrete tensile strength, values of 9,4 MPa and 11,9 MPa were obtained from tensile splitting test and three point bending tests, respectively.

The average value achieved for the secant modulus of elasticity was 43,3 MPa.

6.2.2 Local anchorage zone

The load transfer tests on prismatic specimens were intended to assess the dimensions of the concrete cross-section and the confining reinforcement needed for a specific anchorage and a certain type of concrete.

In the case of tests on HPFRC specimens, the intention was to reduce the cross-section area to the minimum possible, so that the dimension corresponding to the width of the anchorage and concrete cover on each side was adopted.

Since the steel fibers are expensive and require an extra step in the mixing procedure of the HPFRC it was decided to test a specimen of high performance concrete without fibers. However, due to the low tensile strength presented by this type of concrete, the specimen had an early failure, showing that it would not be a good solution. This test

confirmed the importance of the concrete tensile strength in the resistance of the local anchorage zone.

It was observed that, generally, for specimens with identical type and amount of reinforcement, the failure load of the specimen increased and the crack width decreased with increasing compressive and tensile strengths.

From the analysis of the test results it can be concluded that the use of HPFRC allows the suppression of the confining reinforcement for the type of anchorage chosen if the same concrete section is used as specified for the ordinary reinforced concrete specimens. The use of HPFRC also allows the reduction of the concrete cross-section and of the confining reinforcement.

The suppression of all the confining reinforcement is however not advisable, since the non-randomness of fibre orientation can lead to formation of cracks with unacceptable width.

The comparison of the experimental tests results with the models of other authors showed that, for unreinforced concrete specimens, the predicted failure loads were significantly higher than those obtained in the tests. The main reason was the use of special anchorage devices in the tests, instead of simple plates, for which the used equations were assessed.

For the reinforced concrete specimens, the predicted loads proved to be, in most cases, against safety. One of the causes of the differences could be related to the fact that the different confinement reinforcement levels had different strains along the height of the confined zone, and just some of the reinforcing bars attained yielding. This fact may have led to the existence of non uniform confinement forces along the height and, smaller than the ones considered in the proposed equations. Besides the confinement force, the use of special anchorage devices instead of simple plates also affects the results.

For reinforced HPFRC specimens it was proposed to use the formulation proposed by Wollmann and Roberts-Wollmann (2000) for extrapolation of special bearing plate acceptance test results with a calibration factor of 0,83.

The non-linear analysis used to simulate the behaviour of the prismatic test specimens, in order to assess the parameters to define the materials, for further application in the non-linear analysis of the anchorage blister specimens, proved to be an extremely slow process. The analysis running time of the models until failure was approximately four and two days for the ORC and HPFRC specimens, respectively.

The failure loads obtained in the non-linear analysis were close to the experimental values, namely in the case of the HPFRC specimens, having a maximum difference of only 1% for specimens P6.

The numerical models calibrated in this work can be used for parametric analysis, varying the concrete characteristics, the geometry and amount of steel reinforcement, and the type of post-tensioning anchorage.

6.2.3 Tests on anchorage blister models

The tests on anchorage blister models were conditioned by the fact that the ducts and anchorage bearing plates adopted were designed for 7 strands, to not misrepresent the behaviour of the specimen. Despite the fact of being possible to use 9 strands in a duct of 7 strands, which increased the value of force that could be applied, it was not sufficient to achieve the failure of the models.

Despite this limitation, the design value of the load was achieved with acceptable levels of cracking for a serviceability situation, so the proposed objectives were accomplished.

The HPFRC blister and the HPFRC precast blister models showed a very similar behaviour during test. No significant difference regarding cracking was observed except for the crack formed in the connection between the blister and the bottom slab. Measurements of the relative displacement transducers in that zone showed that the relative displacement become higher for the precast blister model from a load value of approximately 1250 kN. Anyway, the crack width did not exceed 0,3 mm for the maximum load achieved in the test.

As the failure of the models in the laboratory test was not achieved, a non-linear analysis was performed reproducing the experimental tests. The blister displacements and crack patterns obtained in the tests and in the non-linear analysis were compared, and a good agreement was observed between them. Regarding the attained failure loads, ratios between the average failure load and the design load of 3,9 and 3,6, and ratios between the average failure load and the breaking load of a tendon with 7 strands of 1,7 and 1,6 were achieved for the ORC and HPFRC blister models, respectively.

The HPFRC precast blister model was not analysed with ATENA software due to the difficulty of the accurate simulation of the mechanisms that contribute to the shear strength of the interface, namely the dowel action.

Using the formulation proposed in the Model Code 2010 (2012) for the evaluation of the resistance of the interface between the HPFRC precast blister and the web and slab of the model, a ratio between the average failure load and the design load of 3,0, and a ratio between the average failure load and the breaking load of a tendon with 7 strands of 1,3 were obtained.

In conclusion, the use of HPFRC in anchorage corner blisters is a very interesting

solution regarding the saving of materials and the reduction of the steel reinforcement density near the local anchorage zone, with the obvious advantages in concrete quality.

The adoption of solutions with HPFRC precast blisters avoids the production and casting with two different concretes on site. This solution can be advantageous with regard to quality control in the execution of HPFRC blisters and reduction of the execution time.

6.3 Future developments

Possible future developments could involve the optimisation of the production of high performance concrete and the improvement of the composition for the mixture to be less sensitive to ambient temperature.

This thesis was based on a half-scale model of an anchorage corner blister of an existing bridge. For this reason only blisters with tendons for 7 strands were studied and the load transfer tests performed for this anchorage dimension. Typically, small anchorages have dimensions governed by minimum geometrical conditions and not necessarily by strength. Therefore, load transfer tests with larger anchorages should be performed.

With the HPFRC mixture and the type of anchorage bearing plate that was utilised in this study, it was possible to reduce the blister dimension to the minimum possible, so that the anchorage edge distance was the dimension corresponding to half-width of the anchorage plus concrete cover. It would be interesting to find from what concrete strength would it be possible to have the mentioned edge distance, including the case of larger anchorages.

The application of precast solutions with HPFRC in anchorage zones could also be an interesting solution in the cases of end zones of prestressed bridge I-girders or anchorage zones for external post-tensioning in box girder bridges.

The failure loads achieved in the non-linear analysis of the anchorage blisters should be confirmed experimentally in future works.

References

[1] (1992). *External Post-tensioning*. VSL Report Series 1. VSL International Ltd., Berne, Switzerland.

[2] AASHTO (2002). *Standard Specifications for Highway Bridges*. American Association of State Highway and Transportation Officials, Inc., Washington, D.C., 17th edition.

[3] Acker, P. and Behloul, M. (2004). Ductal® technology: A large spectrum of properties, a wide range of applications. In Schmidt, M., Fehling, E., and Geisenhanslüke, C., editors, *International Symposium on Ultra-High Performance Concrete*, pages 11–23. University of Kassel, Germany.

[4] Ahmed, T., Burley, E., and Rigden, S. (1998). Bearing capacity of plain and reinforced concrete loaded over a limited area. *Structural Journal*, 95(3):330–342.

[5] Alford, N. M. (1987). Production of fibre-reinforced cementitious composition. Canadian Patent 1216220. January 6, 1987.

[6] Alford, N. M. and Birchall, J. D. (1985). Fibre toughening of MDF cement. *Journal of Materials Science*, 20(1):37–45.

[7] Alfsen, M. H. (1918). Procédé pous couler le béton ou le béton renforcé. French Patent 485601. January 24, 1918.

[8] Ali, M. A., Majumdar, A. J., and Singh, B. (1975). Properties of glass fibre cement - the effect of fibre length and content. *Journal of Materials Science*, 10(10):1732–1740.

[9] Arıoglu, N., Girgin, Z. C., and Arıoglu, E. (2006). Evaluation of ratio between splitting tensile strength and compressive strength for concretes up to 120 mpa and its application in strength criterion. *ACI Materials Journal*, 103(1):18–24.

[10] Aspdin, J. (1824). An improvement in the mode of producing an artificial stone. Patent BP 5022. October 21, 1824.

[11] Au, T. and Baird, D. L. (1960). Bearing capacity of concrete blocks. *ACI Journal Proceedings*, 56(3):869–880.

[12] Aveston, J. and Kelly, A. (1973). Theory of multiple fracture of fibrous composites. *Journal of Materials Science*, 8(3):352–362.

[13] Ay, L. (2004). *Steel fibrous cement based composites*. Phd thesis, Royal Institute of Technology, Stockholm, Sweden.

[14] Bach, C. (1905). Druckversuche mit eisenbetonkörpern. *Mitteilungen tiber Forschungsarbeiten*, 29.

[15] Bache, H. H. (1979). Shaped article and composite material and method for producing same. European Patent 0010777 A1. November 5, 1979.

[16] Bache, H. H. (1986). Shaped article and composite material and method for producing same. US Patent 4588443. May 13, 1986.

[17] Bache, H. H. (1987). Compact reinforced concrete. International Patent WO 87/07597. December 17, 1987.

[18] Bache, H. H. (1991). Densified cement ultra-fine particle-based materials. In *Proceedings of The Second International Conference on Superplasticizers in Concrete, Ottawa, Ontario, Canada*.

[19] Bamonte, G., Ceraldi, C., and Ermolli, E. R. (2001). Construction of structural schemes for ancient timber structures.

[20] Bauschinger, J. (1876). Versuche mit quadern aus natursteinen (tests with blocks of natural stone). Technical report, Mechanical and Technical Laboratory, Technical University of Munich, vol.6.

[21] BBA (1993). *Expamet hy-rib permanent formwork*. British Board of Agrément.

[22] Bennett, D. F. H. (2002). *Innovations in Concrete*. Thomas Telford, London.

[23] Bérard, A. (1874). Improvement in artificial stone. US Patent 157903. December 15, 1874.

[24] Bergmeister, K., Breen, J. E., Jirsa, J. ., and Kreger, M. E. (1993). Detailig for structural concrete. Technical Report 1127-3F, Center for Transportation Research.

[25] Bhanja, S. and Sengupta, B. (2005). Influence of silica fume on the tensile strength of concrete. *Cement and Concrete Research*, 35(4):743–747.

[26] BIBM, CEMBUREAU, ERMCO, EFCA, and EFNARC (2005). *The European Guidelines for Self Compacting Concrete. Specification, Production and Use*. SCC European Project Group.

[27] Billig, K. (1948). *A Proposal for a Draft Code of Practice for Prestressed Concrete*. Cement and Concrete Association, London.

[28] Birchall, J. D., Howard, A., and Kendall, K. (1982a). A cement spring. *Journal of Materials Science Letters*, 1(3):125–126.

[29] Birchall, J. D., Howard, A. J., and Kendall, K. (1981a). Flexural strength and porosity of cements. *Nature*, 289(5796):388–390.

[30] Birchall, J. D., Howard, A. J., Kendall, K., and Raistrick, J. H. (1983). Cemente composition and product. US Patent 4410366. October 18, 1983.

[31] Birchall, J. D., Kendall, K., and Howard, A. J. (1981b). Cementitious product. European Patent 0021682 B1. January 7, 1981.

[32] Birchall, J. D., Kendall, K., and Howard, A. J. (1982b). Cementitious composition and cementitious product of high flexural strength. European Patent 0055035 A1. June 30, 1982.

[33] Biryukovich, K., Biryukovich, Y., and Biryukovich, D. (1965). *Glass fibre reinforced cement*. Civil Engineering Research Association.

[34] Bonetti, R. A. (2005). Ultimate strength of the local zone in load transfer tests. Master's thesis, Faculty of the Virginia Polytechnic Institute and State University.

[35] Breen, J. E., Burdet, O., Roberts, C., Sanders, D., and Wollmann, G. (1991). Anchorage zone reinforcement for post-tensioned concrete girders. Technical Report Final Report 10-29, National Cooperative Highway Research Program.

[36] Breen, J. E., Fenves, G., and Burdet, O. (1987). Anchorage zone reinforcement for post-tensioned concrete girders. Technical Report Interim Report 10-29, National Cooperative Highway Research Program.

[37] Buitelaar, P. (2004). Ultra high performance concrete: Developments and applications during 25 years. In *Plenary Session International Symposium on UHPC*.

[38] Burdet, O. L. (1990). *Analysis and design of anchorage zones in post-tensioned concrete bridges*. PhD thesis, University of Texas at Austin.

[39] Carrasquillo, P. M. and Carrasquillo, R. L. (1988). Evaluation of the use of current concrete practice in the production of high strength concrete. *ACI Materials Journal*, 85(1):49–54.

[40] Cervenka, J. and Cervenka, V. (2010). *On the uniqueness of numerical solutions of shear failure of deep concrete beams*, pages 281–290. CRC Press. doi:10.1201/b10546-34.

[41] Cervenka, J. and Pappanikolaou, V. (2008). Three dimensional combined fracture-plastic material model for concrete. *International Journal of Plasticity*, 24(12):2192–2220.

[42] Cervenka, V., Cervenka, J., and Sistek, M. (2011). Verification of global safety assited by numerical simulation. In *Proceedings of the fib Symposium Prague 2011*, pages 62–68, Prague.

[43] Cervenka, V. and Ganz, H. R. (2014). Validation of post-tensioning anchorage zones by laboratory testing and numerical simulation. *Structural Concrete*, 15(2):258–268.

[44] Cervenka, V., Jendele, L., and Cervenka, J. (2014). *ATENA Program Documentation, Part 1, Theory*. Cervenka Consulting, Ltd., Prague, www.cervenka.cz.

[45] Cheyrezy, M., Maret, V., and Frouin, L. (1995). Microstructural analysis of RPC (reactive powder concrete). *Cement and Concrete Research*, 25(7):1491–1500.

[46] Considère, A. (1903). *Experimental Researches on Reinforced Concrete*. McGraw Publishing Company, New York.

[47] Considère, A. (1907a). Le béton fretté et ses aplications. *Le Génie civil : revue générale des industries françaises et étrangères*. 50(15):246-248, 50(16):260-262, 50(17):289-290, 50(18):298-302.

[48] Considère, A. (1907b). Le béton fretté et ses aplications. *Le Génie civil : revue générale des industries françaises et étrangères*, 50(16):260–262.

[49] Constantinesco, G. (1943). Substitute for metal castings. GB Patent 568066. Feb 12, 1943.

[50] Constantinesco, G. (1954). Reinforced concrete. US Patent 2677955. May 11, 1954.

[51] CSI Computers and Structures Inc. (2007). Sap2000 advanced: Static and dynamic finite element analysis of structures. Analysis Reference Manual.

[52] Denneman, E., Kearsley, E. P., and Visser, A. T. (2011). Splitting tensile test for fibre reinforced concrete. *Materials and Structures*, 44:1441–1449.

[53] Dischinger, F. (1934). Eisenbetontragwerk, insbesondere für balkenbrücken. DE Patent 727429. December 8, 1934.

[54] Dischinger, F. (1935). Improvements relating to reinforced concrete beams, girders, bridges and the like. GB Patent 464361. December 9, 1935.

[55] Dobromil, P. and Cervenka, J. (2015). *ATENA Program Documentation, Part 11, Troubleshooting Manual*. Cervenka Consulting, Ltd., Prague, www.cervenka.cz.

[56] Dooley, S. (2004). *The development of material-adapted structural form*. Phd thesis, École Polythecnique Fédérale de Lausanne, Lausanne.

[57] Dugat, J., Roux, N., and Bernier, G. (1996). Mechanical properties of reactive powder concretes. *Materials and Structures*, 29(4):233–240.

[58] Eddy, B. W. (1894). Composition for artificial stone. US Patent 531520. December 25, 1885.

[59] EN 10002-1 (2001). *Metallic materials - Tensile testing - Part 1: Method of test at ambient temperature*. EN 10002-1:2001. European Committee for Standardization, Brussels.

[60] EN 12350-8 (2010). *Testing fresh concrete - Part 8: Self-compacting concrete - Slump-flow test*. EN 12350-8-2010. European Committee for Standardization, Brussels.

[61] EN 12350-9 (2010). *Testing fresh concrete - Part 9: Self-compacting concrete - V-funnel test*. EN 12350-8-2010. European Committee for Standardization, Brussels.

[62] EN 12390-1 (2000). *Testing hardened concrete - Part 1: Shape, dimensions and other requirements for specimens and moulds*. EN 12390-1:2000. European Committee for Standardization, Brussels.

[63] EN 12390-3 (2001). *Testing hardened concrete - Part 3: Compressive strenght of test specimens*. EN 12390-3:2001. European Committee for Standardization, Brussels.

[64] EN 12390-5 (2000). *Testing hardened concrete - Part 5: Flexural strength of test specimens*. EN 12390-5:2000. European Committee for Standardization, Brussels.

[65] EN 12390-6 (2000). *Testing hardened concrete - Part 6: Tensile splitting strenght of test specimens*. EN 12390-6:2000. European Committee for Standardization, Brussels.

[66] EN 14651 (2007). *Test method for metallic fibre concrete - Measuring the flexural tensile strenght (limit of proportionality (LOP), residual)*. EN 14651:2007. European Committee for Standardization, Brussels.

[67] EN 1992-1-1 (2004). *Eurocode 2 - Design of Concrete Structures - Part 1.1: General rules and rules for buildings*. EN 1992-1-1:2004. European Committee for Standardization, Brussels.

[68] EN 1992-2 (2005). *Eurocode 2 - Design of Concrete Structures - Concrete bridges - Design and detailing rules*. EN 1992-2:2005. European Committee for Standardization, Brussels.

[69] Etheridge, H. (1933). Concrete construction. US Patent 1913707. June 13, 1933.

[70] European Organisation for Technical Approvals (2002). *Guideline for European Technical Approval of Post-Tensioning Kits for Prestressing of Structures*. ETAG 013. EOTA, Brussels.

[71] Ficklen, W. (1914). Improvements in reinforced structures and wearing surfaces of hydraulic, bituminous, or the like cement, concrete, asphalt or the like. GB Patent 111754. May 13, 1914.

[72] FIP Recomendation (1993). *Recommendations for the acceptance of post-tensioning systems*. Federation Internationale de la Precontrainte, London.

[73] Freyssinet, E. (1928). Procédé de fabrication de pièces en béton armé. French Patent 680547. October 2, 1928.

[74] Freyssinet, E. (1929). Process for the manufacture of articles of reinforced concrete. GB Patent 338864. June 18, 1929.

[75] Freyssinet, E. and Seailles, J. (1932). Mortar or concrete article manufacture. Canadian Patent CA 325205. August 16, 1932.

[76] Ganz, H.-R. (2008). Prestressed structural concrete: New developments and applications. In Lourenço, P., Barros, J., S., C. J., Pipa, M., Faria, R., and Ferreira, M., editors, *Encontro Nacional Betão Estrutural 2008*, pages 3–20, Guimarães, Portugal.

[77] Gergely, P. and Sozen, M. A. (1967). Design of anchorage-zone reinforcement in prestressed concrete beams. *PCI Journal*, 12(3):63–75.

[78] Gergely, P., Sozen, M. A., and Siess, C. P. (1963). The effect of reinforcement on anchorage zone cracks in prestressed concrete members. Issued as a Part of Progress Report no. 12 of the Investigation of prestressed reinforced concrete for highway bridges, University of Illinois, Urbana, Illinois.

[79] Gomes, F. and Nunes, S. (2010). Betão auto-compactável reforçado com fibras. aplicação em zonas de ancoragem de cabos de pré-esforço.

[80] Graham, G. M. (1911). Reinforced concrete. US Patent 983274. February 7, 1911.

[81] Graybeal, B. and Hartmann, J. (2003). Ultra-high performance concrete material properties. In *Proceedings of The Transportation Research Board Conference*.

[82] Grob, J. and Thürlimann, B. (1976). *Ultimate Strength and Design of Reinforced Concrete Beams under Bending and Shear*, volume 63 of *Institut für Baustatik und Konstruktion*, chapter 1, pages 107–120. Birkhäuser Basel.

[83] Groth, P. and Nemegeer, D. (1999). The use of steel fibres in self-compacting concrete. In Skarendahl, Å. and Petersson, Ö., editors, *Proceedings of the first international RILEM symposium on self-compacting concrete*, pages 497–507, Stockholm, Sweden.

[84] Grünewald, S. (2004). *Performance-based design of self-compacting fibre reinforced concrete*. Phd thesis, Delft University of Technology, Delft, The Netherlands.

[85] Guyon, Y. (1953). *Prestressed Concrete*. John Wiley and Sons, New York.

[86] Haroon, S., Yazdani, N., and Tawfiq, K. (2006). Posttensioned anchorage zone enhancement with fiber-reinforced concrete. *Journal of Bridge Engineering*, 11(5):566–572.

[87] Hawkins, N. M. (1968a). The bearing strength of concrete loaded trough flexible plates. *Magazine of Concrete Research*, 20(63):95–102.

[88] Hawkins, N. M. (1968b). The bearing strength of concrete loaded trough rigid plates. *Magazine of Concrete Research*, 20(62):31–40.

[89] Hawkins, N. M. (1970). The bearing strength of concrete for strip loadings. *Magazine of Concrete Research*, 22(71):87–98.

[90] Hennebique, F. (1892). Combinaison particulière du métal et du ciment en vue de la création de poutraisons très légères et de haute résistance.

[91] Hennebique, F. (1897). Improvements in the construction of joists, girders, and the like of cement strengthned with iron or the like.

[92] Holschemacher, K., Dehn, F., Klotz, S., and Weiße, D. (2004). Ultra high strength concrete under concentrated loading. In Schmidt, M., Fehling, E., and Geisenhanslüke, C., editors, *International Symposium on Ultra-High Performance Concrete*, pages 471–480. University of Kassel, Germany.

[93] Homrich, J. R. and Naaman, A. E. (1988). Stress-strain properties of SIFCON in uniaxial compression and tension. Technical report, Univerity of Michigan.

[94] Hyland, M. W. and Chen, W.-F. (1970). Bearing capacity of concrete blocks. *ACI Journal Proceedings*, 67(3):228–236.

[95] Ibell, T. J. and Burgoyne, C. J. (1993). Experimental investigation of behaviour of anchorage zones. *Magazine of Concrete Research*, 45(165):281–292.

[96] Ichiki, Y. (1950). Experimental studies on reinforced concrete rockers: on the strength of contact surface. *Memoirs of the Faculty of Engineering, Hokkaido University*, 8(3-1):41–66.

[97] Imam, M., Vandewalle, L., and Mortelmans, F. (1995). Are current concrete strength tests suitable for high strength concrete? *Materials and Structures*, 28(7):384–391.

[98] Johnson, S. (2006). Analytical modeling of fiber reinforced post-tensioned concrete anchorage zones. Msc thesis, The Florida State University, FAMU-FSU College of Engineering.

[99] Kelly, A. (1972). Reinforcement of structural materials by long strong fibres. *Metallurgical and Materials Transactions B*, 3(9):2313–2325.

[100] Khayat, K. H. and Roussel, Y. (1999). Testing and performance of fiber-reinforced, selfconsolidating concrete. In Skarendahl, Å. and Petersson, Ö., editors, *Proceedings of the first international RILEM symposium on self-compacting concrete*, pages 509–521, Stockholm, Sweden.

[101] Kim, Y. Y., Kong, H.-J., and Li, V. C. (2003). Design of engineered cementitious composite suitable for wet-mixture shotcreting. *ACI Materials Journal*, 100(6):511–518.

[102] Kleinlogel, A. (1921). Verfahren zur herstellung einer künstlichen bearbeitungsfähigen eisenmasse (method of producing a workable artificial iron mass). German Patent DE 338959C. July 8, 1921.

[103] Komendant, A. E. (1952). *Prestressed Concrete Structures*. McGraw-Hill, New York, first edition.

[104] Kong, H.-J., Bike, S. G., and Li, V. C. (2003). Constitutive rheological control to develop a self-consolidating engineered cementitious composite reinforced with hydrophilic poly(vinyl alcohol) fibers. *Cement and Concrete Composites*, 25(3):333–341.

[105] Kupfer, H. (1964). Erweiterung der mörschschen fachwerkanalogie mit hilfe des prinzips vom minimum formanderungarbeit (extension to the truss-analogy of Mörsch using the principle of minimum potential energy). *CEB Bulletin d'Information*, No. 40.

[106] Lampert, P. and Thürlimann, B. (1971). Ultimate strength and design of reinforced concrete beams in torsion and bending. *IABSE Publications*, 31:107–131.

[107] Lankard, D. R. (1982). Highly reinforced refractory concrete with 4-20 volume steel fibers. US Patent 4366255. December 28, 1982.

[108] Lankard, D. R. (1984). Properties, applications: Slurry infiltrated fiber concrete (SIFCON). *Concrete International*, 6(12):44–47.

[109] Larrard, F. and Sedran, T. (1994). Optimization of ultra-high performance concrete by the use of a packing model. *Cement and Concrete Research*, 24(6):997–1009.

[110] LBA (1899a). Troisième congrès du béton de ciment armé. *Le Béton Armé*, 1(12):1–4.

[111] LBA (1899b). Troisième congrès du béton de ciment armé. *Le Béton Armé*, 1(10):1–4.

[112] LBA (1901). Le béton armé au tribunal civil. *Le Béton Armé*, 3(32):1–9.

[113] Leonhardt, F. (1965). Reducing the shear reinforcement in reinforced concrete beams and slabs. *Magazine of Concrete Research*, 17(53):187–198.

[114] Leung, C. K. Y., Zhang, X., and Xia, Q. (2009). The application of pseudo-ductile cementitious composites in the anchorage zone of post-tensioned concrete members. *Materials and Structures*, 42:1221–1231.

[115] Li, V. C. (1993). From micromechanics to structural engineering - the design of cementitous composites for civil engineering applications. *JSCE Journal of Structural Mechanics and Earthquake Engineering*, 10(2):37–48.

[116] Li, V. C. (1998). Engineered cementitious composites (ECC) - tailored composites through micromechanical modeling. In Banthia, N., Bentur, A., and Mufti, A., editors, *Fiber Reinforced Concrete: Present and the Future*, pages 64–97, Montreal. Canadian Society of Civil Engineers.

[117] Li, V. C. (2002). Advances in ECC research. *ACI Special Publication*, 206.

[118] Li, V. C. (2003). On engineered cementitious composites (ECC). *Journal of Advanced Concrete Technology*, 1(3):215–230.

[119] Li, V. C. (2008). Engineered cementitious composite (ECC): Material, structural, and durability performance. In Nawy, E., editor, *Concrete Construction Engineering Handbook*, chapter 24. CRC Press, second edition.

[120] Li, V. C. and Fischer, G. (2002). Reinforced ECC - an evolution from materials to structures. In *1st fib congress - Concrete Structures in the 21st Century*, pages 105 –122, Osaka.

[121] Li, V. C., Fischer, G., and Lepech, M. (2009). Shotcreting with ECC. In Kusterle, W., editor, *Spritzbeton-Tagung Proceedings of CD*.

[122] Li, V. C. and Kanda, T. (1998). Engineered cementitious composites for structural applications. *ASCE Journal of Materials in Civil Engineering*, 10(2):ASCE Journal of Materials in Civil Engineering.

[123] LNEC E 397 (1993). *Hardened concrete - Determination of the modulus of elasticity of concrete in compression*.

[124] LNEC E 398 (1993). *Hardened concrete - Determination of the shrinkage and the swelling*.

[125] Love, A. E. H. (1906). *A treatise on the mathematical theory of elasticity*. Cambridge University Press, second edition.

[126] Malaikah, A. S. (2005). Effect of specimen size and shape on the compressive strength of high strength concrete. *Pertanika Journal of Science & Technology*, 13(1):87–96.

[127] Marchão, C. A., Nunes, S. B., Lúcio, V. G., Brás, A. A., and Figueiras, J. A. (2012). Development and application of a high performance fibre reinforced self-compacting concrete in post-tensioning anchorage zones. In Barros, J., Sena-Cruz, J., Ferreira, R., Valente, I., Azenha, M., and Dias, S., editors, *Proceedings of The Eighth RILEM International Symposium on Fibre Reinforced Concrete (BEFIB2012): Challenges and Opportunities*, pages 125–126, Guimarães, Portugal. RILEM Publications SARL.

[128] Marković, I. (2006). *High-Performance Hybrid-Fibre Concrete - Development and Utilisation*. Phd thesis, Delft University of Technology, Delft, The Netherlands.

[129] Marti, P. (1985a). Basic tools of reinforced concrete beam design. *ACI Journal Proceedings*, 82(1):46–56.

[130] Marti, P. (1985b). Truss models in detailing. *Concrete International*, 7(12):66–73.

[131] Martin, G. C. (1927). Method of forming pipe. US Patent 1633219. June 21, 1927.

[132] Meischke-Smith, W. (1920). Ferroconcrete construction. US Patent 1349901. August 17, 1920.

[133] Meyerhof, G. G. (1953). The bearing capacity of concrete and rock. *Magazine of Concrete Research*, 4(12):107–116.

[134] Miao, B., Chern, J. C., and Yang, C. A. (2003). Influences of fiber content on properties of self-compacting steel fiber reinforced concrete. *Journal of the Chinese Institute of Engineers*, 26(4):523–530.

[135] Middendorf, K. H. (1963). Practical aspects of end zone bearing of post-tensioning tendons. *PCI Journal*, 8(4):57–62.

[136] Mielenz, R. C. (1984). History of chemical admixtures for concrete. *Concrete International*, 6(4):40–53.

[137] Mitchell, D. and Collins, M. P. (1974). Diagonal compression field theory-a rational model for structural concrete in pure torsion. *ACI Journal Proceedings*, 71(8):396–408.

[138] Model Code 2010 (2012). *Model Code 2010 - Final Draft, Vol. 1.* Bulletin 65. Fédération Internationale du Béton, Lausanne, Switzerland.

[139] Mörsch, E. (1907a). Versuche über die schubwirkungen bei eisenbetonträgern. *Deutsche Bauzeitung*, 41(30):207–212.

[140] Mörsch, E. (1907b). Versuche über die schubwirkungen bei eisenbetonträgern. *Deutsche Bauzeitung*, 41(32):223–228.

[141] Mörsch, E. (1907c). Versuche über die schubwirkungen bei eisenbetonträgern. *Deutsche Bauzeitung*, 41(35):241–243.

[142] Mörsch, E. (1908). *Der Eisenbetonbau: Seine Theorie und Anwendung.* K. Wittwer, Stuttgart, 3rd edition.

[143] Mörsch, E. (1909). *Concrete-steel Construction (Der Eisenbetonbau).* The Engineering news publishing company, New York, third edition.

[144] Mörsch, E. (1924). über die berechnung der gelenkquader. *Beton-und Eisen*, 12. pp. 156-161.

[145] Mörsch, E. and Wayss & Freytag, AG (1906). *Der Eisenbetonbau: Seine Theorie und Anwendung*. K. Wittwer, Stuttgart, 2nd edition.

[146] Müller, P. (1976a). Failure mechanisms for reinforced concrete beams in torsion and bending. *IABSE publications*, 36:147–163.

[147] Müller, P. (1976b). *Failure Mechanisms for Reinforced Concrete Beams in Torsion and Bending*, volume 65 of *Institut für Baustatik und Konstruktion ETH Zürich*, chapter 1, pages 147–163. Birkhäuser Basel.

[148] Müller, P. (1978). Plastische berechnung von stahlbetonscheiben und -balken. Technical Report 83, Institut für Baustatik und Konstruktion ETH Zürich.

[149] Mummery, L. (1992). *Surface Texture Analysis: The Handbook*. Hommelwerke GmbH.

[150] Muttoni, A., Schwartz, J., and Thürlimann, B. (1997). *Design of Concrete Structures With Stress Fields*. U.S. Government Printing Office.

[151] Muttoni, A., Schwartz, J., and Thürlimann, B. (1988). *Bemessen und Konstruieren von Stahlbetontragwerken mit Spannungsfeldern*. Vorlesungsunterlagen Stahlbeton AK, ETH-Zürich.

[152] Naaman, A. E. (1985). Fiber reinforcement for concrete. *Concrete International*, 7(3):21–25.

[153] Naaman, A. E. (1987). High performance fiber reinforced cement composites. In *Proceedings of the IABSE Symposium on Concrete Structures for the Future*, pages 371–376.

[154] Naaman, A. E. (2008). *High performance fiber reinforced cement composites*, volume 1 of *Engineering Materials for Technological Needs*, chapter 3, pages 91–154. World Scientific Publishing Co. Pte. Lda, Singapore.

[155] Neville, A. M. (1975). *Properties of Concrete*. Addition Wesley Lapman Ltd, England, 3rd edition. p. 252.

[156] Niyogi, S. K. (1973). Bearing strength of concrete - geometric variations. *ASCE Journal of the Structural Division*, 99(ST7):1471–1490.

[157] Niyogi, S. K. (1975). Bearing strength of reinforced concrete blocks. *ASCE Structural Division Journal*, 105(ST5):1125–1137.

[158] Okamura, H. (1997). Self-compacting high-performance concrete. *Concrete International*, 19(7):50–54.

[159] Okamura, H. and Ouchi, M. (2003). Self-compacting concrete. *Journal of Advanced Concrete Technology*, 1(5):5–15.

[160] Okamura, H., Ozawa, K., and Ouchi, M. (2000). Self-compacting concrete. *Structural Concrete*, 1(1):3–17.

[161] Okamura, K., Maekawa, and Mishima, T. (2005). Performance based design for self-compacting structural high-strength concrete. *ACI Special Publication*, 228:13–34.

[162] Ozawa, K., Maekawa, K., and Okamura, H. (1992). Development of high performance concrete. *Journal of the Faculty of Engineering, University of Tokyo*, XLI(3):381–439.

[163] Palladio, A. (1570). *Quattro libri dell'architettura (Four Books on Architecture)*. D. de' Franceschi, Venetia.

[164] Porter, H. F. (1910). The preparation of concrete - from selection of materials to final deposition. *ACI Journal Proceedings*, 6(2):287–303.

[165] Ramos, A., Almeida, A., Faria, D., Fernandes, H., Inácio, M., Gouveia, N., Mamede, N., Azevedo, N., and Lúcio, V. (2014). Flat - comportamento de lajes fungiformes sujeitas a acções cíclicas e sísmicas. Project Final Report PTDC/ECM/114492/2009, Fundação da Faculdade de Ciências e Tecnologia da Universidade Nova de Lisboa.

[166] Randl, N. (2013). Design recommendations for interface shear transfer in fib Model Code 2010. *Structural Concrete*, 14(3):230–241.

[167] Richard, P. and Cheyrezy, M. (1995). Composition of reactive powder concretes. *Cement and Concrete Research*, 25(7):1501–1511.

[168] Richart, F. E., Brandtzaeg, A., and Brown, R. L. (1928). A study of the failure of concrete under combined compressive stresses. Technical Report bulletin no.185, University of Illinois, Urbana.

[169] Richart, F. E., Brandtzaeg, A., and Brown, R. L. (1929). Failure of plain and spirally reinforced concrete in compression. Technical Report bulletin no.190, University of Illinois, Urbana.

[170] Ritter, W. (1899). Die bauweise hennebique (the hennebique design method). *Schweizerische Bauzeitung*, 33(5/6/7):41–43, 49–52, 59–61.

[171] Rogowsky, D. and Marti, P. (1996). *Detailing for Post-Tensioning*. VSL Report Series 3. VSL International Ltd., Berne, Switzerland.

[172] Romualdi, J. P. (1969). Two-phase concrete and steel material. US Patent 3429094. February 25, 1969.

[173] Romualdi, J. P. and Batson, G. B. (1963). Behavior of reinforced concrete beams with closely spaced reinforcement. *ACI Journal Proceedings*, 60(6):775–790.

[174] Romualdi, J. P. and Mandel, J. A. (1964). Tensile strength of concrete affected by uniformly distributed and closely spaced short lengths of wire reinforcement. *ACI Journal Proceedings*, 61(6):657–672.

[175] Rossi, P. (1997). High performance multimodal fiber reinforced cement composites (HPMFRCC): the LCPC experience. *ACI Materials Journal*, 94(6):478–783.

[176] Rossi, P., Acker, P., and Malier, Y. (1987). Effect of steel fibres at two different stages: The material and the structure. *Materials and Structures*, 20(6):436–439.

[177] Rotinoff, A. G. (1926). Improvements relating to reinforced concrete. GB Patent 252975. June 10, 1926.

[178] Roy, D. M. and Gouda, G. R. (1973). High strength generation in cement pastes. *Cement and Concrete Research*, 3(6):807–820.

[179] Sanders, D. H. (1990). *Design and behavior of anchorage zones in post-tensioned concrete members*. PhD thesis, University of Texas at Austin.

[180] Santos, P. M. D. and Júlio, E. N. B. S. (2013). A state-of-the-art review on roughness quantification methods for concrete surfaces. *Construction and Building Materials*, 38(0):912–923.

[181] Santos, P. M. D. and Júlio, E. N. B. S. (2014). Interface shear transfer on composite concrete members. *ACI Structural Journal*, 111(1):113–121.

[182] Santos, P. M. D., Júlio, E. N. B. S., and Silva, V. D. (2007). Correlation between concrete-to-concrete bond strength and the roughness of the substrate surface. *Construction and Building Materials*, 21(8):1688–1695.

[183] Sato, Y., Van Mier, J. G., and Walraven, J. C. (2000). Mechanical characteristics of multi-modal fiber reinforced cement based composites. In Rossi, P. and Chanvillard, G., editors, *Fifth RILEM Symposium on Fibre-Reinforced Concretes*, pages 791–800. RILEM Publications SARL.

[184] Schlaich, J. and Schäfer, K. (1984). Towards a consistent design of reinforced concrete structures.

[185] Schlaich, J. and Schafer, K. (1989). *Konstruieren im Stahlbetonbau (Design for Concrete Structures)*. Betonkalender, Berlin.

[186] Shelson, W. (1957). Bearing capacity of concrete. *ACI Journal Proceedings*, 54(11):405–414.

[187] Shi, C., Mo, Y. L., and Dhonde, H. B. (2008). *High performance concrete*, volume 1 of *Engineering Materials for Technological Needs*, chapter 2, pages 19–90. World Scientific Publishing Co. Pte. Lda, Singapore.

[188] Stang, H. and Li, V. (1999). Extrusion of ECC-material. In Reinhardt, H. W. and Naaman, A. E., editors, *Third International RILEM Workshop on High Performance Fiber Reinforced Cement Composites*, pages 203 – 211. RILEM Publications SARL.

[189] Suzuki, K. and Nakatsuka, T. (1982). Estimation of bearing strength of reinforced anchorage zone in post-tensioned prestressed concrete members. *Transactions of the Architectural Institute of Japan*, 315:17–28.

[190] Suzuki, K. and Nakatsuka, T. (1984). Estimation of bearing strength of reinforced anchorage zone in post-tensioned prestressed concrete members : Anchorage zone with the combination of square bearing plate, square loaded surface and circular spiral reinforcement. *Transactions of the Architectural Institute of Japan*, 341:19–26.

[191] Talbot, A. N. (1907). Tests of concrete and reinforced concrete columns: Series of 1907. Technical Report bulletin no.20, University of Illinois, Urbana.

[192] Talbot, A. N. (1909). Tests of reinforced concrete beams. series of 1906. Technical Report bulletin no. 31, Urbana.

[193] Thürlimann, B. (1979). Plastic analysis of reinforced concrete beams. *IABSE reports of the working commissions*, 28:71–90.

[194] Van Rickstal, F. (2000). *Grout injection of masonry, scientific approach and modeling*. PhD thesis, Katholieke Universiteit Leuven.

[195] Vecchio, F. J. and Collins, M. P. (1986). The modified compression-field theory for reinforced concrete elements subjected to shear. *ACI Journal Proceedings*, 83(2):219–231.

[196] Vekey, R. C. and Majumdar, A. J. (1970). Interfacial bond strength of glass fibre reinforced cement composites. *Journal of Materials Science*, 5(2):183–185.

[197] Vos, E. (1983). *Influence of loading rate and radial pressure on bond in reinforced concrete, a numerical and experimental approach*. PhD thesis, Technical University of Delft.

[198] VSL International (2008). Use of GC anchorages. Unpublished Internal Memorandum.

[199] VSL International (2012). *European Technical Approval No. ETA-06/0006 - Version of 4th May 2012*. SETRA. European Organisation for Technical Approvals, Paris.

[200] Walraven, J. (2009). High performance concrete: a material with a large potential. *Journal of Advanced Concrete Technology*, 7(2):145–156.

[201] Weakley, R. D. (1912). Bonding means for reinforced concrete structures. US Patent 1046913. December 10, 1912.

[202] Wheen, R. and Rogers, D. (1978). The bearing strength of plain concrete. *Materials and Structures*, 11(1):11–20.

[203] Whitacre, J. J. (1908). Concrete reinforcement. US Patent 906479. December 8, 1908.

[204] Withey, M. O. (1907). Tests of plain and reinforced concrete, series of 1906. Bulletin of the University of Wisconsin, Engineering Series IV(1), University of Wisconsin.

[205] Withey, M. O. (1908). Tests of plain and reinforced concrete, series of 1907. Bulletin of the University of Wisconsin, Engineering Series IV(2), University of Wisconsin.

[206] Wollmann, G. P. (1992). *Anchorage Zones in Post-Tensioned Concrete Structures*. PhD thesis, The University of Texas at Austin.

[207] Wollmann, G. P. and Roberts-Wollmann, C. L. (2000). *Anchorage Zone Design: Preprint of Chapter VIII, Post-tensioning Manual*. Post-Tensioning Institute, sixth edition.

[208] Wurm, P. and Daschner, F. (1977). Versuche uber teilflaechenbelastung von normalbeton. Technical report, Deutscher Ausschuss fur Stahlbeton.

[209] Wurm, P. and Daschner, F. (1983). Teilflaechenbelastung von normalbeton verusche an bewehrten scheiben. Technical report, Deutscher Ausschuss fur Stahlbeton.

[210] Yettram, A. L. and Robbins, K. (1969). Anchorage zone stresses in axially post-tensioned members of uniform rectangular section. *Magazine of Concrete Research*, 21:103–112.

[211] Yi, S.-T., Yang, E.-I., and Choi, J.-C. (2006). Effect of specimen sizes, specimen shapes, and placement directions on compressive strength of concrete. *Nuclear Engineering and Design*, 236(2):115–127.

[212] Yun, Y. M. (2005). Evaluation of ultimate strength of post-tensioned anchorage zones. *Journal of Advanced Concrete Technology*, 3(1):149–159.

[213] Zhou, F. P., Barr, B. I. G., and Lydon, F. D. (1995). Fracture properties of high strength concrete with varying silica fume content and aggregates. *Cement and Concrete Research*, 25(3):543–552.

[214] Zitkevič, N. (1917). Improvements in reinforced concrete. GB Patent 515003. November 23, 1939.